

ULTRASONIC AND GEOCHEMICAL
CHARACTERISATION OF ASPHALTENE
AGGREGATION IN WATER-IN-OIL EMULSIONS

ALEKSANDRA SVALOVA

Thesis submitted for the degree of
Doctor of Philosophy



*School of Natural and Environmental Sciences
Newcastle University
Newcastle upon Tyne
United Kingdom*

September 2018

Acknowledgements

The last four years have been outstanding and of that I have little to attribute towards myself, thus I am in debt of acknowledging the people who helped me on this journey.

Firstly, my deepest regards go to my supervisors Nick Parker and Geoff Abbott. I am grateful for their trust and faith in me, especially at the beginning of my PhD, as my need for change was as deep as my fear of it. I am thankful to Nick for taking the risk of persuading me to apply to this project and to Geoff whose guidance helped me to grow as a researcher. Furthermore, this work would not have been possible without the collaborative effort of Melvin Holmes and Megan Povey from the University of Leeds, thus my regards go to them also.

It has been amazing to work with the lab technicians Dave Earley, Paul Donohoe and Berni Bowler- you have been my support at times of smothering confusion. I will miss your wonderful sense of humor and an unconditional willingness to help. Despite all the glassware I have broken, your patience towards me has remained (almost) intact.

It truly takes the entire village to raise a child and I am very grateful to my friends, colleagues and teachers in the Geosciences and Maths departments. Thank you to David Walshaw for a sense of direction in my seemingly never-ending statistical shenanigans. I am grateful to Dominic White who has been my mentor and a lovely friend. Few are aware how crucial you have been to keeping me in one piece during times of struggle. I am very grateful to the communities that have supported and inspired me, including the Universities' Catholic Chaplaincy and St Mary's Cathedral Choir. I did my best to cause no mischief and follow the notes in the right order, most of the time.

My family has been crucial to supporting me too. Their love, wisdom and patience have been instrumental to my success and I really cannot thank them enough. Thank you to Clement Lee who were by my side in a cold office of the Cassie Building as I was completing my thesis write-up, day or night.

A PhD is little but a dent in the current barriers of our understanding of the Universe. What can one hope for by completing it? Only to fall in love with wisdom, as philosophy is the love of it.

Abstract

Asphaltenes constitute the heaviest, most polar and aromatic fraction of petroleum crucial to the formation of highly-stable water-in-crude oil emulsions. The latter occur during petroleum production as well as spills and cause difficulties to efficient remediation practice. This work investigates the aggregation of asphaltene ‘monomers into nanoaggregates, the latter analogous to surfactant micelles. It is generally accepted in the literature that in nanoaggregate form, asphaltenes create elastic layers around water droplets enhancing the stability of emulsions. A better understanding of the nanoaggregation process would enable a more efficient spill remediation practice.

Ultrasonic characterisation is deployed to infer asphaltene nanoaggregation in toluene. Ultrasonic velocity measurement is a high-resolution non-invasive tool in colloidal analysis shown to successfully identify surfactant micelle formation and has been applied to asphaltene nanoaggregation in toluene. The high sensitivity of acoustic velocity to molecular rearrangements and ease in implementation renders it an attractive method to study asphaltene phase properties. Currently, the onset of aggregate formation is thought to correspond to an intersection of two concentration-ultrasonic velocity regressions that suggest a critical nanoaggregate concentration. In this work, measurements indicate a variation in the proximity of nanoaggregation which could be investigated further. This uncertainty is attributed to physico-chemical heterogeneity of the asphaltene fraction driven by variation in molecular size and a critical nanoaggregation region is proposed.

Asphaltenes were obtained from four petroleum samples and treated with ruthenium ion catalysed oxidation to obtain information about their molecular structure. Statistical analysis was performed to investigate the coupling between asphaltene structures and velocity measurements and their impact on aggregation. A geochemical characterisation of the parent oils was also performed. Finally, Bayesian modelling of the ultrasonic measurements was performed to estimate the statistical likelihoods of a single aggregation concentration versus the aggregation region hypotheses.

Contents

1	Introduction	1
2	Colloids and Surfactants	11
2.1	An Introduction to Surfactants	11
2.2	Micellarisation	13
2.2.1	<i>The critical micelle concentration</i>	18
2.2.2	<i>Multiple micellarisation</i>	19
2.3	An Introduction to Colloids	20
2.4	Kinetics of Colloidal Interactions	21
2.4.1	<i>Electrokinetic interactions</i>	21
2.4.2	<i>Steric stabilisation</i>	23
2.4.3	<i>Gibbs-Marangoni effect</i>	23
2.4.4	<i>Droplet skin formation</i>	24
2.4.5	<i>Pickering stabilisation</i>	24
3	Asphaltenes	26
3.1	Introduction	26
3.2	The Yen-Mullins Model of Petroleum Asphaltenes	28
3.2.1	<i>Asphaltene monomers</i>	28
3.2.2	<i>Asphaltene nanoaggregates</i>	31
3.3	Nanoaggregates Versus Surfactant Aggregates	32
4	Petroleum Biomarkers	37
4.1	Introduction	37
4.2	Stereochemistry of Biomarkers	40
4.2.1	<i>Hopanes and steranes in petroleum</i>	41
4.3	Biodegradation of Biomarkers	41
4.3.1	<i>Aerobic bioegradation</i>	42

4.3.2	<i>Anaerobic biodegradation</i>	43
4.4	Compositional Alteration	44
4.5	Biomarkers in Asphaltenes	47
5	Petroleum Maturity and Source Assessment Using Compound Ratios	49
5.1	Maturity Assessment Using Non-Biomarker ratios	49
5.1.1	<i>Saturated hydrocarbon fraction</i>	49
5.1.2	<i>Aromatic hydrocarbon fraction</i>	50
5.2	Maturity Assessment Using Biomarker Ratios	50
5.2.1	<i>Saturated hydrocarbon fraction</i>	50
5.2.2	<i>Aromatic hydrocarbon fraction</i>	52
5.3	Source Assessment Using Compound Ratios	53
6	Ultrasonic Characterisation of Molecular Aggregation	56
6.1	Introduction	56
6.2	Acoustic Propagation in Homogeneous Fluids and Colloids	57
6.2.1	<i>Fundamentals of acoustic wave propagation</i>	57
6.2.2	<i>Acoustic propagation through a single continuous fluid</i>	59
6.2.3	<i>Ultrasonic propagation through a colloid</i>	61
6.3	Velocity Measurement Methods	62
6.3.1	<i>Pulse-echo/pitch-catch</i>	62
6.3.2	<i>Acoustic resonance</i>	63
6.4	Micelle Detection Using Ultrasonic Velocity Measurements	65
7	Geochemical Characterisation	68
7.1	Cleaning and Safety Procedures	68
7.2	Asphaltene Precipitation	68
7.3	Ruthenium Ion Catalysed Oxidation of Asphaltenes	69
7.4	Maltene Analysis	70
7.5	Analytical Instruments	71
8	Ultrasonic Characterisation	72
8.1	Sample Preparation	72
8.2	Analytical Instruments	73
8.3	Constrained Optimization with Penalty Functions	75

9	Bayesian Inference of Asphaltene Nanoaggregation	78
9.1	Introduction to Empirical Bayesian Inference	79
9.2	Model Setup	80
9.2.1	<i>Asphaltene nanoaggregation single-changepoint model</i>	81
9.2.2	<i>Asphaltene nanoaggregation two-changepoint model with a Brownian bridge</i>	83
10	Geochemical Characterisation of Petroleum Samples	88
10.1	Maturity Assessment of the Sample Oils	88
10.2	Source Assessment of the Sample Oils	92
10.3	Biodegradation Assessment of the Sample Oils	95
11	Ruthenium Ion Catalysed Oxidation	105
11.1	Ruthenium Ion Catalysed Oxidation of Alkylated Mono- and Diaromatic Standard Compounds	105
11.2	Ruthenium Ion Catalysed Oxidation of Asphaltenes	114
11.2.1	<i>Fatty acid methyl esters and di-fatty acid dimethyl esters</i>	114
11.2.2	<i>Alpha-branched fatty acid methyl esters</i>	115
11.2.3	<i>Phenylalkylketones and benzenecarboxylic acid methyl esters</i>	116
12	Ultrasonic Characterisation	124
12.1	Ultrasonic Characterisation of Cetyltrimethylammonium Bromides	124
12.1.1	<i>Pre-processing of velocity data</i>	124
12.1.2	<i>The critical micelle concentration estimation in cetyltrimethylammonium bromide aqueous solutions</i>	128
12.2	Ultrasonic Characterisation of Asphaltenes	129
12.2.1	<i>Pre-processing of velocity data</i>	132
12.2.2	<i>Constrained optimisation of the CNR</i>	135
12.2.3	<i>Results of the asphaltene CNR estimation</i>	139
13	Empirical Bayesian Inference of Asphaltene Nanoaggregation	141
13.1	Model Calibration with Synthetic Data	141
13.1.1	<i>One changepoint model</i>	141
13.1.2	<i>Two-changepoint model with a Brownian bridge</i>	146
13.2	Experimental Data	150
13.2.1	<i>Prior elicitation</i>	150

13.2.2	<i>One changepoint model</i>	151
13.2.3	<i>Brownian bridge model</i>	154
13.2.4	<i>Model comparison</i>	156
14	General Discussion	161
15	Conclusions	169
A	Supplementary Material for Geochemical Characterisation of Maltenes	223
B	Supplementary Material for Ruthenium Ion Catalysed Oxidation of Asphaltenes	245
C	Supplementary Material for Ultrasonic Characterisation Studies	260
C.1	Cetyltrimethylammonium bromide diagnostic data	260
C.2	Asphaltene diagnostic data	266
D	Supplementary Material for the Empirical Bayesian Inference of the Asphaltene Critical Nanoaggregation Region	281
D.1	Synthetic data	281
D.2	Sample data	287
D.2.1	<i>One-changepoint model</i>	287
D.2.2	<i>Brownian bridge model</i>	289

List of Figures

1.1	Global energy consumption by source in quadrillion British thermal units (Btu). One Btu \approx 1055 Joules. Petroleum and other liquid fuels and denoted ‘Liquids’. The author presumes renewable energy sources and hydrogen fuels are denoted ‘Other’. Data taken from (USEIA, 2017).	1
-----	--	---

1.2	Petroleum lost due to tanker oil spills, data shown in thousands of tonnes. The pie chart indicates the number of spill incidences associated with a loss of >700 tonnes of oil. Data taken from ITOPF (2017).	2
1.3	Booms used in oil spill remediation. Image taken from Marine Safety and Response Equipment Ltd (msar.eu).	5
1.4	Investigation workflow.	8
2.1	Phase plot of surfactant phase separation. Adapted from Clint (1992c).	13
2.2	Plot of surfactant micellarisation detection. (a) pure surfactant, (b) surfactant with impurity that lowers the interfacial tension more, (c) surfactant with impurity that lowers the interfacial tension less. Adapted from Clint (1992d).	14
2.3	Particle interactions in colloidal mixtures. Adapted from (McLean <i>et al.</i> , 1998)	21
3.1	A schematic of SARA fractionation.	26
3.2	Proposed asphaltene structures (Mullins, 2011; Schuler <i>et al.</i> , 2017). Schuler <i>et al.</i> (2017a) is the Supplementary Information attached to Schuler <i>et al.</i> (2017). Unknown atoms and side-chains are denoted X and R respectively.	30
4.1	Examples of biomarkers in the aliphatic fraction of petroleum. Adapted from Peters <i>et al.</i> (2005e).	38
4.2	Examples of PAHs and heteroatomic compounds in petroleum. Adapted from Peters <i>et al.</i> (2005e).	39
4.3	Wenger <i>et al.</i> (2002) biodegradation scale, adapted from Peters <i>et al.</i> (2005a). Sequence of alteration of alkylated PAH based on Fisher <i>et al.</i> (1996b, 1998). Bars indicate where compound classes are initially altered (pale gray), substantially depleted (solid gray), and completely removed (black). *Hopanes degraded without the formation of 25- <i>nor</i> -hopanes.	45
5.1	Relations used in sample source assessment. References for plots (a) and (b) are Hughes <i>et al.</i> (1995) and (Peters <i>et al.</i> , 2005h, Figure 13.77 (GeoMark Research Inc., Zumberge 2000, personal communication)) respectively. Plot (c) adapted from Moldowan <i>et al.</i> (1985).	54

6.1	Schematic of different types of sound waves. In plots (a,b) red and green arrows indicate the direction of phase and group velocity propagation respectively.	58
6.2	The pulse-echo/pitch-catch measurement method, adapted from Povey (1997a). The ultrasonic path length is denoted x	63
6.3	The acoustic resonance method, adapted from Eggers & Funck (1973). Resonator cavities are labeled Q_1 and Q_2 , x denotes path length, L denotes liquid volume in the sample, f_n denotes characteristic frequencies.	64
8.1	Resoscan Research System, image taken from TF Instruments (2007).	74
9.1	A simulated Brownian bridge path.	84
10.1	Weights of asphaltene fractions. The numbers represent 3-replicate averages, except the E1 asphaltene weight which had two replicates, the bars indicate confidence intervals based on standard deviation.	88
10.2	Ratios used in the maturity estimation of petroleum samples.	92
10.3	Relations used in petroleum source estimation. In plot (a) E3 is marked in red as the Pr/Ph ratio could not be calculated due to a high biodegradation of the sample. The key to interpretation of the plots is in Figure 5.1	93
10.4	Ratios used in petroleum source estimation.	95
10.5	Partial mass chromatograms of the E1 aliphatic fraction, showing the distributions of n -alkanes. Labels are listed in Table 10.2.	98
10.6	Partial m/z 191 mass chromatograms of the E1 and E2 aliphatic fraction. Labels are listed in Table 10.2.	99
10.7	Partial mass chromatograms of the E1 aliphatic fraction, showing sterane biomarkers. Labels are listed in Table 10.2.	100
10.8	Partial mass chromatograms of the E1 aromatic fraction, showing aromatic steroid biomarkers. Labels are listed in Table 10.3.	101
11.1	Reactions occurring during RICO of asphaltenes (Peng <i>et al.</i> , 1999).	106
11.2	Reactions occurring during RICO of asphaltenes. Theoretical reaction A is according to Peng <i>et al.</i> (1999), observed reactions are inferred from mass spectrometric analysis of RICO products performed on standard compounds, Figure 11.4	108

11.3	Reactions occurring during RICO of asphaltenes. Theoretical reaction B are according to Peng <i>et al.</i> (1999), observed reactions are inferred from mass spectrometric analysis of RICO performed on standard compounds, Figure 11.5	109
11.4	Total ion chromatograms (TIC) of RICO products performed on alkylated mono-aromatic standards, compound labels are given in Table 11.1.	110
11.5	Total ion chromatograms (TIC) of RICO performed on alkylated di-aromatic standards, compound labels are given in Table 11.1.	111
11.6	Mass spectra of phenylalkylketones identified in RICO products of monoaromatic standards.	112
11.7	Mass spectra of phenylalkyl acid methyl esters identified in RICO products of diaromatic standards.	113
11.8	Relative abundances of RICO products based on peak heights, Figures 11.10, B.1-B.3 and Table 11.2.	114
11.9	Mass spectrum of benzoic acid methyl ester.	116
11.10	Partial ion chromatograms of (a) <i>n</i> -alkanoic fatty acid and (b) α,ω -di- <i>n</i> -alkanoic di-fatty acid methyl esters of E1 ROCP products.	118
11.11	Partial ion chromatograms of (a) <i>n</i> -alkanoic, (b) α -methyl- <i>n</i> -alkanoic, (c) α -ethyl- <i>n</i> -alkanoic and (d) α -propyl- <i>n</i> -alkanoic fatty acid methyl esters of E1 RICO products.	120
11.12	Partial ion chromatograms for phenylalkylketones.	121
11.13	Partial ion chromatograms for benzenecarboxylic acid methyl esters.	122
11.14	Background-subtracted mass spectra of compounds eluting at ca.12.6 min. Percentage values indicate a match with the NIST (2005) entry of BAME.	123
12.1	Schematic of C_n TAB, $n=12,14$ molecules.	124
12.2	Time (s) (x-axis) versus velocity ($m\ s^{-1}$) (y-axis) plots of C_{12} TAB ultrasonic measurements. Titles indicate C_{12} TAB concentration, legends indicate measurement temperature in $^{\circ}C$. Measurement temperature was set at $25^{\circ}C$	125

12.3	Time (s) versus velocity (m s^{-1}) plots of C_{12}TAB ultrasonic measurements illustrating the effect of air bubbles on velocity. Titles indicate C_{12}TAB concentration, legends indicate measurement temperature in $^{\circ}\text{C}$	126
12.4	Correlation plots of C_{12}TAB ultrasonic measurements. Temperature and velocity are abbreviated as ‘temp’ and ‘vel’ respectively. Pearson’s correlation and corresponding p -values are indicated in bold and italic respectively.	126
12.5	Estimation of the CMC for C_{12}TAB . Red shading indicates the CMC region estimation, dashed lines in plot (b) indicate the corresponding fitted regressions. Plots (c) and (d) indicate the changes in R^2 as more data is added to a regression model.	127
12.6	Concentration-velocity measurements of CTAB pure and mixed aqueous solutions (Svalova <i>et al.</i> , 2017). In (c-f), CMC1 and CMC2 are primary and secondary micelle formation respectively. Black points indicate data that were not included in regression estimation.	129
12.7	Time versus velocity (m s^{-1}) plots of E1 asphaltene ultrasonic measurements. Titles indicate E1 concentration, legends indicate measurement temperature in $^{\circ}\text{C}$	131
12.8	Correlation plots of E1 asphaltene ultrasonic measurements. Temperature and velocity are abbreviated as ‘temp’ and ‘vel’ respectively. Labels in bold and italic indicate Pearson’s correlation coefficient and their p -values respectively.	133
12.9	Time (s) versus velocity (m s^{-1}) plot of E1 asphaltene ultrasonic measurements, the 284.48 mg L^{-1} sample, Figure 12.7 (p). In all plots, ‘linear regression’ is abbreviated ‘LR’. In plots (a,b) the legend indicates measurement temperature in $^{\circ}\text{C}$, in plot (c) ‘res’ abbreviates residuals obtained from single (LR1) and multiple (LR2) linear models.	134
12.10	Effect of outlier removal and averaging over different time intervals for E1 asphaltene.	135
12.11	Linear model selection criteria in the CNR estimation for E1 asphaltene.	137
12.12	Barplot of the CNR_1 and CNR_2 (mg L^{-1}) estimation of E1 asphaltene as a function of varying penalty weights. In plots (b) and (d) a single bar is drawn indicating that no other values have been estimated. . .	138

12.13	Concentration-velocity measurements of asphaltene-toluene mixtures. Dashed lines illustrate estimated linear models using constrained optimisation, CNR1 and CNR2 refer to the onset and decline of the critical nanoaggregation region respectively.	139
13.1	Synthetic data for testing the single-changepoint model following (13.1).	141
13.2	MCMC traces of γ conditional marginal posterior using 201-point and 21-point data sets (abbreviated 201-data and 21-data respectively), prior mean is set at the true parameter value. Solid red and dashed cyan lines indicate prior and posterior means respectively.	143
13.3	Posterior density plots of γ assuming a one-changepoint model using synthetic data. The densities are based on the final 50% of 10^6 iterations.	144
13.4	MCMC trace of γ posterior density using 201-point and 21-point data sets, prior mean is set at 1.5 times true parameters value. Solid red and dashed cyan lines indicate true γ and posterior mean respectively. The prior γ mean of is beyond the plot range.	145
13.5	Synthetic data for testing the Brownian bridge model following (13.2).	146
13.6	MCMC traces of γ_1 and γ_2 posterior densities using 201-point and 21-point data sets, prior mean is set at the true parameter value. Solid red and dashed cyan lines indicate prior and posterior means respectively.	147
13.7	Plots of marginal conditional posterior posterior densities of γ_1 and γ_2 , prior means are set at true parameter values.	148
13.8	Marginal conditional posterior posterior densities of γ_1 and γ_2 , prior means set at 1.5 times true parameter values.	149
13.9	Velocity characterisation of asphaltene aggregation in E1-E4 asphaltenes (Svalova <i>et al.</i> , 2017).	150
13.10	Densities of the parameters assuming a one-changepoint model with $\gamma = 100$ using data from constrained optimisation.	151
13.11	Variation of posterior single changepoint model performance with the change in tuning parameter ν using E1 asphaltene data.	152
13.12	Trace plots of 10^6 MCMC iterations of the γ conditional marginal posterior distribution, first 50% discarded as a burn-in. Solid red and dashed cyan lines indicate prior and posterior means respectively.	153

13.13	Density plots of the conditional marginal posterior distributions of γ . Black solid and dashed lines represent prior density and mean respectively, cyan solid and dashed lines represent posterior density and mean respectively.	153
13.14	Partial autocorrelation plots of the MCMC draws from γ conditional marginal posterior distribution.	154
13.15	Trace plots of 10^6 MCMC iterations of the γ_1 and γ_2 conditional marginal posterior distribution ² , first 50% discarded as a burn-in. Solid red and dashed cyan lines indicate prior and posterior means respectively.	155
13.16	Density plots of the conditional marginal posterior distributions of γ_1 and γ_2 . Black solid and dashed lines represent prior density and mean respectively, cyan solid and dashed lines represent posterior density and mean respectively.	155
13.17	Predictive distributions of E1-E4 assuming the single changepoint underlying model, red lines indicate the model means, red shading indicates the 95% predictive intervals.	158
13.18	Predictive distributions of γ_1 and γ_2 , red shading indicates the 95% predictive intervals.	159
13.19	Plots of predicted versus observed quantities of E1-E4 asphaltenes, using the single changepoint (Single) and Brownian bridge (Bridge) models. The black line indicates the ‘Observed=Predicted’ regression.	160
14.1	Sample separation based on the first two principal components. Loadings for plots (a) and (b) are given in Tables 14.2 and 14.3 respectively.	163
14.2	Sample separation based on the first two principal components (Table 14.4).	166
A.1	Partial mass chromatograms of the E2 aliphatic fraction, showing the distributions of n -alkanes. Labels are listed in Table 10.2.	224
A.2	Partial mass chromatograms of the E3 and E4 aliphatic fractions, showing the distributions of n -alkanes. Labels are listed in Table 10.2.	225
A.3	Partial mass chromatograms of the E4 aliphatic fraction, showing the distributions of n -alkanes. Labels are listed in Table 10.2.	226
A.4	Partial m/z 191 mass chromatograms of the E3 and E4 aliphatic fraction. Labels are listed in Table 10.2.	227

A.5	Partial m/z 177 mass chromatograms of the E1 and E3 aliphatic fraction. Labels are listed in Table 10.2.	228
A.6	Additional mass spectra for biodegradation assessment.	229
A.7	Partial mass chromatograms of the E2 aliphatic fraction, showing sterane biomarkers. Labels are listed in Table 10.2.	230
A.8	Partial mass chromatograms of the E3 aliphatic fraction, showing sterane biomarkers. Labels are listed in Table 10.2.	231
A.9	Partial mass chromatograms of the E4 aliphatic fraction, showing sterane biomarkers. Labels are listed in Table 10.2.	232
A.10	Partial mass chromatograms of the E1 aromatic fraction, showing naphthalene biomarkers. Labels are listed in Table A.1.	234
A.11	Partial mass chromatograms of the E2 aromatic fraction, showing naphthalene biomarkers. Labels are listed in Table A.1.	235
A.12	Partial mass chromatograms of the E3 aromatic fraction, showing naphthalene biomarkers. Labels are listed in Table A.1.	236
A.13	Partial mass chromatograms of the E4 aromatic fraction, showing naphthalene biomarkers. Labels are listed in Table A.1.	237
A.14	Partial mass chromatograms of the E1 aromatic fraction, showing phenanthrene biomarkers. Labels are listed in Table A.1.	238
A.15	Partial mass chromatograms of the E2 aromatic fraction, showing phenanthrene biomarkers. Labels are listed in Table A.1.	239
A.16	Partial mass chromatograms of the E3 aromatic fraction, showing phenanthrene biomarkers. Labels are listed in Table A.1.	240
A.17	Partial mass chromatograms of the E4 aromatic fraction, showing phenanthrene biomarkers. Labels are listed in Table A.1.	241
A.18	Partial mass chromatograms of the E2 aromatic fraction, showing aromatic steroid biomarkers. Labels are listed in Table 10.3.	242
A.19	Partial mass chromatograms of the E3 aromatic fraction, showing aromatic steroid biomarkers. Labels are listed in Table 10.3.	243
A.20	Partial mass chromatograms of the E4 aromatic fraction, showing aromatic steroid biomarkers. Labels are listed in Table 10.3.	244
B.1	Partial ion chromatograms of (a) n -alkanoic fatty acid and (b) α, ω -di- n -alkanoic di-fatty acid methyl esters of E2 asphaltene.	246

B.2	Partial ion chromatograms of (a) <i>n</i> -alkanoic fatty acid and (b) α, ω -di- <i>n</i> -alkanoic di-fatty acid methyl esters of E3 asphaltene.	247
B.3	Partial ion chromatograms of (a) <i>n</i> -alkanoic fatty acid and (b) α, ω -di- <i>n</i> -alkanoic di-fatty acid methyl esters of E4 asphaltene.	248
B.4	Partial ion chromatograms of (a) <i>n</i> -alkanoic, (b) α -methyl- <i>n</i> -alkanoic, (c) α -ethyl- <i>n</i> -alkanoic and (d) α -propyl- <i>n</i> -alkanoic fatty acid methyl esters of E2 asphaltene.	249
B.5	Partial ion chromatograms of (a) <i>n</i> -alkanoic, (b) α -methyl- <i>n</i> -alkanoic, (c) α -ethyl- <i>n</i> -alkanoic and (d) α -propyl- <i>n</i> -alkanoic fatty acid methyl esters of E3 asphaltene.	250
B.6	Partial ion chromatograms of (a) <i>n</i> -alkanoic, (b) α -methyl- <i>n</i> -alkanoic, (c) α -ethyl- <i>n</i> -alkanoic and (d) α -propyl- <i>n</i> -alkanoic fatty acid methyl esters of E4 asphaltene.	251
B.7	Partial ion chromatograms for the identification of benzenealkyl acid methyl esters of E2 asphaltene.	252
B.8	Partial ion chromatograms for the identification of benzenealkyl acid methyl esters of E3 asphaltene.	253
B.9	Partial ion chromatograms for the identification of benzenealkyl acid methyl esters of E4 asphaltene.	254
B.10	Partial ion chromatograms for the identification of phenylalkylketones of E2 asphaltene.	255
B.11	Partial ion chromatograms for the identification of phenylalkylketones of E3 asphaltene.	256
B.12	Partial ion chromatograms for the identification of phenylalkylketones of E4 asphaltene.	257
B.13	Mass spectra of 1-butanone-1-phenyl.	258
B.14	Mass spectra of dodecanophenone.	259
C.1	Time (s) versus velocity (ms^{-1}) plots of C_{14}TAB ultrasonic measurements. Titles indicate C_{14}TAB concentration, legends indicate measurement temperature in $^{\circ}\text{C}$	261
C.2	Time (s) versus velocity (ms^{-1}) plots of $\text{C}_{12}\text{TAB}/\text{C}_{14}\text{TAB}$ 1/1 M ultrasonic measurements. Titles indicate C_{12}TAB concentration, legends indicate measurement temperature in $^{\circ}\text{C}$	262

C.3	Time (s) versus velocity (ms^{-1}) plots of $\text{C}_{12}\text{TAB}/\text{C}_{14}\text{TAB}$ 2/1 M ultrasonic measurements. Titles indicate C_{12}TAB concentration, legends indicate measurement temperature in $^{\circ}\text{C}$	263
C.4	Correlation plots of C_{14}TAB ultrasonic measurements. Temperature and velocity are abbreviated as ‘temp’ and ‘vel’ respectively. Pearson’s correlation and corresponding p -values are indicated in bold and italic respectively.	264
C.5	Correlation plots of $\text{C}_{12}\text{TAB}/\text{C}_{14}\text{TAB}$ 1/1 M ultrasonic measurements. Temperature and velocity are abbreviated as ‘temp’ and ‘vel’ respectively. Pearson’s correlation and corresponding p -values are indicated in bold and italic respectively.	264
C.6	Correlation plots of $\text{C}_{12}\text{TAB}/\text{C}_{14}\text{TAB}$ 2/1 M ultrasonic measurements. Temperature and velocity are abbreviated as ‘temp’ and ‘vel’ respectively. Pearson’s correlation and corresponding p -values are indicated in bold and italic respectively.	264
C.7	Estimation of the CMC for C_{14}TAB . Red shading indicates the CMC region estimation, dashed lines in plots (b) and (c) indicate the corresponding fitted regressions.	265
C.8	Estimation of the CMC for $\text{C}_{12}\text{TAB}/\text{C}_{14}\text{TAB}$ 1/1 M. Red shading indicates the CMC region estimation, dashed lines in plot (b) and (c) indicate the corresponding fitted regressions.	265
C.9	Estimation of the CMC for $\text{C}_{12}\text{TAB}/\text{C}_{14}\text{TAB}$ 2/1 M. Red shading indicates the CMC region estimation, dashed lines in plot (b) indicate the corresponding fitted regressions.	266
C.10	Time versus velocity (m s^{-1}) plots of E2 asphaltene ultrasonic measurements. Titles indicate E2 concentration, legends indicate measurement temperature in $^{\circ}\text{C}$	267
C.11	Time versus velocity (m s^{-1}) plots of E3 asphaltene ultrasonic measurements. Titles indicate E3 concentration, legends indicate measurement temperature in $^{\circ}\text{C}$	268
C.12	Time versus velocity (m s^{-1}) plots of E4 asphaltene ultrasonic measurements. Titles indicate E4 concentration, legends indicate measurement temperature in $^{\circ}\text{C}$	269

C.13	Time versus velocity (m s^{-1}) plots of S1 asphaltene ultrasonic measurements. Titles indicate S1 concentration, legends indicate measurement temperature in $^{\circ}\text{C}$	270
C.14	Time versus velocity (m s^{-1}) plots of S3 asphaltene ultrasonic measurements. Titles indicate S3 concentration, legends indicate measurement temperature in $^{\circ}\text{C}$	271
C.15	Correlation plots of E2 asphaltene ultrasonic measurements. Temperature and velocity are abbreviated as ‘temp’ and ‘vel’ respectively. Pearson’s correlation and corresponding p -values are indicated in bold and italic respectively.	272
C.16	Correlation plots of E3 asphaltene ultrasonic measurements. Temperature and velocity are abbreviated as ‘temp’ and ‘vel’ respectively. Pearson’s correlation and corresponding p -values are indicated in bold and italic respectively.	272
C.17	Correlation plots of E4 asphaltene ultrasonic measurements. Temperature and velocity are abbreviated as ‘temp’ and ‘vel’ respectively. Pearson’s correlation and corresponding p -values are indicated in bold and italic respectively.	272
C.18	Barplot of the CNR_1 and CNR_2 estimation of E3 asphaltene as a function of varying penalty weights.	280
C.19	Barplot of the CNR_1 and CNR_2 estimation of E4 asphaltene as a function of varying penalty weights.	280
D.1	MCMC traces of the initial 5×10^4 simulations of γ (a,b,e) or γ_1 (c,d,f). In plots (a-d) synth. and missp. abbreviates synthetic and misspecified.	281
D.2	MCMC trace plots of the one-changepoint model using 201-point synthetic data, prior means are set at the true parameter values. Solid red and dashed cyan lines indicate prior and posterior means respectively.	282
D.3	MCMC trace plots of the one-changepoint model using 21-point synthetic data, prior means are set at the true parameter values. Solid red and dashed cyan lines indicate prior and posterior means respectively.	282

D.4	Posterior density plots of the one-changepoint model using synthetic data, prior means are set at the true parameter values. In the legend, data obtained using the 201-point and 21-point data sets are abbreviated ‘201pt’ and ‘21pt’.	283
D.5	Plots of the partial autocorrelation function for the 201-point synthetic data set posterior conditional marginal draws assuming a single-changepoint underlying model, prior means are set at true parameter values.	283
D.6	MCMC trace plots of the Brownian bridge model using 21-point synthetic data, prior means are set at the true parameter values. Solid red and dashed cyan lines indicate prior and posterior means respectively.	284
D.7	Posterior density plots of the Brownian bridge using synthetic data, prior means are set at true parameter value, orange and cyan vertical lines indicate density means.	285
D.8	Plots of the partial autocorrelation function for the 201-point synthetic data set posterior conditional marginal draws assuming a Brownian bridge underlying model, prior means are set at true parameter values.	286
D.9	Chain mixing plots of the MCMC sampling from the conditional posterior distributions of the single changepoint model of E1 asphaltene.	287
D.10	Conditional posterior density plots of the single changepoint model of E1 asphaltene. Solid red and dashed cyan lines indicate prior and posterior means respectively.	287
D.11	Partial autocorrelation plots of the MCMC sampling from the conditional posterior distributions of the single changepoint model of E1 asphaltene.	288
D.12	Chain mixing plots of the MCMC sampling from the conditional posterior distributions of the Brownian bridge model of E1 asphaltene. Solid red and dashed cyan lines indicate prior and posterior means respectively.	289
D.13	Conditional posterior density plots of the Brownian bridge model of E1 asphaltene.	290

D.14 Partial autocorrelation plots of the MCMC sampling from the conditional posterior distributions of the Brownian bridge model of E1 asphaltene.	291
---	-----

List of Tables

10.1 Ratios used in petroleum maturity estimation. In (10.14) and (10.15) AS refers to aromatic steroids. References for ratios and full compound names can be found in Chapter 5.1.	91
10.2 Compound table for biomarkers in the saturated hydrocarbon fraction. Reference key is (1) NIST (2005), (2) Zumberge (1993), (3) Peters (2000), (4) Nytoft & Bojesen-Koefoed (2001), (5) Stout & Wang (2008), (6) Moldowan <i>et al.</i> (1991), (7) Wang <i>et al.</i> (2006), (8) Grantham (1986).	103
10.3 Compound table of the isomers of 17 β -methyl-18-norcholesta-8,11,13-triene (monoaromatic steroids, MAS) and 17 β -methyl-18,19-dincholesta-1,3,5(10),6,8,11,13-heptane (triaromatic steroids, TAS) (Abbott <i>et al.</i> , 1985). Reference key is (1) Mackenzie <i>et al.</i> (1981), (2) Moldowan & Fago (1986), (3) Abbott <i>et al.</i> (1985), (4) Yang <i>et al.</i> (2015 <i>b</i>).	104
11.1 Compound table for RICO experiments (NIST, 2005).	119
11.2 Abundance (%) of different compound series in RICO products. α -FAME abbreviates the α -branched FAMEs.	119
12.1 Summary of CTAB concentration-velocity data (Svalova <i>et al.</i> , 2017). Mean sample standard deviation is denoted SD, subscripts of R^2 refer to models fitted in the estimated monomer (mono), aggregated (aggr) and CMC ₁ -CMC ₂ intermediate (inter) regions.	129
12.2 Constrained nanoaggregation region estimation of E1 asphaltene, monomeric boundary selection using constrained optimisation, $w_2 = 10, w_3 = 1000$. Concentration indicated in mg L ⁻¹ . The length, outlier and slope penalties are abbreviated P_1, P_2 and P_3 respectively. Grey shading indicates concentrations with the highest R^2 and R_p^2	136

12.3	Regression penalised R^2 values of asphaltene concentration-velocity data. Total R_p^2 denotes the sum of R_{mono}^2 and R_{aggr}^2 , Δ CNR denotes the CNR (mg L^{-1}) width, Δu denotes the velocity jump. Subscripts of CNR denote the onset ₁ and decline ₂ of aggregation. Penalised R^2 subscripts refer to estimated models in the monomer and aggregate regions.	140
13.1	Posterior diagnostic criteria for assessing single-change-point model fit. Posterior runs based on true and misspecified prior means are marked accordingly. Correlation (Cor) is calculated for the association between true and predicted values (Fawcett <i>et al.</i> , 2017). Information is calculated on 10^6 draws from posterior distributions discarding the initial 5×10^5 as burn-in.	146
13.2	Posterior diagnostic criteria for assessing Brownian bridge model fit. Posterior runs based on true and misspecified prior means are marked accordingly. Correlation (Cor) is calculated for the association between true and predicted values (Fawcett <i>et al.</i> , 2017). Information is calculated on 10^5 draws from posterior distributions discarding the initial 5×10^4 as burn-in.	149
13.3	Diagnostics for comparing the fit of the single-change-point and bridge models to data, based on (Fawcett <i>et al.</i> , 2017).	160
14.1	Correlation matrix of the variables used in PCA, every cell illustrates a Pearson correlation ρ , followed by its corresponding p -value. Variable abbreviations are V_1 - Δ CNR, V_2 - Δu , V_3 - R_p^2 , V_4 - medium FAMES, V_5 - long FAMES, V_6 - α -methyl FAMES, V_7 - α -ethyl FAMES, V_8 - α -propyl FAMES, V_9 - BAME.	162
14.2	Loadings of the principal components in Figure 14.1(a). Medium and long FAMES are abbreviated M FAME and L FAME.	164
14.3	Loadings of the principal components in Figure 14.1(b). The α -methyl, α -ethyl and α -propyl FAMES are abbreviated α -C ₁ , α -C ₂ and α -C ₃ FAME respectively. Blue indicates principal component loadings analogous to Table 14.2.	164
14.4	Loadings of the principal components in Figure 14.2. Abbreviation key is in Table 14.1.	166

A.1	Compound table for naphthalene and phenanthrene compounds (Stout & Wang, 2008). Abbreviations MN, DMN and TMN refer to methyl-naphthalene, dimethylnaphthalene and trimethylnaphthalene respectively. Abbreviations MP and DMP refer to methylphenanthrene and dimethylphenanthrene respectively.	233
C.1	Constrained nanoaggregation region estimation of E1 asphaltene, aggregated boundary selection using constrained optimisation. The length, outlier and slope penalties are abbreviated P_1 , P_2 and P_3 respectively. Grey shading indicates concentrations with the highest R^2 and R_p^2	273
C.2	Constrained nanoaggregation region estimation of E2 asphaltene, monomeric boundary selection using constrained optimisation, $w_2 = 10, w_3 = 1000$. The length, outlier and slope penalties are abbreviated P_1 , P_2 and P_3 respectively. Grey shading indicates concentrations with the highest R^2 and R_p^2	274
C.3	Constrained nanoaggregation region estimation of E2 asphaltene, aggregated boundary selection using constrained optimisation, $w_2 = 10, w_3 = 1000$. The length, outlier and slope penalties are abbreviated P_1 , P_2 and P_3 respectively. Grey shading indicates concentrations with the highest R^2 and R_p^2	275
C.4	Constrained nanoaggregation region estimation of E3 asphaltene, monomeric boundary selection using constrained optimisation, $w_2 = 1, w_3 = 1000$. The length, outlier and slope penalties are abbreviated P_1 , P_2 and P_3 respectively. Grey shading indicates concentrations with the highest R^2 and R_p^2	276
C.5	Constrained nanoaggregation region estimation of E3 asphaltene, aggregated boundary selection using constrained optimisation, $w_2 = 1, w_3 = 1000$. The length, outlier and slope penalties are abbreviated P_1 , P_2 and P_3 respectively. Grey shading indicates concentrations with the highest R^2 and R_p^2	277

C.6 Constrained nanoaggregation region estimation of E4 asphaltene, monomeric boundary selection using constrained optimisation, $w_2 = 10, w_3 = 1000$. The length, outlier and slope penalties are abbreviated P_1, P_2 and P_3 respectively. Grey shading indicates concentrations with the highest R^2 and R_p^2 278

C.7 Constrained nanoaggregation region estimation of E4 asphaltene, aggregated boundary selection using constrained optimisation, $w_2 = 10, w_3 = 1000$. The length, outlier and slope penalties are abbreviated P_1, P_2 and P_3 respectively. Grey shading indicates concentrations with the highest R^2 and R_p^2 279

Chapter 1. Introduction

The petroleum industry is crucial to meeting the global energy demand. According to the U.S. Energy Information Administration International Energy Outlook 2017 (USEIA, 2017), by 2050 ca. 80% of global energy demand will be supplied by hydrocarbon sources. Figures 1.1 (a,b) illustrate the U.S. Energy Information Administration global energy consumption forecast by source for all sectors (residential, transport, etc.). The role of renewables ('Other') will be only up to a half that of liquid fuels, thus petroleum will remain crucial to global energy supply and security.

The contribution of the petroleum industry to economies on a global scale is hard to underestimate. For example, in countries like Saudi Arabia up to 90% of the profits from extraction are taxed (EY, 2017), whilst the oil and gas sector contributes to ca. 50% of the gross domestic product and 70% of export revenues (OPEC, 2018). Infrastructure developments for new exploration/extraction activities create employment opportunities for local communities, as well as improve the local infrastructure, e.g. building new roads and accommodation facilities. Many petroleum multinational corporations engage in philanthropic activities through charities, e.g.

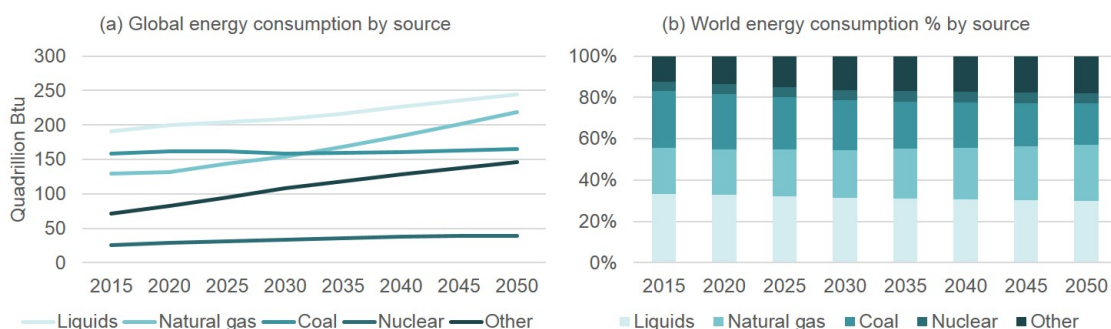


Figure 1.1: Global energy consumption by source in quadrillion British thermal units (Btu). One Btu \approx 1055 Joules. Petroleum and other liquid fuels and denoted 'Liquids'. The author presumes renewable energy sources and hydrogen fuels are denoted 'Other'. Data taken from (USEIA, 2017).

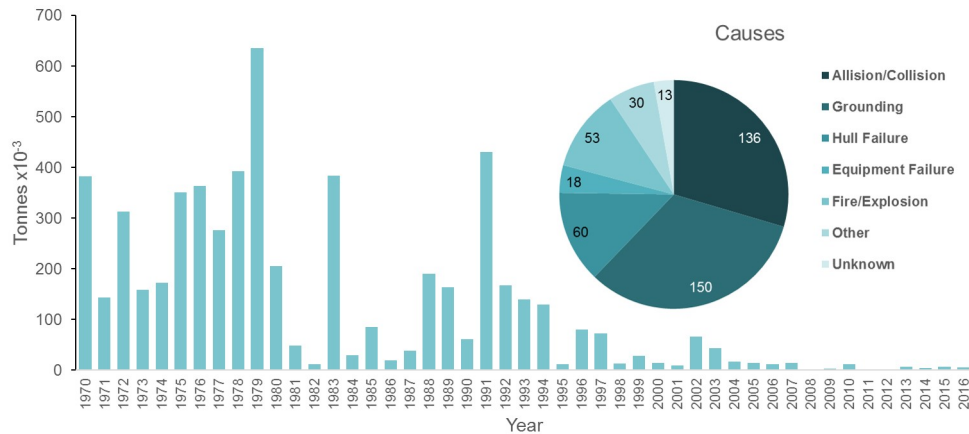


Figure 1.2: Petroleum lost due to tanker oil spills, data shown in thousands of tonnes. The pie chart indicates the number of spill incidences associated with a loss of >700 tonnes of oil. Data taken from ITOPF (2017).

Shell Foundation, Heroes of Tomorrow (Equinor/Statoil) and ExxonMobil Foundation.

The increase in petroleum extraction in the last century and a lack of regulation at the time, however, resulted in significant environmental damages, a great contribution to whom were made by petroleum spills. The latter occur due to anthropogenic (as well as natural) phenomena, such as petroleum exploration, transportation and refining (Franzetti *et al.*, 2009; Zhang *et al.*, 2011; Marchant & Banat, 2012; Rocha e Silva *et al.*, 2014; Sobrinho *et al.*, 2013; Souza *et al.*, 2014). Figure 1.2 illustrates the amount of oil lost during tanker transportation, excluding explorational production platform accidents, intentional discharges of oil and natural seeps. The largest tanker spill was the Atlantic Empress spill in 1979 whereby 287 thousand tonnes of oil was lost (ITOPF, 2017). The environmental hazards that petroleum spills pose include toxicity to the marine and coastal ecosystem, evaporation of volatile substances and contamination of beaches. The *Exxon Valdez* oil spill released ca. 30,770 tonnes (260,000 barrels) of oil resulting in the fatality of 30,000 birds of 90 species (Piatt *et al.*, 1990) and up to 2,800 sea otters (Garrott *et al.*, 1993). Loughlin (2013) reported that 302 harbor seals were affected by the toxic fumes leading to e.g. brain lesions, stress and disorientation (Peterson *et al.*, 2003). The long-term impacts of exposure to hydrocarbons were due to sub-lethal doses, nevertheless were reported to have the potential to affect health, growth and reproduction (Peterson *et al.*, 2003). The spreading of hydrocarbons on water surfaces creates a film that prevents air and sunlight entering the water column impacting the phytoplankton

habitat (Yeung *et al.*, 2011). Figure 1.2, however, illustrates that the amount of oil lost through tanker spillage in the 21st century is an order of magnitude below that in 70-90s.

One of the largest recent oil spill (well blow out) events is the Deepwater Horizon disaster in 2010 (Baelum *et al.*, 2012; Liu *et al.*, 2012; Reddy *et al.*, 2012; Rocha e Silva *et al.*, 2014), whereby 4-5 million barrels (473-592 thousand tonnes) of light crude were lost. The platform operating the Macondo well exploded on the 20th of April of that year (BP, 2010). A combination of eight engineering and operational faults, including operation under a lack of evidence of well integrity and faults in the emergency systems, led to a leakage of gas and hydrocarbons onto the platform causing a chain of explosions and the sinking of the rig (BP, 2010). The casualties included 11 fatality and 17 injury events, and the estimated total cost to BP due to criminal and civil settlements was \$ 42.2 billion (Fontevicchia, February 5, 2013).

Water-in-oil emulsions (WOE) form during petroleum spills as a result of oil mixing with sea water, whereby very little energy is required for emulsification to occur (Berridge *et al.*, 1968). Typically, the volume of water in WOE is ca. 30-90% (Bridie *et al.*, 1980; Fingas *et al.*, 1994; Lee, 1999). The WOE stability is a function of a multitude of factors, including the water content, water salinity (Gafonova & Yarranton, 2001; Alves *et al.*, 2014) and pH (Kokal, 2005; Elsharkawy *et al.*, 2008). The WOE emulsifying petroleum fraction(s) has been reported to be the asphaltenes and (their interaction with) resins/microcrystalline waxes (Mackay *et al.*, 1973; Eley *et al.*, 1988; Lee, 1999; Jestin *et al.*, 2007). The so-called oil ‘chocolate mousses’ are highly-viscous emulsions (McLean *et al.*, 1998) whereby the proportion of water reached 70%, whose formation requires greater shearing forces than that of the aforementioned WOE (Bridie *et al.*, 1980). Due to their high water/oil proportion, mousses can solidify (McLean *et al.*, 1998) and become unresponsive to conventional methods of spill remediation, e.g. the use of dispersants and burning (Bobra *et al.*, 1992). When in the mousse state, the viscosity of the resulting mixture can be orders of magnitude greater than that of crude oil (and water) (Bridie *et al.*, 1980). Combined with the high salt content of the formation water, the high viscosity of the mousse increases pumping costs and may induce corrosion of metal equipment (Kilpatrick, 2012). Sea water salinity can also greatly increase the density of a mousse (Thingstad & Pengerud, 1983).

Asphaltenes, and specifically the natural interfacially-active emulsifiers within them (Stanford *et al.*, 2007a; Kilpatrick, 2012; Rocha *et al.*, 2016), have been extensively re-

ported to be the main cause of the high WOE stability. Bridie *et al.* (1980) weathered fractions of Brent crude oil to initial boiling points (IBP) of 40, 125, 200, 275 °C whereby the two former fractions did not form stable emulsions, the fraction at IBP 200 stabilised emulsions at ≤ 20 °C and the last fraction gave stable emulsions at 30 °C. Additionally, Bridie *et al.* (1980) measured how the formed emulsions would spread on sea water, and the two highest IBP emulsions were stable at 5 °C and 15 °C respectively. In terms of petroleum composition, they reported that the combination of asphaltenes and petroleum waxes was crucial to the formation of stable WOE, whereby the absence of either of the fractions would not be sufficient to stabilise water in oil (Bridie *et al.*, 1980). The importance of waxes and the droplet size distribution in increasing the viscosity of WOE has also been reported numerously (Bridie *et al.*, 1980; Thompson *et al.*, 1985; McLean & Kilpatrick, 1997*b*; Lee, 1999).

The asphaltenes, or the asphaltene petroleum fraction, is a class of compounds that is operationally defined as soluble in toluene and insoluble in *n*-pentane or *n*-heptane (e.g. Andersen & Birdi, 1991; Sheu, 1996; Sjoblom *et al.*, 2003, 2015; Mullins, 2011). The features of an asphaltene fraction, therefore, are defined by the precipitating solvent and can comprise a huge structural polydispersity (Andersen & Birdi, 1991; Sjoblom *et al.*, 2015; Schuler *et al.*, 2015, 2017). A subfraction of the asphaltenes (Wu, 2003; Czarnecki & Moran, 2005; Stanford *et al.*, 2007*a,b*; Czarnecki, 2009), that is reported to be more polar (Gawrys *et al.*, 2005), stabilises the WOE by adsorbing at the water/oil interface forming rigid films resisting droplet coalescence (McLean & Kilpatrick, 1997*a*; Yarranton *et al.*, 2000*a*; Gafonova & Yarranton, 2001; Sztukowski *et al.*, 2003; Kokal, 2005; Elsharkawy *et al.*, 2008; Harbottle *et al.*, 2014; Pauchard *et al.*, 2014). Rocha *et al.* (2016) reported the asphaltenes to be amphoteric materials that can be charged at low and high pH increasing their affinity at the water-oil interface and enhancing emulsion stability (Kokal, 2005; Elsharkawy *et al.*, 2008) by dramatically lowering the interfacial tension (Kilpatrick, 2012). The surface-active asphaltenes self-associate at the nanoscale (Barre *et al.*, 2009) forming nanoaggregates, the latter were reported to form films that stabilise WOE (Jestin *et al.*, 2007; Verruto & Kilpatrick, 2008; Alvarez *et al.*, 2009). The nanoaggregates are ca. 3-10 nm in size, have an ellipsoidal shape and can entrap solvent within the aggregate interior (Fenistein *et al.*, 2000; Fenistein & Barré, 2001; Gawrys & Kilpatrick, 2005; Gawrys *et al.*, 2006; Sirota, 2005; Sirota & Lin, 2007; Barre *et al.*, 2008, 2009; Eyssautier *et al.*, 2011). Recently, asphaltene aggregation state at the



Figure 1.3: Booms used in oil spill remediation. Image taken from Marine Safety and Response Equipment Ltd (msar.eu).

water/oil interface has been debated. Rane *et al.* (2012, 2013, 2015) proposed that the asphaltenes are in a monomeric state or the observed asphaltenic film density at the oil/water interface is that of monomers (although the nanoaggregate thickness is preserved) (Kilpatrick, 2012). However, given the overwhelming evidence of asphaltene surface activity, the assumption of nanoaggregation having an impact on the water-in-oil emulsion stability remains of interest. This will drive the research that will follow.

The environmental hazards and the economical implications of petroleum spills call for efficient remediation practice. The physicochemical changes of oil (c.f. Thingstad & Pengerud, 1983) that accompany its transition from its initial state to a mousse imply relevant changes in spill remediation strategies, thus this process requires thorough understanding (Daling *et al.*, 1990). Factors affecting the WOE formation include evaporation, dissolution and photo-oxidation of oil (Mackay, 1987; Daling *et al.*, 1990). It may be advantageous to prevent WOE formation by adding emulsion inhibitors and leading to an improved dispersion of the oil by sea turbulence (Lichtenthaler & Daling, 1985; Ross, 1986). Current spill remediation technology broadly includes mechanical, chemical and biological (Prendergast & Gschwend, 2014). The

former class includes oil booms (Figure 1.3) and skimmers, as well as controlled burning of oil (Allen *et al.*, 2011). The chemical/biological methods include absorbents and surface-active agents (surfactants) of either synthetic or biogenic nature. Absorbent materials can be used to clean up spilled hydrocarbons and can be separated/removed from the water column with a possibility of recycling (Adebajo *et al.*, 2003). Types of absorbents include inorganic mineral, synthetic organic and organic vegetable (Melvold *et al.*, 1988; Teas *et al.*, 2001; Adebajo *et al.*, 2003). Such materials are porous and include clays, graphite, polymers, cellulose-based materials and elastomers (Daughney, 2000; Reynolds *et al.*, 2001; Teas *et al.*, 2001). The balance between performance factors such as cost, absorption capacity and biodegradability determine the type of clay to be deployed (Carmody *et al.*, 2007). For example, synthetic organic materials have a better adsorption and often lower cost but also lower biodegradability (Choi & Cloud, 1992; Teas *et al.*, 2001), whilst organic vegetable products can have a lower adsorption and poor buoyancy (Choi & Cloud, 1992).

Surfactants used in spill remediation can be synthetic/petroleum-derived and biogenic and generally include ionic or non-ionic substances (Edwards *et al.*, 2003). Biogenically-derived surfactants are produced by e.g. bacteria and fungi (Edwards *et al.*, 2003) and include glyco/phospholipids, lipoproteins/peptides, fatty acids, polymeric surfactants and particulate surfactants (Parra *et al.*, 1989; Desai & Desai, 1993; Nabholz *et al.*, 1993). Edwards *et al.* (2003) tested the toxicity of three types of synthetic and biogenic surfactants each to *Mysidopsis bahia* and *Menidia beryllina*. The most toxic of the observed surfactants were of synthetic nature, although a bioemulsifier also showed a strong impact on the survival, growth and fecundity of the studied microorganisms. After seven days of exposure, the least harmful surfactants were PES-61 (synthetic) followed by Emulsan (biogenic) (Edwards *et al.*, 2003). Biosurfactants are likely to have specific toxicity towards isolated/pure cultures but are less hazardous towards diverse microbial populations (Aingh *et al.*, 2007). The production of biosurfactants can often be performed using waste products, optimising their economic viability and contributing to recycling (Makkar *et al.*, 2011; Dziegielewska & Adamczak, 2013). Biosurfactants have hydrophobic and hydrophilic functionalities that reduce surface tension, increase the contact area of insoluble components and improve bioavailability of hydrocarbons (Aparna *et al.*, 2011). Additionally, due to the presence of specific biological functional groups, biosurfactants can be used to target the detoxification of specific pollutants (Silva

et al., 2014). One of the main factors limiting the use of biosurfactants over standard surfactants is the cost of production, which can be optimised through the utilisation of waste products and renewable resources (Rufino *et al.*, 2014).

Investigation aims and workflow

Considering the global importance of the petroleum industry, the environmental impact of the oil spills and the need for efficient remediation practice, this research is focused on obtaining a better understanding of asphaltene nanoaggregation, which is thought to be a key contributor of WOE stability. The key aims of this investigation are as follows:

- To verify the asphaltene critical nanoaggregate concentration using ultrasonic velocity characterisation (c.f. Andreatta *et al.*, 2005a)
- To understand the impact of asphaltene architecture on asphaltene nanoaggregation
- To investigate/model any anomalies in asphaltene nanoaggregation
- Based on the above, to propose the driving mechanism of asphaltene nanoaggregation, which could then be used to better remediate petroleum spills.

Additionally, parent petroleum biodegradation, maturity and source studies are performed.

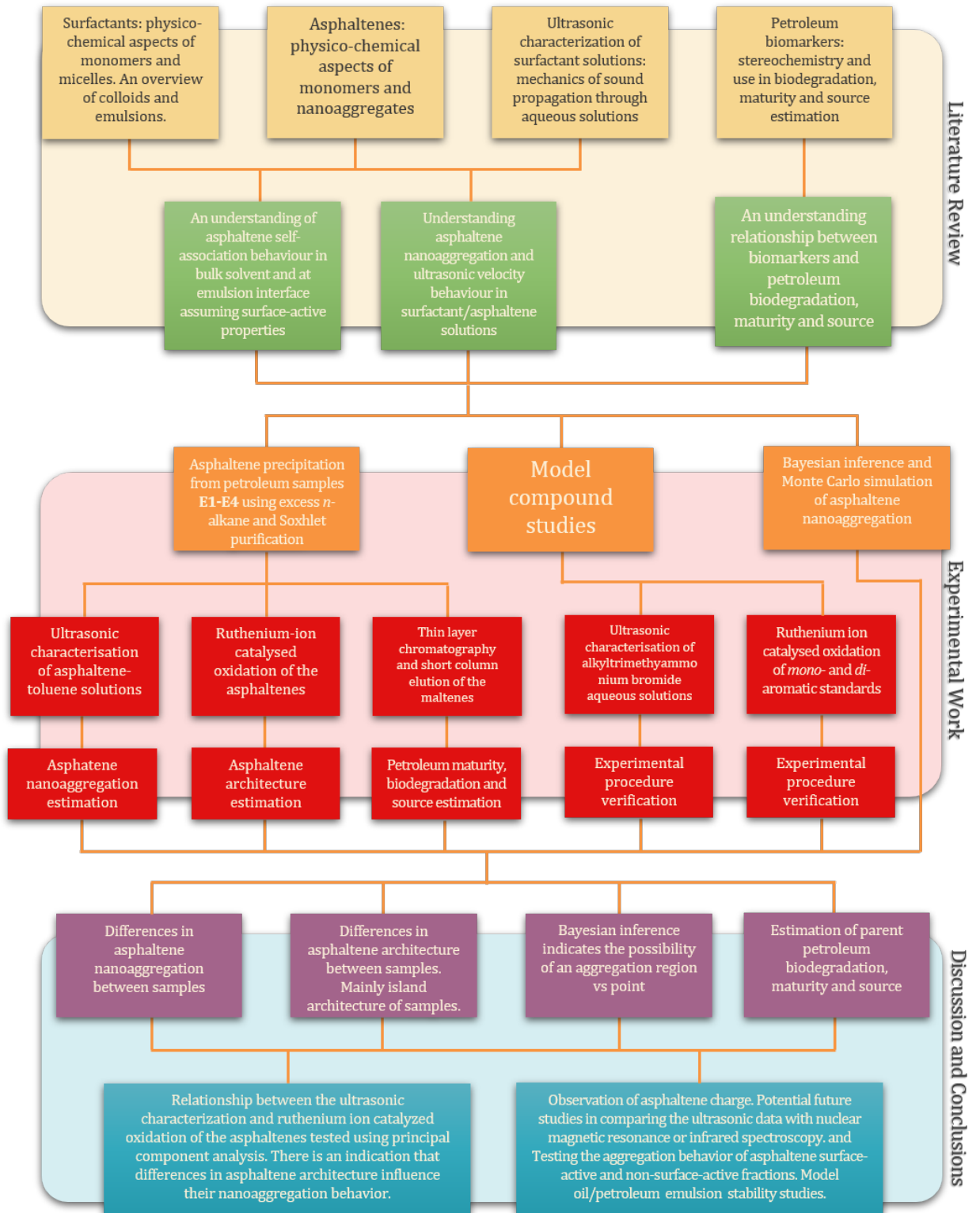


Figure 1.4: Investigation workflow.

The workflow of this investigation is illustrated in Figure 1.4 and is as follows. Firstly, the literature review (Part II) provides a theoretical foundation for this study. Apart from the review of asphaltene architecture, physico-chemical properties and nanoaggregation, other areas of review include colloids and surfactants, geochemistry of petroleum biomarkers and their use in biodegradation, maturity and source estimation and ultrasonic propagation in homogeneous fluids. Following this, an overview of methodology (Part III) highlights the strengths and limitations of the experimental procedures and analytical instruments, echoing relevant parts of the literature review, as well as Bayesian inference. Experimental studies (Part IV) are performed on four petroleum samples (abbreviated E1-E4) obtained from an industrial collaborator from which the asphaltenes will be extracted. Asphaltene precipitation/purification and geochemical characterisation of deasphalted petroleum samples are performed. The latter include biodegradation, maturity and source estimation using petroleum biomarkers. To follow, ultrasonic velocity measurements are used to study asphaltene nanoaggregation (Andreatta *et al.*, 2005a) in the four samples. An estimation of the asphaltene architecture is obtained from ruthenium ion catalysed oxidation measurements. To verify the ultrasonic and oxidation techniques, the two methods are performed on model compounds. Inference about the impact of asphaltene structure on the nanoaggregation behaviour will be performed using statistical inference, including principal component analysis. Additionally, a Bayesian modeling exercise tests various aggregation behaviours. The summary and final discussion of this investigation is presented in Part V together with future directions that this research can take.

Literature Review

Chapter 2. Colloids and Surfactants

This Chapter provides an overview of surfactant and colloid theory in order to better understand the impact of asphaltene monomers and nanoaggregates on the stabilisation of water-in-oil emulsions. Additionally, a comparison is provided between the two to assess the advantages and limitations of the surfactant analogy regarding the asphaltenes.

2.1 An Introduction to Surfactants

Surfactants (SURFace ACTive AgeNTs) are agents that accumulate at surfaces, and change the properties of those surfaces, for liquids often reducing their surface tension (Clint, 1992*f*; Hummel, 1999). Understanding the phenomena of colloids and surfactant aggregation at interfaces (Clint, 1992*f*) will aid in the understanding of asphaltene nanoaggregation and emulsion stabilisation.

Water-soluble surfactants comprise hydrophilic (head) and hydrophobic (tail) groups. The hydrophilicity of the head groups often stems from its polarity, and include anionic (e.g. soaps and detergents), cationic (e.g. anti-static agents), zwitterionic (e.g. cosmetics) and (e.g. detergents and emulsifiers) (Laughlin, 1978*b,a*; Clint, 1992*f*). The hydrophobic tail is often a hydrocarbon (e.g. C₁₂₋₂₀ *n*-alkanes) or a benzene-containing compound that is not hydrophilic (Hunter, 2001). Surfactants of this type have a very strong affinity to adsorb at the air-water interface. Adding a hydrocarbon phase to an aqueous surfactant solution will result in the partitioning of the tail groups in the oil phase depending on the relative surfactant groups concentration in each phase (Clint, 1992*f*). This often results in emulsification. Interfacial activity of surfactants rises due to the minimisation of a solution's chemical potential when surfactant molecules are located at the phase interface (Davies & Rideal, 1963; Clint, 1992*a,f*). The Maxwell-Boltzmann distribution would thus imply that the abundance of surfactant molecules at the oil/water interface would be high as the molecules would be in the lowest energy state allowed by a given system (Lau-

rendeau, 2005). Hydrocarbon tails are not repelled by water rather, the attraction of a tail to water is approximately equal to its attraction to itself (Tanford, 1980; Clint, 1992*f*). Asphaltene monomers are reported to have an alkyl side-chain and a polycyclic aromatic hydrocarbon core (Mullins, 2011). The hydrophobicity of the alkyl appendages is determined by the presence of heteroatomic functionalities, e.g. acidic/basic groups. For example, Siffert *et al.* (1984) reported that asphaltenes with an imbalance between the acidic and basic groups formed more stable emulsions. This is presumably due to the preference of the polar groups to enter the water phase, with the aromatic components remaining in hydrocarbons (Kuznicki *et al.*, 2008). Molecular dynamic simulations of asphaltene-like molecules have highlighted the increase in the interfacial activity of asphaltenes due to polar groups (Kuznicki *et al.*, 2008). A subsequent simulation study by Kuznicki *et al.* (2009) confirmed that the asphaltene model molecules remain in the toluene phase, with those with polar functional groups travelling to the water/oil interface, which is consistent with experimental observations on asphaltene side-chain polarity (Masliyah *et al.*, 2002; Peña *et al.*, 2005). This will be discussed further in Section 3.3.

The close packing of surfactant molecules at the phase interface results in the formation of monolayers that also reduce surface tension (Gelbart *et al.*, 1989). Surfactant self-association also produces micelles (Section 2.2), vesicles and liposomes, and at higher concentrations liquid crystals may form Clint (1992*c*). Such structures are dynamic and can transfer from one type to another with variations in system conditions, such as temperature, pH or ionic strength (Clint, 1992*a*). In hydrophilic/hydrophobic mixtures, the surfactant architecture will determine whether a water-in-oil or oil-in-water emulsion will form (Clint, 1992*f*). If the cross-sectional area of the head is greater than that of the tail, then oil-in-water emulsions will be formed, and vice versa. Thus, changing the balance between surfactant group areas will lead to phase inversions, which can be achieved by the addition of other surfactants, changing the emulsion temperature (non-ionic compounds) or increasing electrolyte concentration (ionic compounds) (Clint, 1992*a*). The area per surfactant molecule at an interface will be determined by the balance between attractive forces of the heads and steric repulsion of the tails (Israelachvili, 1987; Clint, 1992*a*). Again, this will also determine the minimum surfactant energy, whereas the type of solvent and surfactant geometry will determine the minimum surface tension possible in a system. The phase-temperature dependence of surfactants is illustrated in Figure 2.1, where the solution temperature and surfactant concentration deter-

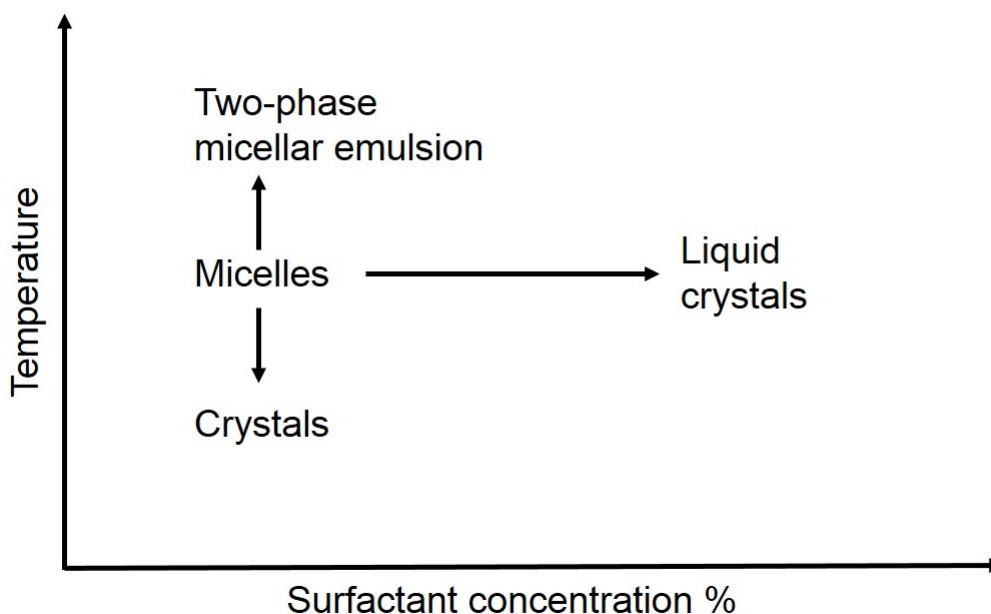


Figure 2.1: Phase plot of surfactant phase separation. Adapted from Clint (1992c).

mines whether the surfactants are in a micellar, crystalline or liquid crystalline state (Clint, 1992c). The Krafft temperature is the temperature below which the surfactant becomes insoluble (Krafft, 1899).

2.2 Micellarisation

In contrast to conventional solutes, the aggregation properties of surfactants in aqueous solutions have a non-monotonic relationship with concentration (Clint, 1992d). This is due to the self-association phenomenon, otherwise known as micellarisation. The micelle structure depends on the solution temperature and concentration, as well as the molecular architecture of the surfactant molecules (Hunter, 2001). In non-aqueous solvents, the addition of small amounts of water will lead to the formation of reverse micelles, whereby the surfactant heads stabilise droplets (Hunter, 2001). The formation of micelles (aggregates) corresponds to a critical micelle concentration (CMC), causing a change of dependence of a range of solution physicochemical properties on concentration. These properties include osmotic pressure, turbidity, solubilisation, magnetic resonance, surface tension (Clint, 1992d), auto-diffusion (Lindman *et al.*, 1982) and ultrasonic velocity (Zielinski *et al.*, 1986). At

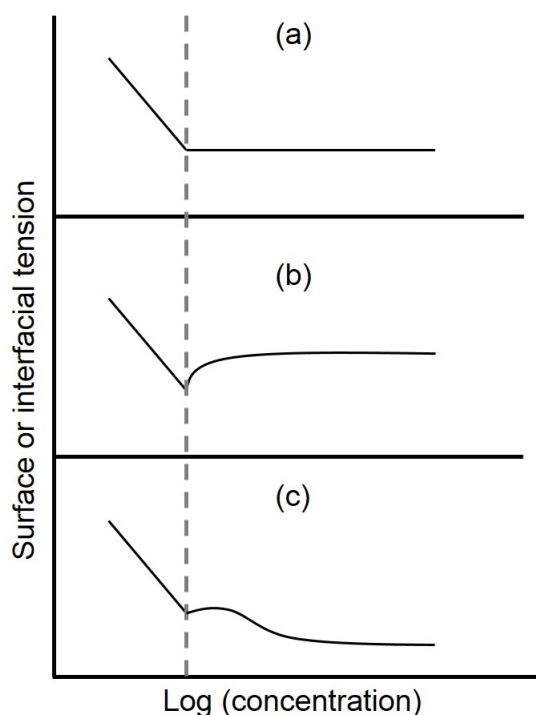


Figure 2.2: Plot of surfactant micellisation detection. (a) pure surfactant, (b) surfactant with impurity that lowers the interfacial tension more, (c) surfactant with impurity that lowers the interfacial tension less. Adapted from Clint (1992*d*).

and above the CMC, the interfacial tension and concentration of monomeric surfactant remain constant, whereas any additional surfactant molecules aggregate into micelles (Clint, 1992*a*). Temporal micelle behaviour is dynamic, thus the aggregation number is an average amount of molecules leaving and joining the micelles. The kinetics of micellar aggregation can be studied using ultrasonic relaxation (Gettins *et al.*, 1980; Kato *et al.*, 1988), temperature or pressure jump (Aniansson *et al.*, 905-922) and NMR spectroscopy (Fendler & Fendler, 1975). The latter assume that two major relaxation processes are involved in micellar kinetics, namely faster relaxation (microseconds) due to exchange of surfactant monomers between the micelles and the bulk and slower relaxation (microseconds) due to the total dissipation of micelles to monomers (Clint, 1992*d*). The dissociation of micelles is strongly dependent on the alkyl chain length as hydrophobic bonding is stronger for larger groups. Kato *et al.* (1988) reported that for a variety of surfactants, regardless of the head groups, any two additional methylene groups on the surfactant tail will decrease the dissociation rate by two orders of magnitude.

Surface tension γ relates to the work w required to change the area σ of a surface (Atkins, 2014a)

$$dw = \gamma d\sigma \quad (2.1)$$

and is one of the most common methods of detecting the CMC or measuring the impact of surfactant monolayers. After the surfactant concentration reaches the critical micelle concentration, solution surface tension remains constant for pure solutes despite increasing surfactant concentration (Figure 2.2(a)). The Figure also illustrates the impact of alien compounds whereby post-CMC the interfacial tension becomes affected by the impact of impurities. What follows provides a brief description of surface tension measurement using Gibbs equations of state (Gibbs, 1948; Clint, 1992a). For a pure surfactant solution, the molecules at the interface are at a lower free energy than those in bulk. Surface tension relates to the amount of work to create a unit area of surface. Due to the minimised surface energy state, less work is needed to create unit area of surface than unit area of bulk.

Surface tension γ is defined as the integral of sum chemical potentials μ of solution species i (Clint, 1992a)

$$-d\gamma = \sum_i \Gamma_i d\mu_i \quad (2.2)$$

where Γ_i is the interfacial concentration of component i or the number of moles of i per unit area. In a pure surfactant solution, two-phase system of solvent₁ and solute₂ that is surface-active and uncharged, the rate of change of γ with respect to change in chemical potentials is

$$-d\gamma = \Gamma_1 d\mu_1 + \Gamma_2 d\mu_2. \quad (2.3)$$

The term Γ_i is also defined as the surface excess, which is the difference between bulk and (total) interfacial concentration. In other words, it is the difference between the concentration of solute absorbed at the interface and that which would be if the bulk concentration continued to the interface (Clint, 1992a). It is presumed that at the interface, the surface excess of the solvent Γ_1 is zero, thus

$$-d\gamma = \Gamma_2 d\mu_2. \quad (2.4)$$

For changes in surfactant concentration,

$$d\mu_2 = RT \cdot d\ln a_2, \quad (2.5)$$

where a_2 is the activity of surfactant in solution, T is the temperature and R is the gas constant. The surfactant excess then becomes

$$\Gamma_2 = -\frac{1}{RT} \cdot \frac{d\gamma}{d\ln(a_2)}. \quad (2.6)$$

For dilute surfactant solutions, assuming that a_2 can be approximated to concentration c_2 (Gibbs, 1948; Clint, 1992a)

$$\Gamma_2 = -\frac{1}{RT} \cdot \frac{d\gamma}{d\ln(c_2)}. \quad (2.7)$$

In this formalism, the following assumptions have been made. The solute (surfactant) is presumed to be a single component, that a surface for which $\Gamma_1 = 0$ can be defined and that $a_2 = c_2$ is true (Clint, 1992a). Applying Equation (2.7) to liquid-liquid interfaces, it is required that the surfactant groups can partition into both of the (immiscible) phases. The emulsion droplet radius can depend on the surfactant packing geometries. Ignoring the effect of polydispersity, the relation between equilibrium/constant interfacial tension γ_c and droplet radius r , or equally the bending energy per unit area is (Clint, 1992a)

$$\gamma_c = \frac{K}{2r^2} \quad (2.8)$$

where K is the elastic bending modulus that can be measured by ellipsometry (Binks *et al.*, 1989). Liquid drops tend to be spherical due to the smallest surface-to-volume ratio of the shape (Atkins, 2014a). At planar liquid interfaces (i.e. $r = \infty$), $\gamma \neq 0$ as energy is required to straighten the natural surfactant packing curvature. Interfacial tension is an equilibrium quantity whereby the adsorbed surfactants are in a dynamic equilibrium (arriving and leaving at the same rate) (Clint, 1992a). Changes in surfactant arrival/departure rates will result in instantaneous tension gradients and interfacial monolayer disturbance. The presence of surfactant aggregates, e.g. micelles will complicate the rebalancing of the monolayer whereby lower CMCs will lead to higher re-equilibration times (Clint, 1992a).

The onset of the CMC leads to constant surface tension, that is above the CMC $d\gamma = 0$ using Equation (2.4).

The number of molecules in a micelle can be determined by a number of techniques e.g. small-angle neutron scattering (Hayter & Penfold, 1981; Chen, 1986; Chevalier

& Zemb, 1990), steady-state fluorescence quenching (Turro & Yetka, 1978; Almgren & Lofroth, 1981), time-resolved fluorescence quenching (Almgren & Lofroth, 1981, 1982), nuclear magnetic resonance and Raman and infra-red spectroscopy (Chevalier & Zemb, 1990). For a pure surfactant solution, increasing the number of molecules per micelle may lead to changes in its shape. Clint (1992*d*) describes the change in aggregate shape for sodium dodecyl sulphate (SDS) in aqueous solutions of 0.4 dm m^{-3} NaCl. Given a fixed salt concentration, the increase in SDS concentration did not lead to a change in molecule number per micelle. However increasing NaCl concentration (fixed SDS) the number of molecules per micelle increased, leading to a transition from spherical to cylindrical aggregates (Kratohvil, 1980; Warr *et al.*, 1986; Berr & Jones, 1988). The sphere-to-rod transition (Hayashi & Ikeda, 1980) is caused by the reduction of the effective head group area (Clint, 1992*d*).

Dissociation of surfactants in a micelle is much lower than that of single molecules in solution due to counterion binding. The surface of a micelle has a charge induced by the head-groups, which will lead to a greater (electrostatic) attraction of counterions than that induced by single molecules. This electrostatic attraction can be described by the cell model (Gunnarson *et al.*, 1980) whereby the concentration of counterions decays continuously with distance from the micelle surface (Clint, 1992*d*). Generally, the counterions normally are thought of as immediately ‘bound’ and diffuse (electrical double layer) (Lindman *et al.*, 1982). The degree of counterion binding β_{ci} is the concentration of bound ions divided by the concentration of surfactant in a micelle. The concentration of counterions of type i at a distance r from a micelle’s surface m_0^i is (Gunnarson *et al.*, 1980)

$$m^i(r) = m_0^i \exp \left\{ -\frac{z_i e \psi(r)}{kT} \right\}. \quad (2.9)$$

In the above, z_i is the counterion valency and $\psi(r)$ is the electrostatic potential at a radial distance r from the micellar centre. In pure ionic surfactant mixtures, β_{ci} is independent of surfactant concentration (Clint, 1992*d*). In solutions where both ionic and non-ionic surfactants are present, the non-ionic groups reduce the charge density at the micelle surface (Scamehorn, 1986; Clint, 1992*e*). This leads to a reduction of β_{ci} . Treiner *et al.* (1989) illustrated this reduction by measuring β_{ci} in an SDS solution as a function of a mole fraction of a non-ionic component. Despite an evident decline the relative surface charge remained constant and independent of

non-ionic surfactant concentration (Treiner *et al.*, 1989).

Surfactants can also adsorb on solid surfaces, whereby adsorption would be affected by a surface's hydrophobicity, charge H bonding and type (organic/inorganic) (Clint, 1992*b*). The amount of surfactant adsorbed on a surface is more difficult to calculate than at liquid-liquid or liquid/air interfaces and spectroscopic methods are normally used, as well as (Langmuir) adsorption isotherms (Clint, 1992*b*).

2.2.1 *The critical micelle concentration*

The critical micelle concentration (CMC) of a surfactant is the minimal concentration required to form a micelle (Clint, 1992*d*). The CMC is influenced by the minimum of the standard chemical potential of a surfactant molecule in an aggregate with N molecules (Israelachvili, 1987; Clint, 1992*d*). For aqueous systems this minimum will depend on the hydrophobicity of the head and the tail (alkyl chain length). Polar head groups that are highly hydrophobic will lead to an increase in the CMC, whereas increasing the alkyl chain length will decrease the CMC. Increasing the valency of ionic head groups will decrease the CMC. Non-ionic surfactants will generally have much lower CMC values as polar groups of ionic compounds produce greater and wider CMC ranges. For zwitterionic surfactants, crucial for the CMC is the charge separation as at very short separation distances, the two opposite charges will neutralise. At a critical distance, the positive and negative groups will maximise the electric dipole moment maximising the CMC in water, whereas at very long chain lengths more hydrophobic groups will be induced, decreasing the CMC (Chevalier *et al.*, 1988; Clint, 1992*d*).

In the presence of ionisable groups (including carboxylic acids), solution pH will strongly influence the degree of surfactant dissociation (Tokiwa, 1972). Zwitterionic surfactants can become ionic at low pH (Corkill *et al.*, 1969) which will change their CMC. Adding electrolyte to systems of ionic surfactants will reduce the CMC as electrostatic repulsion between the molecules will be reduced (Clint, 1992*d*), whereas in non-ionic systems this effect will be variable (Schick, 1962; Schott, 1962). Temperature will also have an effect on micellarisation, with the CMC of non-ionic surfactants decreasing monotonically with increasing temperature. For ionic surfactants, the CMC is likely to have a parabolic relation with temperature (and pressure) (La Mesa, 1990; Clint, 1992*d*). Atkins (2014*b*) stated that micelles only form above the Krafft temperature and that the CMC corresponds to a transition concentration region whereby the physical properties vary smoothly but nonlinearly

with concentration.

2.2.2 Multiple micellarisation

Multiple micellarisation is a phenomenon whereby a surfactant solution is prone to forming micelles of two sizes, corresponding to CMC_1 and CMC_2 (Georges & Chen, 1986; Clint, 1992*a*; Ray *et al.*, 2005). It is thought that the former micelle type (CMC_1) undergoes a structural transition to the second type (CMC_2) (Ray *et al.*, 2005). The latter occurs in some pure substances and is very common in mixtures of cationic surfactants with a variation in the hydrophobic tail length (Georges & Chen, 1986; Treiner & Makayssi, 1992; Ray *et al.*, 2005). The CMC_2 is assumed to occur due to an alteration in the counterion condensation but not interfacial tension (Treiner & Makayssi, 1992; Prasad *et al.*, 2004, 2005), thus tensiometry is incapable of detecting it (Ray *et al.*, 2005). It has been suggested that above CMC_2 the degree of counterion condensation is constant (Treiner & Makayssi, 1992). The methods that can monitor this structural transition include conductometry, isothermal titration calorimetry (Prasad *et al.*, 2004, 2005), ultrasound characterisation (Andreatta *et al.*, 2005*a*; Svalova *et al.*, 2017), viscometry (Ekwall *et al.*, 1971), NMR (Fabre *et al.*, 1980) and solubilisation (Bury *et al.*, 1991). A comprehensive investigation of multiple micellarisation was presented in Ray *et al.* (2005) and is explained in some detail as follows. Viscosity, enthalpy, surface tension and specific conductance was measured for cetyltrimethylammonium bromide ($\text{CH}_3(\text{CH}_2)_{n-1}\text{N}(\text{Br})(\text{CH}_3)_3$, $n=10,12,14,16$; abbrev. C_nTAB) surfactants (pure and mixtures) in aqueous and 0.05 M NaBr solutions. For pure $\text{C}_{12,16}\text{TAB}$ solutions, only one CMC was observed. Prior to CMC, viscosity would sharply decline and flatten out afterwards. For mixed $\text{C}_{12,16}\text{TAB}$ solutions, CMC_1 would be manifested by an increase in viscosity gradient and CMC_2 - by a further flattening out of the slope with an increasing surfactant concentration. This was observed for both, aqueous and NaBr solutions. The most blunt indication of multiple micellarisation in CTAB mixtures was observed using enthalpograms obtained from microcalorimetry measurements. Specific conductance showed a very subtle change in response to multiple micellarisation, whereas surface tension measurements was only able to detect CMC_1 in surfactant mixtures (Ray *et al.*, 2005).

2.3 An Introduction to Colloids

According to Atkins (2014*b*), “a colloid [...] is a dispersion of small particles of one material in another that does not settle under gravity”, whereby small refers to < 500 nm or nanoparticle suspension size (diameter up to 100 nm), with a lower limit of c.a. 1 nm (Hunter, 2001). Colloidal dispersions are systems where the kinetic units that are dispersed through the solvent are much larger than the solvent molecules (Hunter, 2001), which would be the case for the trapped water droplets in water-in-oil emulsions and petroleum mousses. Colloids are used in a variety of industries and science fields, including petroleum extraction (Littman, 1997), medicine (De & Maitra, 1997), cosmetics and food (Challis *et al.*, 2005) to name just a few. An emulsion is a colloid where the dispersed and continuous phase are both liquid (Challis *et al.*, 2005), or a thermodynamically unstable dispersion of two immiscible liquids the stability of which is characterised by a non/slow flocculation/coalescence of the dispersed droplets (McLean *et al.*, 1998).

The particle size distribution (PSD) is one of the key factors affecting the long-term stability of a colloidal mixture (Jillavenkatesa *et al.*, 2001; Challis *et al.*, 2005), whereby homogenised emulsions are most stable (Atkins, 2014*b*). A monodisperse mixture corresponds to a system with similarly-sized particles and a small size standard deviation (Challis *et al.*, 2005). Equivalently, colloidal stability depends on the kinetic state of the system. Droplet-droplet interactions, resulting in the long-term stability or phase separation, depend on the energy of attraction between individual atoms (on the droplet surface) and their total interactions (Atkins, 2014*a*). In particular, the attraction energy between two atoms in different colloidal particles separated by a distance R declines $\sim R^{-6}$, however the sum of all pairwise interactions declines $\sim R^{-2}$. Therefore, the latter play a greater role in the long-term colloidal stability. Stabilisation techniques to prevent flocculation and coalescence (coagulation) for colloidal system include addition of surfactants, or by increasing the viscosity of the continuous phase thus reducing Brownian diffusion (Challis *et al.*, 2005) that is easily induced by thermal fluctuations (Batchelor, 1976). The latter description of a stable colloid is consistent with the literature definition of stable crude oil mousses, that are characterised by a high viscosity and a small water droplet size (Lee, 1999).

2.4 Kinetics of Colloidal Interactions

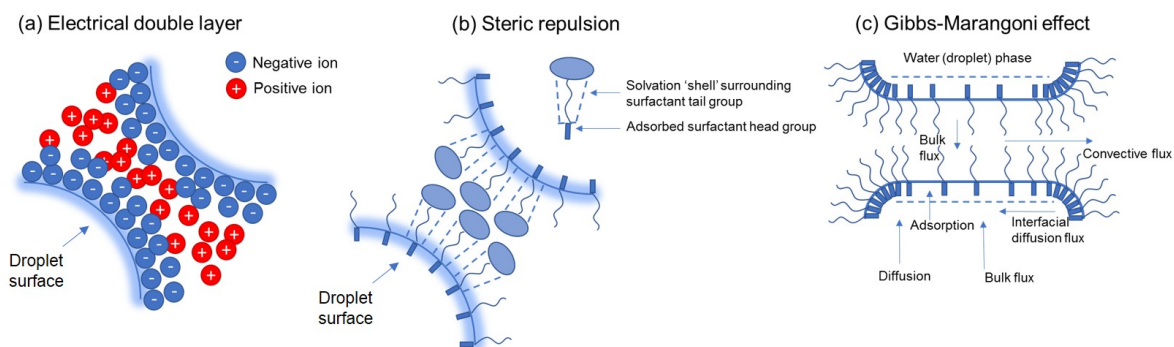


Figure 2.3: Particle interactions in colloidal mixtures. Adapted from (McLean *et al.*, 1998)

Emulsion destabilisation occurs following the movement of the dispersed droplets towards each other, droplet deformation and formation of a thin parallel film between them and droplet coalescence as the parallel film thickness reduces below a critical value (Zapryanov *et al.*, 1983; McLean *et al.*, 1998). Some of the mechanisms responsible for the emulsions stability include the electrical double layer, steric repulsion, the Gibbs-Marangoni effect, a rigid, cross-linked network formation of the adsorbed interfacial layers (McLean *et al.*, 1998) and Pickering stabilisation (Norton *et al.*, 2013). These are described in some detail as follows, the former three phenomena are described in more detail in (McLean *et al.*, 1998).

2.4.1 *Electrokinetic interactions*

The stability/repulsion of lyophobic (solvent-repelling) (Haring, 1926; Atkins, 2014b) dispersions can be formulated following the Derjaguin, Landau, Verwey, and Overbeek (DLVO) theory (Hunter, 1987; McLean *et al.*, 1998). The latter assumes that colloidal interactions are balanced by the van der Waals interactions between molecules in the adsorbed surfactants and the coulombic repulsion of the electrical double layers. Additionally, Born repulsion occurs as the electron clouds of the particles at the droplet interface overlap (Schramm, 1992). The following summarises the two former concepts.

Van der Waals theory attempts to describe the long-range attractive forces between atoms (Van der Waals, 1873) often used to understand colloidal stability (Clint, 1992a; Hoier & Whitson, 2001; Ratulowski *et al.*, 2003; Mullins, 2011; Atkins,

2014*b*). The London theory (London, 1930) explains the van der Waals (dispersion) force as arising from the interaction between a temporary dipole on one molecule and the induced dipole on another (Israelachvili, 1974). Following Bohr's model of the H atom, the instantaneous dipole moment of H can be calculated from the ground state formulation a_0

$$a_0 = \frac{e^2}{8\pi\epsilon_0\hbar v} \quad (2.10)$$

where e is the proton charge, ϵ_0 is the permittivity of free space, \hbar is Planck's constant and v is a characteristic frequency of the electron's motion around the nucleus. From the formalism of a_0 , the magnitude of the induced dipole moment is $p_1 \approx a_0 e$. The rest of van der Waals formulations can be found in Hunter (2001). If a neutral atom is nearby H, it will be polarised by p_1 and acquire an induced dipole moment of strength p_2 . The individual atom-atom interactions will decay following R^{-6} where R is the separation distance. In particular, the van der Waals interaction energy $V_{\text{int}}(R)$ (London's equation)

$$V_{\text{int}}(R) = -\frac{3}{4}\hbar\omega_0(R_0/R)^6, \quad R_0^6 = \frac{\alpha_A^0\alpha_B^0}{(4\pi\epsilon_0)^2}, \quad \omega_0 = \frac{\frac{2e}{\sqrt{m_e}}}{\sqrt{\frac{\alpha_A^0}{N_A}} + \sqrt{\frac{\alpha_B^0}{N_B}}}. \quad (2.11)$$

between two polarisable molecules A and B depends on their separation distance R , number of electrons in each molecule, N_A and N_B , and electron mass m_e . The polarisabilities α_A^0 and α_B^0 are zero-frequency quantities (London, 1930).

Lyophobic colloids are those in which the minimum system energy corresponds to the dispersed phase condensed in one large aggregate, which can be prevented by electrostatic and steric stabilisation (Hunter, 2001). In electrostatic stabilisation, the electrical double layer (EDL) gives rise to the kinetic non-lability of colloids (Atkins, 2014*b*). The EDL comprises two regions of charge: the tightly-adhering immobile layer of ions with the electrokinetic potential ζ and an oppositely-charged atmosphere of ions 2.3 (a). The repulsion energy $V_{\text{repulsion}}$ of two EDLs depends on the separation distance of the layer centres and surfaces, as well as the thickness of the EDL. Flocculation occurs at high ionic strengths that result in a dense (compressed) ionic atmosphere (Hunter, 2001). Coagulation (merging particles) occurs when the separation between EDLs is sufficiently small and the van der Waals forces dominate (Atkins, 2014*b*). In water-oil emulsions, however, the EDL is assumed to not have a significant effect due to the low dielectric constant of oil (Strassner, 1968;

Carroll, 1976; McLean *et al.*, 1998).

2.4.2 *Steric stabilisation*

In steric stabilisation (Figure 2.3 (b)), the surface of a lyophobic colloid is covered by lyophilic material (Napper & Hunter, 1983; Hunter, 2001), or surfactants that partition into the lyophobic/lyophilic phases according to their molecular structure. Steric repulsion arises due to the strong interaction of the adsorbed material (surfactants) and the sorbent phase which give rise to enthalpic and entropic repulsion as two emulsion droplets approach (Mackor, 1951; McLean *et al.*, 1998). Where it arises from nonionic polymers, steric repulsion is assumed to be the main stabilisation mechanism (Mackor & van der Waals, 1952). McLean *et al.* (1998) reported that the electrokinetic mechanisms mentioned above are associated with stabilisation energies lower than those observed in the water-in-oil emulsions stabilised by resins and asphaltenes. The required solvation energies are typical of H bonding and it is presumed that steric stabilisation is required (McLean *et al.*, 1998).

2.4.3 *Gibbs-Marangoni effect*

The Gibbs-Marangoni effect (GME) is a phenomenon that stabilises emulsions with relatively low interfacial tension at the droplet interface (Mukherjee & Kushnick, 1988; Krawczyk *et al.*, 1991; Shetty *et al.*, 1992). When two droplets approach, the continuous phase between them drains out and ‘drags’ the adsorbed surfactants, and a tension gradient is created at the droplet interface (Figure 2.3 (c)). The diffusion flux arising due to the surfactant depletion opposes the drainage by increasing interfacial rigidity and acts as a stabilisation mechanism (McLean *et al.*, 1998). To promote coalescence in emulsions stabilised by this mechanism, the interfacial activity and diffusivity of the adsorbed surfactants must be sufficiently high (Hirato *et al.*, 1991; Krawczyk *et al.*, 1991; Wasan, 1992; Kim *et al.*, 1993). Otherwise, to destabilise an emulsion where the GME is significant, the interfacial shear viscosity and dynamic tension gradient must be reduced (Mukherjee & Kushnick, 1988). Due to the high interfacial tensions and elastic moduli reported for the water-in-oil emulsions, it appears unlikely for the GME to be a dominant mechanism in emulsion stabilisation (Fordedal *et al.*, 1996).

2.4.4 Droplet skin formation

The following (mechanical) stabilisation phenomenon has been observed in/applied to mainly asphaltene-stabilised water-in-oil systems. The indigenous surface-active material in petroleum, namely resins and asphaltenes, has been assumed to create an interfacial ‘skin’ and be primarily responsible for stabilising water-in-oil emulsions (Van der Waarden, 1958; Kimbler *et al.*, 1966; Eley *et al.*, 1976; Wasan, 1992; Mohammed *et al.*, 1993; Fordedal *et al.*, 1996). The two component groups were reported to contribute to stabilisation (Fordedal *et al.*, 1996) through the formation of a cross-linked asphaltene aggregate network (possibly, but not necessarily) solvated by resins, that has a high viscosity and rigidity (McLean *et al.*, 1998). Additionally, the forces which govern the physicochemical state of the asphaltenes at the phase interface are assumed to be of the magnitude of hydrogen bonds or electron donation/acceptance, which are, again, greater than the electrokinetic phenomena (McLean *et al.*, 1998). More on asphaltene skin formation round water droplets will be explained in the next Chapter.

2.4.5 Pickering stabilisation

Emulsions whereby interfaces are kinetically stabilised with colloidal particles are known as Pickering emulsions (Binks, 2002; Norton *et al.*, 2013). The stabilising particles don’t form micelles (Binks, 2002) and, unlike surfactants, irreversibly adsorb at the oil-water interface creating a mechanical barrier against droplet coalescence (Arditty *et al.*, 2004). The factors determining stabilisation properties of the adsorbed particles include concentration, size, shape, particle-particle interactions and wettability (Frasch-Melnik, 2011; Norton *et al.*, 2013). The latter is one of the most important factors and, in turn, can be measured the particle contact angle at the interface (Schulman & Leja, 1954; Binks, 2002). In water/oil emulsions, for Pickering stabilisation to occur the particle contact angle at the phase interface should be $> 90^\circ$. Wettability can be measured by goniometry or tensitometry (Norton *et al.*, 2013). Particle size is also an important factor in the Pickering mechanism, whereby the adsorbed particles need to be at least an order of magnitude smaller than the droplets in an emulsion (Norton *et al.*, 2013).

Surfactants and stabilising particles can interact to further enhance emulsion stability at the interface (Norton *et al.*, 2013). In particular, lower molecular weight surfactants can adsorb onto the particles and trigger their flocculation at the water-

oil interface (Norton *et al.*, 2013). Surfactants can also displace particles at the interface and stabilise the droplets instead, if this is energetically favourable in a given emulsion (Vashisth *et al.*, 2010). Pichot *et al.* (2009) proposed a two-part mechanism giving rise to the long-term stability of an emulsion. They studied monoolein (surfactant)/silica (particle) mixtures to propose that the presence of surfactants can initially reduce the interfacial tension and allow droplet formation, providing time for the less mobile particles to travel to the interface, displace the surfactant and provide long-term stability of an emulsion. Their further studies suggested that whether silica or surfactants remain at the phase interface is determined by the relative surfactant concentration (Pichot *et al.*, 2010). The droplet size in mixture-stabilised systems will be influenced by concentrations of either of the phases (Pichot *et al.*, 2010).

Chapter 3. Asphaltenes

3.1 Introduction

Petroleum can be separated into four SARA fractions, namely saturate, aromatic, resin and asphaltene (Aske *et al.*, 2001; Gafonova & Yarranton, 2001; Sjoblom *et al.*, 2003; Peters *et al.*, 2005g; Klein *et al.*, 2006a), as illustrated in Figure 3.1. Asphaltenes constitute the highest molecular weight, most polar and aromatic fraction of crude oil (Gafonova & Yarranton, 2001; Dicharry *et al.*, 2006). The molecular definition of asphaltenes is problematic given their high structural heterogeneity (Schuler *et al.*, 2015, 2017), thus asphaltenes are defined as a solubility class, namely the hydrocarbon fraction soluble in toluene and insoluble in light normal

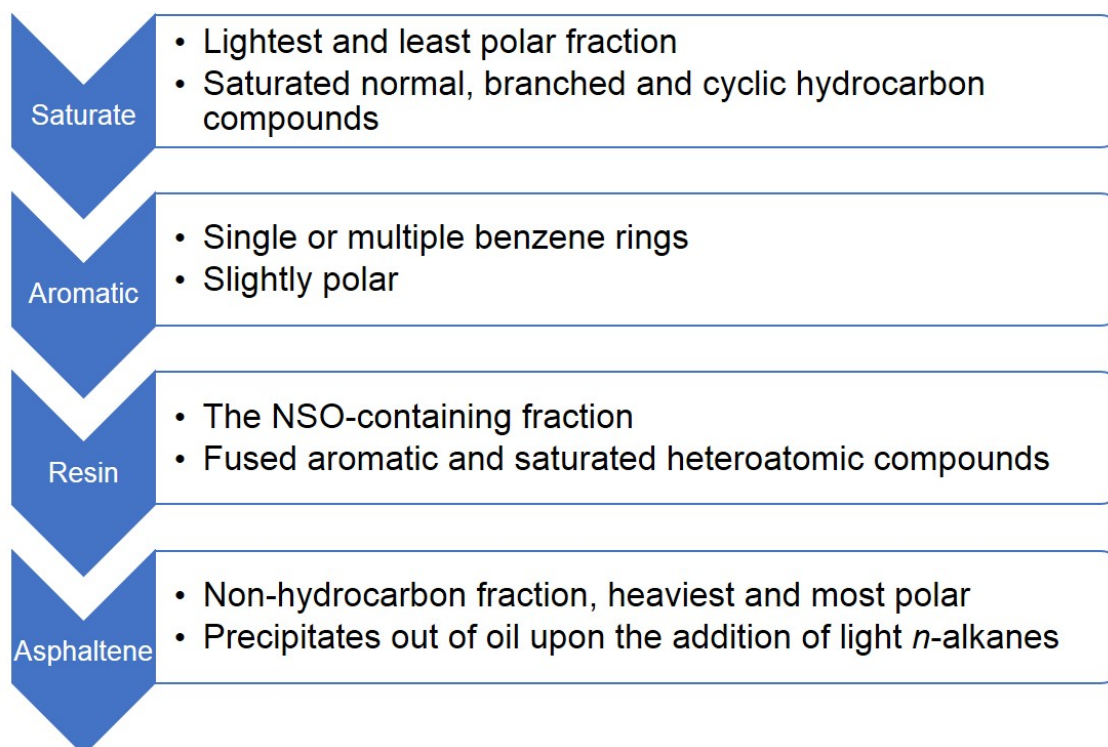


Figure 3.1: A schematic of SARA fractionation.

alkanes (e.g. n -C₅₋₇) (Chilingarian & Yen, 1978; Mullins *et al.*, 1998; Sjoblom *et al.*, 2003; Mullins *et al.*, 2007; Mullins, 2011; Mullins *et al.*, 2012). A ‘typical’ asphaltene molecule has both aromatic and saturated groups; this will be discussed in detail in Section 3.2. The asphaltene solubility fraction is governed by a balance of attractive and repulsive forces of its molecules (Betancourt *et al.*, 2009), that is the balance between the van der Waals aromatic attraction and side-chain repulsion (Buenrostro-Gonzalez *et al.*, 2001). An increase in the relative abundance of side-chains on asphaltene molecules would increase their solubility (Betancourt *et al.*, 2009). In contrast, larger asphaltene molecules with a complete removal of alkane side-chains are completely insoluble (Buch *et al.*, 2003).

Asphaltenes possess heteroatomic functionality and include elements such as N, O, S, V, Ni and Fe (Speight, 1999; Fossen *et al.*, 2007; Mullins *et al.*, 2007). A commonly-used method to separate asphaltenes from petroleum is the addition of excess n -alkane whereby the yield (%) of the asphaltenes will depend on the solvent weight (Peters *et al.*, 2005*g*), n -C₅ typically generating a higher yield (Speight, 1999) by 15-98% (Strausz, 2002). The molecular weight of the precipitating solvent will also affect the physico-chemical properties of the asphaltene fraction (Bunger & Li, 1981; Ovalles *et al.*, 2011; McKenna *et al.*, 2013). Resins and low molecular weight asphaltenes can also precipitate with the asphaltenes which can be separated from asphaltenes by Soxhlet extraction (Frakman *et al.*, 1990; Peng *et al.*, 1997; Strausz *et al.*, 1999*a*) and gel permeation chromatography (Ignasiak *et al.*, 1983). In acetone Soxhlet extractions (Strausz *et al.*, 1999*a*), the molecular weight of the acetone extract is a third to a half of that of the resulting asphaltene. The compounds identified in the acetone extract (Frakman *et al.*, 1990; Peng *et al.*, 1997) included biomarkers and heteroatom compounds, including ketones, alcohols, sulfoxides attached to polycyclic terpenoids, and polycyclic terpanes. Carboxylic acid-containing compounds included those derived from polycyclic terpenoids (tricyclics and hopanoids), dibenzothiophene, n -alkanes, polyaromatics and fluorene. Nitrogen-containing compounds included different groups of benzocarbazoles (Frakman *et al.*, 1988).

Asphaltene precipitation from crude oil depends on a number of factors, including aromaticity, polarity, molecular weight and structure, temperature and pressure (Speight, 2004; Fossen *et al.*, 2007). Further, ‘standardised’ n -alkane precipitated asphaltenes may lose or mask important properties of a ‘genuine’ asphaltene fraction (Fossen *et al.*, 2007). Laboratory-obtained asphaltenes (n -C₇ precipitation)

were found to differ from those precipitated under petroleum recovery (pressure drop) (Klein *et al.*, 2006b). Noting that ‘live’ crude refers to a petroleum sample under reservoir pressure (and thus, the volatile compounds have been preserved) the *n*-C₇ asphaltenes had a higher aromatic and double-bond content and a lower abundance of the N-, NS-, NS₂-, O- and S- containing species than pressure drop asphaltenes (Klein *et al.*, 2006b). Nevertheless, the *n*-alkane precipitation ensures that asphaltenes are mostly isolated from resins in laboratory conditions (Alboudwarej *et al.*, 2002; Goual & Firoozabadi, 2002), although further purification (e.g. Soxhlet extraction) may be needed. Asphaltenes can be further fractionated into subfractions according to their polarity (Nalwaya *et al.*, 1999), solubility in different solvents (Nalwaya *et al.*, 1999; Speight, 1999; Hu & Guo, 2001; Aquino-Olivos *et al.*, 2003; Trejo *et al.*, 2004; Acevedo *et al.*, 2005; Wattana *et al.*, 2005) and heteroatomic content (Speight, 1999). The solubility of asphaltenes will depend on the source type and H/C ratio- Speight (1999) observed that coal asphaltenes have a very poor solubility in toluene at room temperature and atmospheric pressure compared to those precipitated from crude oil.

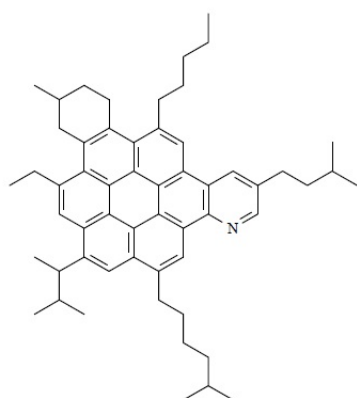
The molecular weight of asphaltenes has been debated for decades due to their self-association phenomenon (Mullins, 2011; Sjoblom *et al.*, 2015). Due to the advances in spectroscopic techniques, such as fluorescence depolarisation, the average asphaltene molecular weight has been generally agreed as ca. 750 Da (± 250 Da) (Groenzin & Mullins, 1999, 2000; Buenrostro-Gonzalez *et al.*, 2001; Buch *et al.*, 2003; Groenzin *et al.*, 2003; Badre *et al.*, 2006). A number of studies investigated the heterogeneity of the asphaltene fraction through further fractionation (Sjoblom *et al.*, 2015). Asphaltene samples were fractionated by ultracentrifugation (Fenistein & Barré, 2001; Barre *et al.*, 2008) or obtained by different *n*-alkane/crude oil ratios (Fossen *et al.*, 2007, 2011) to discover that the asphaltenes from different fractions formed aggregates of varying viscometric properties compared to the unfractionated asphaltene.

3.2 The Yen-Mullins Model of Petroleum Asphaltenes

3.2.1 Asphaltene monomers

The Yen-Mullins model (Mullins, 2011) is one of the most widely used in describing asphaltene molecular structure and self-association. It proposes that a ‘generic’ asphaltene molecule comprises a polycyclic aromatic hydrocarbon core (PAH) and aliphatic side-chains (Figure 3.2 (i-iii)). The latter architecture known as the ‘island’.

The average number of rings in a PAH is $7 (\pm 3)$, confirmed by scanning tunneling microscopy (Zajac *et al.*, 1994; Mullins, 2011), Raman spectroscopy (Bouhadda *et al.*, 2007; Mullins, 2011), time-resolved fluorescence depolarisation (Groenzin & Mullins, 1999, 2000; Buch *et al.*, 2003), mass spectroscopy (Boduszynski, 1988) and recently by atomic force microscopy (Schuler *et al.*, 2015, 2017). The alternative model for asphaltene architecture is the archipelago (Groenzin & Mullins, 2000), whereby asphaltenes are thought to comprise several (1-4 member) PAH connected by alkyl bridges. The size of an archipelago molecule can reach ca. 2000 Da (Snowdon *et al.*, 2016) (Figure 3.2 (iv-v)).



(i) Island architecture, Mullins (2011)

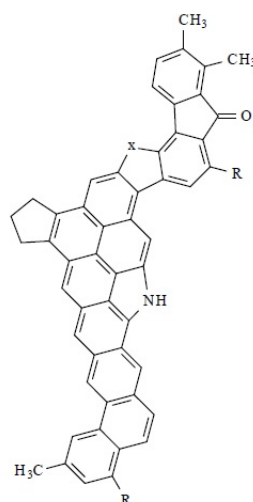
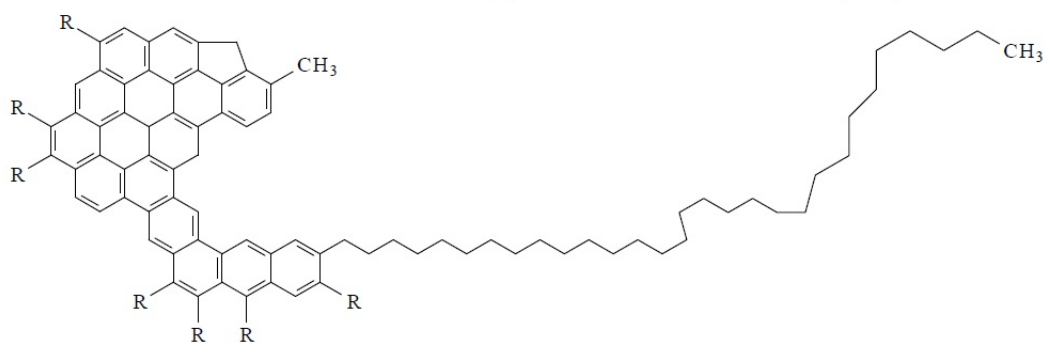
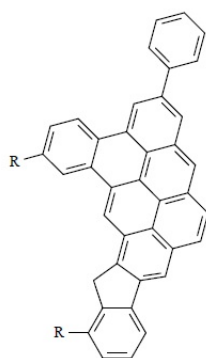
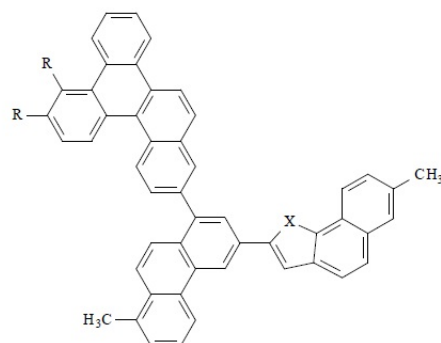
(ii) Island architecture, Schuler *et al.* (2017)(iii) Island architecture, Schuler *et al.* (2017)(iv) Archipelago architecture, Schuler *et al.* (2017)(v) Archipelago architecture, Schuler *et al.* (2017a)

Figure 3.2: Proposed asphaltene structures (Mullins, 2011; Schuler *et al.*, 2017). Schuler *et al.* (2017a) is the Supplementary Information attached to Schuler *et al.* (2017). Unknown atoms and side-chains are denoted X and R respectively.

This structure, however, is uncommon and recent atomic force microscopy studies of coal (Schuler *et al.*, 2015) and petroleum (Schuler *et al.*, 2017) asphaltenes illustrated their very low abundance. A possible explanation for this is the low stability of archipelago compounds versus island structures as confirmed by laser fragmentation experiments (Borton *et al.*, 2010; Sabbah *et al.*, 2011). The size of a PAH in an island molecule has been estimated at 7 fused rings (Sjoblom *et al.*, 2015), as studied by high-resolution transmission electron microscopy (Sharma *et al.*, 2002a), molecular orbital analysis (Ruiz-Morales & Mullins, 2009) and atomic force microscopy (Schuler *et al.*, 2015, 2017). Hosseini-Dastgerdi *et al.* (2015) suggested that as different analytical methods to determine asphaltene architecture indicated different models, the asphaltene molecular structure to be a “continuum of island and archipelago types”. Coal asphaltenes were reported to be smaller than petroleum asphaltenes (Groenzin & Mullins, 2000, 2007; Guerra *et al.*, 2007; Hortal *et al.*, 2007; Martinez-Haya *et al.*, 2007; Schneider *et al.*, 2007). Studies using ^{13}C NMR (Buenrostro-Gonzalez *et al.*, 2001) and atomic force microscopy (Schuler *et al.*, 2015) confirmed that coal asphaltenes have very little or no alkyl side-chains.

3.2.2 Asphaltene nanoaggregates

The first stage of asphaltene self-association is nanoaggregation, occurring at concentrations of ca. 100 mg L^{-1} ($\pm 50 \text{ mg L}^{-1}$) in toluene (Andreatta *et al.*, 2005a; Mullins, 2011; Mullins *et al.*, 2012). This concentration has also been termed as the critical nanoaggregate concentration (CNAC) (Andreatta *et al.*, 2005a; Mullins, 2010). In petroleum, it has been estimated that asphaltenes are also present as nanoaggregates with a colloidal size estimate of ca. 1.6 nm (which corresponds to nanoaggregate size) (Betancourt *et al.*, 2009). The CNAC has been estimated using high- Q ultrasonic measurements (Andreatta *et al.*, 2005a; Svalova *et al.*, 2017), direct conductivity (with a very subtle indication of the changepoint) (Zeng *et al.*, 2009) and nuclear magnetic resonance (Freed *et al.*, 2009). Two forces are assumed to govern the dynamics of nanoaggregation, namely $\pi - \pi$ attraction between PAH cores (van der Waals) and steric repulsion between side-chains (Buenrostro-Gonzalez *et al.*, 2001; Mullins, 2011). The balance between the two forces should determine the number of monomers in a nanoaggregate (Mullins, 2011) and (presumably for the island architecture) is estimated to be up to 10 monomers indicated by equation-of-state estimations (Betancourt *et al.*, 2009), centrifugation experiments (Goual *et al.*, 2011) and surface compression analyses (Orbulescu *et al.*, 2010a,b). It has

been suggested that the number of molecules in nanoaggregates is constant with increasing concentration (Andreatta *et al.*, 2005*a,b*, 2007). At sufficiently high concentrations, corresponding to the critical clustering concentration (CCC), which is the next stage of aggregation (Mullins, 2011), asphaltene nanoaggregates form clusters causing a strong change in flocculation kinetics (Anisimov *et al.*, 1995; Yudin & Anisimov, 2007). Asphaltene clustering has been reported to form at a g L⁻¹ scale (Friberg *et al.*, 2007; Oh & Deo, 2007; Yudin & Anisimov, 2007). Clustering indicates a change in aggregation kinetics (Anisimov *et al.*, 1995; Yudin & Anisimov, 2007) whereby nanoaggregates are held together by much weaker forces (Sheu *et al.*, 1995*a*; Sheu, 2002) than the asphaltenes within nanoaggregates.

3.3 Nanoaggregates Versus Surfactant Aggregates

In the present investigation, asphaltene nanoaggregation is compared to surfactant micellarisation allowing the use of sonic velocity models to detect the CNAC (Zielinski *et al.*, 1986; Andreatta *et al.*, 2005*a*). This section presents the strengths and limitations of this assumption. The definition of surfactant micellarisation that is used is comparison with asphaltene nanoaggregates is consistent with the key model used with ultrasonic velocity measurements (Zielinski *et al.*, 1986), ‘*Surfactant molecules in aqueous solutions exist in the monomeric form below the critical micelle concentration (CMC), while they can be in either monomeric or micellar forms, if the surfactant concentration exceeds the CMC.*’.

Asphaltenes are often compared to surfactants due to their surface activity at the solid/liquid (Acevedo *et al.*, 1998, 2003; Dudasova *et al.*, 2008; Simon *et al.*, 2009) and liquid/liquid (Jeribi *et al.*, 2002) interfaces. Bikky (2012) likened the asphaltenes to weak ionic surfactants and those adsorbed at a water-oil interface were enriched with O and S groups (Wu, 2003; Jarvis *et al.*, 2015). The structure of the adsorbed layer is speculated to depend on asphaltene concentration (Sjoblom *et al.*, 2015) and has been reported to be that of a monolayer (Gonzales & Middea, 1988; McLean *et al.*, 1998; Dudasova *et al.*, 2008; Simon *et al.*, 2009) or stepwise/linear adsorption (Acevedo *et al.*, 1995, 1998, 2003). For liquid/liquid adsorption, two stages (rapid and slow), have been observed during interfacial tension experiments (Jeribi *et al.*, 2002; Harbottle *et al.*, 2014). Several explanations have been reviewed in Sjoblom *et al.* (2015). Asphaltenes are reported to contribute to WOE stabilisation through steric effects (Spiecker *et al.*, 2003; Wang *et al.*, 2010; Tchoukov

et al., 2014) and the formation of a ‘skin’ (McLean *et al.*, 1998; Bauget *et al.*, 2001; Jeribi *et al.*, 2002).

Surfactants tend to be located at the interface between two liquid phases as this corresponds to their lowest energy state (Clint, 1992*f*). Such interfacial activity agrees with the phenomenon of asphaltene ‘skin’ formation around water droplets (Singh *et al.*, 1999; Khristov *et al.*, 2000; Yarranton *et al.*, 2000*b*; Jestin *et al.*, 2007; Mullins, 2011; Rane *et al.*, 2012, 2013). Whether water-in-oil or oil-in-water emulsions are formed is determined by the ratio of hydrophobic to hydrophilic group areas of surfactant molecules, and predominance of hydrophobic groups will lead to WOE formation (Clint, 1992*f*). In WOE, water is present as a dispersed phase as asphaltene polar groups, e.g. carboxylic or nitrogen compounds (Sjoblom *et al.*, 2015), are orders of magnitude smaller than the hydrophobic aromatic/alkyl parts. Molecular dynamics of non-charged asphaltene model compounds illustrated that asphaltenes do not partition into the bulk water phase but are present in the bulk oil and interface boundary (Teklebrhan *et al.*, 2014).

Similarly to surfactants, crucial to asphaltene surface activity are the charged/polar functionalities. Molecular dynamic simulations of asphaltenes illustrated that model compounds with highest surface activity (with charged functional groups) were located at the toluene/water interface after 7 ns of simulation (mostly in cluster form), whereas non-charged moieties mostly remained in bulk toluene (Kuznicki *et al.*, 2008, 2009). The latter study developed compounds that were structurally similar to the atomic force microscopy (AFM) images from Schuler *et al.* (2015, 2017), thus the results are representative. Simulations of non-charged asphaltene model compounds illustrated that such asphaltenes were a lot more likely to remain in bulk oil rather than travel to the water/oil boundary (Teklebrhan *et al.*, 2014). Model emulsion studies fractionating asphaltenes into interfacial and bulk material found that the interfacial fraction corresponds to about 2% wt (Yang *et al.*, 2014) and that its removal decreases emulsion stability (Yang *et al.*, 2014; Jarvis *et al.*, 2015). Nanoaggregation (self-association) of asphaltenes occurs upon reaching the CNAC, whereby crucial to asphaltene solubilisation are steric repulsion of the alkane substituents and $\pi - \pi$ stacking of the aromatic cores (Buenrostro-Gonzalez *et al.*, 2001; Zhang *et al.*, 2003; Andreatta *et al.*, 2005*a*). Steric hindrance restricts the number of asphaltenes in a nanoaggregate and a further addition of asphaltenes to the system will lead to a change in aggregate number, as opposed to size (Andreatta *et al.*, 2005*a*; Friberg, 2007). In other words, nanoaggregation kinetics are controlled by as-

phaltene (poor) solubility (Buckley *et al.*, 2007) and strong asphaltene-asphaltene interactions (Friberg, 2007); in an aqueous environment micellarisation is controlled by solvent-surfactant interactions. Nanoaggregation is analogous to surfactant micellarisation, whereby self-association of surfactants is controlled by physical forces (Clint, 1992*f*). Following Hartely's model (Hartley, 1936), in a spherical micelle the surfactant alkyl chains form a hydrocarbon core and the polar groups form a charged surface. This is somewhat contradicting to the nanoaggregate structure, whereby the asphaltene molecules are stacked (Mullins, 2011). The implications of this, including the charge density of a micellar surface versus the nanoaggregate may be a subject of further investigation.

The surface activity of asphaltenes has been reported to occur from polar heteroatomic groups (Yang *et al.*, 2014, 2015*a*) and asphaltenes recovered from emulsion phase interfaces were found to have a high heteroatom content (Zhang *et al.*, 2003; Czarnecki, 2009; Tchoukov *et al.*, 2014; Jarvis *et al.*, 2015). Compounds that were found to contribute to increased emulsion stability included those with N and O groups (Varadaraj & Brons, 2007) sulfoxides (Czarnecki, 2009; Qiao *et al.*, 2017*a,b*) and vanadyl porphyrins (McKenna *et al.*, 2009). Interfacial tension (IFT) is one of the most widespread measurements in analysing surfactant emulsion-stabilisation properties (Friberg, 2007). Obtaining a plot of surface tension versus the logarithm of surfactant concentration will illustrate a decreasing trend and the critical micelle concentration (CMC). Noteworthy, interfacial tension measurements require that the activity coefficient a_s in the Gibbs adsorption equation (estimating interfacial tension) is constant, which is true for many aqueous systems (Friberg, 2007).

The issues regarding the use of IFT measurements for asphaltene systems are as follows. Firstly, asphaltene activity coefficient is reported to have contradictory properties, whereby some studies report an approximation of unity (Yarranton & Masliyah, 1996), and other suggest that it is not constant (Friberg, 2007). The surface tension of toluene is two and a half times lower than that of water, and loading high-energy asphaltenes onto the toluene surface may increase surface tension (Mostowfi *et al.*, 2009). As only a subfraction of the asphaltene (fraction) is surface-active (acts as an emulsifier) (Stanford *et al.*, 2007*a*; Kilpatrick, 2012; Rocha *et al.*, 2016), the surface tension measurements should be performed with a great caution, otherwise the results will be misleading.

Whether asphaltene monomers or nanoaggregates stabilise the water-in-oil emulsions is still a subject of debate. Alvarez *et al.* (2009) reported that larger nanoag-

gregates were more likely to adsorb at the water/oil interface. The nanoaggregates are asphaltenes with a higher apparent molecular weight and that the latter is positively related to the degree of self-association (Mullins *et al.*, 2007; Yarranton *et al.*, 2013; McKenna *et al.*, 2013). The increase in the nanoaggregate size improves the asphaltene film thickness and surface coverage at the W/O interface (Yarranton *et al.*, 2000b; Jestin *et al.*, 2007). In an asphaltene model oil emulsion study (Rocha *et al.*, 2016), interfacial material of $> 7000 \text{ g mol}^{-1}$ (mass surface coverage of 5 mg m^{-2}) created stable emulsions, this size is assumed to correspond to the nanoaggregates. On the other hand, in Langmuir-Blodgett (Friberg *et al.*, 2007) and pendant droplet (Rane *et al.*, 2012, 2013) experiments, monomeric asphaltenes were shown to decrease surface tension more than the nanoaggregates. Studies by Rane *et al.* (2012, 2013) illustrated that in water-model oil systems with 10-50 ppm (i.e. monomeric asphaltenes) asphaltene fraction, dynamic interfacial tension decreased with no reported asymptotic value, whereas emulsions with 50-200 ppm asphaltenes illustrated an asymptotic limit at 20 mN m^{-1} . Interestingly, the 50-200 ppm asphaltene concentration range is consistent with estimations of the critical nanoaggregation region in Svalova *et al.* (2017), and their nuclear magnetic resonance (NMR) data illustrates a linear dependence of asphaltene concentration on NMR signal breaking around a similar 80-200 ppm range. Furthermore, Rane *et al.* (2012, 2013, 2015) used the Langmuir equation of state to suggest that it is asphaltene monomers that stabilise water-in-model oil emulsions rather than nanoaggregates although their NMR analysis suggested that nearly half of molecules present in model oil were nanoaggregates (Rane *et al.*, 2012).

The complexity of using IFT for understanding asphaltene impact on water/oil emulsions is illustrated in the following studies on asphaltene IFT. The addition of asphaltenes to toluene will has been shown to reduce the interfacial tension between toluene and water (Sheu *et al.*, 1992, 1995b; Xu, 1995; Jeribi *et al.*, 2002; Acevedo *et al.*, 2005; Horváth-Szabó *et al.*, 2005; Poteau *et al.*, 2005). In model emulsion experiments, Fossen *et al.* (2007) reported that the interfacial tension (IFT) at toluene/water boundary was 38 mN m^{-1} . The presence of asphaltenes reduced the IFT to up to 15 mN m^{-1} for the 18:1 *n*-pentane:oil precipitated asphaltenes, as compared to up to $23\text{-}28 \text{ mN m}^{-1}$ for the 40:1 *n*-pentane:oil precipitated asphaltenes. To explain the IFT decay behaviour, a bi-exponential model (weighted sum of two exponents) was proposed with a very good fit ($R^2 \geq 0.98$) (Fossen *et al.*, 2007). They proposed that the 18:1 *n*-pentane:oil precipitated asphaltenes

are more soluble. The presence of the NSO functionality will increase the preference of asphaltenes to water which will lower the oil/water IFT (Fossen *et al.*, 2007). Contradicting this, other surface tension experiments showed that nanoaggregation caused an increase in surface tension as high-energy molecules were aggregating on the surface of low-energy toluene (Friberg *et al.*, 2005; Sjoblom *et al.*, 2015).

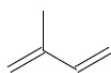
The above comparison illustrated similarities and differences between asphaltene nanoaggregates and surfactant micelles. In many respects, asphaltenes do behave similarly to surfactants, however considering their structural polydispersity some phenomena are less comparable than others. In particular, the non-uniformity of the interfacial activity properties of the asphaltene fraction lead to contradictory conclusions about the asphaltene aggregation state at the water/oil interface. As it is widely accepted that the nanoaggregates stabilise water/oil emulsions, this study will still focus on studying nanoaggregation. Considering the issues associated with the asphaltene IFT measurement, the investigation of asphaltene aggregation state at water droplet interface should be a subject of further studies.

Chapter 4. Petroleum Biomarkers

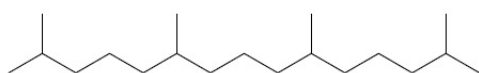
4.1 Introduction

Biological markers (biomarkers) are compounds that provide an unambiguous link between a chemical compound and its biological precursor (Eglinton & Calvin, 1967; Peters *et al.*, 2005f). These preserve the chemical signature of the hydrocarbon source rock, allowing oil-source and oil-oil correlation as well as thermal maturity and biodegradation estimation. Biomarkers comprise a variety of chemical compounds, including branched and cyclic/aromatic compounds. Isoprene (Figure 4.1(a)) is the basic constituent of most non-aromatic biomarkers (Peters *et al.*, 2005e), such biomarkers would then be called terpenoids, isoprenoids or isopentenoids (Nes & McKean, 1977). Isoprene biomarkers are divided into groups (e.g. hopanes and steranes) according to linearity/number of aliphatic rings in a molecule (Peters *et al.*, 2005e), Figure 4.1 illustrates examples of linear and cyclic biomarkers. Aromatic hydrocarbons follow the formula C_nH_{2n-6y} , where y is the number of aromatic rings (Peters *et al.*, 2005e). Polynuclear aromatic hydrocarbons (PAHs) are multi-ring aromatic compounds, including naphthalene, phenanthrene and coronene, Figure 4.2. Common alkylated aromatics include toluene, phenyldodecane and diphenylpropane. The non-hydrocarbon compounds in petroleum include heteroatoms, e.g. the NSO compounds. Sulfur groups are common and include thiols, sulfides and thiophenes/benzothiophenes. Nitrogen compounds occur as neutral (e.g. benzocarbazoles) or basic (e.g. pyridine, indoline) species. Oxygen moieties are present forming neutral (e.g. furan, fluorenone) and acidic groups (e.g. phenol, carboxylic acid groups). Acids can occur due to both, depositional and biological processes (Peters *et al.*, 2005e).

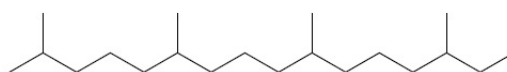
(a) Isoprene (C_5)



(b) Diterpanes

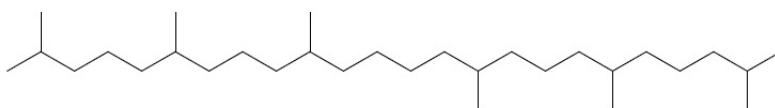


(i) 2,6,10,14-Tetramethylpentadecane (Pristane; C_{19})

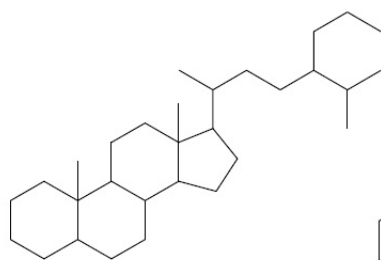


(ii) 2,6,10,14-Tetramethylheptadecane (Phytane; C_{20})

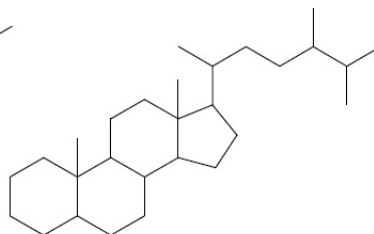
(c) Triterpanes



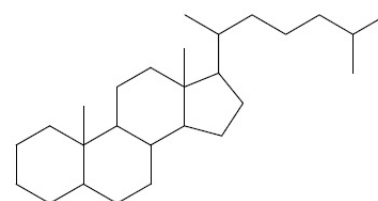
(i) Squalane (linear)



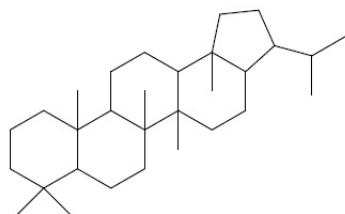
(ii) 24-*n*-Propylcholestane (C_{30})



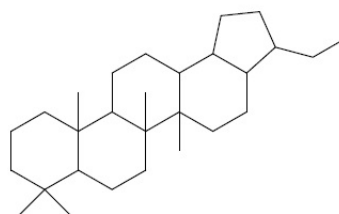
(iii) 24-Methylcholestane (Ergostane; C_{28})



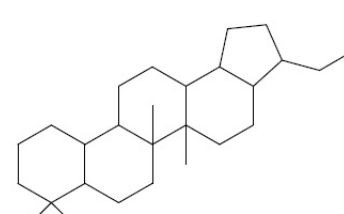
(iv) Cholestane (C_{27})



(v) Hopane (C_{30})



(vi) 28,30-Bisnorhopane (C_{28})



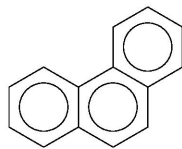
(vii) 25,28,30-Trisnorhopane (C_{27})

Figure 4.1: Examples of biomarkers in the aliphatic fraction of petroleum. Adapted from Peters *et al.* (2005e).

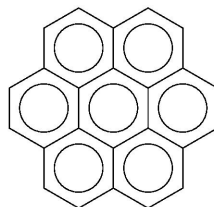
(a) Mono/polynuclear aromatic hydrocarbons



(i) Benzene

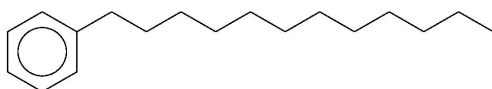


(ii) Phenanthrene

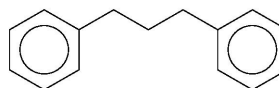


(iii) Coronene

(b) Alkylated aromatic hydrocarbons

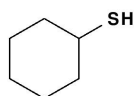


(i) Phenyldecane



(ii) Diphenylpropane

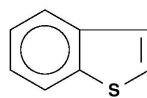
(c) Sulfur-containing compounds



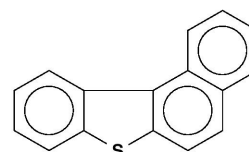
(i) Cyclohexanethiol



(ii) Thiophene

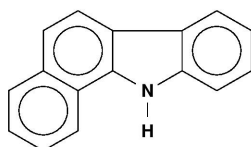


(iii) Benzothiophene

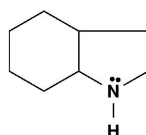


(iv) Naphthobenzothiophene

(d) Nitrogen-containing compounds



(i) Benzo(a)carbazole



(ii) Indoline



(iii) Pyridine

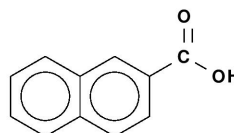
(e) Oxygen-containing compounds



(i) Furan



(ii) Phenol



(iii) Naphthalene-2-carboxylic acid

Figure 4.2: Examples of PAHs and heteroatomic compounds in petroleum. Adapted from Peters *et al.* (2005e).

4.2 Stereochemistry of Biomarkers

Stereochemistry is the study of molecular shapes and symmetries (Clayden *et al.*, 2001; Peters *et al.*, 2005e). Molecular structures that are not identical but mirror images of each other are enantiomers. Chiral molecular structures are enantiomers (mirror images) that cannot be superimposed. Thus, achiral isomers are superimposable. If a molecule contains a carbon atom with four different groups, it will be chiral (not have a plane of symmetry). The asymmetric carbon is called a stereogenic or chiral centre. Molecules that have more than one chiral centre and at least one but not all of those are the same, the resulting stereoisomers are called diastereomers. A racemic mixture is a mixture of equal quantities of a pair of enantiomers. According to Clayden *et al.* (2001), if the starting compounds of a chemical reaction are achiral, and the products are chiral, the latter will be racemic. In nature, however, many chiral molecules are present as single enantiomers. Configuration refers to the arrangement of bonds around the chiral carbon, and is labeled *S* or *R* depending on the order of the attached groups. The configuration assignment procedure in (Cahn *et al.*, 1966; Clayden *et al.*, 2001), which is the Cahn-Ingold-Prelog convention is summarised as follows. Given a chiral centre, the four attached groups (C is tetravalent) should be ranked (1-4) according to decreasing atomic numbers, e.g. 1- highest, 4-lowest. The molecule should then be arranged with rank 4 (lowest atomic number) pointing away. If the groups 1-3 are in a clockwise order, the chiral centre has an *R* configuration, and *S* otherwise. Epimers are stereoisomers that differ at only one centre, diastereomers are those differing at more than one but not all centres and enantiomers are two stereoisomers that differ in all stereogenic centres. For polycyclic terpanes, chiral centres are located outside the molecule's ring carbons (Peters *et al.*, 2005e). Groups (or atoms) that face below or above a molecule's plane (at ring carbons) are indicated α and β respectively (Peters *et al.*, 2005e).

Stereochemistry of sterane and hopane biomarkers is used in petroleum maturity (and often biodegradation) assessment. No asymmetric *n*-alkanes are possible, but asymmetric acyclic isoprenoids include pristane, whereby the stereochemistry is characteristic to thermal maturity. Methyl groups at positions C-6 and C-10 are in the *6R*, *10S* configuration and have been reported to change to a mixture of *6R*,*10S*, *6S*,*10S* and *6R*,*10R* in the ratio 2:1:1 as a result of thermal maturation (Patience *et al.*, 1980). Separation of the *S* and *R* isomers often requires a chiral sta-

tionary phase during chromatographic separation, although e.g. C₃₁₋₃₅ homohopane 22 *S* and *R* isomers are well-separated using achiral stationary phases.

4.2.1 Hopanes and steranes in petroleum

The hopanes include three stereoisomeric series, including 17 α ,21 β –, 17 β ,21 β – and 17 β ,21 α (*H*)– (Peters *et al.*, 2005*e*). The ($\alpha\beta$) configuration in C₂₇₋₃₅ hopane compounds is characteristic of petroleum due to the strong thermodynamic stability, compared to the ($\beta\beta$) and ($\beta\alpha$) less stable configurations (Peters *et al.*, 2005*e*), or ($\alpha\alpha$) that is not found in the natural products (Bauer *et al.*, 1983). Hopanes with ≤ 30 carbon atoms have asymmetric centres at C-21 and all ring junctures (Peters *et al.*, 2005*e*). *Homo*-hopanes are a class of hopanes with more than 30 carbons and an additional methylene group attached to C₃₀ hopane.

The precursor for the sterane biomarkers are sterols having a very large number of possible stereoisomers although very few are found in living organisms (Peters *et al.*, 2005*e*). In particular, in living organisms, sterols are in the 8 β ,9 α ,10 β (CH₃),13 β (CH₃),14 α ,17 α (H)20*R* configuration. The configurations at positions C-8,-9,-10 and -13 remain stable (and/or are highly energetically favourable) throughout petroleum maturation. Isomers exist at the C-5 and C-24 positions as mixtures of (α , β) configurations, and organic sterols show only the 20*R* configuration (Nes & McKean, 1977). In the resulting steranes, the configuration at the C-24 positions is a mixture of *R* and *S* in source rocks. The stereochemistry at C-5 is a mixture of 5 α and 5 β , although the former is more likely. The configurations at positions C-14 and C-17 are transposed from (α , α) to (β , β) due to a higher thermodynamic stability (Peters *et al.*, 2005*e*).

4.3 Biodegradation of Biomarkers

Biodegradation of petroleum occurs due to its alteration by organisms (bacteria) primarily by means of oxidation (Connan, 1984; Blanc & Connan, 1994; Milner *et al.*, 1977*a*; Peters *et al.*, 2005*a*). Biodegradation is a ‘quasi-sequential’ process (Peters & Moldowan, 1993), whereby organisms preferentially remove and/or alter (e.g. deform or oxidise) compounds in the order of increasing molecular weight, complexity (e.g. branching) and aromaticity, producing CO₂. Biodegradation alters petroleum physico-chemical properties, decreasing the API gravity and increasing the inorganic gas content, viscosity, NSO compounds and trace metals (Peters *et al.*, 2005*a*). Microbial biodegradation in reservoirs is a metabolic process requiring favourable

conditions, such as the presence of electron acceptors, inorganic nutrients, water, temperatures of ca. 80 °C, water salinity of ca. 100-150 ppt (Wenger & Isaksen, 2002) and a low H₂S content. The bioavailability of hydrocarbons is facilitated through an enzyme addition that makes them water-soluble, or direct consumption at the oil/water interface.

Microbial degradation includes aerobic and anaerobic pathways, described below. Both organism types require trace amounts of inorganic nutrients to survive, including N and P as well as metals e.g. Mo, Co and Cu. Temperatures, greater than 80 °C are thought to ‘sterilise’ a reservoir and prevent biodegradation, and corresponds to ca. 2000 m burial depth under normal geothermal gradients (Connan, 1984; Palmer, 1993; Blanc & Connan, 1994). Thermophilic bacteria, however, thrive at much greater temperatures and burial depths (Blöchl *et al.*, 1997). Given a low geothermal gradient, the geopressure does not appear to be a biodegradation-limiting factor. Bacteria have been reported to remain active in depths of 4000 m (Walters, 1999) under pressures of up to 1680 MPa and afterwards in atmospheric conditions (Sharma *et al.*, 2002*b*). Generally, a H₂S content of > 5% is unsuitable for living organisms, although extreme cases have been reported where microbes thrived in pH 0 (Edwards *et al.*, 2000). The rates of biodegradation are typically higher for aerobic bacteria, confirmed by empirical (Jobson *et al.*, 1972; Larter *et al.*, 2000) and laboratory studies (Yamane *et al.*, 1997). Air oxidation is an alternative pathway for aerobic degradation, especially polar compounds, such as steroid ketones, benzothophenic acids and sulfones (Charrié-Duhaut *et al.*, 2000).

4.3.1 *Aerobic bioegradation*

In aerobic degradation, oxygen activates hydrocarbons making them bioavailable for the microorganisms and also acts as the terminal electron acceptor. Carbon dioxide and H₂O are produced as by-products, whereas H₂S needs to be absent. Oxygenases are enzymes which catalyse reactions where dioxygen is incorporated directly into organic compounds (Harayama *et al.*, 1992). Monooxygenases incorporate one OH group into substrates, whereby two atoms of dioxygen are reduced to one OH group and an H₂O. Oxygenases initiate the degradation of alkanes and aromatics (Harayama & Timmis, 1989). As aerobic biodegradation requires molecular oxygen, active surface recharge waters are necessary for biodegradation (Peters *et al.*, 2005*a*). Furthermore, water washing induces biodegradation with selective removal of light aromatics (Bailey *et al.*, 1973; Palmer, 1984, 1993).

4.3.2 Anaerobic biodegradation

Anaerobic biodegradation is assumed to be the dominant mechanism of hydrocarbon bio-alteration in reservoirs (Jones *et al.*, 2008). This is supported by the chemical/biological composition of formation waters, including the depletion of oxygen to reduce the likelihood of petroleum oxidation (Horstad *et al.*, 1992) and the presence of anaerobic microorganisms (Bastin, 1926; Magot *et al.*, 1994), as well as anaerobic biodegradation metabolites in reservoir-degraded petroleum (Aitken *et al.*, 2004; Jones *et al.*, 2008). Anaerobic bacteria utilise electron acceptors, such as nitrate, sulphate and ferric iron, instead of oxygen (Widdel & Rabus, 2001) and can tolerate up to ca. 5% of H₂S. Pathways for anaerobic biodegradation include fumarate addition (Widdel & Rabus, 2001) and activation of the terminal carbon by a C₁ compound. Examples of degradation through fumarate addition include alkylnaphthalene (Annweiler *et al.*, 2000) and *n*-alkanes (Kropp *et al.*, 2000). The C₁ moiety addition to the terminal carbon is an alternative way for alkane activation (Aeckersberg *et al.*, 1998). The mechanisms for the benzene and PAH degradation remain unknown (Peters *et al.*, 2005a), although Coates *et al.* (1996) have reported biodegradation of PAHs by unidentified sulfate-reducing organisms. Head *et al.* (2003) and Jones *et al.* (2008) suggested that methanogenic biodegradation is the main mechanism of anaerobic hydrocarbon biodegradation in-reservoir. Jones *et al.* (2008) performed microcosm experiments under methanogenic conditions, monitoring petroleum alteration and gas generation to propose that the observed alteration of compound classes mimics that of in-reservoir. They suggested that $\delta^{13}\text{C}_{\text{CO}_2}$ related to oil biodegradation in marine petroleum systems can be very isotopically heavy, ranging from -25 to +20, which would suggest closed-system reduction of CO₂ to CH₄ (Boreham *et al.*, 2001; Pallaser, 2000; Masterson *et al.*, 2000). Biodegradation is a quasi-sequential process, whereby hydrocarbon compound classes are removed in a step-wise manner (Wenger *et al.*, 2002; Peters *et al.*, 2005a). In-reservoir biodegraded oil typically has alkylated naphthalenes and 2-/3-ring aromatic compounds removed only after the biodegradation of *n*-alkanes and acyclic isoprenoids (e.g. pristane/phytane) (Volkman *et al.*, 1984; Williams *et al.*, 1986; Wenger *et al.*, 2002). This is not, however, characteristic of aerobic biodegradation, as laboratory studies show evidence of the removal of light aromatic compounds during early stages of biodegradation (i.e. before *n*-alkane removal). Jones *et al.* (2008) performed biodegradation experiments using an oil from a North Sea field comparing it

with a common-source rock oil from Gullfaks field that has been (naturally) biodegraded anaerobically in-reservoir. Their results illustrate that the biodegradation of oil performed under methanogenic conditions (as opposed to sulphate-reducing) most closely resembles the Gullfaks samples.

4.4 Compositional Alteration

During biodegradation, the composition of petroleum is altered whereby the lighter, less complex and polar compounds are preferentially removed by living organisms (Peters *et al.*, 2005a). The latter leads to an enrichment in the heavy and polar NSO fraction and trace metals and a decrease in the API gravity, thus subsequently in commercial value of a petroleum. The initial fraction to be removed is the C₆₋₁₂ *n*-alkanes, followed by branched alkanes. Light aromatic compounds are first to be degraded from the aromatic fraction by either microbial alteration or water-washing (Palmer, 1983), the latter presumably accommodated by polar interactions. Chromatography is typically used in analysing petroleum biodegradation. The Wenger *et al.* (2002) biodegradation scale describes the sequence of biodegradation and is illustrated in Figure 4.3, based on empirical field observations (Peters *et al.*, 2005a). The biodegradation order is quasi-sequential (Peters & Moldowan, 1993), i.e. it does not occur in the strict stepwise pattern but reflects differences in the rates of catabolism under a variety of conditions (Peters *et al.*, 2005a). The Wenger *et al.* (2002) biodegradation rank is qualitative, whereas quantitative assessment of biodegradation measures the amount of hydrocarbons destroyed given the assumption about the structure of unaltered material. The latter can be inferred from sample thermal maturity, source type, migration and reservoir conditions (Peters *et al.*, 2005a). Given the removal of biomarkers (severe biodegradation), asphaltene-trapped biomarkers may be used (Cassani & Eglinton, 1986; Philp *et al.*, 1988; Dembicki & Mathiesen, 1994; Rooney *et al.*, 1998; Odden *et al.*, 2002).

Common degradation patterns include the strong preference of isoprenoids to steranes (Peters *et al.*, 2005a), the preference of hopanes to steranes is variable. The *n*-alkanes C₈₋₁₂ are removed at the initial biodegradation stages (Peters *et al.*, 2005a), followed by the longer *n*-alkanes. The net effect of biodegradation is a decrease in wet gas components, increase in unaltered CH₄ and biogenic CO₂ from microbial oxidation. Branched alkanes have a higher resistance to biodegradation, especially at higher degrees of branching, e.g. acyclic isoprenoids (Pirnik *et al.*, 1974). Com-

Wenger <i>et al.</i> (2002) Biomarker Biodegradation Scale	Severe										
	0	1	2	3	4	5	6	7	8	9	10
Normal alkanes		█	█	█	█						
Alkylcyclohexanes			█	█	█	█					
Isoprenoids			█	█	█	█					
C ₁₄₋₁₆ bicyclic terpanes				█	█	█	█	?			
Hopanes (25-norhopanes formed)							█	█	█		
Steranes							█	█	█		
25-norhopanes or hopanes*									█	█	
Diasteranes									█	█	█
C ₂₆₋₂₉ aromatic steroids										█	█
Porphyrins											█
Methyl- and dimethylnaphthalenes		█	█	█	█	█					
Trimethylnaphthalenes				█	█	█					
Methylphenanthrenes					█	█					
Tetramethylnaphthalenes						█	█	█	█		
Dimethylnaphthalenes							█	█	█		
Methylbiphenyls							█	█	█		
Ethylphenanthrenes								█	█		
Ethyl- and trimethylbiphenyls									█	█	?

Figure 4.3: Wenger *et al.* (2002) biodegradation scale, adapted from Peters *et al.* (2005a). Sequence of alteration of alkylated PAH based on Fisher *et al.* (1996b, 1998). Bars indicate where compound classes are initially altered (pale gray), substantially depleted (solid gray), and completely removed (black). *Hopanes degraded without the formation of 25-*nor*-hopanes.

monly, isoprenoid/*n*-alkane ratios are used to estimate biodegradation levels, e.g. pristane/*n*-C₁₇ and phytane/*n*-C₁₈ (Miget *et al.*, 1969; Winters & Williams, 1969; Peters *et al.*, 2005a). Isoprenoid/sterane or isoprenoid/hopane ratios can be used to differentiate heavily from severely biodegraded oils, assuming a single charge (Peters *et al.*, 2005a). Highly-branched alkanes and isoprenoids are constituents of the unresolved complex mixture and persist at high biodegradation levels (Gough & Rowland, 1990; Killops & Al-Juboori, 1990). Bicyclic terpane compounds C₁₄₋₁₆ are more resistant to biodegradation than isoprenoids but are removed entirely before the onset of sterane and hopane biodegradation (Hoffmann & Strausz, 1986; Williams *et al.*, 1986) and can be also removed by water washing (Kuo, 1994). Due to their solubility in water, alkylphenols can be removed from petroleum by either microbial removal or water washing (Taylor *et al.*, 2001). Alkylbenzenes tend to be present after the total removal of isoprenoids (Peters *et al.*, 2005a) and PAH compounds increase in their resistance to biodegradation with an increase in the number of rings (Peters *et al.*, 2005a) and the number alkyl substituents (Volkman

et al., 1984; Williams *et al.*, 1986).

Sterane microbial alteration follows a sequence $\alpha\alpha\alpha 20R \gg \alpha\beta\beta 20R \geq \alpha\beta\beta 20S \geq \alpha\alpha\alpha 20S \gg$ diasteranes and $C_{27} > C_{28} > C_{29} > C_{30}$ (Seifert & Moldowan, 1979; McKirdy *et al.*, 1983; Seifert *et al.*, 1984; Chosson *et al.*, 1991), and the C_{20-21} steranes are reported to have a susceptibility similar to that of the diasteranes (Peters *et al.*, 2005a). Whilst the C_{27-30} $\alpha\alpha\alpha 20R$ steranes are generally most susceptible to degradation (Seifert *et al.*, 1984; Chosson *et al.*, 1991; Wang *et al.*, 2001) the relative susceptibility of the $\alpha\beta\beta 20R$, $\alpha\beta\beta 20S$ and $\alpha\alpha\alpha 20R$ compounds is more variable, perhaps depending on the microbial organism population (Peters *et al.*, 2005a). The enrichment of the 25-*nor*-hopanes with the selective removal of steranes is variable (Volkman *et al.*, 1983; Seifert *et al.*, 1984; Chosson *et al.*, 1992). The susceptibility of sterane isomers to biodegradation tends to decrease with increasing carbon number (Seifert *et al.*, 1984; Zhang *et al.*, 1988; Chosson *et al.*, 1991; Wang *et al.*, 2001; Peters *et al.*, 2005a).

Hopanes and 25-*nor*-hopanes (demethylated hopanes) are generally more resistant than steranes, although this depends on the microbial population and environmental conditions (Peters *et al.*, 2005a). Demethylated hopanes can be formed by the loss of a methyl group at the C-10 position in hopanes, as revealed by nuclear magnetic resonance (NMR) spectroscopy (Rullkötter & Wendisch, 1982). Demethylated hopanes are useful in biodegradation assessment as they tend to occur in oils when hopanes have been degraded but are absent whereby steranes are preferentially removed to hopanes (Rullkötter & Wendisch, 1982; Peters & Moldowan, 1991; Peters *et al.*, 2005a). In particular, the high abundance of 25-*nor*-hopanes is characteristic of severe biodegradation (Rullkötter & Wendisch, 1982; Volkman *et al.*, 1984; Trendel *et al.*, 1990). Also, in oils where the steranes have been biodegraded before the normal hopane removal, the 25-*nor*-hopanes were found to be absent too (Seifert *et al.*, 1984). In other studies, hopanes were found to be biodegraded without the 25-*nor*-hopane removal (Seifert & Moldowan, 1979; Goodwin *et al.*, 1983; Connan, 1984). The 25-*nor*-hopane distribution is analogous to that of the unaltered hopanes, shifted by one carbon number (Peters *et al.*, 2005a). Caution should be used with using the 25-*nor*-hopanes for biodegradation assessment as their dominant m/z 177 ion can also be produced by the regular hopanes (Peters *et al.*, 2005a). Vice versa, the 25-*nor*-hopanes have been reported to yield an m/z 191 ion that is characteristic of hopanes (Dzou *et al.*, 1999). No microorganisms have been reported to biosynthesize the 25-*nor*-hopanes or their possible biological precursors (Goodwin

et al., 1983; Chosson *et al.*, 1992; Bost *et al.*, 2001; Peters *et al.*, 2005a). Despite these limitations, the 25-*nor*-hopanes are used to assess biodegradation, for example McCaffrey *et al.* (1996) reporting that in a set of biodegraded oils (ranks 6-9) the quantity of individual hopanes were inversely proportional to their 25-*nor*-hopane equivalents, hopanes decreasing with increasing biodegradation rank.

4.5 Biomarkers in Asphaltenes

Asphaltenes have been reported to preserve biomarkers removed from petroleum by depositional processes and biodegradation (Rubinstein *et al.*, 1979), as this is the petroleum fraction least susceptible to biodegradation (Arefyev *et al.*, 1980). Studies used hydrolysis (Bowden *et al.*, 2006) to investigate the distributions of bound tricyclic terpanes, hopanes and steranes in asphaltenes from an early Jurassic deposit, comparing them with the biomarkers from the kerogen resin and free fractions. They found that the asphaltene and resin fraction had significant differences in the proportion of tricyclic to pentacyclic (hopane) terpanes, whereby the resin and asphaltene fractions showed more prominent peaks of tricyclics and C₃₂ hopanes. However, they also discovered that the marine environment indicator (C₃₀ $\alpha\alpha\alpha$ regular sterane) was present in all fractions allowing source identification (Bowden *et al.*, 2006). Trapped/occluded *n*-alk-1-enes and terpenes were reported by (Yang *et al.*, 2009), where the asphaltenes had occluded terpene biomarkers as well as *n*-alkanoic acid ethyl esters. In the latter fraction, Yang *et al.* (2009) observed a general even-odd predominance. Often, the biomarkers preserved in asphaltenes are of lower maturity than those in the maltene fraction as asphaltenes form and trap biomarkers at an early stage petroleum expulsion (Cassani & Eglinton, 1986). Biomarkers can be preserved in asphaltenes as both occluded and covalently bound species (Snowdon *et al.*, 2016). Techniques to recover the biomarkers include pyrolysis (Behar & Pelet, 1984; Cassani & Eglinton, 1986; Jones *et al.*, 1987), chemical reduction by metals (Ekweozor, 1985), hydrolysis (Snape *et al.*, 1989; Russell *et al.*, 2004) and ruthenium ion catalysed oxidation (Strausz *et al.*, 1999b,c; Ma *et al.*, 2008; Svalova *et al.*, 2017). The latter techniques enable to release biomarkers trapped as asphaltene moieties. Asphaltene-occluded biomarkers, on the other hand, may be trapped within an asphaltene aggregate (Murgich *et al.*, 1999; Snowdon *et al.*, 2016). Therefore, the size and stability through geological time of the asphaltenes and their aggregates will impact what information they can preserve

from alteration (Snowdon *et al.*, 2016). The time of asphaltene formation and their aggregation properties in different media will determine the information they will be able to preserve as well. Gray *et al.* (2011), Zhao *et al.* (2012) and Snowdon *et al.* (2016) suggested that an asphaltene monomer of an average mass of 750 Da would not likely occlude biomarkers of mass ca. 400 Da, thus it is the asphaltene nanoaggregates that are the source of occlusions.

Chapter 5. Petroleum Maturity and Source Assessment Using Compound Ratios

5.1 Maturity Assessment Using Non-Biomarker ratios

5.1.1 *Saturated hydrocarbon fraction*

Some of the most common non-biomarker maturity ratios are

$$\frac{\text{Pristane}}{n\text{-C}_{17}} \quad \text{and} \quad \frac{\text{Phytane}}{n\text{-C}_{18}},$$

whereby the two decrease with thermal maturity as the yield of n -alkanes from kerogen is increased by thermal cracking (Tissot *et al.*, 1971). Caution has to be used when using the above ratios due to their susceptibility to alteration due to organic matter input (Alexander *et al.*, 1981) and secondary alteration processes e.g. biodegradation (Peters *et al.*, 2005*d*). Ratios based exclusively on the n -alkanes include the carbon preference index (CPI) (Bray & Evans, 1961) and odd-to-even predominance indexes (OEP₁ and OEP₂) (Scalan & Smith, 1970):

$$\text{CPI} = \frac{1}{2} \left(\frac{\sum_{i=25,27,\dots,33} C_i}{\sum_{i=24,26,\dots,32} C_i} + \frac{\sum_{i=25,27,\dots,33} C_i}{\sum_{i=26,28,\dots,34} C_i} \right),$$

$$\text{OEP}_1 = \frac{C_{21} + 6C_{23} + C_{25}}{4C_{22} + 4C_{24}} \quad \text{and} \quad \text{OEP}_2 = \frac{C_{25} + 6C_{27} + C_{29}}{4C_{26} + 4C_{28}}.$$

Low thermal maturity is indicated by CPI or OEP values significantly above (odd preference) or below (even preference) 1.0 (Peters *et al.*, 2005*d*). In practice, OEP are adjusted to include a desired range of carbon numbers and are used in conjunction with other biomarker parameters that are not organic-matter input dependent (Peters *et al.*, 2005*d*).

5.1.2 Aromatic hydrocarbon fraction

The methylphenanthrene index (MPI) (Radke & Welte, 1983)

$$\text{MPI} = \frac{1.5(2\text{-MP} + 3\text{-MP})}{\text{P} + 1\text{-MP} + 9\text{-MP}}$$

provides an analogous maturity assessment to vitrinite reflectance (Peters *et al.*, 2005*d*), e.g. for oil an MPI of 0.65-1.35 suggesting an oil window maturity and 1.35-2 indicating a higher one. An alternative MPI was proposed by Cassani *et al.* (1988)

$$\text{MPI}_1 = \frac{1.89(2\text{-MP} + 3\text{-MP})}{\text{P} + 1.26(1\text{-MP} + 9\text{-MP})}$$

However, MPI has been reported to show very similar values for oils of different maturity (Radke & Welte, 1983), depending on the type of organic matter and lithology (Cassani *et al.*, 1988) and petroleum migration (Radke *et al.*, 1982*b*) indicating that the ratios are not purely maturity-dependent. It is recommended that the index also is to be calibrated separately for each petroleum system (Peters *et al.*, 2005*d*). Both, dimethylnaphthalene index (DMNI) (Radke *et al.*, 1982*b*; Alexander *et al.*, 1983; Radke *et al.*, 1984) and trimethylnaphthalene index (TMNI) (Alexander *et al.*, 1985) are specific for high thermal maturity ranges

$$\text{DMNI} = \frac{2,6\text{-DMN} + 2,7\text{-DMN}}{1,5\text{-DMN}} \quad \text{and} \quad \text{TMNI} = \frac{2,3,6\text{-TMN}}{1,4,6\text{-TMN} + 1,3,5\text{-TMN}}$$

Alexander *et al.* (1985) reported that both, DMNI and TMNI increase with sample depth maturity, whereby the DMNI values of ca. > 2.5 would indicate maturity as the 1,5-DMN isomer might rearrange to 2,6- and 2,7,0 DMN (Radke *et al.*, 1982*a*). The generality of TMNI was assessed in Alexander *et al.* (1985) whereby it was correlated with the ratio (10.11) whereby a strong correlation was found. They reported that the TMNI values of ca. > 0.5 indicated thermal maturity.

5.2 Maturity Assessment Using Biomarker Ratios

5.2.1 Saturated hydrocarbon fraction

One of the first biomarker reactions to occur as a result of thermal maturation is isomerisation at C-22 in the regular hopanes (Peters *et al.*, 2005*c*). The C₃₁₋₃₅ 17 α ,21 β -*homo*-hopane C-22 isomerisation ratios (Ensminger *et al.*, 1978; Schoell

et al., 1983) can be used with any *homo*-hopane doublet (most frequently C₃₁ or C₃₂), e.g.

$$\frac{C_{31}17\alpha, 21\beta\text{-}30\text{-}homo\text{-}hopane\ 20S}{C_{31}17\alpha, 21\beta\text{-}30\text{-}homo\text{-}hopane\ 20S + C_{31}17\alpha, 21\beta\text{-}30\text{-}homo\text{-}hopane\ 20R} \quad \text{or} \\ \frac{C_{32}17\alpha, 21\beta\text{-}30,31\text{-}dihomo\text{-}hopane\ 20S}{C_{32}17\alpha, 21\beta\text{-}30,31\text{-}dihomo\text{-}hopane\ 20S + C_{32}17\alpha, 21\beta\text{-}30,31\text{-}dihomo\text{-}hopane\ 20R}.$$

Ratios within the 0.57-0.62 range indicate a mature oil, whereas values within 0.50-0.54 indicates an early stage of oil generation. Very low values of this indicator, e.g. below ca. 0.5 would suggest very low thermal stress (Seifert *et al.*, 1980; Peters *et al.*, 2005c). The drawbacks of using the above include lithology-dependent rates of 17 α , 21 β -*homo*-hopane isomerisation (Moldowan *et al.*, 1992). Peters & Moldowan (1991) showed that in laboratory burial maturation simulations *homo*-hopanes attached to the kerogen isomerise at a slower rate than free compounds in the bitumen.

The moretane/hopane ratio (Mackenzie *et al.*, 1980; Seifert *et al.*, 1980)

$$\frac{C_{29}17\beta, 21\alpha\text{-}hopane}{C_{29}17\alpha, 21\beta\text{-}hopane}$$

is used in maturity estimation as the 17 β , 21 α -moretanes are less stable than the 17 α , 21 β -hopanes. The minimum ratio of 17 α , 21 β -hopanes to 17 β , 21 α -moretanes is close to 20:1 (Peters *et al.*, 2005c), decreasing from ca. 0.8 in immature samples to less than 0.15 in mature rocks (Mackenzie *et al.*, 1980; Seifert *et al.*, 1980).

The ratio between Ts (C₂₇ 18 α , 21 β -22,29,30-*trinorneo*-hopane) and Tm (C₂₇ 17 α , 21 β -22,29,30-*trinor*-hopane), often expressed as Ts/Tm (Moldowan & Fago, 1986) and is useful for estimating thermal alteration from immature to postmature states

$$\frac{T_s}{T_s + T_m}.$$

During thermal maturation (catagenesis) Ts is more stable than Tm (Seifert & Moldowan, 1978), although its unknown whether the conversion of Tm to Ts also occurs (Peters *et al.*, 2005c). Values of 0.6-0.8 typically indicate thermal maturity (Moldowan *et al.*, 1986b). Although it is strongly influenced by the source of petroleum and should be used with caution for oils from different source, for common-source samples the Ts/Tm is reported to be one of the most reliable (Peters *et al.*, 2005c). Caution should be used when identifying the two compounds as

they commonly elute with other tricyclic/tetracyclic hopanes (Peters *et al.*, 2005c). Sterane isomerisation at C-20 in the C₂₉ 5 α , 14 α , 17 α compounds (Seifert & Moldowan, 1986) or % 20*S* steranes out of the C₂₉ 5 α , 14 α , 17 α doublet is used to infer maturity from immature to mature

$$\frac{C_{29} \text{ 5}\alpha, \text{ 14}\alpha, \text{ 17}\alpha \text{ 20}S}{C_{29} \text{ 5}\alpha, \text{ 14}\alpha, \text{ 17}\alpha \text{ 20}S + C_{29} \text{ 5}\alpha, \text{ 14}\alpha, \text{ 17}\alpha \text{ 20}R}$$

With increasing maturity, the isomerisation of the unaltered *R* configuration, e.g. the ratio value $\simeq 0$, increases to ca. 0.5 of the doublet mixture. The ratio equilibrium was reported to be 0.52-0.55 (Seifert & Moldowan, 1986). Another C₂₉ sterane ratio uses isomerisation at C-14 and C-17 to infer sample maturity, as the 5 α , 14 β , 17 β configuration is more stable through thermal stress than the 5 α , 14 α , 17 α configuration. The ratio is defined as

$$\frac{C_{29} \text{ 5}\alpha, \text{ 14}\beta, \text{ 17}\beta \text{ 20} S + R}{(C_{29} \text{ 5}\alpha, \text{ 14}\beta, \text{ 17}\beta \text{ 20} S + R) + (C_{29} \text{ 5}\alpha, \text{ 14}\alpha, \text{ 17}\alpha \text{ 20} S + R)}$$

whereby values of ca. 0.7 would suggest thermal maturity, with an equilibrium of 0.67-0.71 (Seifert & Moldowan, 1986).

5.2.2 *Aromatic hydrocarbon fraction*

In what follows, the abbreviation MAS refers to 17 β -methyl-18-*nor*-cholesta-8,11,13-triene (monoaromatic steroids) and TAS refers to 17 β -methyl-18,19-*dinor*-cholesta-1,3,5(10),6,8,11,13-heptane (triaromatic steroids) (Abbott *et al.*, 1985).

The mono- to triaromatic steroid ratio

$$\frac{C_{26+27+28} \text{ TAS}}{C_{26+27+28} \text{ TAS} + C_{27+28+29} \text{ MAS}}$$

is specific to samples ranging from immature to mature (Peters *et al.*, 2005c), although its value can be affected by expulsion which negatively affects the retention of the more polar triaromatic steroids (Hoffmann *et al.*, 1984b; Peters *et al.*, 1990). It is presumed that conversion of monoaromatic to triaromatic steroids occurs during maturation through the loss of a methyl group at the A/B ring junction in the MAS (Mackenzie *et al.*, 1981; Peters *et al.*, 2005c). Values above ca. 0.5 were reported to correspond to greater burial depths (Mackenzie *et al.*, 1981; Mackenzie,

1984). Finally, the short/short+long chain MAS and TAS ratios

$$\frac{C_{21+22} \text{ MAS}}{C_{21+22+27+28+29} \text{ MAS}} \quad \text{and} \quad \frac{C_{20+21} \text{ TAS}}{C_{20+21+26+27+28} \text{ TAS}}$$

provide inference about the mature-late mature range (Peters *et al.*, 2005a). Experimental evidence suggests that the ratio increases with maturity due to the preferential degradation of the long-chain compounds (Mackenzie *et al.*, 1981; Beach *et al.*, 1989).

5.3 Source Assessment Using Compound Ratios

What follows provides biomarker and non-biomarker relations from which the depositional environment of petroleum samples can be estimated. The ratio of dibenzothiophene to phenanthrene (DBT/P) can distinguish between a carbonate (DBT/P > 1) and a shale (DBT/P < 1) source (Hughes *et al.*, 1995). When used together with Pr/Ph, the DBT/P has a high specificity towards a source rock's depositional environment and lithology, this is known as a Hughes plot (Hughes *et al.*, 1995), Figure 5.1(a).

The $C_{31}R/C_{30}$ hopane ratio can be used to indicate a marine vs lacustrine source deposition (Peters *et al.*, 2005h). A value of > 0.25 indicates a marine shale, carbonate and marl source rocks. For better specificity, the ratio should be used together with C_{26}/C_{25} tricyclic terpanes, as shown in Figure 5.1(b), although areas of overlap are still prominent. Redox conditions can be inferred from the 30-*nor*-hopane/regular hopane ratio, whereby values > 1 would indicate an anoxic carbonate or marl source (Peters *et al.*, 2005h). The C_{27} - C_{28} - C_{29} sterane ternary diagram provides very good specificity towards distinguishing different source rocks (Peters *et al.*, 2000) or different organic facies of the same source rock (Grantham *et al.*, 1988). This sterane relation provides limited specificity to distinguish marine from non-marine depositional environments (Figure 5.1(c)), except plants with a strong input from higher-plant organic matter (Moldowan *et al.*, 1985), thus should be used in conjunction with other source indicators.

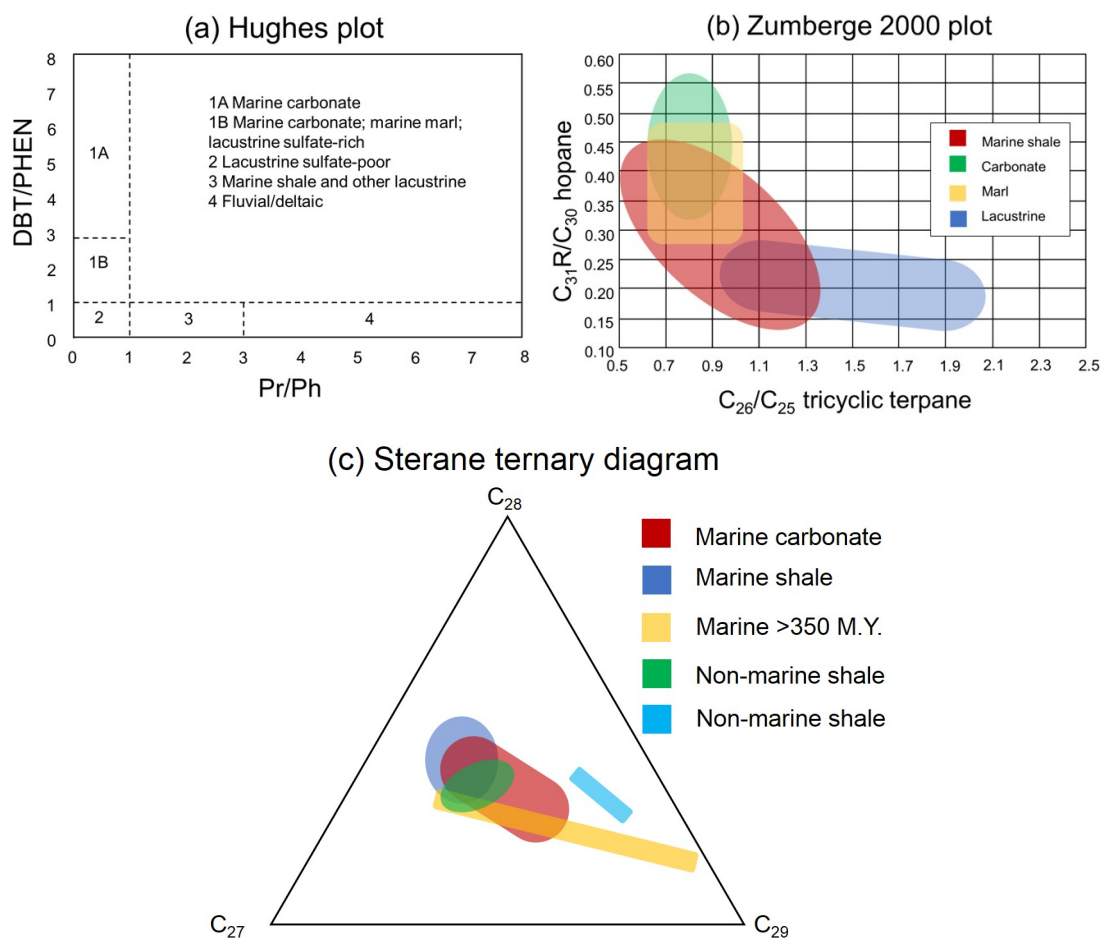


Figure 5.1: Relations used in sample source assessment. References for plots (a) and (b) are Hughes *et al.* (1995) and (Peters *et al.*, 2005*h*, Figure 13.77 (GeoMark Research Inc., Zumberge 2000, personal communication)) respectively. Plot (c) adapted from Moldowan *et al.* (1985).

Two versions of the gammacerane (Ga) index (GI),

$$GI_1 = \frac{Ga}{Ga + C_{30}17\alpha, 21\beta\text{-hopane}} \times 10 \quad \text{and}$$

$$GI_2 = \frac{Ga}{C_{31}17\alpha, 21\beta\text{-30-homo-hopane } 22R \text{ hopane}},$$

provide a high specificity for water-column stratification during source rock deposition, which may indicate hypersalinity at depth (Sinninghe Damsté *et al.*, 1995). The interpretation should be made with caution, however, as hypersalinity can also result from temperature gradients (Peters *et al.*, 2005*h*). When in low quantities, gammacerane can coelute with other peaks thus should be used carefully (the *m/z*

412 ion fragmentogram can be assessed as well).

The pristane/phytane ratio is extensively used in thermal maturity assessment (thus is affected by it) and provides some specificity towards redox conditions of the source rock (Peters *et al.*, 2005*h*). According to Didyk *et al.* (1978), Pr/Ph < 1 can be related to source rock anoxia, and oxic conditions otherwise. The ratio is used to differentiate between marine carbonate/marine shale/lacustrine source input also, as is illustrated in the Hughes plot above (Figure 5.1 (a)). However, for petroleum samples within the oil generation window, Ph/Ph can only be used at extreme values, as it is otherwise weakly correlated with redox conditions. The ratio values > 3 indicates an oxic terrigenous organic matter deposition and anoxic, hypersaline/carbonate deposition for Pr/Ph < 0.8 (Peters *et al.*, 2005*h*). For better specificity, Pr/(Pr+Ph) can be plotted against the C₂₇ Dia/(Dia+Regular) sterane ratio which has a strong positive correlation (Moldowan *et al.*, 1994b, 1986*a*). The C₃₀/(C₂₇-C₃₀) regular sterane index has a high specificity to marine organic matter input (Moldowan *et al.*, 1985; Peters *et al.*, 1986). The C₃₅ *pentahomo*-hopane index

$$\frac{C_{35} \text{ } 17\alpha, 21\beta\text{-}30,31,32,33,34\text{-pentahomo-hopane } 22S+R}{C_{31+32+\dots+35} \text{ } 17\alpha, 21\beta\text{-homo-hopanes } 22S+R}$$

indicates high anoxic conditions where the index value is above ca. 20% (Peters & Moldowan, 1991; Peters *et al.*, 1995). McKirdy *et al.* (1983) also used a C₃₄/C₃₅ 22*S* *homo*-hopane index to illustrate that carbonate source rocks have a ratio of > ca. 0.9, whereas Peters *et al.* (2005*h*) noted that lower values would indicate a shale source.

Chapter 6. Ultrasonic Characterisation of Molecular Aggregation

6.1 Introduction

Particle molecular aggregation and/or particle flocculation can be detected by a variety of methods, such as optical microscopy, confocal microscopy, near-infrared microscopy (Miller, 1996; Cosgrove & Zasadzinski, 1998; Habdas & Weeks, 2002; Challis *et al.*, 2005), calorimetry (Anderson & Birdi, 1991; Bury *et al.*, 1991; Loh *et al.*, 2004; Smirnovas *et al.*, 2005; Sun *et al.*, 2005) and nuclear magnetic resonance (Fabre *et al.*, 1980; Zajac *et al.*, 1994; Freed *et al.*, 2009), to name a few. Ultrasonic characterisation is another of such techniques, widely used for commercial and academic research purposes due to its high sensitivity to molecular rearrangement, invariance to sample opacity and the availability of non-destructive on-line sampling (Zaman *et al.*, 2004; Xiaobo *et al.*, 2016). The power levels that are typically deployed during ultrasonic measurements are ca. 10 kW m^{-2} (Puskar, 1982) and it is assumed that displacements induced by ultrasonic pressure are elastic (Povey, 1997b). The method allows to detect changes in volumetric/elastic properties of samples, such as the particle size distribution (Challis *et al.*, 2005; Povey, 2013, 2017), contrasts in viscous/density properties (Challis *et al.*, 2005), aggregation (Zielinski *et al.*, 1986; Andreatta *et al.*, 2005a; Ray *et al.*, 2005; Abbott & Povey, 2012; Svalova *et al.*, 2017), particle stability (creaming/flocculation) (Shukla *et al.*, 2007) and crystallisation (Dickinson *et al.*, 1996; Povey, 2017). Advantages of ultrasound over light spectroscopic techniques include the phase sensitivity of acoustic transducers, a higher frequency range (10^{-1} to 10^{13} Hz vs $3\text{-}6 \times 10^{16}$ Hz), coherence between pulses and non-polarization of the sound pulse (Povey, 1997b).

Ultrasound has been applied to study phase behaviour properties of e.g. proteins, fats, ionic solutions and surfactants. For example, Taulier & Chalikian (2001) used ultrasonic velocity along with density, fluorescence anisotropy and circular dichroism measurements to understand conformational transitions in β -lactoglobulin. The

temperature-induced aggregation and denaturation of the same protein was characterised using ultrasonic velocity and absorption in heat-catalysed conditions (Ochendusko & Buckin, 2010). Airborne ultrasound measurements have been used to monitor the volume and size distributions of air bubbles in chocolate (Watson *et al.*, 2014). Low-intensity ultrasound has also been successfully used to promote periodontal alveolar bone regeneration in dogs (Wang *et al.*, 2018). For present purposes, of particular interest is ultrasonic characterisation of colloidal mixtures and solutions of surfactants. Ultrasound has been widely used to study aggregation of surfactant solutions. Zielinski *et al.* (1986) proposed an ultrasonic velocity model determining the critical micelle concentration of alkyltrimethylammonium bromide surfactants in water. Ray *et al.* (2005) have demonstrated secondary micellarisation of the same type of compound using ultrasound, as well as tensiometric, conductometric, fluorimetric and calorimetric methods. Assuming asphaltenes behave similarly to surfactants, Andreatta *et al.* (2005a) used ultrasound to estimate the critical nanoaggregate concentration of asphaltenes in toluene as well as aggregation of Tween 80 and sodium dodecyl sulphate surfactants. What follows provides an introduction into sound mechanics and defines mathematical apparatus in order to detect micellarisation and nanoaggregation in solutions using ultrasonic characterisation.

6.2 Acoustic Propagation in Homogeneous Fluids and Colloids

6.2.1 *Fundamentals of acoustic wave propagation*

The sound wave is a mechanical phenomenon, whereby oscillations of pressure occur about an equilibrium point through a transmission medium (Povey, 1997b). Sound waves in liquids are compressional/longitudinal (Pierce, 1981) whereby the particle motion is parallel to the direction of pulse propagation (Povey, 1997b), Figure 6.1(c,d). In solids, sonic waves can additionally be supported in a shear mode over macroscopic distances whereby the particles in medium are displaced at a right angle (transverse) to the direction of sound wave propagation (Povey, 1997b; Mason & Peters, 2002), Figure 6.1(d).

Consider a plane wave of sound, as shown in Figure 6.1(a), which can be characterised by the following parameters:

- Wavelength λ - the length between two successive sound wave peaks,

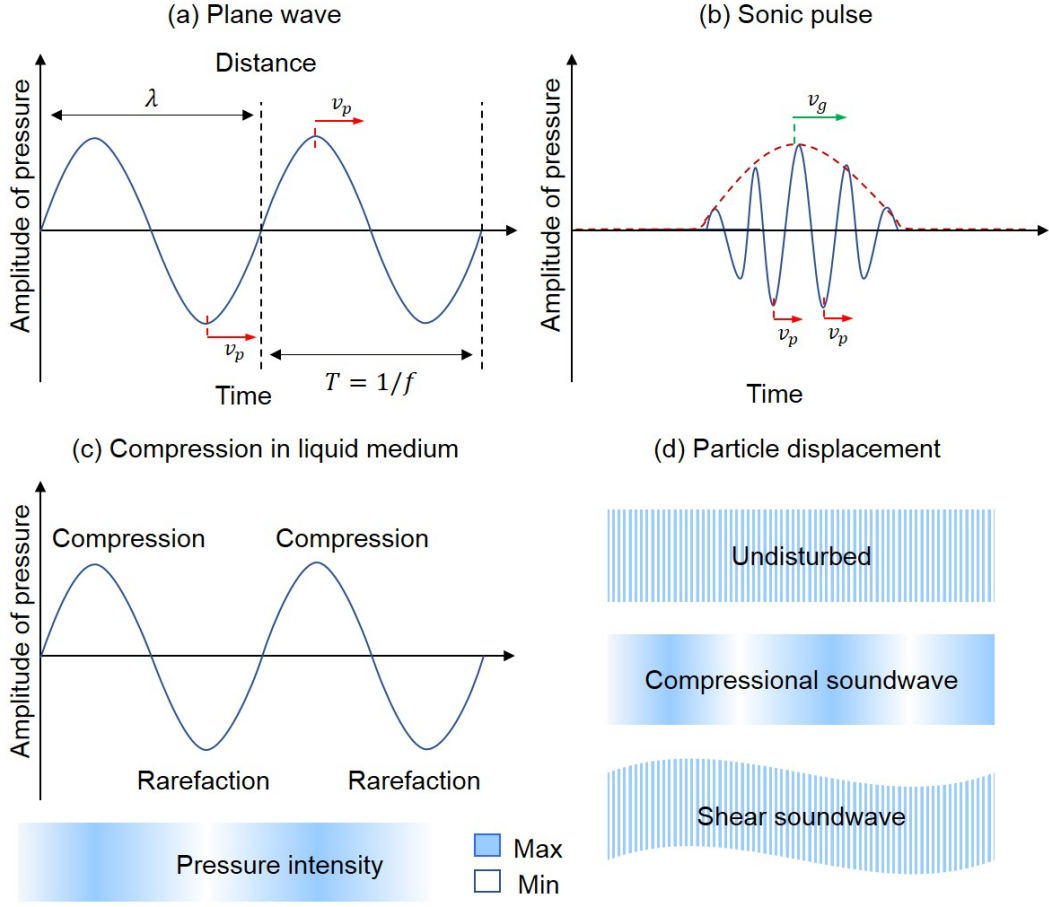


Figure 6.1: Schematic of different types of sound waves. In plots (a,b) red and green arrows indicate the direction of phase and group velocity propagation respectively.

- Frequency f - number of wave oscillations per unit time (Hz- number of oscillations per second). It follows that the period of the oscillation T is $T = f^{-1}$.

The evolving amplitude of a wave, $A(x, t)$, can be expressed as

$$A(x, t) = A_0 \exp(i(\omega t - kx)), \quad \omega = 2\pi f, \quad k = \frac{2\pi}{\lambda} \quad (6.1)$$

where A_0 is the amplitude, ω is the angular frequency and k is the wavenumber of the wave. The speed of the wave (travel), in particular that of constant phase locations on the wave, is given by the phase velocity,

$$v_p = \frac{\omega}{k} = f\lambda. \quad (6.2)$$

In Figure 6.1 the wave amplitude is depicted as being constant. In reality, as it propagates through any real medium, the wave will lose energy, leading to a decay in its oscillation amplitude with propagation distance. Equation (6.1) can be modified to account for decay due to attenuation as

$$A(x, t) = A_0 \exp(i(\omega t - kx) - \alpha x), \quad (6.3)$$

where the final term in the exponential describes this exponential decay of amplitude, with α being the attenuation coefficient (typically expressed in units of Nepers m^{-1}). A number of factors contribute to α , including the non-ideality of a sound transmitter/resonator, viscous losses, thermal dissipation, chemical relaxation effects and scattering effects. Given that α is significantly smaller than the wavenumber k , attenuation does not strongly impact velocity and can be ignored in situations where the sound velocity is the sole quantity of interest. On the other hand, under high attenuation the wavefront of an ultrasonic pulse does not preserve the original phase relationship and sound propagation follows a diffusion process whereby v_p can no longer be used (Povey, 1997a).

Sound can also propagate as a pulse, which is a group of sound waves whose amplitude is modulated by a finite-sized envelope, as illustrated in Figure 6.1(b). The velocity at which the peak of the envelope travels is given by the group velocity

$$v_g = \frac{d\omega}{dk}. \quad (6.4)$$

Ultrasound waves are sound waves that have a frequency above that detectable by human hearing, which is typically above 20 kHz (Mason & Peters, 2002).

6.2.2 Acoustic propagation through a single continuous fluid

To derive the equation for sonic velocity in a single continuous fluid, firstly consider an infinitesimally small mass of the fluid m , which extends over a volume V . If the pressure experienced by this fluid mass increases, then its volume will decrease, and vice versa. The propensity of the fluid for changing volume with pressure p through the adiabatic compressibility β can be defined as

$$\beta = -\frac{1}{V} \left(\frac{\partial V}{\partial p} \right) = \frac{1}{\rho} \left(\frac{\partial \rho}{\partial p} \right) \quad (6.5)$$

where ρ is density and $V = m\rho^{-1} \propto \rho^{-1}$. Acoustic waves generate a pressure front that change the local fluid density, thus velocity v_p can be defined as a derivative of pressure with respect to density (Kristensen, 2010),

$$v_p = \sqrt{\left(\frac{\partial p}{\partial \rho}\right)}. \quad (6.6)$$

Finally, the speed of sound v_p can be linked to β and ρ by substituting the right hand side of (6.5) into (6.6),

$$v_p = \sqrt{\frac{B}{\rho}} = \frac{1}{\sqrt{\rho\beta}}, \quad (6.7)$$

where $B = \beta^{-1}$ is the bulk modulus. The above formalism is known as the Newton-Laplace equation (normally using B) or the Wood equation (using β) (Wood, 1941, 1964).

An ideal mixture, whereby there is no interaction between the mixture substances, can be considered a homogeneous/single continuous fluid (Kristensen, 2010), which is typically the case in aqueous surfactant solutions. This study presumes that this is the case for asphaltene-toluene solutions. What follows illustrates a derivation of sonic velocity in a binary liquid sample with two components, denoted component₀ and component₁ (Kristensen, 2010). Here, volume fraction ϕ is used, whereas for (surfactant or ionic) solutions the weight concentrations c of each of the mixture components is used (Zielinski *et al.*, 1986). The density of the mixture ρ can be broken into the two mixture contributions,

$$\rho = \frac{m_0 + m_1}{V_0 + V_1} = (1 - \phi)\rho_0 + \phi\rho_1. \quad (6.8)$$

Similarly, β of solution can be broken down into solvent and solute components using (6.5),

$$\frac{\partial V}{\partial p} = \frac{\partial(V_0 + V_1)}{\partial p} = -(V_0\beta_0 + V_1\beta_1). \quad (6.9)$$

Using equations (6.8)and (6.9), the adiabatic compressibility of a mixture is

$$\beta = (1 - \phi)\beta_0 + \phi\beta_1. \quad (6.10)$$

Finally, combining (6.8) and (6.10), the sonic velocity through an ideal mixture is

$$v_p = \{((1 - \phi)\rho_0 + \phi\rho_1)((1 - \phi)\beta_0 + \phi\beta_1)\}^{-\frac{1}{2}}. \quad (6.11)$$

A generalisation of (6.11) can be applied to multi-phase dispersions (colloids) (Urlick, 1947)

$$v_p = \frac{1}{\sqrt{\beta\rho}}, \quad \beta = \sum_{i=1}^n \phi_i\beta_i, \quad \rho = \sum_{i=1}^n \phi_i\rho_i, \quad (6.12)$$

where ϕ is the volume fraction and $i = 1, 2, \dots, n$ is the number of solution phases; typically $i = 1$ refers to the continuous phase and the remaining phases are dispersed solids (Povey, 1997a). Similarly, sonic velocity can detect micellarisation concentration using density and compressibility differences pre- and post-micellarisation. Section 6.4 details the method.

6.2.3 Ultrasonic propagation through a colloid

Ultrasonic propagation in colloids will involve significant velocity and attenuation changes, especially at the phase boundary, giving rise to the scattering phenomenon (Challis *et al.*, 2005). Firstly, in colloidal mixtures the phase velocity and attenuation will be a ‘weighted average’ of the velocity and attenuation in the two phases, taking into account sound diffraction at the phase boundary (Urlick, 1947; Povey, 1997a). Contrasts in physical properties of the colloidal phases, including compressibility, thermal conductivity and density may contribute to energy losses of the sound wave or induce a phase shift (Challis *et al.*, 2005). Phase density contrasts and viscosity, in particular, induce scattering of sound in liquid samples. In the present investigation, particles in solution are measured (Svalova *et al.*, 2017), thus multi-phase resonance contrasts are ignored. The multi-phase nature of mixtures and presence of inhomogeneities cause issues, such as reflection, rarefaction, scattering and interference in the propagating wavefront (Povey, 1997c).

The above issues give rise to sound scattering. Povey (1997c) defined sound wave scattering as “any process which takes energy in one form or mode of motion and transforms it into another”. Scattering of sound causes its wave amplitude to change in all directions and/or causes a phase shift. As very few liquids are ‘truly’ homogeneous, particle displacements will be associated with inter-particle interactions and restoring forces (Povey, 1997c). Although (9.2) describes velocity propagation through colloids as through a ‘homogenized’ fluid, it can be shown to be a special

case of scattering theory (Povey, 1997c). Also, sound wave propagation is isothermal only at frequencies above 10^{12} Hz, thus although the adiabatic approximation is satisfactory for present purposes, ultrasonic propagation is accompanied by thermal waves (on the scale of mK) (Povey, 1997c). Understanding the phenomenon of scattering, however, allows to obtain a better understanding of the physical sample properties. This includes creaming/sedimentation (Pinfield, 1996), crystallisation (Dickinson *et al.*, 1993) and particle size determination (Alba, 1992; Roberts, 1996; Hazlehurst *et al.*, 2014). Thermoacoustic scattering, in particular, is one of the main phenomena used in the ultrasonic characterisation of colloids and determining the particle size distribution (Hazlehurst *et al.*, 2014). The formalisms of scattering theory can be found in the above references, as well as earlier works (Strutt, 1896; Epstein & Carhart, 1953; Lloyd & Berry, 1967; Allegra & Hawley, 1972).

6.3 Velocity Measurement Methods

This section describes two methods of measuring ultrasonic velocity. In all our experiments, the acoustic resonance method is used.

6.3.1 *Pulse-echo/pitch-catch*

The pulse-echo/pitch-catch method is a widely-used ultrasonic velocity characterisation method, and the following description draws from the work of Povey (1997a,b). The method measures the group velocity v_g of an ultrasonic pulse, Equation 6.4, as shown in Figure 6.1 (b). A piezoelectric transducer is normally installed in a metal cell that is temperature-controlled to a high precision, generating a pulsed sound wave illustrated by Figure 6.2. In particular, the source transducer is excited by an electrical pulse, which causes a pulsed vibration. This vibration stimulates the generation of sound waves in the fluid, emanating from the transducer face. In the pulse-echo method, these propagate through the cell, reflect against the back wall of the measurement cell, and are detected by the source. In the pitch-catch method, a receiving transducer detects the sound pulse. A timer records the (two-way for pulse-echo and one-way for pitch-catch) time of the pulse in sample which is then converted to velocity. When a reflected wave is received, reverberations need to be taken into account. In particular, the received pulse will be a succession of the pulse that travelled through the sample only, and that which penetrated the wall off the sample cell also. Given that the speed of sound through metals is much greater than

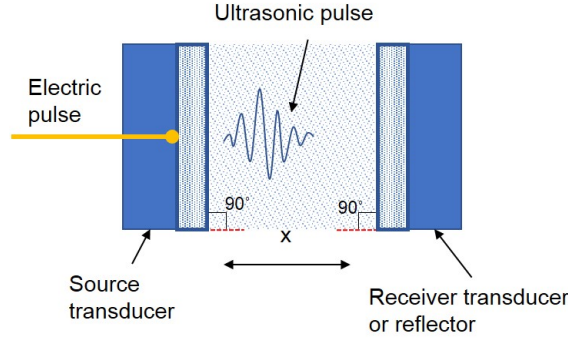


Figure 6.2: The pulse-echo/pitch-catch measurement method, adapted from Povey (1997a). The ultrasonic path length is denoted x .

through liquids, reverberations may need to be taken special account for, e.g. by ensuring sufficient cell wall thickness. The source transducer need to be installed to a high degree of parallelism with respect to the back wall of the measurement cell (pulse-echo) or the receiver (pitch-catch), otherwise causing phase variation and errors in velocity measurement.

6.3.2 Acoustic resonance

The acoustic resonance method (Eggers & Funck, 1973) measures the phase velocity v_p , Equation (6.6), and will be used to perform ultrasonic characterisation through homogenous liquid samples throughout this study. Figure 6.3 (a) illustrates a schematic of a resonator unit. The latter consists of two metal transducer plates, often quartz (Eggers & Funck, 1973), labeled Q_1 and Q_2 . The ultrasonic characterisation instrument used in this study, ResoScan, uses gold and lithium niobate piezocrystals (TF Instruments, 2007). A (sine wave) oscillator sends a pulse through Q_1 producing a standing sound wave in the liquid at characteristic frequencies f_n . The output plate Q_2 receives voltage pulses which are processed and displayed as frequency peaks on an oscilloscope or processing software, Figure 6.3 (b).

In order to measure the sonic velocity, the pressure (a function of frequency) at the receiving Q_2 is the sum of all partial waves in the resonator (Musa, 1958). It is assumed that the wave reflection at the transducers is ideal and the reflection loss due to attenuation in the liquid corresponds to one wave transfer (Eggers & Funck, 1973). Any non-idealities in the transducer plates can contribute to additional attenuation of the sound wave and errors in the velocity measurement. A measurement setup whereby the resonator plates' diameter is large compared to the

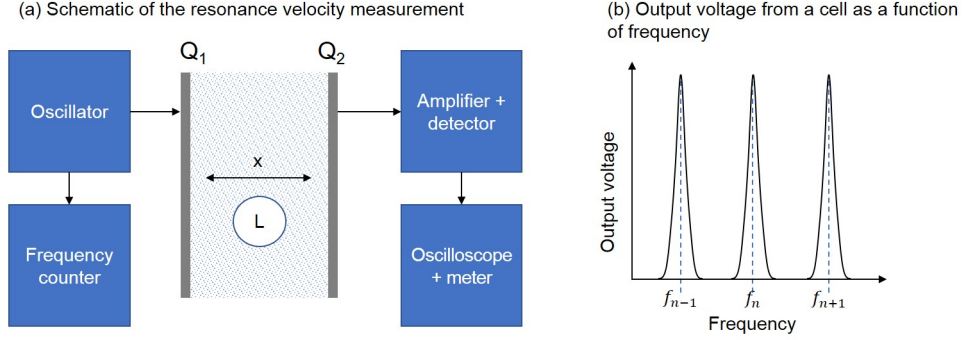


Figure 6.3: The acoustic resonance method, adapted from Eggers & Funck (1973). Resonator cavities are labeled Q_1 and Q_2 , x denotes path length, L denotes liquid volume in the sample, f_n denotes characteristic frequencies.

sound wavelength in the liquid, the plane wave field is enhanced which is in contrast to the complex near field of a piston transducer (Del Grosso, 1966) in the pulse-echo or time-of-flight techniques. Further, the resonance method offers a higher signal-to-noise ratio (Andreatta *et al.*, 2007). What follows lists the formalisms used to estimate ultrasonic velocity using the resonance method, as given in Andreatta *et al.* (2007). Given an ideal one-dimensional isolated resonator, the amplitude A of an ultrasonic wave propagating in the x direction is given by the Equation (6.3). For the frequency of the n^{th} longitudinal resonance f_n is

$$f_n = \frac{nv_p}{2l_s}, \quad (6.13)$$

where l_s is the path in solution (Bolef & Miller, 1971). Given that l_s is constant, the relative change in velocity can be related to a relative change in the resonant frequency

$$\frac{\partial v_p}{v_p} = \frac{\partial f_n}{f_n}. \quad (6.14)$$

Specific to the resonance method is the quality factor Q which is the relative energy loss per oscillation cycle of a system (Davis, 2009)

$$Q = 2\pi \frac{E_{\text{total}}}{\Delta E} \quad (6.15)$$

whereby E_{total} is the total energy of the resonator and ΔE is the energy loss per oscillation cycle (Kristensen, 2010). The Q -factor also explains the loss of sharpness

of a resonant peak in frequency space through the amount of energy dissipation

$$Q = \frac{f_n}{\Delta f_n} \quad (6.16)$$

where Δf_n is the full width at maximum divided by $\sqrt{2}$. The peak number can then be determined using the frequencies of two adjacent modes

$$\frac{f_{n+1} - f_n}{f_n} = \frac{1}{n}. \quad (6.17)$$

6.4 Micelle Detection Using Ultrasonic Velocity Measurements

What follows details the mathematical model in order to detect micellarisation and nanoaggregation in solutions using ultrasonic phase velocity denoted u ,

$$u = v_{p,ultrasound}. \quad (6.18)$$

An extension of (6.7) allows to detect the onset of surfactant aggregation into micelles, as proposed by Zielinski *et al.* (1986). In a surfactant solution of volume V , solvent has a weight w_0 and the dissolved surfactant has a weight of $w = w_1 + w_m$ which is a sum of monomeric₁ and micellar_m forms. The total volume of the solution is then related to the component weights following

$$V = w_0 v_0 + w_1 \tilde{v}_1 + w_m \tilde{v}_m \quad (6.19)$$

where v is specific volume and \tilde{v} is the apparent specific volume of solvent₀, monomeric surfactant₁ and micellar surfactant_m. The total solution weight w_T is a product of volume V and density ρ

$$w_T = \rho V = w_0 + w_1 + w_m. \quad (6.20)$$

The solution density can be re-written in terms of surfactant concentrations and solvent density using (6.19) and (6.20)

$$\rho = \rho_0 + (1 - \tilde{v}_1 \rho_0) c_1 + (1 - \tilde{v}_m \rho_0) c_m, \quad c_1 = \frac{w_1}{V}, \quad c_m = \frac{w_m}{V}, \quad (6.21)$$

where c_1 and c_m are weight concentrations of monomeric and micellar surfactant respectively. Using (6.21) adiabatic compressibility of the solution β can be defined as a partial derivative of concentration with respect to pressure p (at constant entropy S)

$$\frac{\partial c_1}{\partial p} = c_1\beta, \quad \frac{\partial c_m}{\partial p} = c_m\beta, \quad (6.22)$$

defining adiabatic compressibility of the solvent β_0

$$\beta = \beta_0 + (\tilde{\beta}_1 - \beta_0)\tilde{v}_1c_1 + (\tilde{\beta}_m - \beta_0)\tilde{v}_m c_m. \quad (6.23)$$

The apparent surfactant compressibility is then defined as

$$\tilde{\beta}_1 = -\frac{1}{\tilde{v}_1} \left(\frac{\partial \tilde{v}_1}{\partial p} \right)_S, \quad \tilde{\beta}_m = -\frac{1}{\tilde{v}_m} \left(\frac{\partial \tilde{v}_m}{\partial p} \right)_S. \quad (6.24)$$

Finally, ultrasonic velocity in (6.7) can be related to concentrations of monomeric and micellar surfactants

$$u = u_0 + \frac{u_0}{2} \left(\tilde{v}_1 \left(2 - \frac{\tilde{\beta}_1}{\beta_0} \right) - v_0 \right) c_1 + \frac{u_0}{2} \left(\tilde{v}_m \left(2 - \frac{\tilde{\beta}_m}{\beta_0} \right) - v_0 \right) c_m. \quad (6.25)$$

Further,

$$\begin{cases} \text{if } c \leq \text{CMC, then } c_1 = c, \text{ and } c_m = 0, \text{ otherwise} \\ \text{if } c > \text{CMC, then } c_1 = \text{CMC, and } c_m = c - \text{CMC.} \end{cases} \quad (6.26)$$

The model (6.25) implies that pre- and post-micellarisation, sonic velocity is related to surfactant concentration as a combination of two linear behaviours whose intersection estimates the CMC. Assuming that asphaltenes are similar to surfactants (Andreatta *et al.*, 2005a) and have emulsion-stabilising properties, (6.25) will be used to study asphaltene nanoaggregation in toluene.

Methodology

Chapter 7. Geochemical Characterisation

7.1 Cleaning and Safety Procedures

A laboratory coat, safety goggles and rubber gloves were worn at all times to ensure personal safety and reduce contamination. Glassware used in all geochemical experiments was pre-washed in a laboratory automatic dish washer and/or rinsed with dichloromethane (DCM) or DCM/methanol (MeOH) mixtures as appropriate and dried under nitrogen, air-dried or in a glass oven as appropriate. Metal tools, e.g. spatulas and tongs, were wiped with paper towels using DCM or DCM/MeOH as appropriate. Filter media, e.g. glass/cotton wool and paper thimbles, were cleaned by Soxhlet extraction with DCM prior to use. Filter media for chromatographic separation, including alumina and silica-coated glass plates, were cleaned by DCM as appropriate and activated in an oven at 125°C. Experiments involving the use of volatile and/or toxic liquids were performed in a fume cupboard. A cup-shaped respirator was used when appropriate. Laboratory bench/fume cupboard surfaces were covered with tin foil prior to experiments to reduce contamination. All glass containers were rinsed with DCM at least three times, plastic lids were gently rinsed or wiped with DCM or MeOH.

7.2 Asphaltene Precipitation

Asphaltenes were precipitated from their parent petroleum following a 40-fold excess *n*-alkane addition (Groenzin & Mullins, 1999; Yu *et al.*, 2014; Svalova *et al.*, 2017). Crude oil (5 g) was mixed with 200 ml of *n*-pentane (*n*-C₅), ultrasonicated for 2 h and left to settle overnight. The mixture was then centrifuged for 15 min at 3500 rotations per minute (rpm), maltene supernatant decanted (first maltene) and stored for biodegradation characterisation and maturity assessment. The asphaltene fraction was further washed following a cycle of (i) 200 ml *n*-C₅ addition, (ii) ultrasonication for 30 min, (iii) equilibration for 1 h, (iv) centrifugation for 15

min at 3500 rpm and (v) decanting of the supernatant. The maltene fraction from the washing cycles was reduced under reduced pressure to ca. 10 ml and stored. Asphaltenes were then air-dried overnight and/or dried with nitrogen gas before purification using Soxhlet extraction with toluene (Yu *et al.*, 2014). The obtained asphaltene-toluene extract was evaporated under reduced pressure to 2-5 ml and washed for a final time as described above (i-v) for further use in ultrasonic characterisation and oxidation experiments.

7.3 Ruthenium Ion Catalysed Oxidation of Asphaltenes

Inference about asphaltene architecture was performed using ruthenium ion catalysed oxidation (RICO) (Peng *et al.*, 1999; Ma *et al.*, 2008; Snowdon *et al.*, 2016; Svalova *et al.*, 2017). The reaction products are homologous series of *n*-alkanoic fatty acid methyl esters (FAMEs) representing *n*-alkyl appendages that were attached to PAHs and α, ω -*di-n*-alkanoic fatty acid *di*-methyl esters (DFAMEs) and α -branched FAMEs (Strausz *et al.*, 1999a; Peng *et al.*, 1999; Snowdon *et al.*, 2016). Asphaltenes (50 mg) were firstly dissolved in 4 ml DCM and then mixed with 4 ml acetonitrile, 5 ml 12% aqueous sodium periodate (NaIO_4) and 5 mg ruthenium trichloride ($\text{RuCl}_3 \cdot x\text{H}_2\text{O}$). The mixture was shaken for at least 18 h using an orbital shaker. Dichloromethane and MeOH (15 ml each) were added to the mixture, shaken vigorously and centrifuged for 15 min at 3500 rpm. The two-phase supernatant was decanted into a separating funnel, the remaining sediment was further mixed with 10 ml MeOH and DCM each, centrifuged for 15 min at 3500 rpm and supernatant decanted into the same funnel to be combined with the initial washing. This cycle was repeated three times. The sediment remaining in the centrifuge tubes was of laurel green colour and had a grainy texture, and was transferred into glass vials for storage. When combined, the four supernatant washings had no phase separation, thus care was required to separate the heavier organic phase. The washings were combined with 5 ml of 4% aqueous sodium hydroxide (NaOH), shaken vigorously and left to settle under gravity for 30 min. Organic acids were washed out from the aqueous phase using DCM. In particular, 20 ml of DCM was added to the separating funnel, shaken vigorously and the lower ca. 50% of volume decanted into a round-bottom flask. This washing was repeated further four times; after the second-third wash a phase boundary could be seen in the mixture. The remaining aqueous phase was decanted into a glass container for storage. The organic phase

was returned into the funnel and mixed with 5 ml 13.5% hydrochloric acid (HCl) and gently shaken. If required, up to 40 ml of deionised water was added in order to obtain phase separation. The two-phase mixture was washed with DCM further three times. This was then evaporated under reduced pressure until dryness. A cloudy appearance of the organic phase during volume reduction would be indicative of aqueous traces which would be removed by the addition of anhydrous sodium sulphate (Na_2SO_4). When dry, the organic acids would be re-dissolved in 1 ml DCM, mixed with 5 ml 98:2 mixture of MeOH and sulfuric acid (H_2SO_4) and reflux-heated for 3h. The obtained esters were mixed with 10 ml deionised water and washed with DCM four times. Finally, the washings were mixed with 4 ml 2% aqueous NaHCO_3 and evaporated under reduced pressure with Na_2SO_4 to ca. 5 ml. The products were pipetted out avoiding aqueous traces and blown down with N_2 gas to 1 ml for gas-chromatography-flame ionisation detection (GC-FID) and gas chromatography-mass spectrometry (GC-MS).

7.4 Maltene Analysis

Maltene (deasphalted) petroleum samples were separated into aliphatic/saturate, aromatic and polar fractions using thin layer chromatography (TLC) and short column elution (Svalova *et al.*, 2017). Silica gel was prepared with 30 g Merck Silica 60 G powder and 70 ml deionised water. Washed and DCM-purified glass plates were covered with 0.5 mm silica gel, left to air-dry and activated in an oven at 125 °C for at least 4 h or overnight. The plates were then further decontaminated by elution in DCM, marking a gap on the silica layer 2 cm away from the top eliminate the DCM-eluted contamination, and activated at 125 °C for 30 min. Capillary tubes were prepared from glass pipettes for sample application to ensure a better application control and homogeneity. Glass tanks filled with ca. 200 ml petroleum ether (for maltene chromatography) or DCM (for plate purification) were lined with TLC paper to ensure a volatile eluent atmosphere. The tanks were ready for use when the paper lining has been fully-saturated with the eluent. Maltenes (10 mg) were spotted on the plates using capillary tubes with eicosane ($\text{C}_{20}\text{H}_{42}$; aliphatic), phenyldodecane ($\text{C}_{12}\text{H}_{25}\text{C}_6\text{H}_5$; monoaromatic) and anthracene ($\text{C}_{14}\text{H}_{10}$; triaromatic) elution standards and eluted in the glass tanks. Short columns were prepared by filling with cotton wool and activated alumina as filter layers. The separated aliphatic and aromatic fractions were placed in short columns on top of the filter media and

eluted with petroleum ether and DCM respectively. The final fractions were reduced to 1 ml and analysed by GC-FID and GC-MS with heptadecylcyclohexane (C₂₃H₄₆) and *p*-terphenyl (C₆H₅C₆H₄C₆H₅) as internal aliphatic and aromatic standards respectively.

7.5 Analytical Instruments

The following information has been published earlier in Svalova *et al.* (2017). Maltene and RICO products were analysed using an Agilent 6890 instrument for GC-FID and an Agilent 7975C instrument for GC-MS.

Initial compound screening was performed using the GC-FID equipped with a 30 m HP5-MS column (0.25 mm internal diameter, 0.25 μ m polysiloxane stationary phase; J&W Scientific, USA). Helium was used as carrier gas at a flow rate of 1 ml min⁻¹. The GC oven was initially held at 50 °C for two minutes and then raised at a rate of 5 °C min⁻¹ to a final temperature of 310 °C where it was held isothermally for 20 min. The instrument was run in splitless mode, whereby the injector was held at 280 °C and the FID at 300 °C. Product detection was carried out using Agilent 7890A GC split/splitless injector at 280 °C linked to an Agilent 5975C mass spectrometer. The oven was operated at the same temperature mode as GC-FID using a 30 m HP5-MS column (specification as above, J&W Scientific, USA). A mass selective detector was used in selected ion monitoring and full scan modes (m/z 50-700). Compound identification was based on the NIST05 (NIST, 2005) mass spectral library as well as comparison to mass spectra and relative retention times reported in other studies and in-house guides.

Chapter 8. Ultrasonic Characterisation

This chapter describes the methodology of using ultrasonic velocity characterisation to better understand the asphaltene nanoaggregation. This includes sample preparation, ultrasonic instrument description and operation and a probabilistic framework of constrained optimisation used to estimate the nanoaggregation region concentration from experimental data.

8.1 Sample Preparation

Tetradecyltrimethylammonium bromide ($\text{CH}_3(\text{CH}_2)_{13}\text{N}(\text{CH}_3)_3\text{Br}$; C_{14}TAB) and dodecyltrimethylammonium bromide ($\text{CH}_3(\text{CH}_2)_{11}\text{N}(\text{CH}_3)_3\text{Br}$; C_{12}TAB) 99% and 98% purity respectively, were obtained from Sigma Aldrich. Their solutions were prepared with Milli-Q 18 M Ω deionised water. Asphaltenes were purified by Soxhlet extraction, as described in Section 7.2. Extra-pure toluene ($\geq 99.99\%$ purity) was purchased from Sigma Aldrich.

The concentration ranges of C_nTAB ($n = 12, 14$) aqueous and asphaltene-toluene solutions were prepared by successive dilution using volumetric flasks and volumetric pipettes. Plastic and glass stoppers were used for C_nTAB and asphaltene solutions respectively.

The concentration ranges of asphaltene and surfactant solutions were prepared as follows. A starting weight of a solute C would be diluted in a volumetric flask of volume V_f . The solution would be mixed (by tipping the volumetric flask 3-5 times) and a volume V_p taken out by a volumetric (graduated) pipette and placed in a sample vial (Sample₀). The solute concentration of Sample₀ would thus be CV_f^{-1} . Then, the solution in the volumetric flask would be topped back to V_f , the solution in this flask is now of the concentration C_1 ,

$$C_1 = \frac{C}{V_f} \left(1 - \frac{V_p}{V_f} \right). \quad (8.1)$$

A sample of C_1 would then be taken into a sample vial (Sample₁) and the solution in the flask would be made up back to V_f that would give the total mixture concentration of C_2 (Sample₂)

$$C_2 = C_1 \times \left(1 - \frac{V_p}{V_f}\right) = \frac{C}{V_f} \left(1 - \frac{V_p}{V_f}\right) \left(1 - \frac{V_p}{V_f}\right) = \frac{C}{V_f} \left(1 - \frac{V_p}{V_f}\right)^2. \quad (8.2)$$

Thus, after n dilutions, the concentration of Sample _{n} would be C_n

$$C_n = \frac{C}{V_f} \left(1 - \frac{V_p}{V_f}\right)^n. \quad (8.3)$$

For the asphaltenes, the initial solute concentrations were weighted out in 1 ml gas chromatographic vials or weighing boats, as appropriate, on a Mettler Toledo MT5 microbalance (Mettler Toledo, 1999) using a resolution setting of 10^{-2} mg. For C_n TAB solutions, the initial solute concentrations were weighted out in 3 ml glass vials or weighing boats using a balance.

8.2 Analytical Instruments

The Resoscan Research System (TF Instruments, 2007) was used to perform high-resolution ultrasonic measurements. The Resoscan (Figure 8.1) performs simultaneous ultrasonic wave velocity u and attenuation α measurements through liquid samples. The measurement is performed by a two-channel resonator unit (Figure 8.1 (1)) that has a fixed path length of 7 mm. Ultrasonic waves are generated by gold and lithium niobate piezocrystals that are the resonator cavities, and given a homogeneous liquid this will give a precision of $\Delta u/u = 10^{-16}$. The instrument has two 250 μ L sample cells, requiring ca. 170 μ L sample volume. The two cells can either be used independently or the second cell can be filled with a reference liquid, e.g. the main solvent in the first cell. Temperature is controlled via two units, cell temperature measurement unit, Figure 8.1 (2), and Peltier thermostat control unit, Figure 8.1 (3). Samples can be measured at 5 °C - 85 °C, with a temperature resolution of 10^{-3} °C and precision of $\pm 5 \times 10^{-3}$ °C, isothermally or with temperature gradients. The present investigation performed measurements at 25 °C. The small sample requirement of 170-250 μ L and a high temperature stability enable to measure conformational changes on a molecular scale. In the vicinity of 25 °C the sound velocity changes by around 5 m s⁻¹ °C. Therefore, the preci-

sion limit of temperature corresponds to a systematic error in velocity of around $2.5 \times 10^{-2} \text{ m s}^{-1}$, which is sufficiently small that it does not affect our results. The fundamental frequency of the instrument is 10 MHz, with range of 7-11.5 MHz, the precise frequency chosen to maximise the quality factor of the acoustic resonant cell.



Figure 8.1: Resoscan Research System, image taken from TF Instruments (2007).

Prior to measurement the ultrasonic device was calibrated with solvent for which sound velocity is known, e.g. distilled water (del Grosso & Mader, 1972; Povey, 1997a) or toluene. A significant factor determining the quality of measurement is the removal of air bubbles. Whilst dissolved air plays no significant role in the reduction of measurement quality, air bubbles seriously disrupt the ultrasound propagation and it is crucial to remove them (Povey, 1997a). Also, sample injection should be performed slowly to avoid mixing with air. Cetyltrimethylammonium bromide aqueous solutions were injected using an auto-pipette with a $200 \mu\text{L}$ plastic tip. The instrument was left to equilibrate for 1 min and up to 30 measurements taken for every concentration sample, from which an average velocity was determined. Asphaltene solutions in toluene were injected using a $500 \mu\text{L}$ glass syringe with an aluminum needle. The instrument was allowed to equilibrate for 3-4 min and left to take around 100 measurements for every solution concentration. During

sample insertion an injector was held vertically parallel to the cell borehole and injection performed during 30-60 s to minimize air entrapment. The obtained data was analysed for extreme outliers, caused by air bubbles and other artefacts. Mean velocity values were plotted versus solute concentration to which piecewise linear regression models were fitted.

8.3 Constrained Optimization with Penalty Functions

What follows describes the use of constrained optimisation for the critical nanoaggregation region (CNR) estimation. Constrained optimisation (CO) is a statistical method allowing to select an optimal model from a set of several possibilities (Bertsekas, 1982; Smith & Coit, 1995). Suppose there exists a number of models that show similar performance quality based on some statistic, called the objective function Ω . When the use of Ω alone is insufficient to make a reliable model choice, a set of rules/constraints is applied, whose violation results in penalising Ω , resulting on $\Omega_p = \Omega - \sum \text{penalties}$. In linear model selection, we apply CO by penalising the coefficient of determination R^2 , which becomes the objective function, thus $\Omega_p = R_p^2$. The definitions of linear regression models and R^2 are revisited as follows. Given a set of observations $\mathbf{y} = (y_1, y_2, \dots, y_n)$ and $\mathbf{x} = (x_1, x_2, \dots, x_n)$ where \mathbf{y} are assumed dependent and \mathbf{x} are explanatory, a simple linear regression model is defined as

$$y_i = \beta_0 + \beta_1 x_i + \varepsilon_i, \quad \varepsilon_i \sim N(0, \sigma^2), \quad i = 1, 2, \dots, n \quad (8.4)$$

where ε_i is normally distributed with a zero mean and variance σ^2 . The regression model can, therefore, be redefined as

$$f_i = \beta_0 + \beta_1 x_i, \quad \varepsilon_i = y_i - f_i, \quad (8.5)$$

where ε_i is the residual not explained by the linear relationship f_i . The coefficient of determination R^2 is a measure of linear model performance that is the ratio of total variability explained by the model f_i , $\sum_{i=1}^n (f_i - \bar{y})^2$, to total variability in the

data $\sum_{i=1}^n (y_i - \bar{y})^2$,

$$R^2 = \frac{\sum_{i=1}^n (f_i - \bar{y})^2}{\sum_{i=1}^n (y_i - \bar{y})^2} = 1 - \frac{\sum_{i=1}^n \varepsilon_i^2}{\sum_{i=1}^n (y_i - \bar{y})^2}, \quad \bar{y} = \frac{1}{n} \sum_{i=1}^n y_i \quad (8.6)$$

where

$$\sum_{i=1}^n \varepsilon_i^2 = \sum_{i=1}^n (y_i - f_i)^2 = \sum_{i=1}^n (y_i - \bar{y})^2 - \sum_{i=1}^n (f_i - \bar{y})^2 \quad (8.7)$$

This implies that in data sets where \mathbf{x} and \mathbf{y} are perfectly linearly correlated $R^2 = 1$ and as linear dependence decreases, $R^2 \rightarrow 0$.

In an optimisation problem (Smith & Coit, 1995) the objective function is re-evaluated by penalties $P(\cdot)$, given the observance or violation of user-defined constraints. This produces the formalism of a penalised objective function, R_p^2 in our case, defined as

$$R_p^2 = R^2 - \sum_{i=1}^n \delta_i w_i P_i(x), \quad i = 1, 2, \dots, n, \quad n - \text{number of constraints}, \quad (8.8)$$

$$\delta_i = \begin{cases} 1 & \text{if constraint } i \text{ is violated,} \\ 0 & \text{if constraint } i \text{ is met.} \end{cases}$$

The constant/weight w_i represents the penalty magnitude for the violation of constraint i which may be set to increase with the magnitude of constraint violation. When applied to the asphaltene samples, the selected CNR boundaries were generally robust against changes in w_i and the final constants were chosen to satisfy $w_i P_i(\cdot) < 1$ so that the interpretation of the penalties remained intuitive (Section 12.2.2).

We analysed all possible non-overlapping two-regression combinations by varying the number of points in the monomeric/aggregated regressions. Constraints $P_i(\cdot)$ allowed to combine a priori knowledge about the behaviour underlying asphaltene aggregation process with the velocity measurements. Three constraints are proposed as follows.

1. Initial screening of velocity data illustrated that models with a lower number of points often led to higher R^2 values, Tables 12.2 and C.1-C.7. We penalised

all R^2 by $P_1(i) = i^{-0.5}$ where i is the number of points included in a regression.

2. When fitting a linear regression through monomeric/aggregated regions or the CNR, the residual distributions will be different due to varying sources of uncertainty, e.g. instrument measurement error vs a different underlying model. Therefore, $g_2(i)$ is as follows:
 - (a) Fit a linear regression M_i to the first i velocity-concentration measurements.
 - (b) Obtain the residuals of M_i , calculate their 95% confidence interval I .
 - (c) Estimate the value m_{i+1} of the point $_{i+1}$ using M_i .
 - (d) Obtain the residual $e_{i+1} = m_{i+1} - velocity_{i+1}$. If e_{i+1} lies outside I , penalise R^2 by $P_2(i) = e_{i+1}$.
3. Some measurements will cause a change in regression slope without producing a large outlier which may also be a sign of entering the CNR. Therefore, $P_3(i)$ is the difference between regression slopes fitted to the first i and $i + 1$ points.

We tested this model on pure CTAB mixtures and obtained the CMC estimations that matched those in our ultrasonic velocity measurements.

Chapter 9. Bayesian Inference of Asphaltene Nanoaggregation

Bayesian inference allows to combine data from experimental observations summarised in the likelihood with prior beliefs about the parameters of interest (Lee, 2012, p. 36). In the context of asphaltene and petroleum science, Bayesian inference has been used to predict asphaltene precipitation in reservoirs/during enhanced oil recovery (Amin *et al.*, 2010; Alimohammadi *et al.*, 2017), in molecular dynamic simulations of asphaltene aggregation (Sedghi *et al.*, 2013; Goual *et al.*, 2014; Goual & Sedghi, 2015) and molecular weight estimation (Halwachi *et al.*, 2012). In the present investigation it will be used to assess whether a nanoaggregation point or a range is more appropriate for the observed velocity response. What follows describes a method of assessing the likelihood of an asphaltene aggregation point versus an aggregation region given the experimental ultrasonic velocity data and assuming a linear relation is plausible for the monomeric and aggregated regions. The asphaltene concentration-velocity relation will be modelled assuming two different changepoint regression models whose efficiency and accuracy will then be compared. Model one, a one-changepoint formalism, is equivalent to the CNAC assumption (Andreatta *et al.*, 2005a), for which a Bayesian marginal posterior distribution of the changepoint will be derived. Model two is a two-changepoint model with a Brownian bridge (Durham & Gallant, 2002; Chow, 2009) to model the critical aggregation region (CNR) (Svalova *et al.*, 2017). The distributions will be obtained using Markov chain Monte Carlo (MCMC) simulation using Metropolis-Hastings (M-H) and Gibbs updates as appropriate (Brooks *et al.*, 2011; Lee, 2012). The investigation will conclude with a comparison of the CNAC and CNR posteriors of asphaltenes from four petroleum samples E1-E4.

9.1 Introduction to Empirical Bayesian Inference

Bayesian inference is particularly useful in conditions of low data availability and uncertainty in making decisions. As opposed to frequentist methods that are based on high number n of trials and data (ideally, $n \rightarrow \infty$), Bayesian framework allows to incorporate a practitioner's beliefs/plausibility into a probability distribution of the phenomenon of interest when the available information is insufficient (Koch, 2007, p. 1). Suppose, one is interested in a phenomenon Y giving an outcome y assuming an underlying law/process/model M that is controlled by a parameter (vector) θ . In reality, M will never be entirely true, except for synthetic data, due to the inherent nature of chaos and uncertainty, and what suffices is that M is a reasonable approximation of the 'true' law one is interested in, or is included in the family of models that represent the law well. The probability of $Y = y$ assuming M and θ is expressed by a probability density function of y given θ , $f(y|\theta)$ (M and Y are suppressed in notation). The product of f over all possible values of y is called the likelihood function of θ given y , $L(\theta|y) = \prod_{i=1}^n f(y_i|\theta)$ (Dekking *et al.*, 2005; Ando, 2007, p. 313) (sometimes denoted as simply $f(\mathbf{y}|\theta)$ where \mathbf{y} is a vector of observations), and finding the maximum of L will give the most likely value of the control parameter θ assuming M . Notice the difference in conditioning, whereby f gives the probability of y given θ and M , whereby L gives the most likely value of θ given y and M .

Likelihood alone can be used to draw inference about θ and whether M is suitable to model y . However, when i is small or y is deemed unrepresentative of the entirety about Y then L will be misleading even if M is reasonable. Bayesian inference (Koch, 2007; Lee, 2012) offers a solution to this problem by allowing to draw on the knowledge of the user about θ . These beliefs are expressed in a probability distribution $\pi(\theta)$ which can be the same or different to the function f (using π instead of f for denoting Bayesian inference is conventional). The combination of the frequentist and Bayesian components gives a posterior distribution $\pi(\theta|y)$ (Lee, 2012, p. 37)

$$\pi(\theta|y) = \frac{\pi(\theta)L(\theta|y)}{f(y)} \propto \pi(\theta)L(\theta|y). \quad (9.1)$$

The above is known as the Bayes' rule. In practice, the distribution $f(y)$ is unavailable in closed form and obtained by solving the integral $\int_Y \pi(\theta)L(\theta|y)dy = 1$. When the latter is computationally burdensome or analytically unavailable, sampling

methods such as Markov chain Monte Carlo (MCMC) are used.

In conventional Bayes (full Bayes, FB) the prior beliefs about θ are formed before observing the experiments (Ando, 2007). In situations where this is also unreasonable and prior beliefs can only be formed after observing the data, inference about θ is no longer ‘fully’ Bayesian but empirically Bayesian (EB) (Lee, 2012, p. 245, 261). This may arise when prior information is very low and/or specific to a particular experimental event yet a Bayesian approach is still desired to combine experimental, historical and user data. This is indeed the case for asphaltenes as their biological diversity and a lack of and challenges with ultrasonic measurements make a full Bayesian approach complicated. Mathematically, the difference between FB and EB (Ando, 2007) is the parametrisation of $\pi(\theta)$. In FB, the parameters (hyperparameters) that specify $\pi(\theta)$, say ψ , are stochastic implying the full notation of the prior distribution of θ is $\pi(\theta|\psi)$ and ψ should be assigned $\pi(\psi)$. In EB, ψ is non-stochastic and no additional priors are required, although the full form of the prior for θ remains $\pi(\theta|\psi)$ and the posterior of θ is $\pi(\theta|y, \psi)$ (Ando, 2007).

9.2 Model Setup

Nanoaggregation of asphaltenes may be detected by ultrasonic velocity measurements using theory of surface-active compound (surfactant) aggregation (Zielinski *et al.*, 1986; Andreatta *et al.*, 2005a). The full model derivation is given in Section 6.4. Within a uniform liquid, the ultrasonic velocity u is related to density ρ and adiabatic compressibility β of the medium according to the Urlick equation (Urlick, 1947)

$$u = \sqrt{\frac{1}{\rho\beta}}. \quad (9.2)$$

For multi-phase fluids which are well-dispersed, and ignoring the effects of sound scattering (valid for sufficiently low concentration of scatterers and away from scattering resonances) (Povey, 1997a), Equation (9.2) can be applied with density and compressibility represented by weighted averages of the mixture components (Section 6.2). An extension of Equation (9.2) allows to detect the onset of surfactant aggregation into micelles to detect the critical micelle concentration (CMC), as proposed by Zielinski *et al.* (1986). In particular, the sound velocity u is related to

apparent molar solution quantities following the relation

$$u = u_0 + \frac{u_0}{2} \left(\tilde{v}_1 \left(2 - \frac{\tilde{\beta}_1}{\beta_0} \right) - v_0 \right) c_1 + \frac{u_0}{2} \left(\tilde{v}_m \left(2 - \frac{\tilde{\beta}_m}{\beta_0} \right) - v_0 \right) c_m, \quad (9.3)$$

where v denotes specific volume, c - weight concentration, tilde- apparent quantities and subscripts refer to solvent (0), monomer (1) and micellar (m) quantities. Also,

$$\begin{cases} \text{if } c \leq \text{CMC, then } c_1 = c, \text{ and } c_m = 0, \text{ otherwise} \\ \text{if } c > \text{CMC, then } c_1 = \text{CMC, and } c_m = c - \text{CMC.} \end{cases} \quad (9.4)$$

The model (9.3) implies that pre- and post-micellarisation, sonic velocity is related to surfactant concentration as a combination of two linear behaviours whose intersection estimates the CMC.

9.2.1 Asphaltene nanoaggregation single-changepoint model

Formalism 9.3 is equivalent to a single-changepoint linear regression model where the speed of sound y varies with asphaltene concentration x as follows:

$$y_i = \begin{cases} \alpha_1 + \beta_1 x_i + \varepsilon_{1,i}, & \varepsilon_{1,i} \sim N(0, \sigma_1^2), \quad x_i < \gamma, \\ \alpha_2 + \left(\frac{\alpha_1 - \alpha_2 + \beta_1 \gamma}{\gamma} \right) x_i + \varepsilon_{2,i}, & \varepsilon_{2,i} \sim N(0, \sigma_2^2), \quad x_i \geq \gamma. \end{cases} \quad (9.5)$$

In (9.5), γ denotes the changepoint (CNAC), $\{\varepsilon_{j,i}, j = 1, 2\}$ refers to regression residuals that follow a Normal distribution with mean 0 and variance σ_j^2 , subscripts refer to the monomeric _{$j=1$} and aggregated _{$j=2$} concentrations respectively. For convenience, we define the slope of aggregated region $\beta_2 = \frac{\alpha_1 - \alpha_2 + \beta_1 \gamma}{\gamma}$. The likelihood for model (9.5) is derived

$$\begin{aligned} L(\theta|x, y) &= \prod_{i=1}^{n_1} \frac{1}{\sqrt{(2\pi\sigma_1^2)}} \exp \left\{ -\frac{(y_i - \alpha_1 - \beta_1 x_i)^2}{2\sigma_1^2} \right\} \times \\ &\times \prod_{i=1}^{n_2} \frac{1}{\sqrt{(2\pi\sigma_2^2)}} \exp \left\{ -\frac{\left(y_i - \alpha_2 - \left(\frac{\alpha_1 - \alpha_2 + \beta_1 \gamma}{\gamma} \right) x_i \right)^2}{2\sigma_2^2} \right\}. \end{aligned} \quad (9.6)$$

In the above, n_1 and n_2 denote the lengths of $\{\mathbf{x} : \mathbf{x} < \gamma_1\}$ and $\{\mathbf{x} : \mathbf{x} \geq \gamma_2\}$ respectively. Parameter priors were chosen to achieve semi-conjugacy where possible:

$$\begin{aligned}\alpha_1 &\sim N(a_1, \sigma_{\alpha_1}^2), & \alpha_2 &\sim N(a_2, \sigma_{\alpha_2}^2), & \beta_1 &\sim N(b_1, \sigma_{\beta_1}^2), \\ \sigma_1^2 &\sim IGa(\rho_1, \phi_1), & \sigma_2^2 &\sim IGa(\rho_2, \phi_2),\end{aligned}\quad (9.7)$$

where IGa denotes an Inverse-Gamma distribution. Let $\boldsymbol{\theta} = (\alpha_1, \alpha_2, \beta_1, \gamma, \sigma_1, \sigma_2)$. The above setup gives the following marginal posterior distributions.

$$\alpha_1 | \boldsymbol{\theta}_{-\alpha_1}, \mathbf{x}, \mathbf{y} \sim N(M_{\alpha_1}, V_{\alpha_1}), \quad (9.8)$$

$$\begin{aligned}M_{\alpha_1} &= \left(\frac{a_1}{2\sigma_{\alpha_1}^2} + \sum_{i=1}^{n_1} \frac{y_i - \beta_1 x_i}{2\sigma_1^2} + \sum_{i=1}^{n_2} \frac{A}{2\sigma_2^2} \right) \left(\frac{1}{2\sigma_{\alpha_1}^2} + \frac{n_1}{2\sigma_1^2} + \sum_{i=1}^{n_2} \frac{x_i^2}{2\sigma_2^2} \right)^{-1}, \\ A &= x_i \left(y_i - \alpha_2 - x_i \left(\frac{\beta_1 \gamma - \alpha_2}{\gamma} \right) \right), \quad V_{\alpha_1} = 0.5 \left(\frac{1}{2\sigma_{\alpha_1}^2} + \frac{n_1}{2\sigma_1^2} + \sum_{i=1}^{n_2} \frac{x_i^2}{2\sigma_2^2} \right)^{-1}.\end{aligned}$$

$$\beta_1 | \boldsymbol{\theta}_{-\beta_1}, \mathbf{x}, \mathbf{y} \sim N(M_{\beta_1}, V_{\beta_1}), \quad (9.9)$$

$$\begin{aligned}M_{\beta_1} &= \left(\frac{b}{2\sigma_{\beta_1}^2} + \sum_{i=1}^{n_1} \frac{(y_i - \alpha_1)x_i}{2\sigma_1^2} + \sum_{i=1}^{n_2} \frac{A}{2\sigma_2^2} \right) \left(\frac{1}{2\sigma_{\beta_1}^2} + \sum_{i=1}^{n_1} \frac{x_i^2}{2\sigma_1^2} + \sum_{i=1}^{n_2} \frac{x_i^2}{2\sigma_2^2} \right)^{-1}, \\ A &= x_i \left(y_i - \alpha_2 - x_i \left(\frac{\alpha_1 - \alpha_2}{\gamma} \right) \right), \quad V_{\beta_1} = 0.5 \left(\frac{1}{2\sigma_{\beta_1}^2} + \sum_{i=1}^{n_1} \frac{x_i^2}{2\sigma_1^2} + \sum_{i=1}^{n_2} \frac{x_i^2}{2\sigma_2^2} \right)^{-1}.\end{aligned}$$

$$\alpha_2 | \boldsymbol{\theta}_{-\alpha_2}, \mathbf{x}, \mathbf{y} \sim N(M_{\alpha_2}, V_{\alpha_2}), \quad (9.10)$$

$$\begin{aligned}M_{\alpha_2} &= \left(\frac{a_2}{2\sigma_{\alpha_2}^2} + \sum_{i=1}^{n_2} \frac{A \left(1 - \frac{x_i}{\gamma}\right)}{2\sigma_2^2} \right) \left(\frac{1}{2\sigma_{\alpha_2}^2} + \sum_{i=1}^{n_2} \frac{\left(1 - \frac{x_i}{\gamma}\right)^2}{2\sigma_2^2} \right)^{-1}, \\ A &= y_i - x_i \left(\frac{\alpha_1 + \beta_1 \gamma}{\gamma} \right), \quad V_{\alpha_2} = 0.5 \left(\frac{1}{2\sigma_{\alpha_2}^2} + \sum_{i=1}^{n_2} \frac{\left(1 - \frac{x_i}{\gamma}\right)^2}{2\sigma_2^2} \right)^{-1}.\end{aligned}$$

$$\sigma_1^2 | \boldsymbol{\theta}_{-\sigma_1^2}, \mathbf{x}, \mathbf{y} \sim IGa \left(\frac{n_1}{2} + \rho_1, 0.5 \sum_{i=1}^{n_1} (y_i - \alpha_1 - \beta_1 x_i)^2 + \phi_1 \right). \quad (9.11)$$

$$\sigma_2^2 | \boldsymbol{\theta}_{-\sigma_2^2}, \mathbf{x}, \mathbf{y} \sim IGa \left(\frac{n_2}{2} + \rho_2, 0.5 \sum_{i=1}^{n_2} \left(y_i - \alpha_2 - x_i \left(\frac{\alpha_1 - \alpha_2}{\gamma} + \beta_1 \right) \right)^2 + \phi_2 \right). \quad (9.12)$$

In the above n_x denotes the length of vector x and θ_{-z} denotes the vector θ without the variable z . The posterior of the changepoint γ required a Metropolis-Hastings (M-H) update using a Gamma prior; the proposal kernels are outlined in the Results section.

9.2.2 Asphaltene nanoaggregation two-changepoint model with a Brownian bridge

We propose to model the mixing region using a diffusion process, namely the Brownian bridge defined as follows. Consider a standard Brownian motion, $W(t)$ defined as:

$$W(t)|W(0) = 0 \sim N(0, t), \quad t > 0. \quad (9.13)$$

A Brownian bridge $B(t)$ can be defined as a combination of $W(t)$ pinned to start and end at zero (Bhattacharya & Waymire, 1990; Mansuy & Yor, 2007):

$$B(t) = W(t) - \frac{t}{T}W(T), \quad 0 \leq t \leq T, \quad B(0) = B(T) = 0. \quad (9.14)$$

The expectation of $B(t)$ is zero $\forall t$ (Chow, 2009). Using (9.13) variance of $B(t)$ is derived as follows:

$$\begin{aligned} \text{Var}(B(t)) &= \text{Var}\left(W(t) - \frac{t}{T}W(T)\right) = \\ &= \text{Var}(W(t)) - 2\frac{t}{T}\text{Cov}(W(t), W(T)) + \frac{t^2}{T^2}\text{Var}(W(T)) = \\ &= t - 2\frac{t}{T}t + \frac{t^2}{T} = t\left(1 - \frac{t}{T}\right), \end{aligned} \quad (9.15)$$

using $\text{Cov}(W(t), W(s)) = \min(t, s)$. Variance of a Brownian bridge defined on the interval $t \in [0, 1]$ is given in (Bhattacharya & Waymire, 1990).

The M realisations of a Brownian bridge bridge,

$$B(t) = (b_{t_0}, b_{t_1}, \dots, b_T), \quad t_0 < t_1 < \dots < t_{M-1} = T, \quad (9.16)$$

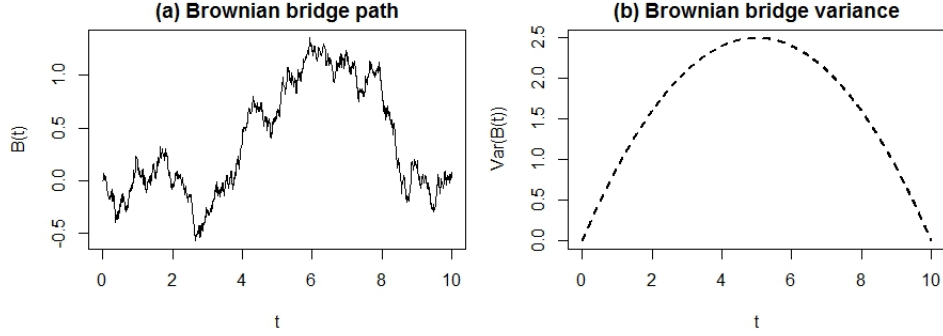


Figure 9.1: A simulated Brownian bridge path.

can be defined recursively for equidistant time intervals and for any end-points as follows (Durham & Gallant, 2002):

$$b_{t_i} = b_{t_{i-1}} + \frac{b_T - b_{t_{i-1}}}{T - t_{i-1}} \delta + \sigma \sqrt{\delta} W, \quad \delta = \frac{T - t_0}{M}, \quad W - \text{standard Brownian motion.} \quad (9.17)$$

The formalism (9.17) is modified to be suitable for non-equidistant t intervals as this is a feature of ultrasonic velocity data used in the present study

$$b_{t_i} = b_{t_{i-1}} + \frac{b_T - b_{t_{i-1}}}{T - t_{i-1}} \delta_i + \sigma \sqrt{\delta_i} W, \quad \delta_i = t_i - t_{i-1}, \quad W - \text{standard Brownian motion.} \quad (9.18)$$

For $B(t)$ to be a ‘true Brownian bridge’ σ must be constant (Durham & Gallant, 2002) which the author assumes to be satisfactory for the asphaltene model. Figure 9.1(a) illustrates a path of $B(t), t = 0, 0.01, \dots, 10$, plot (b) illustrates variance of the bridge as a function of time. Note that $Var(B(t))$ decreases towards end-points thus is convenient to model asphaltne aggregation. The likelihood function for the bridge may be derived as follows. Using (9.17), $B(t)$ has a normal probability density function

$$B(t_i) | B(t_{i-1}) = b_{t_{i-1}} \sim N \left(b_{t_{i-1}} + \frac{b_T - b_{t_{i-1}}}{T - t_{i-1}} \delta_i, \sigma^2 \delta_i \right), \quad \text{or equally,} \\ B(t_i) - B(t_{i-1}) \sim N \left(\frac{b_T - b_{t_{i-1}}}{T - t_{i-1}} \delta_i, \sigma^2 \delta_i \right), \quad \delta_i = t_i - t_{i-1}, \quad (9.19)$$

and a likelihood function for $B(t_i)$

$$L(B(t) | b_0, b_T \sigma^2, t) = \prod_{i=2}^M \frac{1}{\sqrt{2\pi\sigma^2\delta_i}} \exp \left\{ -\frac{(b_{t_i} - b_{t_{i-1}} - \mu_{t_i})^2}{2\sigma^2\delta_i} \right\}, \\ \mu_{t_i} = \frac{b_T - b_{t_{i-1}}}{T - t_{i-1}} \delta_i. \quad (9.20)$$

The dependence of sound velocity y on asphaltene concentration x is then formulated as follows:

$$y_i = \begin{cases} \alpha_1 + \beta_1 x_i + \varepsilon_{1,i}, & \varepsilon_{1,i} \sim N(0, \sigma_1^2), & x_i \leq \gamma_1, \\ y_{i-1} + \frac{\alpha_2 + \beta_2 \gamma_2 - y_{i-1}}{\gamma_2 - x_{i-1}} \delta_i + \kappa \sqrt{\delta_i} W, & W \sim N(0, 1), & \gamma_1 < x_i < \gamma_2, \\ \alpha_2 + \beta_2 x_i + \varepsilon_{2,i}, & \varepsilon_{2,i} \sim N(0, \sigma_2^2), & x_i \geq \gamma_2. \end{cases} \quad (9.21)$$

In Equation (9.21), $\{\varepsilon_{j,i}, l = 1, 2\}$, is the regression residual and κ^2 is the scale of the bridge variance. Equation (9.21) implies that the dependence of the speed of sound on asphaltene concentration is described by a linear regression in monomeric and aggregated regions and a Brownian bridge pinned to start at $\{x, y\} = \{\gamma_1, \alpha_1 + \beta_1 \gamma_1\}$ and end at $\{x, y\} = \{\gamma_2, \alpha_2 + \beta_2 \gamma_2\}$ to describe the mixing region. The model (9.21) results in the following likelihood.

$$\begin{aligned} L(\boldsymbol{\theta} | \mathbf{x}, \mathbf{y}) &= \prod_{i=1}^{n_1} \frac{1}{\sqrt{(2\pi\sigma_1^2)}} \exp \left\{ -\frac{(y_i - \alpha_1 - \beta_1 x_i)^2}{2\sigma_1^2} \right\} \times \\ &\times \prod_{i=2}^{n_2} \frac{1}{\sqrt{(2\pi\kappa^2\delta_i)}} \exp \left\{ -\frac{\left(y_i - y_{i-1} - \frac{\alpha_2 + \beta_2 \gamma_2 - y_{i-1}}{\gamma_2 - x_{i-1}} \delta_i \right)^2}{2\kappa^2\delta_i} \right\} \times \\ &\times \prod_{i=1}^{n_3} \frac{1}{\sqrt{(2\pi\sigma_2^2)}} \exp \left\{ -\frac{(y_i - \alpha_2 - \beta_2 x_i)^2}{2\sigma_2^2} \right\}, \quad n_j = \text{number of entries in vector } j, \end{aligned} \quad (9.22)$$

where $\boldsymbol{\theta} = (\alpha_1, \alpha_2, \beta_1, \beta_2, \gamma_1, \gamma_2, \sigma_1^2, \sigma_2^2, \kappa^2)$. The lengths of $\{\mathbf{x} : \mathbf{x} < \gamma_1\}$, $\{\mathbf{x} : \gamma_1 \leq \mathbf{x} \leq \gamma_2\}$ and $\{\mathbf{x} : \mathbf{x} > \gamma_2\}$ are n_1, n_2 and n_3 respectively. The parameter priors are equivalent to those in (9.7). Additionally,

$$\beta_2 \sim N(b_2, \sigma_{\beta_2}^2), \quad \kappa^2 \sim IGa(\rho, \phi). \quad (9.23)$$

The marginal posteriors of $\boldsymbol{\theta}_{-\{\gamma_1, \gamma_2\}}$ were estimated using a Gibbs sampler. Metropolis-Hastings (M-H) updates were required for γ_1 and γ_2 as their marginal posteriors are unknown and their proposal kernels are outlined in the next section. The semi-conjugate conditional posterior distributions for the two-changepoint model are as follows.

$$\alpha_1 | \boldsymbol{\theta}_{-\alpha_1}, \mathbf{x}, \mathbf{y} \sim N(AB^{-1}, 0.5B^{-1}), \quad (9.24)$$

$$A = \left(\frac{a_1}{2\sigma_{\alpha_1}^2} + \sum_{i=1}^{n_1} \frac{y_i - \beta_1 x_i}{2\sigma_1^2} \right), B = \left(\frac{n_1}{2\sigma_1^2} + \frac{1}{2\sigma_{\alpha_1}^2} \right).$$

$$\beta_1 | \boldsymbol{\theta}_{-\beta_1}, \mathbf{x}, \mathbf{y} \sim N(AB^{-1}, 0.5B^{-1}), \quad (9.25)$$

$$A = \left(\sum_{i=1}^{n_1} \frac{x_i(y_i - \alpha_1)}{2\sigma_1^2} + \frac{b_1}{2\sigma_{\beta_1}^2} \right), B = \left(\sum_{i=1}^{n_1} \frac{x_i^2}{2\sigma_1^2} + \frac{1}{2\sigma_{\beta_1}^2} \right).$$

$$\sigma_1^2 | \boldsymbol{\theta}_{-\sigma_1^2}, \mathbf{x}, \mathbf{y} \sim IGa \left(\frac{n_1}{2} + \rho_1, 0.5 \sum_{i=1}^{n_1} (y_i - \alpha_1 - \beta_1 x_i)^2 + \phi_1 \right). \quad (9.26)$$

$$\alpha_2 | \boldsymbol{\theta}_{-\alpha_1}, \mathbf{x}, \mathbf{y} \sim N(M_{\alpha_2}, V_{\alpha_2}), \quad (9.27)$$

$$M_{\alpha_2} = \left(\sum_{i=2}^{n_2} \frac{AB}{2\kappa^2 \delta_i} + \frac{a_2}{2\sigma_{\alpha_2}^2} + \sum_{i=1}^{n_3} \frac{y_i - \beta_2 x_i}{2\sigma_2^2} \right) \left(\sum_{i=2}^{n_2} \frac{B^2}{2\kappa^2 \delta_i} + \frac{1}{2\sigma_{\alpha_2}^2} + \frac{n_3}{2\sigma_2^2} \right)^{-1},$$

$$V_{\alpha_2} = 0.5 \left(\sum_{i=2}^{n_2} \frac{B^2}{2\kappa^2 \delta_i} + \frac{1}{2\sigma_{\alpha_2}^2} + \frac{n_3}{2\sigma_2^2} \right)^{-1},$$

$$A = y_i - y_{i-1} - \frac{\beta_2 \gamma_2 - y_{i-1}}{\gamma_2 - x_{i-1}} \delta_i, \quad B = \frac{\delta_i}{\gamma_2 - x_{i-1}}.$$

$$\beta_2 | \boldsymbol{\theta}_{-\beta_2}, \mathbf{x}, \mathbf{y} \sim N(M_{\beta_2}, V_{\beta_2}), \quad (9.28)$$

$$M_{\beta_2} = \left(\sum_{i=2}^{n_2} \frac{AB}{2\kappa^2 \delta_i} + \sum_{i=1}^{n_3} \frac{x_i(y_i - \alpha_2)}{2\sigma_2^2} + \frac{b_2}{2\sigma_{\beta_2}^2} \right) \left(\sum_{i=2}^{n_2} \frac{B^2}{2\kappa^2 \delta_i} + \sum_{i=1}^{n_3} \frac{x_i^2}{2\sigma_2^2} + \frac{1}{2\sigma_{\beta_2}^2} \right)^{-1},$$

$$V_{\beta_2} = 0.5 \left(\sum_{i=2}^{n_2} \frac{B^2}{2\kappa^2 \delta_i} + \sum_{i=1}^{n_3} \frac{x_i^2}{2\sigma_2^2} + \frac{1}{2\sigma_{\beta_2}^2} \right)^{-1},$$

$$A = y_i - y_{i-1} - \frac{\alpha_2 - y_{i-1}}{\gamma_2 - x_{i-1}} \delta_i, \quad B = \frac{\gamma_2 \delta_i}{\gamma_2 - x_{i-1}}.$$

$$\sigma_2^2 | \boldsymbol{\theta}_{-\sigma_2^2}, \mathbf{x}, \mathbf{y} \sim IGa \left(\frac{n_3}{2} + \rho_2, 0.5 \sum_{i=1}^{n_3} (y_i - \alpha_2 - \beta_2 x_i)^2 + \phi_2 \right). \quad (9.29)$$

$$\kappa^2 | \boldsymbol{\theta}_{-\kappa^2}, \mathbf{x}, \mathbf{y} \sim IGa \left(\frac{n_2}{2} + \rho, 0.5 \sum_{i=2}^{n_2} \frac{1}{\delta_i} \left(y_i - y_{i-1} - \frac{\alpha_2 + \beta_2 \gamma_2 - y_{i-1}}{\gamma_2 - x_{i-1}} \delta_i \right)^2 + \phi \right). \quad (9.30)$$

In the above equations n_x denotes the length of vector x and $\boldsymbol{\theta}_{-z}$ denotes the vector $\boldsymbol{\theta}$ without the variable z . To estimate asphaltene aggregation point/region, MCMC samplers were written in R statistical software (R Core Team, 2015).

Results and Discussion

Chapter 10. Geochemical Characterisation of Petroleum Samples

This chapter presents maturity, source and biodegradation assessment of the petroleum samples E1-E4. Bar a number of exemplars, partial mass chromatograms used in this work are provided in the Appendix A.

Four petroleum samples have been obtained from an industrial contact. The samples have originated from the La Luna formation, Tithonian type 2 source rock (marl), the charge is likely to be mixed/hybridised. The samples E1 and E2 are from Venezuela and E3 and E4 are from the Gulf of Mexico. Section 10.2 will perform additional assessment of the sample source using biomarker ratios. The weights of the maltene and asphaltene fractions are summarised in Figure 10.1.

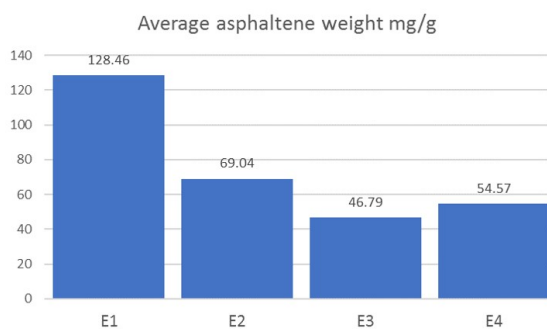


Figure 10.1: Weights of asphaltene fractions. The numbers represent 3-replicate averages, except the E1 asphaltene weight which had two replicates, the bars indicate confidence intervals based on standard deviation.

10.1 Maturity Assessment of the Sample Oils

Table 10.1 lists the ratios used for the source and maturity estimation of the petroleum samples E1-E4, Figure 10.2 illustrates the estimated ratio values. For E3, some of the ratios are absent due to the high biodegradation of this sample (Section 10.3). All of the ratios in this section are in an abbreviated format and the positions of

isomerisation in biomarkers are not indicated. For the full biomarker nomenclature, refer to Chapter 5.

In general, all of the samples are estimated to be mature/in the oil-generating window. Plot (a) shows ratios based on the even-odd predominance of the *n*-alkanes, corresponding to Equations (10.1), (10.3) and (10.4), that are close to unity ± 0.1 , suggesting thermal maturity (Bray & Evans, 1961; Scalan & Smith, 1970). In plot (b), the values of MPI, MPI1, and DMNI, Equations (10.5), (10.6) and (10.7), are within ca. 0.6, 0.7 and < 2.5 respectively, suggesting that the organic matter has entered the oil generation window (Radke & Welte, 1983; Alexander *et al.*, 1985). The DMNI ratio, should be used with caution as alkylated naphthalenes are more susceptible to biodegradation than other aromatic biomarkers (Alexander *et al.*, 1985), e.g. aromatic steroids (Wenger *et al.*, 2002). Alexander *et al.* (1985) reported that TMNI ratio values of ca. 0.5 or above indicate thermal maturity, which is the case for all samples investigated at present. The *homo*-hopane isomerisation indices, Equation (10.9), are also indicating thermal maturity as the values for C_{31,32} compounds are within 0.57 and 0.62 (Seifert *et al.*, 1980). In plot (d), the C₂₉ $\beta\alpha$ /C₂₉ $\alpha\beta$ hopane ratios, Equation (10.10), are all < 0.15 , again indicating thermal maturity (Mackenzie *et al.*, 1980; Seifert *et al.*, 1980). The Ts/Tm ratio is low for samples E1 and E2 and is somewhat higher for E3 and E4, indicating that all of the oils are immature. Although it is presumed that during catagenesis Tm is less stable than Ts, thus higher values of the ratio would indicate a greater maturity, it is also not known whether any conversion of Tm to Ts occurs (Peters *et al.*, 2005c). The Ts/Tm values also depend on the source input, therefore this indicator should be used with caution and applied to samples with common organic source rocks (Moldowan & Fago, 1986). Both sterane ratios in plot (f) indicate thermal maturation. The C₂₉ $\alpha\alpha\alpha$ S/(S+R), Equation (10.11), is at ca. 0.5 (Seifert & Moldowan, 1986), and the C₂₉ $\alpha\beta\beta$ /($\alpha\beta\beta + \alpha\alpha\alpha$), Equation (10.12), is at ca. 0.6 which is below marginally the reported maturity equilibrium of 0.67-0.7 (Seifert & Moldowan, 1986). The aromatic ratios, however, consistently suggest a low maturity of the oil samples. It is presumed that conversion of monoaromatic to triaromatic steroids, Equation (10.13), occurs during maturation through the loss of a methyl group at the A/B ring junction in the MAS (Mackenzie *et al.*, 1981; Peters *et al.*, 2005c). Values above ca. 0.5 were reported to correspond to greater burial depths (Mackenzie *et al.*, 1981; Mackenzie, 1984). The ratio can potentially be affected by expulsion as the TAS are preferentially retained in the source bitumen (Hoffmann *et al.*, 1984a; Peters *et al.*,

1990). Based on this ratio, plot (f), E1 and E2 are low in maturity and E3 and E4 are in the oil generation window. Overall, the maturity ratios suggest that the four samples are mature, except those based on aromatic biomarkers which for E1 and E2 suggest otherwise, this conflict may be due to the aforementioned hybridisation.

Name	Formula
Carbon preference index	$\text{CPI} = \frac{1}{2} \left(\frac{\sum_{i=25,27,\dots,33} C_i}{\sum_{i=24,26,\dots,32} C_i} + \frac{\sum_{i=25,27,\dots,33} C_i}{\sum_{i=26,28,\dots,34} C_i} \right), \quad (10.1)$
	$\text{CPI}_1 = 2 \frac{C_{23}+25+27+29}{C_{22} + 2C_{24}+26+28 + C_{30}} \quad (10.2)$
Odd-even predominance	$\text{OEP}_1 = \frac{C_{21} + 6C_{23} + C_{25}}{4C_{22} + 4C_{24}}, \quad (10.3)$
	$\text{OEP}_2 = \frac{C_{25} + 6C_{27} + C_{29}}{4C_{26} + 4C_{28}} \quad (10.4)$
Methylphenanthrene index	$\text{MPI} = \frac{1.5(2\text{-MP} + 3\text{-MP})}{\text{P} + 1\text{-MP} + 9\text{-MP}}, \quad (10.5)$
	$\text{MPI}_1 = \frac{1.89(2\text{-MP} + 3\text{-MP})}{\text{P} + 1.26(1\text{-MP} + 9\text{-MP})} \quad (10.6)$
Dimethyl- and trimethylnaphthalene index	$\text{DMNI} = \frac{2, 6\text{-DMN} + 2, 7\text{-DMN}}{1, 5\text{-DMN}}, \quad (10.7)$
	$\text{TMNI} = \frac{2, 3, 6\text{-TMN}}{1, 4, 6\text{-TMN} + 1, 3, 5\text{-TMN}} \quad (10.8)$
Hopane isomerisation ratio	$\frac{C_i \alpha\beta S}{C_i \alpha\beta S + C_i \alpha\beta R} \quad i = 31, 32, \dots 35 \quad (10.9)$
Hopane/moretane ratio	$\frac{C_{29} \beta\alpha\text{-hopane}}{C_{29} \alpha\beta\text{-hopane}} \quad (10.10)$

Sterane isomrisation ratio 1	$\frac{C_{29} \alpha\alpha\alpha 20S}{C_{29} \alpha\alpha\alpha 20S + C_{29} \alpha\alpha\alpha 20R}$	(10.11)
---------------------------------	---	---------

Sterane isomerisation ratio 2	$\frac{C_{29} \alpha\beta\beta 20 S + R}{(C_{29} \alpha\beta\beta 20 S + R) + (C_{29} \alpha\alpha\alpha 20 S + R)}$	(10.12)
----------------------------------	--	---------

Mono/triaromatic steroid ratio	$\frac{TAS}{MAS + TAS} LC = \frac{C_{26+27+28} TAS}{C_{26+27+28} TAS + C_{27+28+29} MAS}$	(10.13)
-----------------------------------	---	---------

Short-chain/long- chain AS ratios	$a = \frac{C_{21+22}MAS}{C_{21+22+27+28+29}MAS},$	(10.14)
--------------------------------------	---	---------

	$b = \frac{C_{20+21}TAS}{C_{20+21+26+27+28}TAS}$	(10.15)
--	--	---------

Table 10.1: Ratios used in petroleum maturity estimation. In (10.14) and (10.15) AS refers to aromatic steroids. References for ratios and full compound names can be found in Chapter 5.1.

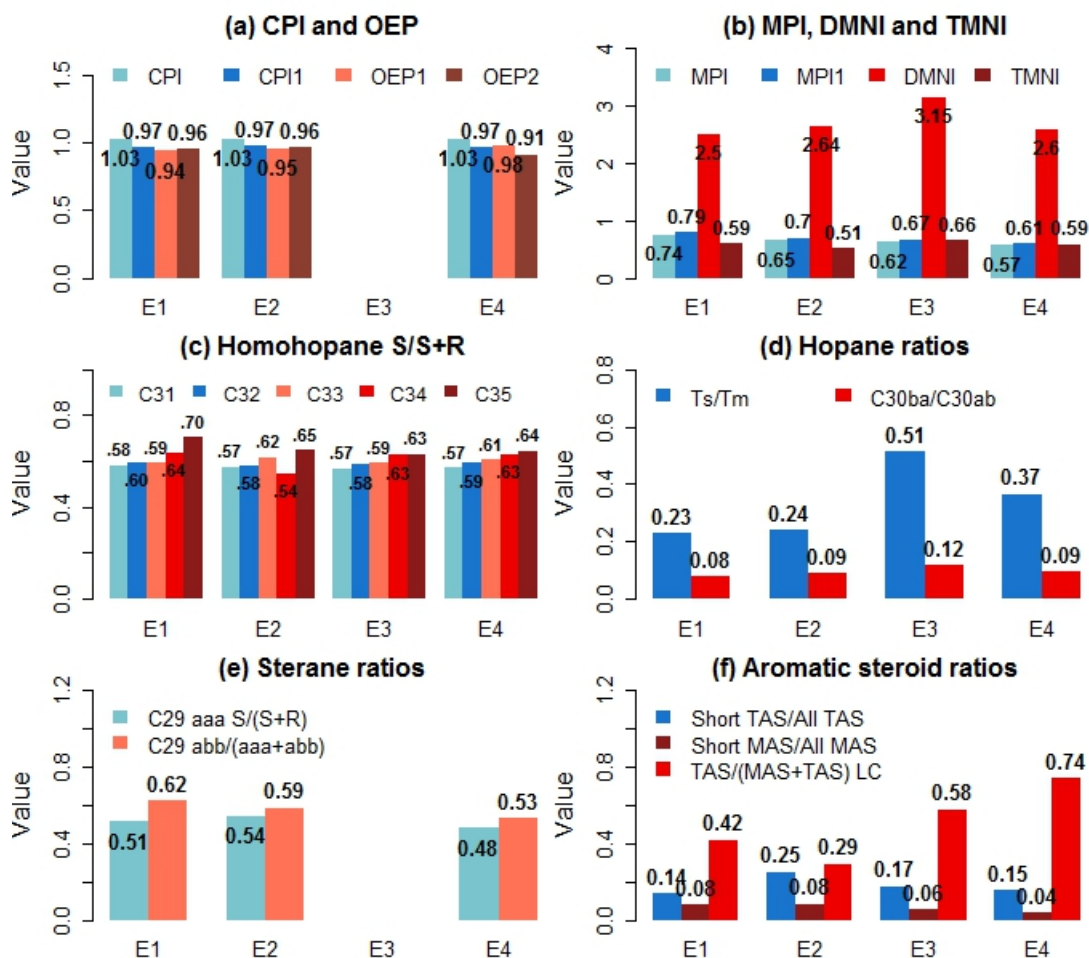


Figure 10.2: Ratios used in the maturity estimation of petroleum samples.

10.2 Source Assessment of the Sample Oils

Figure 10.3 illustrates the source ratios calculated for the deasphalted petroleum samples E1-E4. Noteworthy, for the E3 and E4 samples, their extent of biodegradation (described in Section 10.3) has limited the reliability of the source assessment using the maltene fractions; some of the ratios for E3 are absent due to the removal of biomarkers.

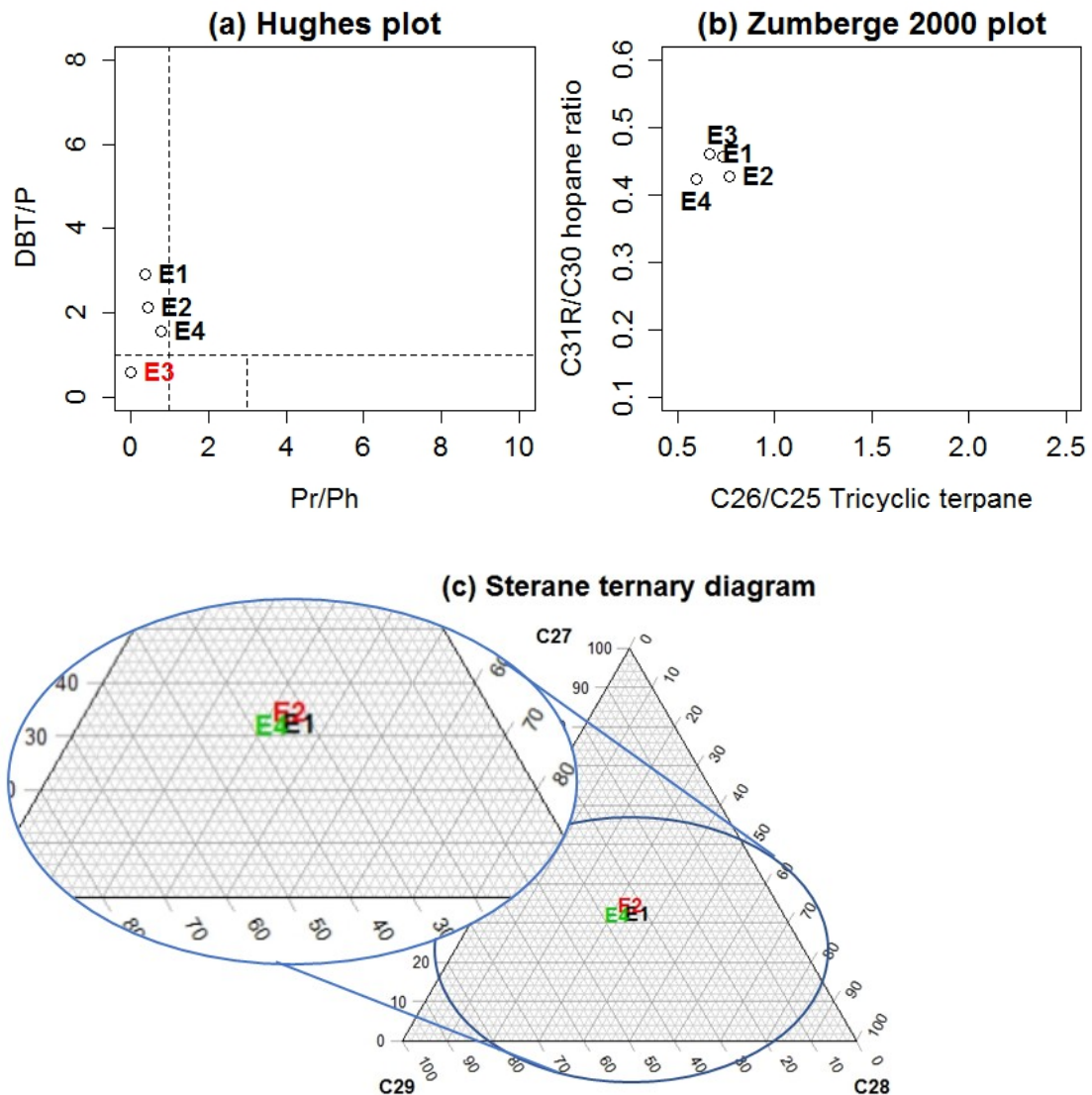


Figure 10.3: Relations used in petroleum source estimation. In plot (a) E3 is marked in red as the Pr/Ph ratio could not be calculated due to a high biodegradation of the sample. The key to interpretation of the plots is in Figure 5.1

A Hughes plot suggests the source of the samples is E1, E2 and E4 marine carbonate/marine marl/lacustrine sulfate-rich (zone 1B) and in zone 1B, whereas E3 is lacustrine sulfate-poor (Zone 2) (Figure 10.3(a)). The plot (b) located all four samples on the intersection of marine shale, marine carbonate and marl. The sterane ternary diagram also located them on the intersection of marine carbonate (predom-

inantly) and marine shale, thus further clarification is needed. Plot 10.4 illustrates source assessment ratios. The Pr/Ph values for E1, E2 and E4 are all < 1 indicative of anoxic source rock conditions (Didyk *et al.*, 1978) and, together with Ph/*n*-C₁₈ values of < 0.3 (Figure 10.2) suggesting a marine carbonate source rock (Peters *et al.*, 2005h, p.536). The C₃₁17 α ,21 β -30-*homo*-hopane 22R/C₃₀17 α ,21 β -hopane (C₃₁R/C₃₀ hopane) values in the Zumberge plot (Figure 10.3(b)) are > 0.25 for all samples ruling out a lacustrine source. The C₂₉17 α ,21 β -30-*nor*-hopane/C₃₀17 α ,21 β -hopane ratio (C₂₉/C₃₀ hop) is > 0.6 for all samples and together with the C₃₄ 17 α ,21 β -30,31,32,33-*tetra*homo-hopane 22S/C₃₅ 17 α ,21 β -30,31,32,33,34-*penta*homo-hopane 22S homohopane ratio (C₃₄/C₃₅ 22S hop) > 0.8 it suggests a marine carbonate source rock (Peters *et al.*, 2005h, p.567), although according to (Fan *et al.*, 1987; Ten Haven & Rullkötter, 1988) a C₂₉ 30-*nor*-hopane/C₃₀ regular hopane ratio of < 1 would suggest a marine shale source for E3 and E4. The gammacerane index (GI₁, expressed in %) should be interpreted with caution as in the present samples it coeluted with other compounds (Figures 10.6 and A.4). A high GI₁ (10-2%) has been reported to negatively correlated with Pr/Ph (1.6-2.6) indicating a lacustrine source (Peters *et al.*, 2005h, p.575). In the present samples, the GI₁ values are below 3, and their Pr/Ph values are significantly below 1.6, thus a lacustrine source is once again ruled out. Finally, the C₃₅/C₃₁₋₃₅ 22 S+R *homo*-hopane ratio (full nomenclature in Table 10.2) is indicative of the redox potential during deposition, whereby high ratio values (e.g. $> 7\%$) would indicate a marine carbonate, possibly hypersaline (Moldowan *et al.*, 1986b), deposition with little/no available oxygen (Peters & Moldowan, 1991). The ratio values estimated for E1-E4 are ca. 0.07 (7%) can still be indicative of a marine carbonate source. This, however, is in contrast to examples shown in Peters & Moldowan (1991), where the C₃₅ *homo*-hopanes are clearly elevated. To conclude, the majority of ratios indicate a marine carbonate source for the four oils.

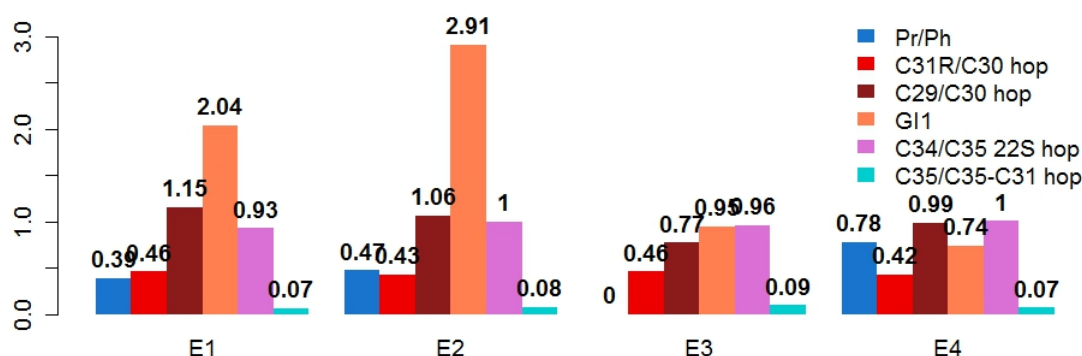


Figure 10.4: Ratios used in petroleum source estimation.

10.3 Biodegradation Assessment of the Sample Oils

Biodegradation of hydrocarbons results in the preferential removal of saturated and aromatic compounds (Milner *et al.*, 1977*b*; Peters *et al.*, 2005*a*). Biodegradation of the deasphalted petroleum samples will be estimated using the petroleum biodegradation scale by Wenger *et al.* (2002), which estimates the extent of biodegradation on levels (LVL) 1-10 (Figure 4.3). Saturated and aromatic compound classes and corresponding mass spectrometric assignments are analysed in order to suggest the LVL of biodegradation, although some of the samples illustrate that the biodegradation order is quasi-sequential (Wenger *et al.*, 2002; Peters *et al.*, 2005*a*). The sample E1 has very few signs of biodegradation. The m/z 85 mass chromatogram in Figure 10.5(a), shows a homologous series of n -alkanes from which only compounds $C_{<10}$ are absent. Consistently, the $Pr/n-C_{17}$ and $Ph/n-C_{18}$ are $\ll 1$, Figure 10.2 (g), suggesting that the biodegradation of n -alkanes has not been extensive. Sterane susceptibility to biodegradation is $5\alpha, 14\alpha, 17\alpha 20R \gg 5\alpha, 14\beta, 17\beta 20R \geq 5\alpha, 14\beta, 17\beta 20S \geq 5\alpha, 14\alpha, 17\alpha 20S \gg$ diasteranes, and $C_{27} > C_{28} > C_{29} > C_{30}$ (Seifert & Moldowan, 1979; McKirdy *et al.*, 1983; Seifert *et al.*, 1984; Peters *et al.*, 2005*a*). Figure 10.7 (a) illustrates that the C_{27} steranes are present and well-resolved, indicating little signs of biodegradation. The diasteranes are in low abundance (plot (b)), except a peak at 48 minutes whose mass spectrum had a strong 259 signal A.6 (a), but was unidentified. As the C_{27} diasteranes are in low abundance with the regular steranes unaltered (Seifert & Moldowan, 1979; McKirdy *et al.*, 1983), it is concluded that the sample is naturally low in the diasterane class. As mentioned in Section 10.3, 25-*nor*-hopanes are assumed to result from a loss of a methyl group at C-10 in normal hopanes (Rullkötter & Wendisch, 1982), thus

their abundance over the normal hopanes is indicative of biological activity. In general, the distribution of the 25-*nor*-hopanes can be matched to hopane series less a C number (Peters *et al.*, 2005a). The problems in identifying the two compound classes are discussed in Section 10.3 as well. Given their absence due to biological input, the 25-*nor*-hopanes are absent where the hopanes are more bioresistant than the steranes (Peters *et al.*, 2005a). The 25-*nor*-hopanes can also result due to oil mixing in reservoir (Volkman *et al.*, 1983). In E1, the abundance of 25-*nor*-hopanes is significantly below that of hopanes, Figure 10.6 (a) and A.5 (a), except the strong 17 α ,21 β -30-*nor*-hopane. Similarly to steranes, the 22*S* homohopane epimers are more resistant to biodegradation than the 22*R* configuration which is observed in Figure 10.6 (a). The aromatic markers are reported to be highly resistant to microbial alteration (Connan, 1984; Peters *et al.*, 2005a), and the C₂₀₋₂₁ triaromatic steroids (TAS) are removed first (Wardroper *et al.*, 1984). Such compounds, including naphthalenes (Figure A.10), phenanthrenes (Figure A.14), and aromatic steroids (Figure 10.8) appear unaltered. Therefore, E1 is classified as LVL 1 biodegraded. The biodegradation extent of E2 is very slightly greater than that of E1 (thus an *m/z* 177 plot is omitted for this sample), indicated by the removal of *n*-C₁₀ from the *n*-alkanes, Figure A.1 (b). The remaining compound classes have very similar distributions to E1, except the lower abundance of the monoaromatic steroids (Figure A.18 (a)). As the MAS are less susceptible to biodegradation than TAS, their low abundance is likely to be due to reasons other than biodegradation, which can include water-washing. Therefore, E2 is is classed as LVL 1-2 biodegraded. In contrast, E3 illustrates a complete removal of the *n*-alkanes, Figure A.2 (a), suggesting a LVL < 4 alteration. The distribution of hopanes (Figure A.4 (a)) is similar to those in E1 and E2, including the relative isomeric abundance of the homohopane compounds, except the removal of the C₂₈₋₂₉ tricyclic terpanes. The latter is unlikely to be due to microbial alteration, as tricyclic terpanes were reported be more resistant to biodegradation than hopanes (Reed, 1977; Seifert & Moldowan, 1979). However, the distribution of compounds in the *m/z* 177 chromatogram is greater than in the remaining samples, Figure A.5 (b) and A.6 (b). The complete selective removal of the C₂₇ 5 α ,14 α ,17 α 20*R* steranes (Peters *et al.*, 2005a; Seifert & Moldowan, 1979; McKirdy *et al.*, 1983; Seifert *et al.*, 1984) and the abundance of diasteranes over regular steranes is indicative of biodegradation (Seifert & Moldowan, 1979; McKirdy *et al.*, 1983), Figure A.8. However, the aromatic markers, including the naphthalenes (Figure A.12), phenanthrenes (Figure A.16) and aromatic steroids

(Figure A.19) are similar to the distributions in the non-degraded E1. Based on the compound distribution in the saturate fraction, namely the complete removal of *n*-alkanes, partial formation of the 25-*nor*-hopanes and the near-complete removal of steranes, E3 would be assigned a biodegradation LVL 5-7. Noteworthy, if the aromatic fraction would be taken into account, the extent of biodegradation would be very limited, i.e. LVL 2 on the Wenger *et al.* (2002) scale. Finally, E4 has slight signs of biodegradation with a slight removal of the *n*-C₇₋₁₀ (Figure A.2 (b)), high Pr/*n*-C₁₇ and Ph/*n*-C₁₈ ratios (Figure 10.2 (g)) and a low abundance of the 25-*nor*-hopanes compared to hopanes (Figure A.4(a)). The abundance of sterane compounds (Figure A.9), is lower than in E1 and E2 with the C₂₈ compounds in a much lower abundance. However, the isomeric signature suggests that due to the higher 5 α , 14 α , 17 α 20*R* peaks than 5 α , 14 α , 17 α 20*S*, the low abundance is not due to biodegradation. Aromatic markers are well-resolved (Figures A.13, A.17 and A.20). Thus, E4 is suggested to be LVL 2-3 degraded due to the slight removal of steranes.

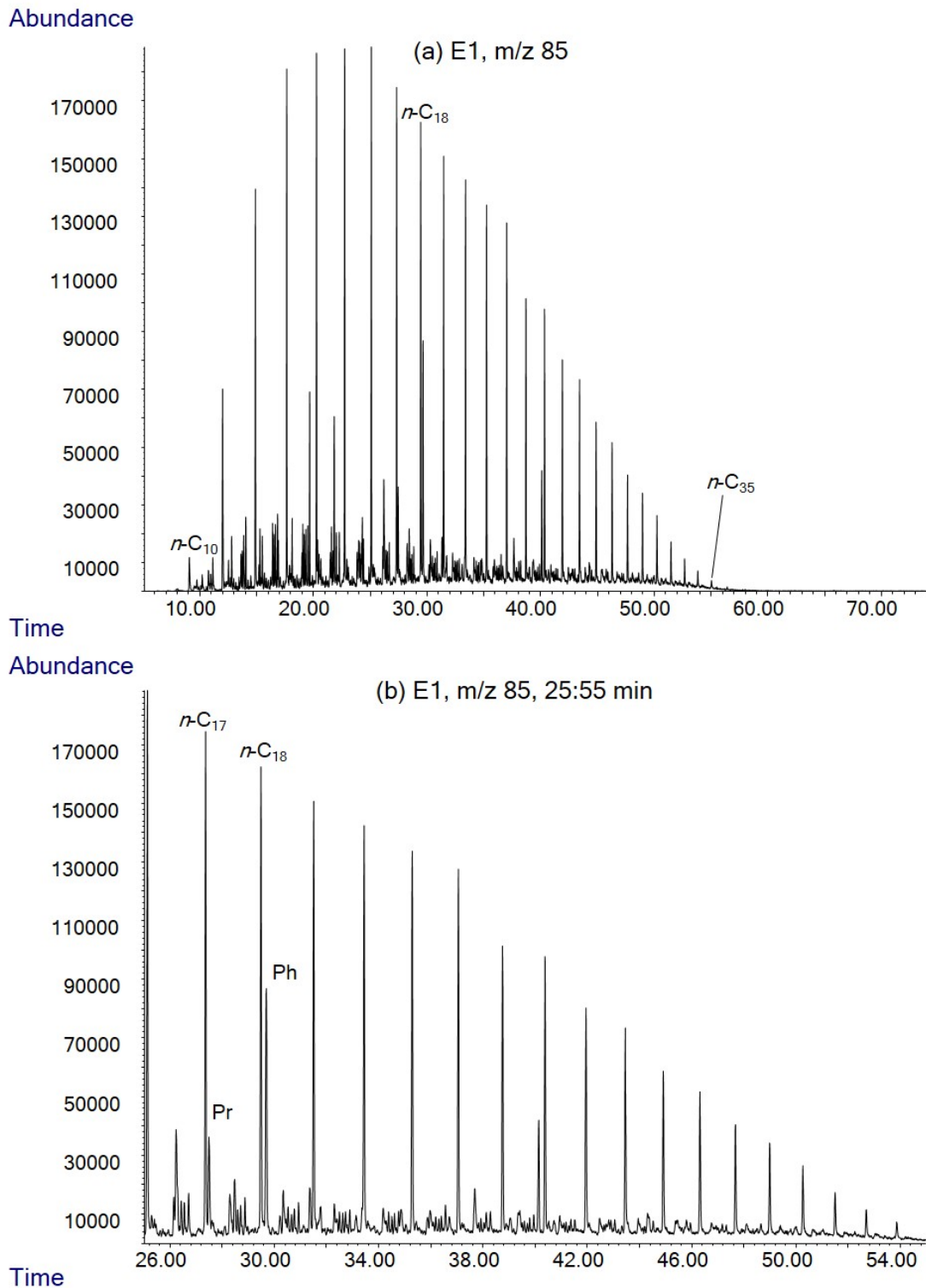


Figure 10.5: Partial mass chromatograms of the E1 aliphatic fraction, showing the distributions of *n*-alkanes. Labels are listed in Table 10.2.

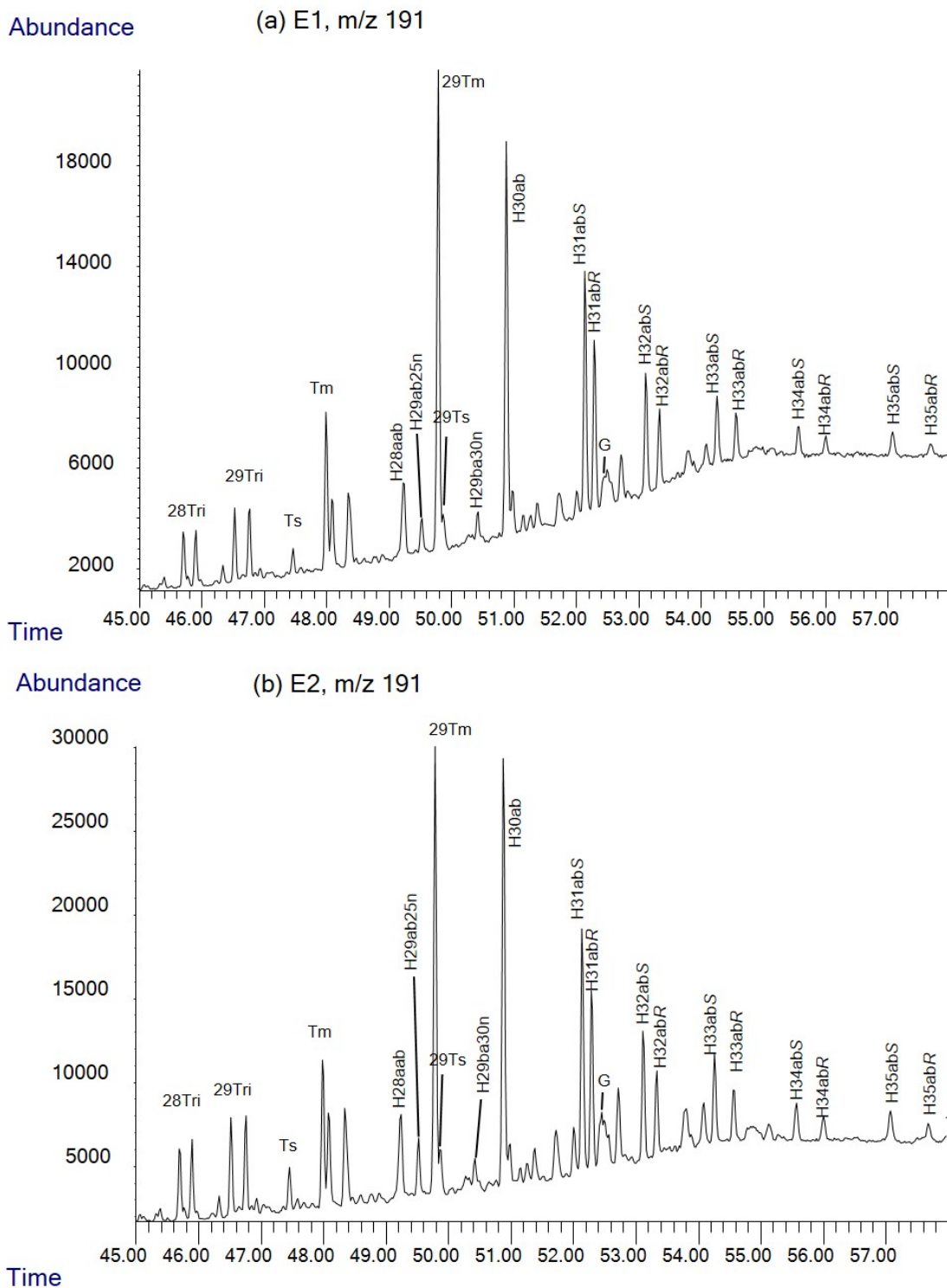


Figure 10.6: Partial m/z 191 mass chromatograms of the E1 and E2 aliphatic fraction. Labels are listed in Table 10.2.

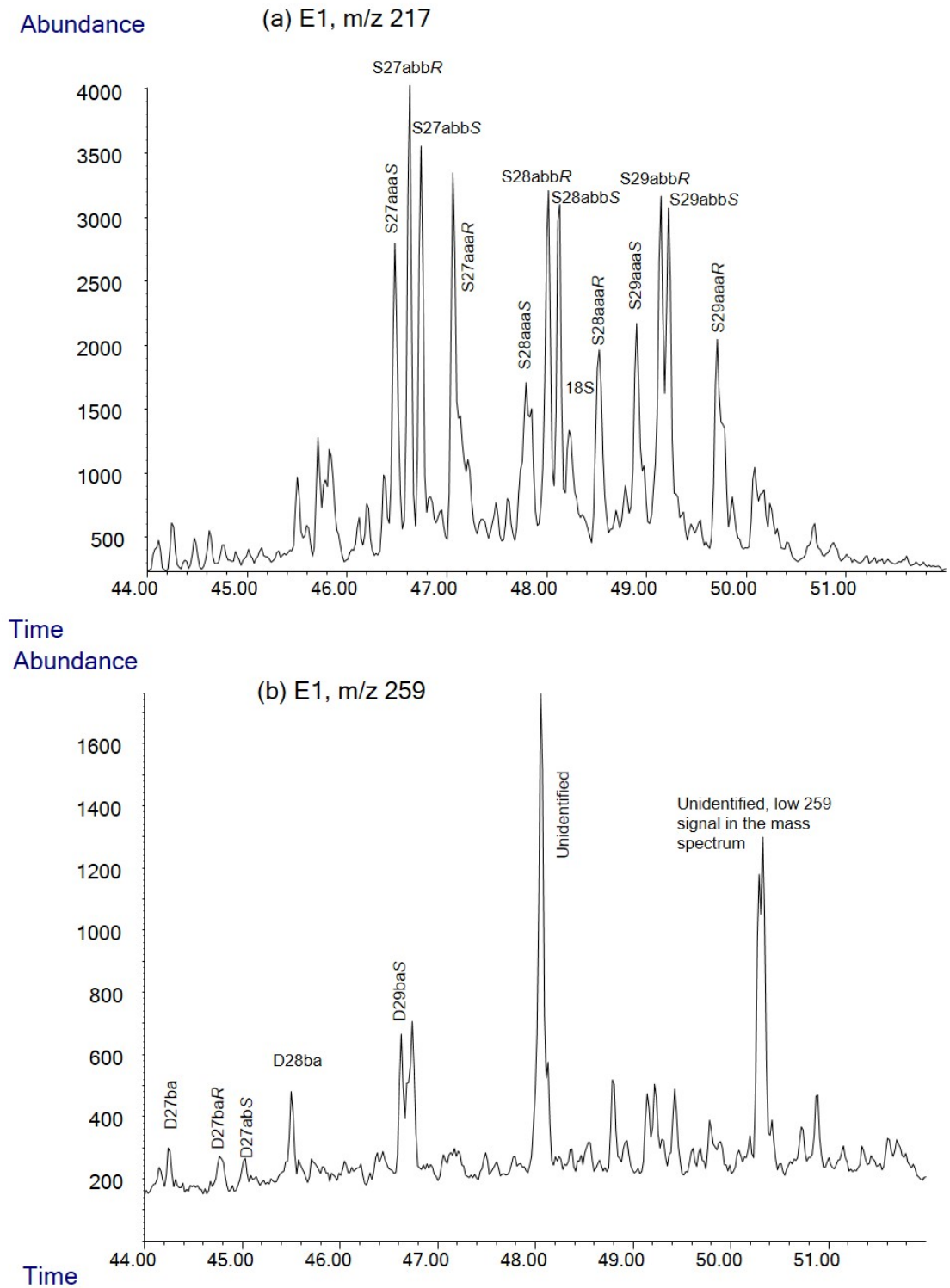


Figure 10.7: Partial mass chromatograms of the E1 aliphatic fraction, showing sterane biomarkers. Labels are listed in Table 10.2.

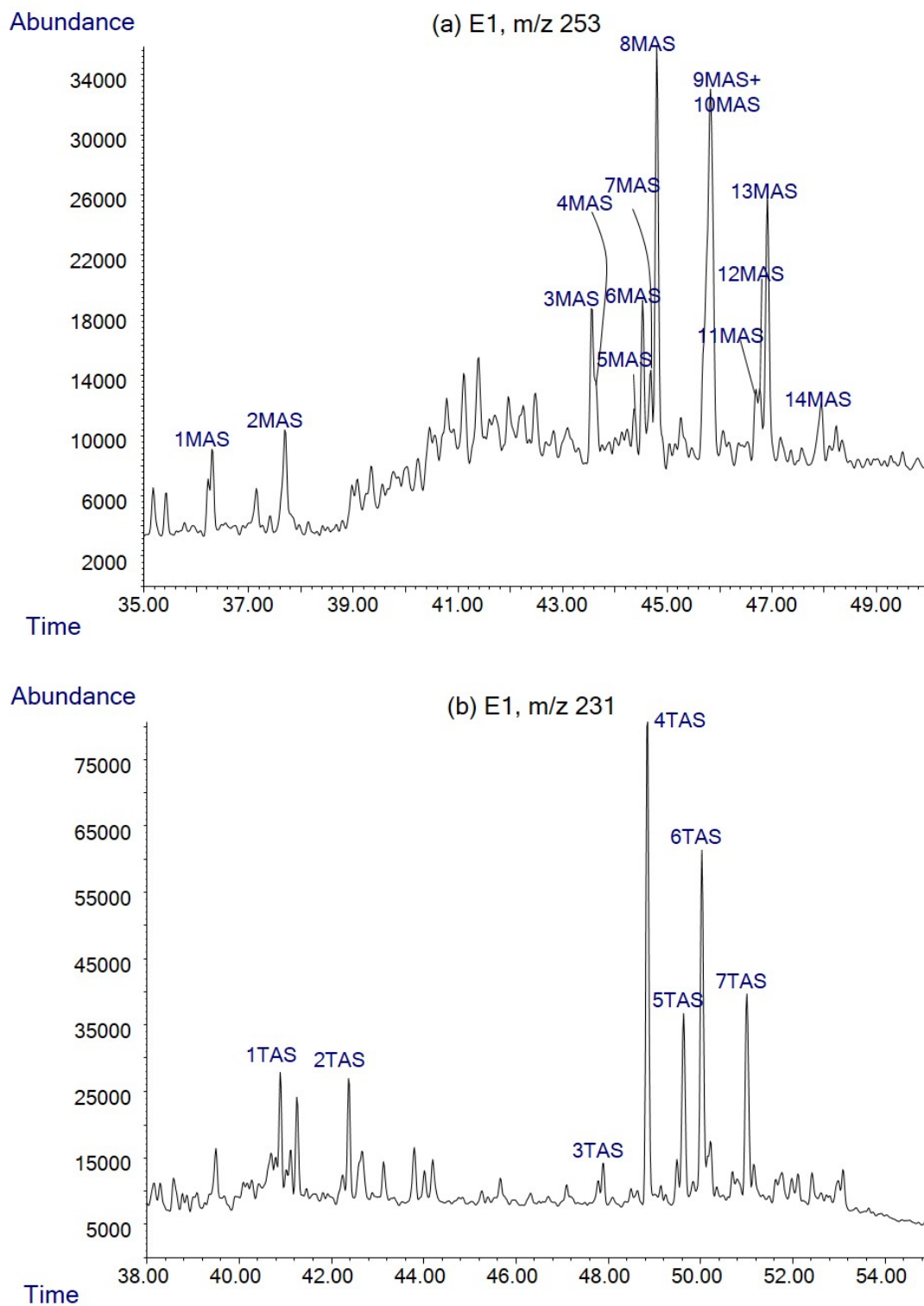


Figure 10.8: Partial mass chromatograms of the E1 aromatic fraction, showing aromatic steroid biomarkers. Labels are listed in Table 10.3.

Label	Name	Formula	Reference
nC_{17}	Normal heptadecane	$C_{17}H_{36}$	(1)
Pr	2,6,10,14-tetramethylpentadecane	$C_{19}H_{40}$	(1)
nC_{18}	Normal octadecane	$C_{18}H_{38}$	(1)
Ph	2,6,10,14-tetramethylhexadecane	$C_{20}H_{42}$	(1)
HDCH	Heptadecylcyclohexane	$C_{23}H_{46}$	(1)
$nTri$	C_n tricyclic terpane, $n = 19, 20, \dots 25$	$C_n H_{2n-4}$	(2)
24Tetra	C_{24} tetracyclic terpane	$C_{24}H_{42}$	(2)
26Tri	C_{26} ($S+R$) tricyclic terpanes	$C_{26}H_{48}$	(2)
28Tri	C_{28} tricyclic terpane	$C_{28}H_{52}$	(3)
29Tri	C_{29} tricyclic terpane	$C_{29}H_{54}$	(3)
Ts	C_{27} $18\alpha, 21\beta$ -22,29,30- <i>trinorneo</i> -hopane	$C_{27}H_{46}$	(2)
Tm	C_{27} $17\alpha, 21\beta$ -22,29,30- <i>trinor</i> -hopane	$C_{27}H_{46}$	(2)
H28aab	$17\alpha, 18\alpha, 21\beta$ -28,30- <i>dinor</i> -hopane	$C_{28}H_{48}$	(4)
H29ab25n	$17\alpha, 21\beta$ -25- <i>nor</i> -hopane	$C_{29}H_{50}$	(5)
29Tm	$17\alpha, 21\beta$ -30- <i>nor</i> -hopane	$C_{29}H_{50}$	(2)
29Ts	$18\alpha, 21\beta$ -30- <i>norneo</i> -hopane	$C_{29}H_{50}$	(2)
H30a	17α - <i>dia</i> -hopane	$C_{30}H_{52}$	(6)
H29ba30n	$17\beta, 21\alpha$ -30- <i>nor</i> -hopane (normoretane)	$C_{29}H_{50}$	(5)
H30ab	$C_{30}17\alpha, 21\beta$ -hopane	$C_{30}H_{52}$	(2)
H30ba	$C_{30}17\beta, 21\alpha$ -hopane (moretane)	$C_{30}H_{52}$	(2)
H31abS	$C_{31}17\alpha, 21\beta$ -30- <i>homo</i> -hopane 22S	$C_{31}H_{54}$	(7)
H31abR	$C_{31}17\alpha, 21\beta$ -30- <i>homo</i> -hopane 22R	$C_{31}H_{54}$	(7)
G	Gammacerane	$C_{30}H_{52}$	(7)
H32abS	C_{32} $17\alpha, 21\beta$ -30,31- <i>dihomo</i> -hopane 22S	$C_{32}H_{52}$	(7)
H32abR	C_{32} $17\alpha, 21\beta$ -30,31- <i>dihomo</i> -hopane 22R	$C_{32}H_{56}$	(7)
H33abS	C_{33} $17\alpha, 21\beta$ -30,31,32- <i>trihomo</i> -hopane 22S	$C_{33}H_{58}$	(7)
H33abR	C_{33} $17\alpha, 21\beta$ -30,31,32- <i>trihomo</i> -hopane 22R	$C_{33}H_{58}$	(7)
H34abS	C_{34} $17\alpha, 21\beta$ -30,31,32,33- <i>tetra</i> -hopane 22S	$C_{34}H_{60}$	(7)
H34abR	C_{34} $17\alpha, 21\beta$ -30,31,32,33- <i>tetra</i> -hopane 22R	$C_{34}H_{60}$	(7)
H35abS	C_{35} $17\alpha, 21\beta$ -30,31,32,33,34- <i>pentahomo</i> -hopane 22S	$C_{35}H_{62}$	(7)

H35abR	C ₃₅ 17 α , 21 β -30,31,32,33,34-pentahomo-hopane 22R	C ₃₅ H ₆₂	(7)
D27baS	C ₂₇ 13 β , 17 α -diasterane 20S	C ₂₇ H ₄₈	(7,8)
D27abS	C ₂₇ 13 α , 17 β -diasterane 20S	C ₂₇ H ₄₈	(7,8)
D27abS	C ₂₇ 13 α , 17 β -diasterane 20R	C ₂₇ H ₄₈	(7,8)
S27aaaS	C ₂₇ 5 α , 14 α , 17 α -cholestane 20S	C ₂₇ H ₄₈	(7,8)
S27abbR	C ₂₇ 5 α , 14 β , 17 β -cholestane 20R	C ₂₇ H ₄₈	(7,8)
S27abbS	C ₂₇ 5 α , 14 β , 17 β -cholestane 20S	C ₂₇ H ₄₈	(7,8)
S27aaaR	C ₂₇ 5 α , 14 α , 17 α -cholestane 20R	C ₂₇ H ₄₈	(7,8)
S28aaaS	C ₂₈ 5 α , 14 α , 17 α -ergostane 20S	C ₂₈ H ₅₀	(7,8)
S28abbR	C ₂₈ 5 α , 14 β , 17 β -ergostane 20R	C ₂₈ H ₅₀	(7,8)
D29abS	C ₂₉ 13 α , 17 β -diasterane 20S	C ₂₉ H ₅₂	(7,8)
S28abbS	C ₂₈ 5 α , 14 β , 17 β -ergostane 20S	C ₂₈ H ₅₀	(7,8)
S28aaaR	C ₂₈ 5 α , 14 α , 17 α -ergostane 20R	C ₂₈ H ₅₀	(7,8)
S29aaaS	C ₂₉ 5 α , 14 α , 17 α -stigmastane 20S	C ₂₉ H ₅₂	(7,8)
S29abbR	C ₂₉ 5 α , 14 β , 17 β -stigmastane 20R	C ₂₉ H ₅₂	(7,8)
S29abbS	C ₂₉ 5 α , 14 β , 17 β -stigmastane 20S	C ₂₉ H ₅₂	(7,8)
S29aaaR	C ₂₉ 5 α , 14 α , 17 α -stigmastane 20R	C ₂₉ H ₅₂	(7,8)

Table 10.2: Compound table for biomarkers in the saturated hydrocarbon fraction. Reference key is (1) NIST (2005), (2) Zumberge (1993), (3) Peters (2000), (4) Nytoft & Bojesen-Koefoed (2001), (5) Stout & Wang (2008), (6) Moldowan *et al.* (1991), (7) Wang *et al.* (2006), (8) Grantham (1986).

Label	Name	Reference
1MAS	C ₂₁ MAS	(1)
2MAS	C ₂₂ MAS	(1)
3MAS	C ₂₇ 5 β , 10 β (CH ₃) 20S MAS	(2)
4MAS	C ₂₇ 5 β (CH ₃),10 β 20S MAS	(2)
5MAS	C ₂₇ 5 β , 10 β (CH ₃) 20R + C ₂₇ 5 β (CH ₃),10 β 20R MAS	(2)
6MAS	C ₂₇ 5 α , 10 β (CH ₃) 20S MAS	(2)
7MAS	C ₂₈ 5 β , 10 β (CH ₃) 20S* MAS	(2)
8MAS	C ₂₈ 5 β (CH ₃), 10 β 20S* MAS	(2)

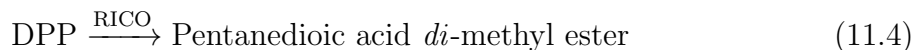
9MAS	$C_{27} 5\alpha, 10\beta(CH_3) 20R + C_{28} 5\alpha, 10\beta(CH_3) 20S$ MAS	(2)
10MAS	$C_{28} 5\beta, 10\beta(CH_3) 20R + C_{28} 5\beta(CH_3), 10\beta 20R +$ $C_{29} 5\beta, 10\beta(CH_3) 20S + C_{29} 5\beta(CH_3), 10\beta 20S$ MAS	(2)
11MAS	$C_{28} 5\alpha, 10\beta(CH_3) 20S$ MAS	(2)
12MAS	$C_{28} 5\alpha, 10\beta(CH_3) 20R$ MAS	(2)
13MAS	$C_{29} 5\beta, 10\beta(CH_3) 20R + C_{29} 5\beta(CH_3), 10\beta 20R$ MAS	(2)
14MAS	$C_{29} 5\alpha, 10\beta(CH_3) 20R$ MAS	(2)
1TAS	C_{20} TAS	(3,4)
2TAS	C_{21} TAS	(3,4)
3TAS	$C_{26} 20S$ TAS	(3,4)
4TAS	$C_{27} 20S + C_{26} 20R$ TAS	(3,4)
5TAS	$C_{28} 20S$ TAS	(3,4)
6TAS	$C_{27} 20R$ TAS	(3,4)
7TAS	$C_{28} 20R$ TAS	(3,4)

Table 10.3: Compound table of the isomers of 17 β -methyl-18-norcholesta-8,11,13-triene (monoaromatic steroids, MAS) and 17 β -methyl-18,19-dinocholesta-1,3,5(10),6,8,11,13-heptane (triaromatic steroids, TAS) (Abbott *et al.*, 1985). Reference key is (1) Mackenzie *et al.* (1981), (2) Moldowan & Fago (1986), (3) Abbott *et al.* (1985), (4) Yang *et al.* (2015b).

Chapter 11. Ruthenium Ion Catalysed Oxidation

11.1 Ruthenium Ion Catalysed Oxidation of Alkylated Mono- and Di-aromatic Standard Compounds

The major reactions products of RICO of the asphaltenes are homologous series of *n*-alkanoic and α,ω -*di-n*-alkanoic fatty acid *di*-methyl esters (FAME, *m/z* 74; DFAME, *m/z* 98) as the oxidised products require methylation to be GC-MS-ameanable (Peng *et al.*, 1999). To verify the reactions suggested in Peng *et al.* (1999), Figure 11.1 theoretical reactions A and B, the RICO procedure was performed on four standard compounds, phenylbutane (Ph-C₄), phenyldodecane (Ph-C₁₂), bibenzyl (BB) and 1,3-diphenylpropane (DPP). It was assumed that oxidising Ph-C₄ and Ph-C₁₂ would produce products consistent with reaction A, whilst oxidising BB and DPP would lead to products from reaction B. Figures 11.2 and 11.3 illustrate the oxidation reactions observed in standard compound results, Figures 11.4 and 11.5 show the corresponding total ion chromatograms (TICs). Following the assumptions of reactions A and B, the expected products from oxidising the standard compounds were as follows:



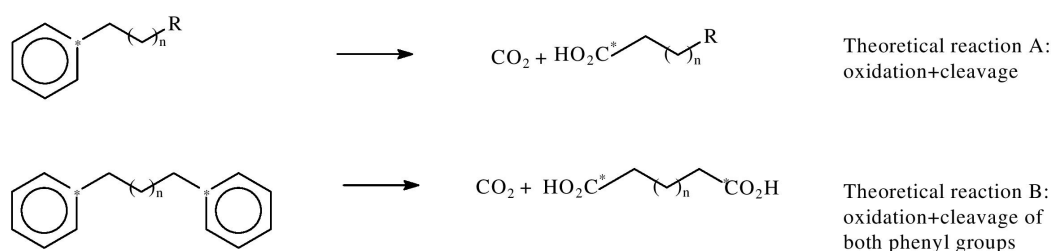


Figure 11.1: Reactions occurring during RICO of asphaltenes (Peng *et al.*, 1999).

None of the reaction products showed a 100% conversion rate. The literature suggests that the lower-weight fatty acid methyl ester (FAME) and *di*-fatty acid *di*-methyl ester (DFAME) compounds suffer from volatility losses during oxidation and methylation (Strausz *et al.*, 1999a), thus their yields were expected to be low. Using diaromatic compounds with long inter-aromatic bridges as standards was not deemed reasonable as the currently-reported archipelago asphaltenes only have direct aromatic alkyl linkages (Schuler *et al.*, 2015, 2017).

The products from the oxidation of Ph-C₄ (reactions in Figure 11.2, products in Figure 11.4) did not include pentanoic acid methyl ester as expected, instead producing 1-butanone-1-phenyl and Ph-C₄ at yields of 7.81% and 78.02% respectively, other peaks were unidentified. Thus, the oxidation of Ph-C₄ was only partially complete, whereby the butyl chain was oxidised but the aromatic ring was not cleaved. The oxidation of Ph-C₁₂ proceeded as expected, the main product was tridecanoic acid methyl ester (77.77%), as well as dodecanoic acid methyl ester (2.30%), methyl-2-hydroxytetradecanoate (1.86%), Ph-C₁₂ (4.80%) and dodecanophenone (5.76%). The latter compound suggests that for ca. 6% of the starting material the oxidation was not complete, which is analogous to the production of 1-butanone-1-phenyl from the oxidation of Ph-C₄. The above results suggest that the oxidation of short-chain alkylated aromatics would suffer from volatility losses making their inference unreliable, whilst medium/long-chain (C_{≥12}) compounds are more stable. This does not impede the use of RICO for asphaltenes as the author assumes that steric hindrance (Section 2.1) affecting nanoaggregation is assumed to only be significant for medium-long side-chains whose oxidation yield was shown to be satisfactory. Although the stability of Ph-C₁₂ products has been shown, FAME compounds from *n*-C₁₁ will be used as this corresponds to the definition of Tissot & Welte (1984) of medium-chain compounds and it is assumed that the stability of *n*-C₁₁ FAME is not dramatically

different from that of n -C₁₃ FAME. Importantly, the production of 1-butanone-1-phenyl and dodecanophenone from Ph-C₄ and Ph-C₁₂ could suggest that one of the products of RICO is the homologous series of phenylalkylketones. The mass spectra of 1-butanone-1phenyl and dodecanophenone are shown in Figure 11.6, where the common ions are 77, 105 and 120. Asphaltene samples were screened for these ions to determine whether phenylalkylketones are present, results reported later in this Chapter.

The oxidation of BB was incomplete, whereby only one of the two phenyl rings was cleaved, producing benzenepropanoic acid (26.87%) and BB (66.02%). It could be interpreted that the oxidation of BB followed the reaction A instead of the assumed reaction B, whereby one of the phenyl groups was analogous to a side-chain functionality and was preserved through the reaction. The oxidation of DPP produced 2.41% of the expected product, pentanedioic acid dimethyl ester, as well as benzenebutanoic acid methyl ester (10.95%) and DPP (77.85%). The products of partial oxidation (or observed reaction A instead of expected reaction B) are greater than that of the full oxidation, whilst the majority of products were the starting material. As with monoaromatic standards, the production of benzenepropanoic acid methyl ester and benzenebutanoic acid methyl ester suggests that RICO of diaromatic compounds linked by alkyl bridges produces benzenecarboxylic acids. The mass spectra of benzenepropanoic and benzenebutanoic acid methyl ester are in Figure 11.7, with common ions at m/z 51, 91 and 104. Again, asphaltenes were screened for benzenecarboxylic acids as well.

In conclusion, the information obtained from RICO is satisfactory for inference about asphaltene medium/long-chain appendages. As will be shown, some inference about the direct phenyl-phenyl linkages can also be sought using the present method. For verification, the analysis of PAH linkages and lower-weight FAMEs/DFAMEs should also be performed using a different RICO procedure (Peng *et al.*, 1999; Strausz *et al.*, 1999a) or other methods. The next Section describes the results of RICO performed on the asphaltene samples. The analysis of the impact of the asphaltene structural differences implied by the RICO results on their nanoaggregation behaviour is in the General Discussion Chapter.

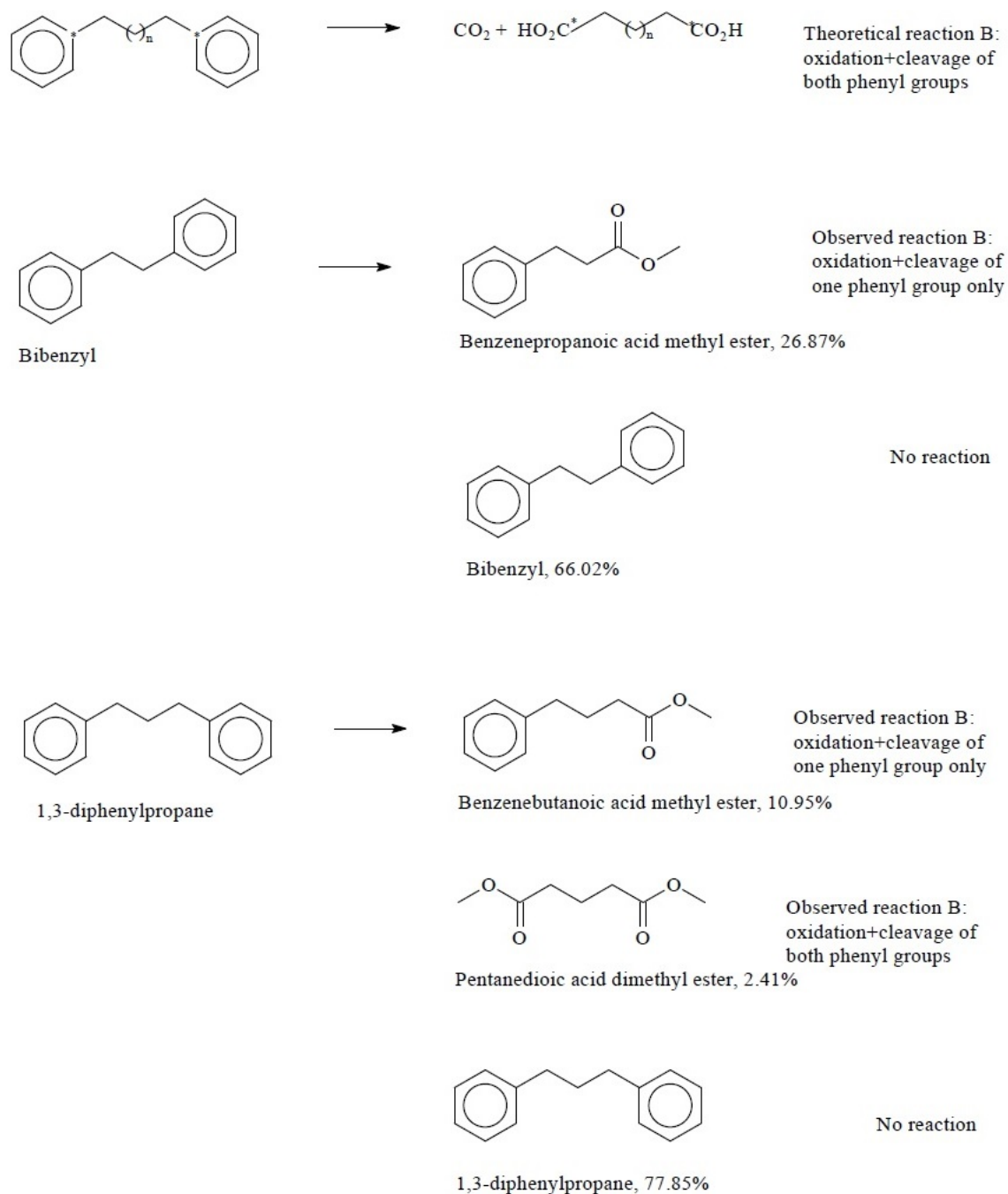


Figure 11.3: Reactions occurring during RICO of asphaltenes. Theoretical reaction B according to Peng *et al.* (1999), observed reactions are inferred from mass spectrometric analysis of RICO performed on standard compounds, Figure 11.5

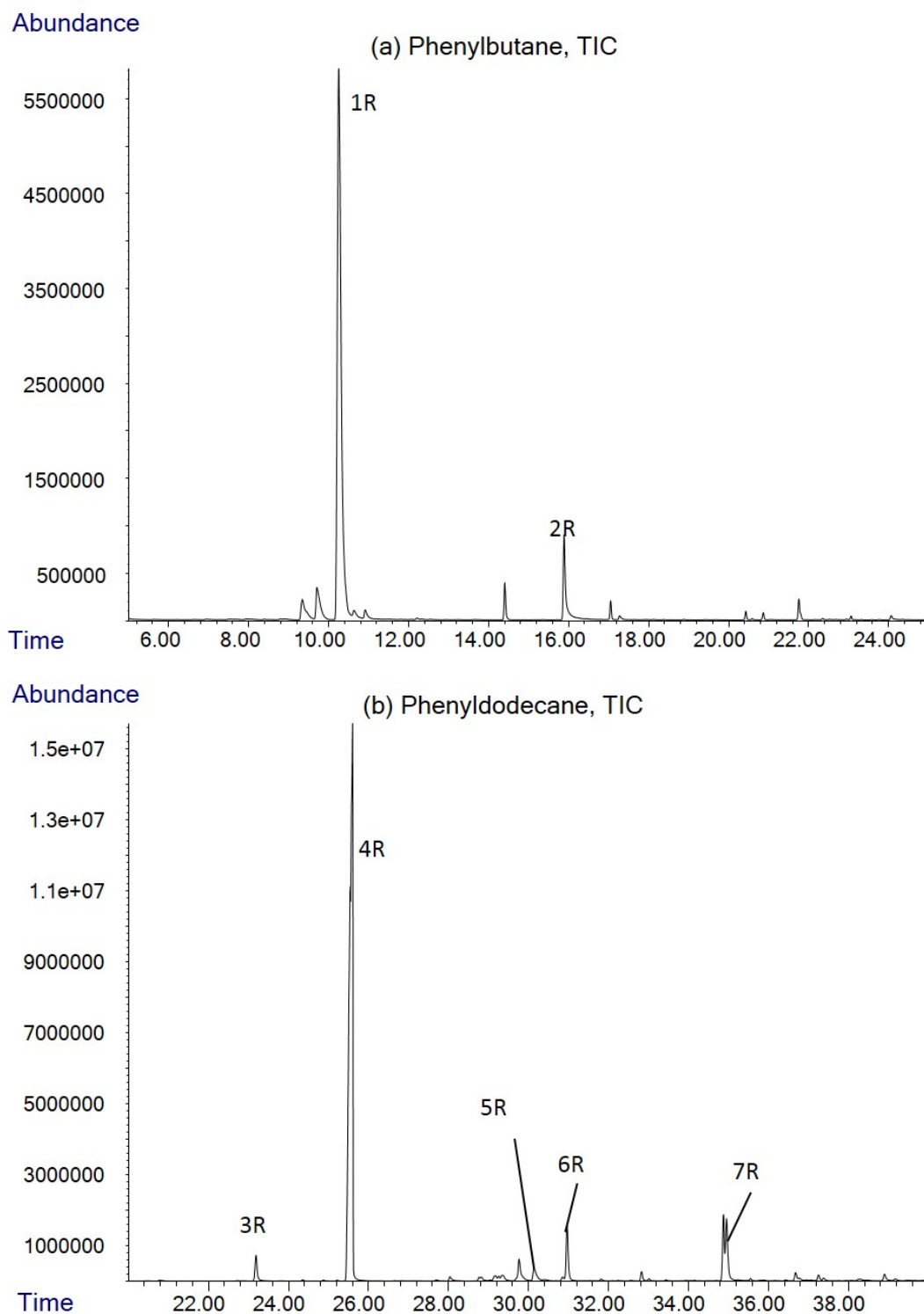


Figure 11.4: Total ion chromatograms (TIC) of RICO products performed on alkylated mono-aromatic standards, compound labels are given in Table 11.1.

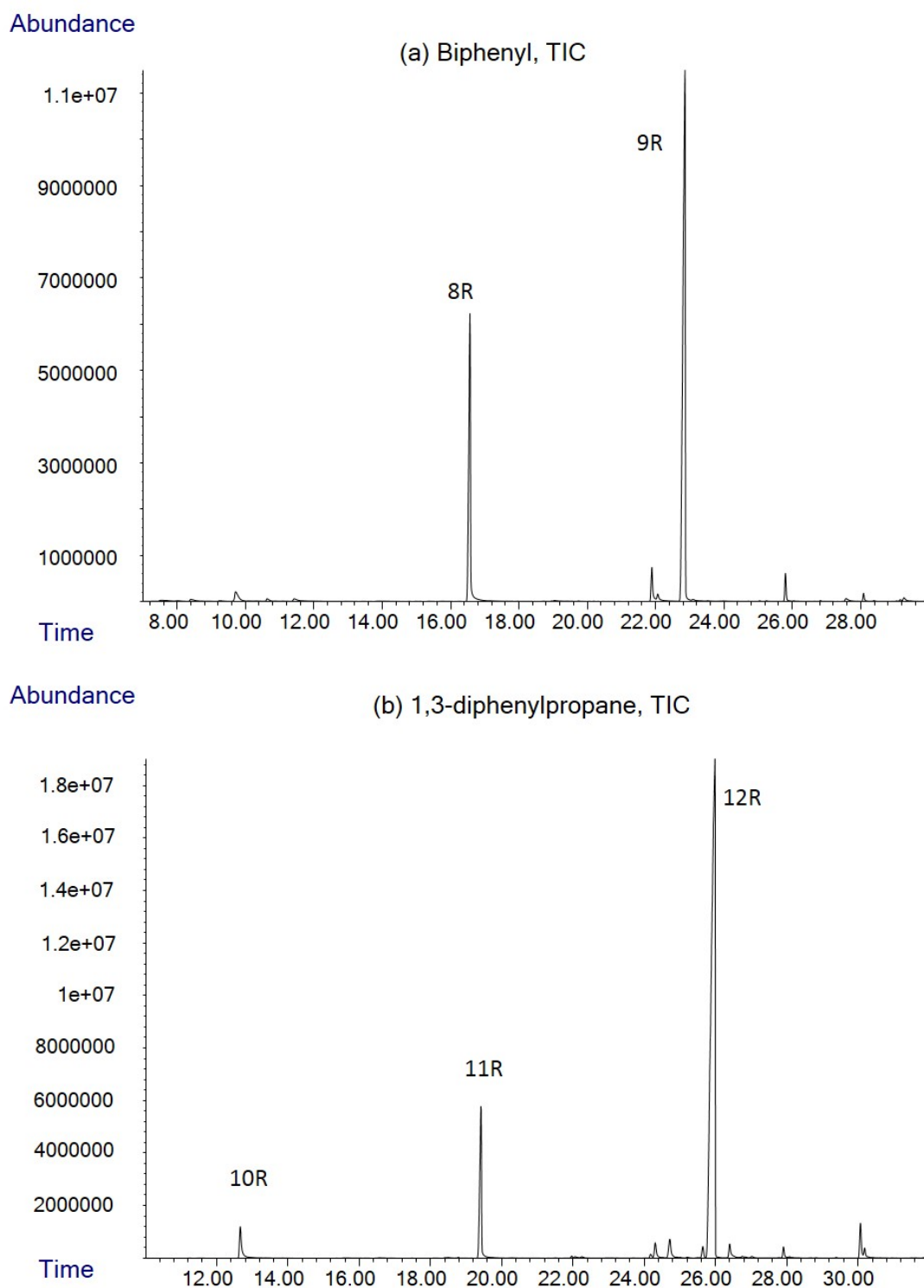


Figure 11.5: Total ion chromatograms (TIC) of RICO performed on alkylated di-aromatic standards, compound labels are given in Table 11.1.

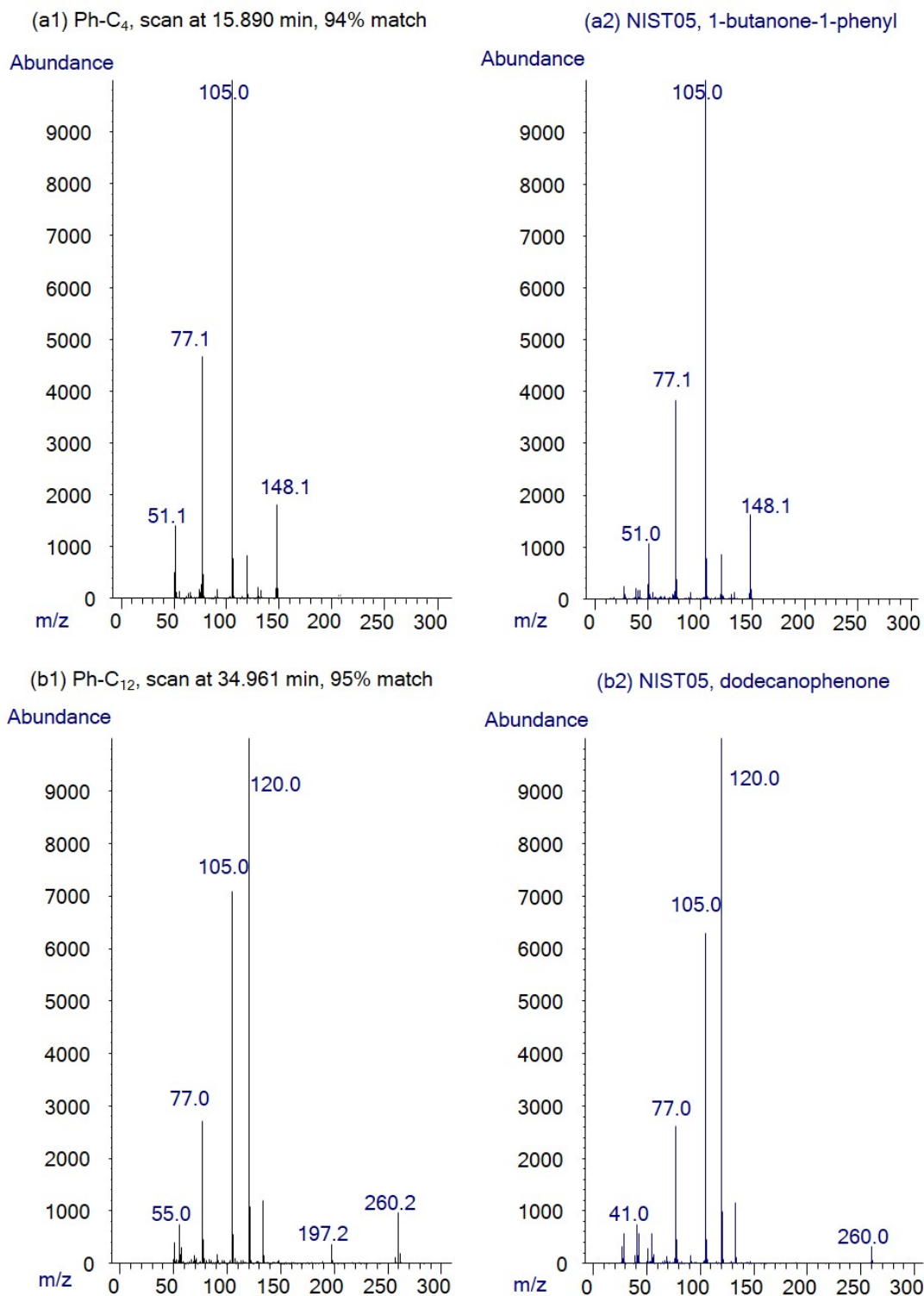


Figure 11.6: Mass spectra of phenylalkylketones identified in RICO products of monoaromatic standards.

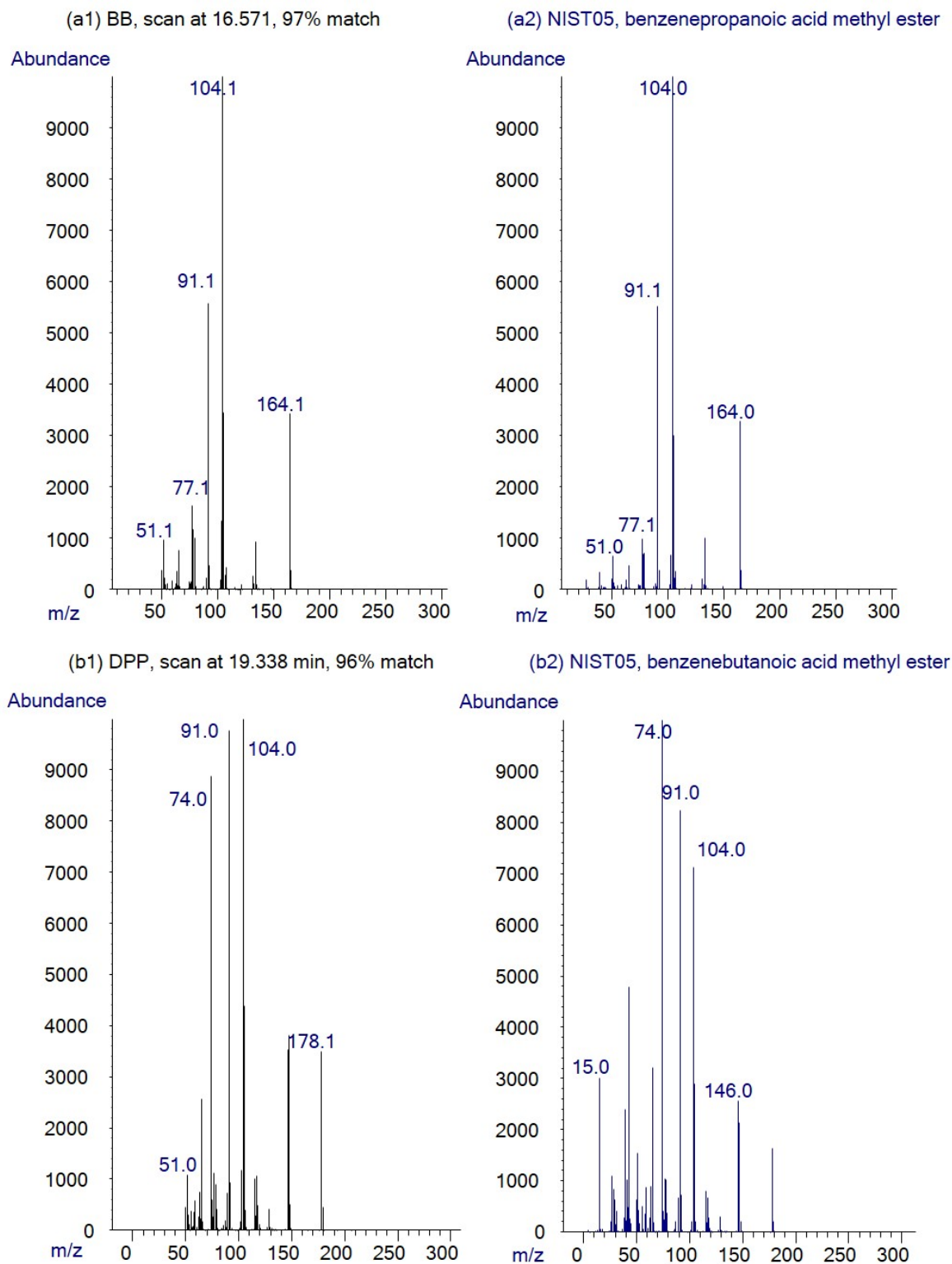


Figure 11.7: Mass spectra of phenylalkyl acid methyl esters identified in RICO products of diaromatic standards.

11.2 Ruthenium Ion Catalysed Oxidation of Asphaltenes

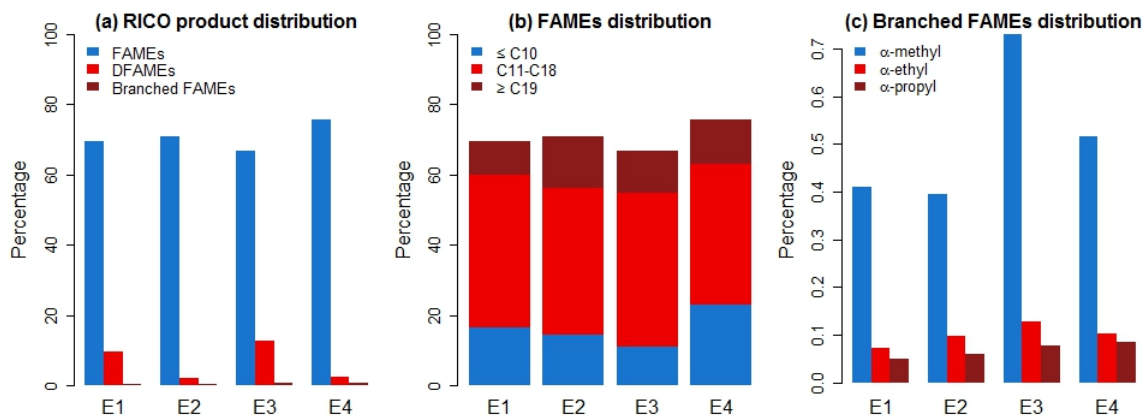


Figure 11.8: Relative abundances of RICO products based on peak heights, Figures 11.10, B.1-B.3 and Table 11.2.

11.2.1 *Fatty acid methyl esters and di-fatty acid dimethyl esters*

Figure 11.8 summarises the asphaltene oxidation results, and plots (a) and (b) illustrate the distributions of FAMEs and DFAMEs. Relative compound abundances are shown in Table 11.2, the m/z 74 and 98 chromatograms are shown in Figures 11.10 for E1 asphaltene and B.1-B.3 in Appendix B for the remaining samples. The FAME series start from n -C₇ to n -C₂₇ due to the heating regime of the analytical instrument, and it is assumed that the abundance of n -C_{≤7} is low and/or such compounds are susceptible to volatility losses. Figure 11.8 (b) shows the distribution of FAMEs according to the alkyl chain lengths. As lower-weight fatty acids are susceptible to volatility losses, their abundance should be interpreted with caution. All of the samples illustrate a mild even-odd predominance of the FAME series with very strong n -C₁₆ and n -C₁₈ peaks. Following the earlier oxidation results performed on standard compounds, it would be expected that the abundance of lower-weight compounds would decrease with decreasing side-chain length. This is observed for all of the samples. Thus, the inference about asphaltene side-chains < ca. n C-10 should be sought using other methods as it is unclear whether their declining abundance in RICO products is caused by incomplete oxidation, volatility loss or low abundance in the starting asphaltene material.

The DFAME series are well-resolved from ca. n -C₈ and continue up to n -C₂₄. It is unclear what gives rise to the abundance of long-chain DFAME compounds

as their derivation from asphaltene archipelago-type compounds is highly unlikely, given present literature knowledge (Schuler *et al.*, 2015, 2017). The occurrence of medium/long-chain double acids should be a subject of further investigation.

The m/z 74 chromatograms for E1 and E2 RICO products, Figures 11.10 (a) and B.1 (a), illustrate left-skewed distributions with a mild even-odd predominance of medium molecular weight compounds. The even-odd medium-length chain ratio (C_{12-18} to C_{11-17}) was calculated and could be used as an indicator of biological activity (Tissot & Welte, 1984). The even/odd ratios were 1.71 and 1.33 for E1 and E2 respectively. Note that the high C_{16} and C_{18} peaks also drive the even-odd predominance of E1 which is highest out of the four samples. The DFAME compounds (plots (b) in earlier Figures) at C_4 - C_6 are mixed with the baseline and become increasingly better resolved after C_7 . The FAME distribution of E3, Figure B.2 (a), is more symmetric, whereby the lower-weight compounds are in lower abundance whereas the shorter mono-acids in E4, Figure B.3 (a), appear to be preserved to the highest extent out of all samples. The even-odd ratios are 1.35 and 1.45 for E3 and E4 respectively. The DFAME series are very well-resolved for E3 using the m/z 98 chromatogram. Interestingly, for E4 the DFAME series are very similar to FAME peak height (m/z 98) which is in contrast to E3. From Table 11.2 it is evident that the FAME and DFAME compounds are negatively correlated. The Pearson's correlation coefficient is -0.92 with a corresponding p -value of 0.076. Although the correlation value is very strong, the p -value is indicating that given present data the evidence that *the correlation between FAMEs and DFAMEs is not zero* is only marginally significant at the 5% level. The author speculates that this correlation arises as during the RICO reaction, the FAME compounds re-fuse with the cleaved phenyl rings, which would explain the occurrence of the long DFAME compounds. This would be a phenomenon of interest for a future investigation.

11.2.2 *Alpha-branched fatty acid methyl esters*

The asphaltene RICO products also contain homologous series of methylated FAME compounds, consistently with those in Strausz *et al.* (1999a); Peng *et al.* (1999). Figure 11.8 (a) and (c) illustrate the relative abundances of the branched acids. Example chromatograms are shown in Figure 11.11, the remaining traces are provided in Appendix B, Figures B.4-B.6. As their abundance is low, the measurement of their chromatographic peak areas is difficult, and the provided estimations should be treated with caution, and only compounds with $\geq C_{11}$ in the acid portion of

the methyl esters are included in quantitation. The latter also avoids errors due to volatility losses. This should especially be taken into account when comparing their abundance to the abundance of FAMEs and DFAMEs in plot (a). Plot (c) illustrates distributions of the the α -methyl, α -ethyl and α -propyl groups whereby their abundance decreases with increasing α -alkyl group length, consistent with literature (Ma *et al.*, 2008). The compounds were identified by analysing background-subtracted mass spectra (NIST, 2005) (Appendix B) and by comparison with the existing literature (Ma *et al.*, 2008).

The E3 and E4 asphaltenes have notably greater abundances of α -methyl FAMEs than E1 and E2, whilst E2 has the greatest proportion of the α -ethyl acids and E4 has the highest proportion of α -propyl FAMEs. The correlation between α -ethyl and α -propyl acids is 0.82 with a p -value of 0.17 which is insignificant at the 5% level. The α -methyl- α -ethyl and α -methyl- α -propyl correlations are 0.69 (p -value of 0.31) and 0.63 (p -value of 0.37) respectively which is moderate. This lack of correlation may suggest that the α -branched acids are genuine asphaltene derivatives and products of ‘re-fusion’ processes during RICO.

11.2.3 Phenylalkylketones and benzenecarboxylic acid methyl esters

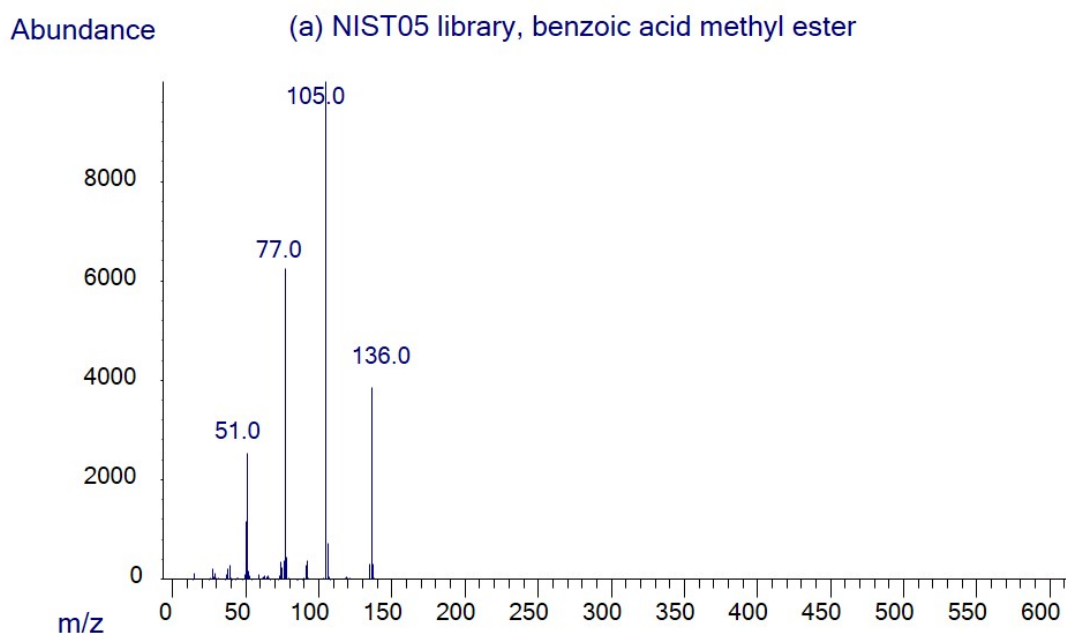


Figure 11.9: Mass spectrum of benzoic acid methyl ester.

Following the results of RICO performed on standard compounds asphaltenes were screened for ions 77, 105 and 120 for phenylalkylketones and 77, 91 and 104 for benzenecarboxylic acids. The major product detected from this search was benzoic acid methyl ester (BAME) in both of the searches and no other identifiable compounds were found. Figure 11.9 illustrates the NIST05 entry for benzoic acid methyl ester, whereby the main ions are 51, 77, 105 and 136. The background-subtracted mass spectra of all samples are provided in Figure 11.14. The compatibility to the library entry of BAME is of varying quality, however the characteristic ions 51, 77, 105 and 136 are present in all samples. The partial ion chromatograms, Figure 11.12 and 11.13 and Figures B.7- B.12 in the Appendix B illustrate the noise associated with identifying BAME. Referring to the RICO performed on diaromatic standards, this would suggest that RICO of asphaltenes has cleaved an alkyl bridge between two mono/polyaromatic units. This is also consistent with results from Schuler *et al.* (2015, 2017) that illustrate archipelago asphaltenes whereby aromatic centres are connected by direct alkyl linkages. The absence/low abundance of longer-chain benzenecarboxylic acids suggests the absence of longer PAH bridge linkages.

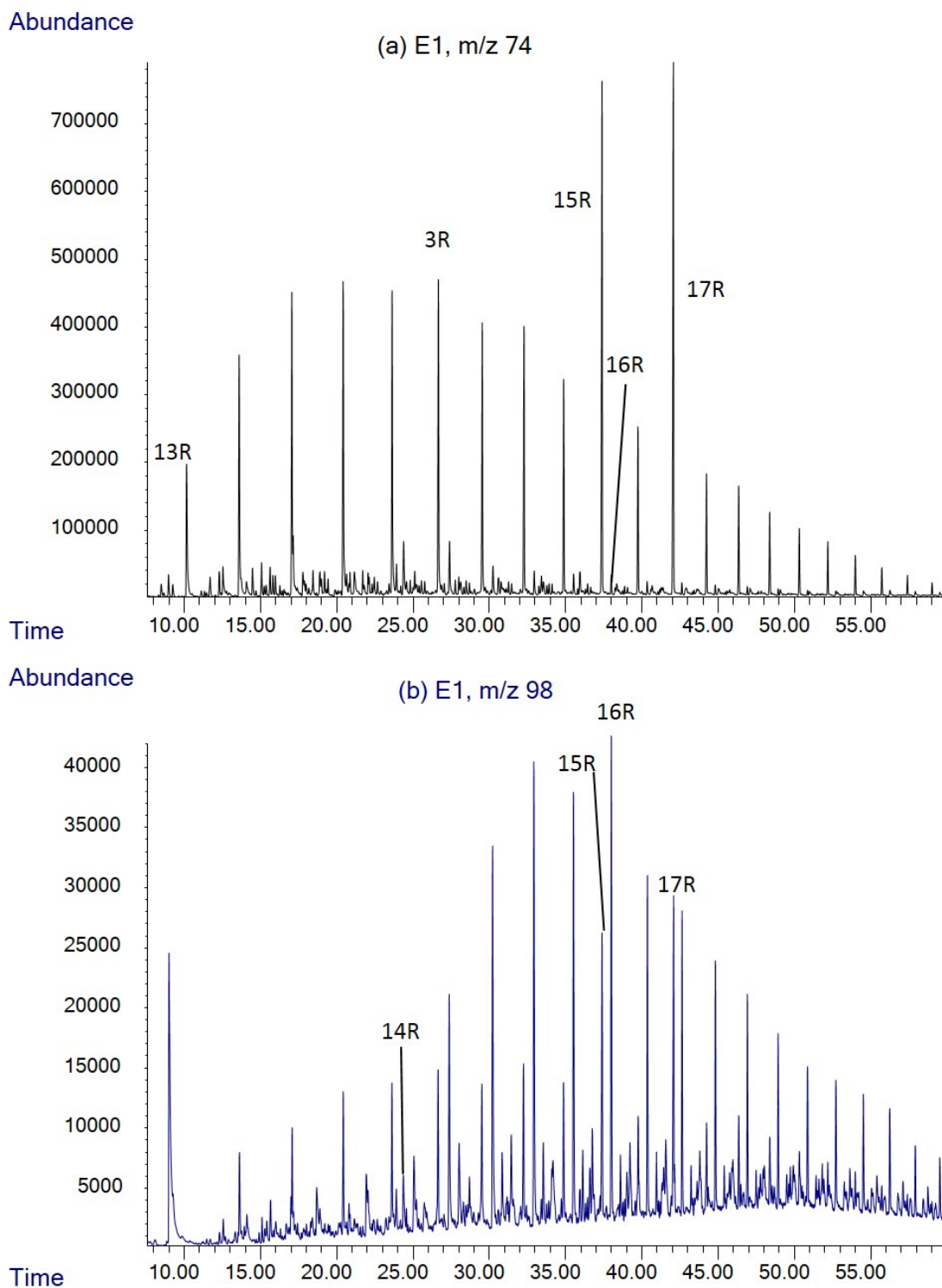


Figure 11.10: Partial ion chromatograms of (a) *n*-alkanoic fatty acid and (b) α,ω -di-*n*-alkanoic di-fatty acid methyl esters of E1 ROCP products.

Compound label	Compound name	Empirical formula
1R	Butylbenzene	C ₁₀ H ₁₄
2R	1-butanone-1-phenyl	C ₁₀ H ₁₂ O
3R	Dodecanoic acid methyl ester	C ₁₃ H ₂₆ O ₂
4R	Tridecanoic acid methyl ester	C ₁₃ H ₂₈ O ₂
5R	Methyl-2-hydroxytetradecanoate	C ₁₅ H ₃₀ O ₃
6R	Phenyldodecane	C ₁₈ H ₃₀
7R	Dodecanophenone	C ₁₈ H ₂₈ O
8R	Benzenepropanoic acid methyl ester	C ₁₀ H ₁₂ O ₂
9R	Bibenzyl	C ₁₄ H ₁₄
10R	Pentanedioic acid dimethyl ester	C ₇ H ₁₂ O ₄
11R	Benzenebutanoic acid methyl ester	C ₁₁ H ₁₄ O ₂
12R	1,3-diphenylpropane	C ₁₅ H ₁₆
13R	Heptanoic acid methyl ester	C ₈ H ₁₆ O ₂
14R	Octanedioic acid dimethyl ester	C ₁₀ H ₁₈ O ₄
15R	Hexadecanoic acid methyl ester	C ₁₇ H ₃₄ O ₂
16R	Tetradecanedioic acid dimethyl ester	C ₁₆ H ₃₀ O ₄
17R	Octadecanoic acid methyl ester	C ₁₉ H ₃₈ O ₂
18R	α -methyl nonadecanoic acid methyl ester	C ₂₀ H ₄₀ O ₂
19R	α -ethyl nonadecanoic acid methyl ester	C ₂₁ H ₄₂ O ₂
20R	α -propyl nonadecanoic acid methyl ester	C ₂₂ H ₄₄ O ₂
21R	Benzoic acid methyl ester	C ₈ H ₈ O ₂

Table 11.1: Compound table for RICO experiments (NIST, 2005).

Sample	FAME	FAME C ₁₁₋₁₈	FAME C _{≥19}	DFAME	α -FAME	BAME
E1	69.5	43.50	9.56	9.58	0.53	0.047
E2	71.0	41.84	14.78	2.36	0.55	0.075
E3	66.7	43.69	11.79	12.89	0.94	0.053
E4	71.8	39.73	12.89	2.72	0.70	0.040

Table 11.2: Abundance (%) of different compound series in RICO products. α -FAME abbreviates the α -branched FAMEs.

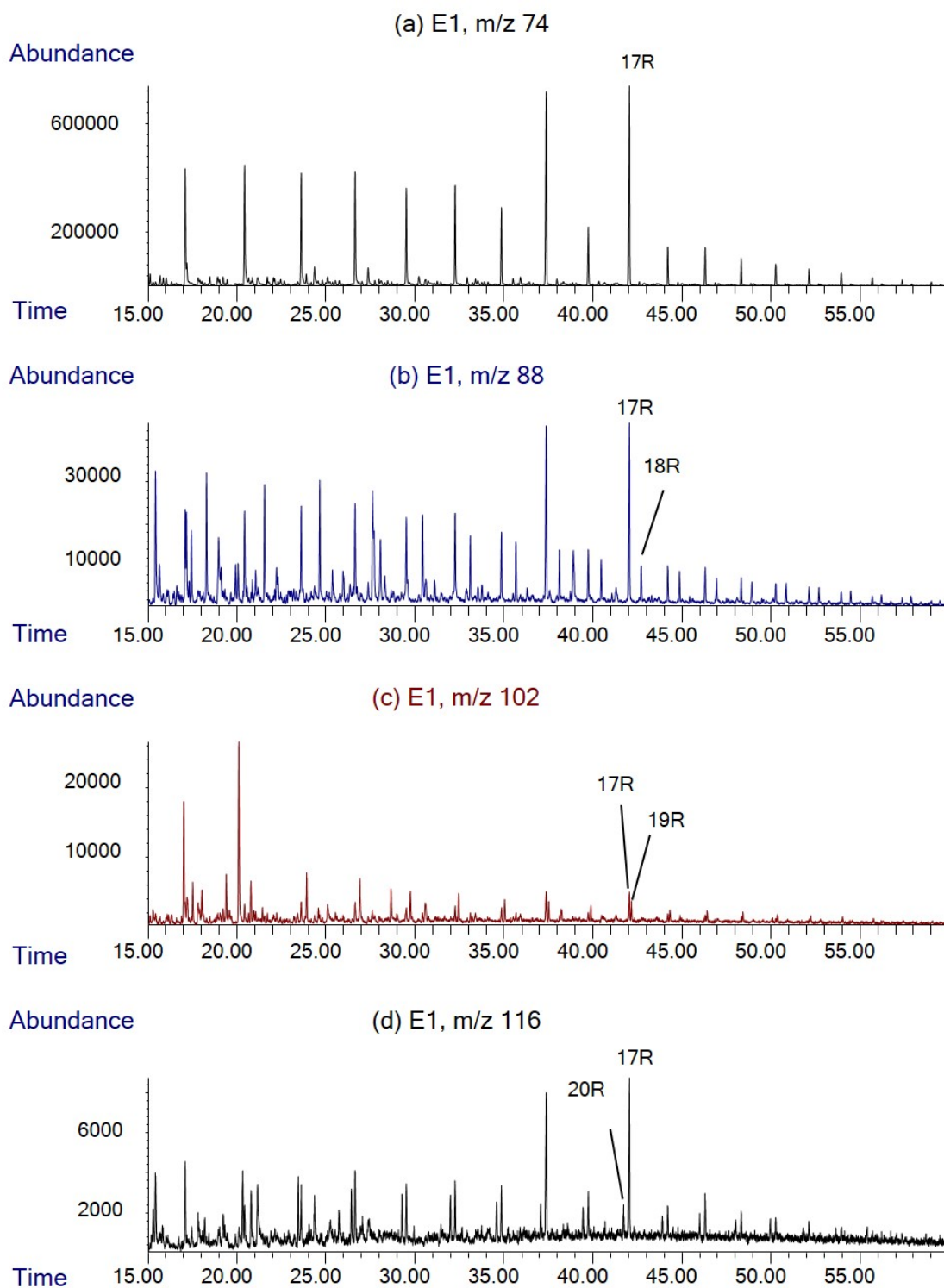


Figure 11.11: Partial ion chromatograms of (a) *n*-alkanoic, (b) α -methyl-*n*-alkanoic, (c) α -ethyl-*n*-alkanoic and (d) α -propyl-*n*-alkanoic fatty acid methyl esters of E1 RICO products.

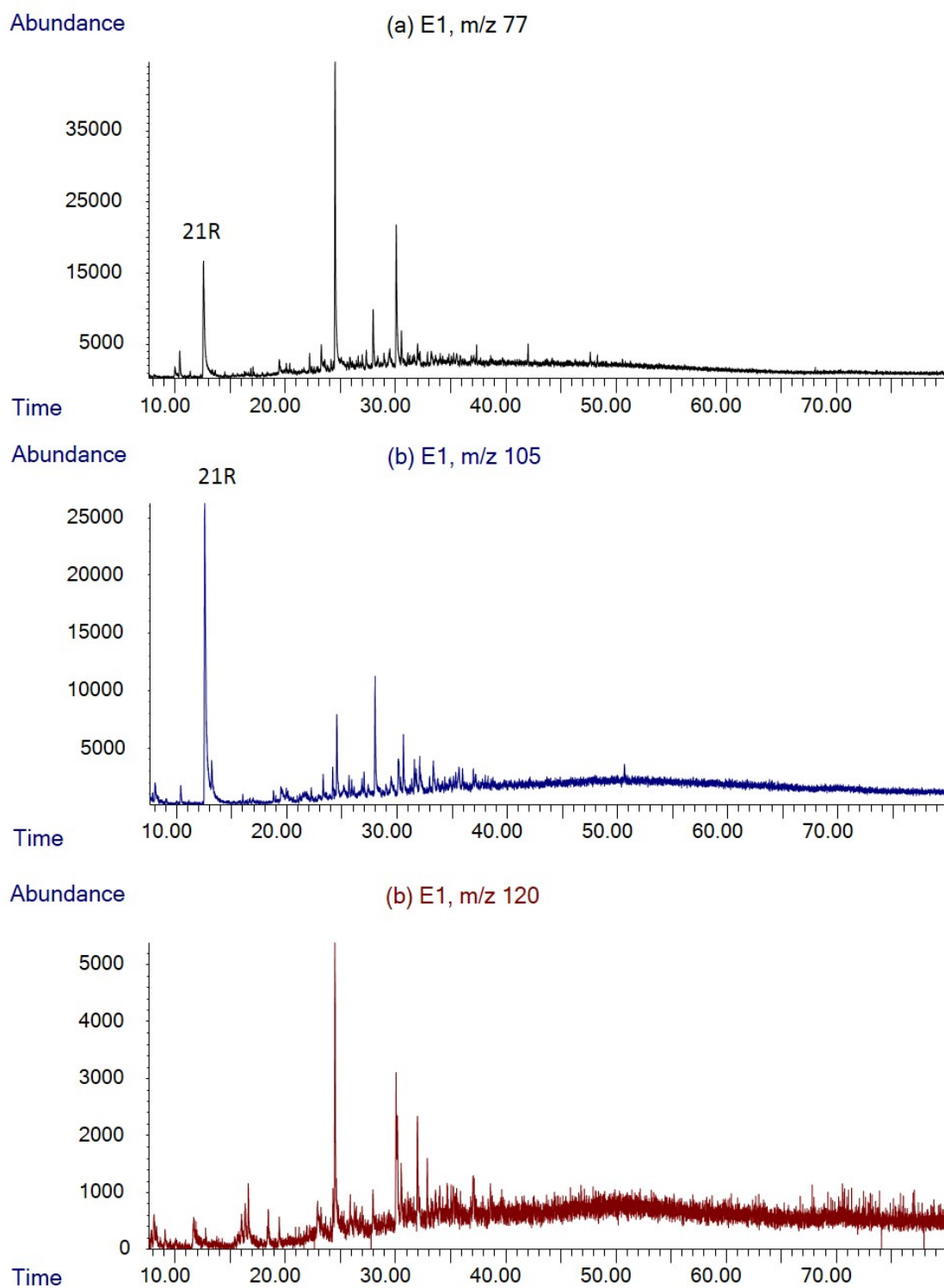


Figure 11.12: Partial ion chromatograms for phenylalkylketones.

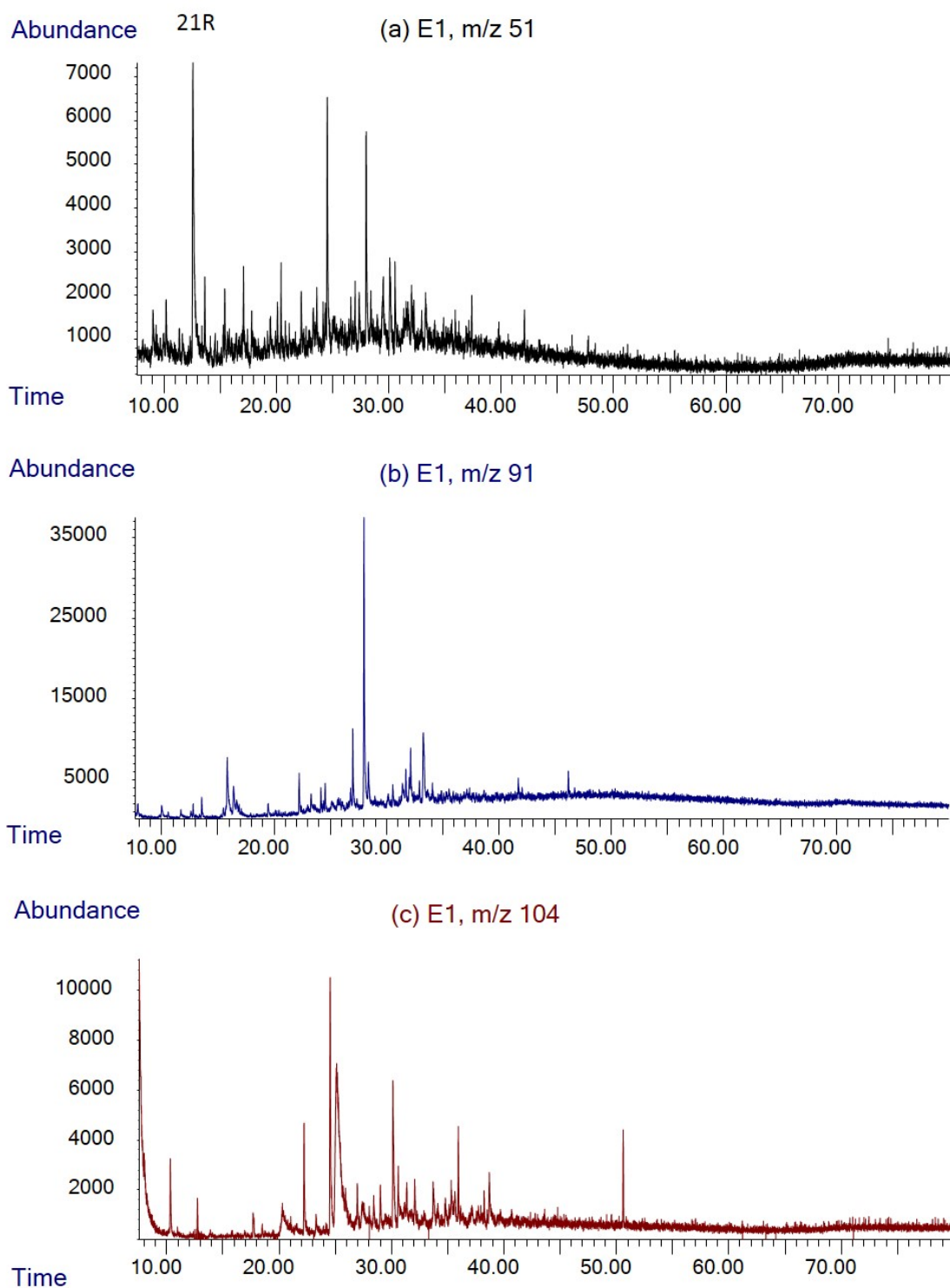


Figure 11.13: Partial ion chromatograms for benzenecarboxylic acid methyl esters.

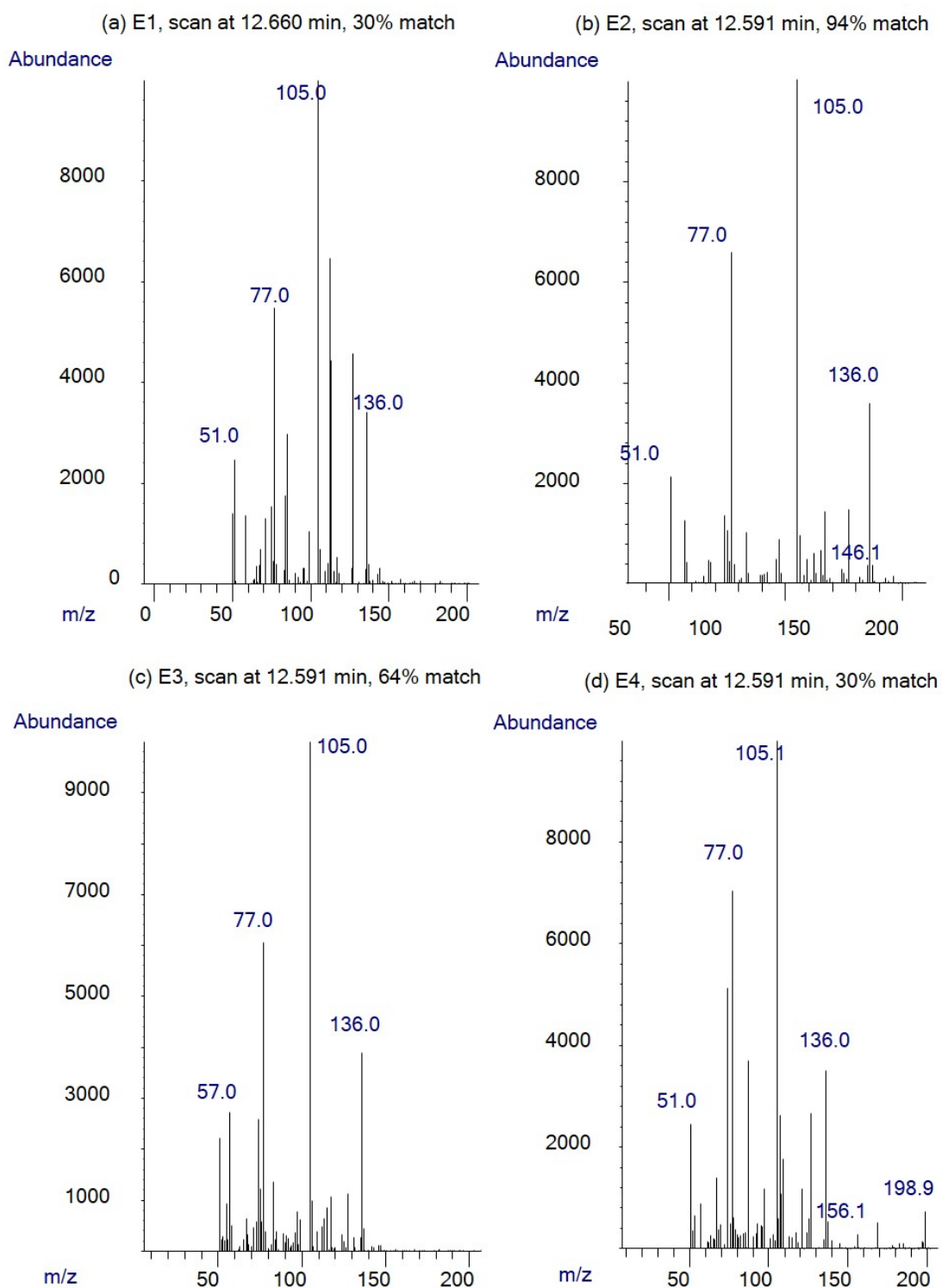


Figure 11.14: Background-subtracted mass spectra of compounds eluting at ca.12.6 min. Percentage values indicate a match with the NIST (2005) entry of BAME.

Chapter 12. Ultrasonic Characterisation

12.1 Ultrasonic Characterisation of Cetyltrimethylammonium Bromides

Calibration of the Resoscan instrument was performed using pure and mixed solutions of cetyltrimethylammonium bromide surfactants ($\text{CH}_3(\text{CH}_2)_n\text{N}(\text{Br})(\text{CH}_3)_3$, abbr. C_nTAB , $n=12,14$), Figure 12.1. Asphaltene and C_nTAB data was processed following the scheme described as follows for C_{12}TAB . Processing results for the remaining data can be found in Appendix C.1.

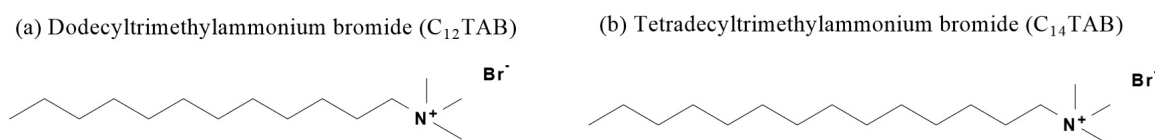


Figure 12.1: Schematic of C_nTAB , $n=12,14$ molecules.

12.1.1 *Pre-processing of velocity data*

Figure 12.2 illustrates the ultrasonic velocity profiles of the C_{12}TAB measurements. The legends indicate measurement temperature, which was very stable with no greater fluctuations than $3 \times 10^{-3} \text{ }^\circ\text{C}$. The effect of trapped air bubbles (Povey, 1997a) is illustrated in Figure 12.3. The extreme outlier in plot (b) is assumed to be characteristic of an air bubble propagating through the cell causing a velocity fluctuation of 185.46 m s^{-1} (plot (a) is an example of an air-free sample). This outlier was removed from final velocity estimations.

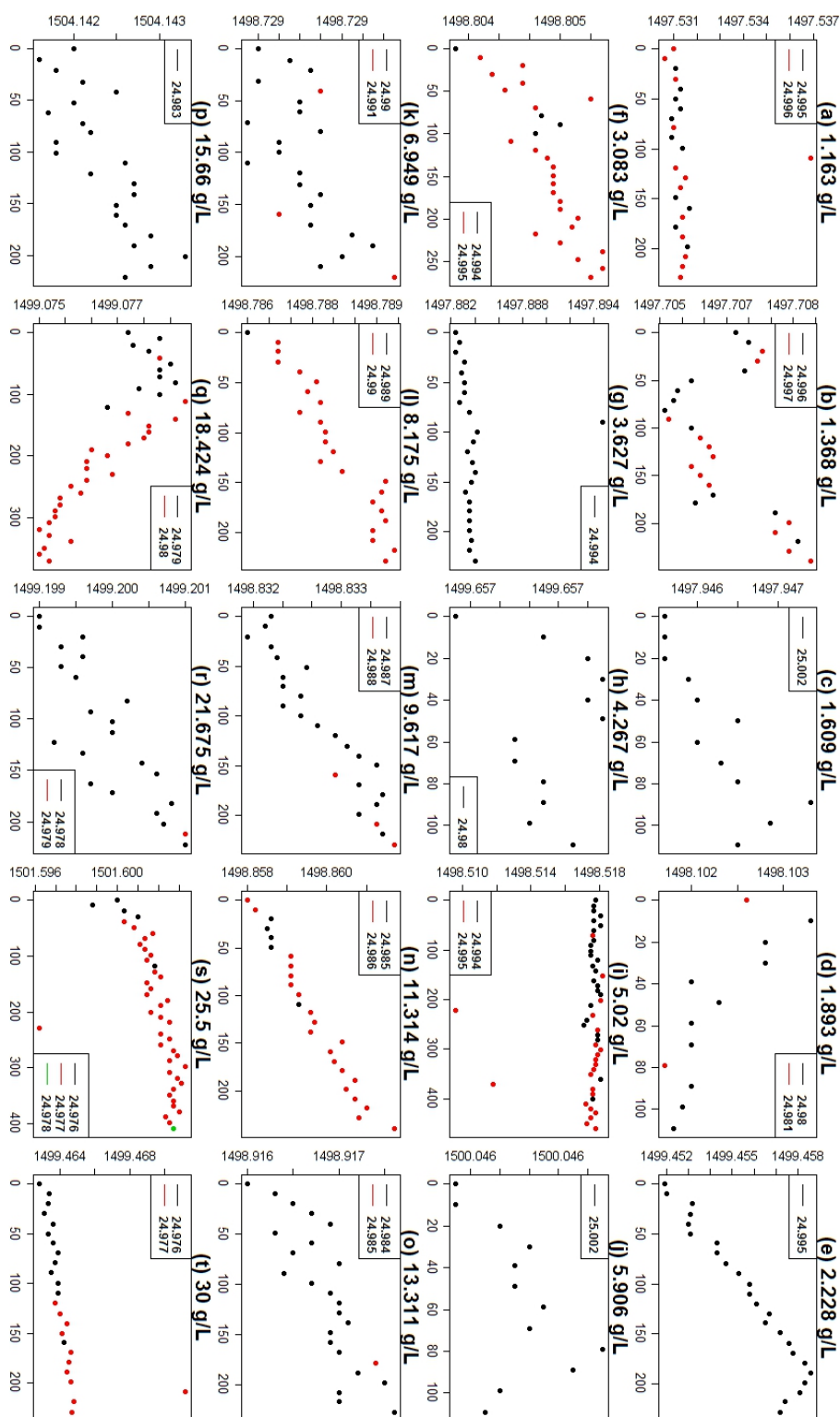


Figure 12.2: Time (s) (x-axis) versus velocity (m s⁻¹) (y-axis) plots of C₁₂TAB ultrasonic measurements. Titles indicate C₁₂TAB concentration, legends indicate measurement temperature in °C. Measurement temperature was set at 25°C.

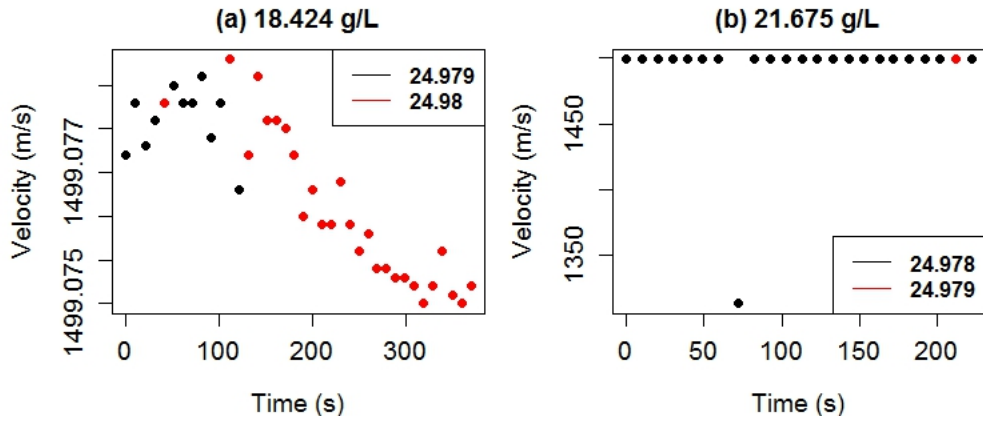


Figure 12.3: Time (s) versus velocity (m s^{-1}) plots of C_{12}TAB ultrasonic measurements illustrating the effect of air bubbles on velocity. Titles indicate C_{12}TAB concentration, legends indicate measurement temperature in $^{\circ}\text{C}$.

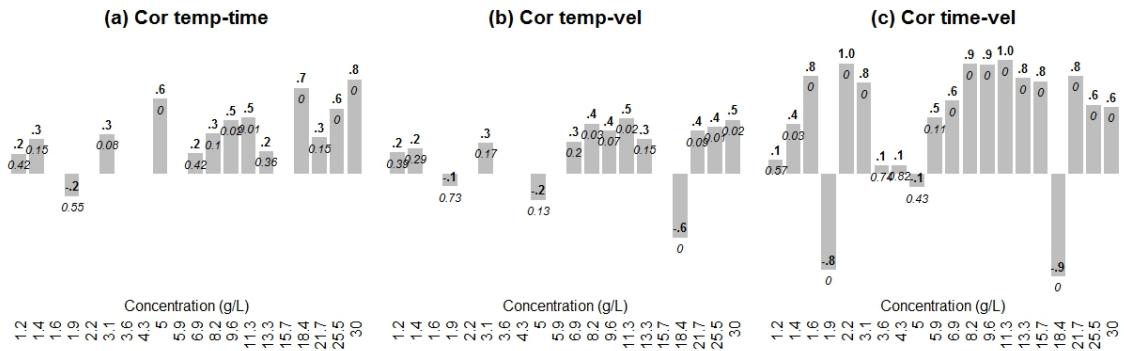


Figure 12.4: Correlation plots of C_{12}TAB ultrasonic measurements. Temperature and velocity are abbreviated as ‘temp’ and ‘vel’ respectively. Pearson’s correlation and corresponding p -values are indicated in bold and italic respectively.

Figure 12.4 illustrates correlations between temperature, time and velocity. Some of the correlation values are missing as for those measurements the temperature was recorded as constant (e.g. within $\pm 5 \times 10^{-4} \text{ }^{\circ}\text{C}$). Pearson’s correlation between variables X and Y is $\text{Cor}(X, Y)$ is

$$\text{Cor}(X, Y) = \frac{\text{Cov}(X, Y)}{\text{SD}(X)\text{SD}(Y)} \tag{12.1}$$

whereby $\text{SD}(\cdot) = 0$ for constant measurements, for which $\text{Cor}(X, Y)$ is undefined. Plot (a) indicates one strong (≥ 0.8) correlation value, indicating a significant time-temperature dependence. As mentioned above, however, the temperature variation

was small enough that it was assumed to not affect the final concentration-velocity relation. The temperature-velocity correlation values in plot (b) are only moderate. Finally, the strongest correlations appear to occur between time and velocity (plot (c)) some of which are near-perfect ($\text{Cor}(X, Y) \simeq 1$). This time trend may arise from microscopic solvent evaporation, however, the observed trends are not strong enough to change the estimation of the CMC and/or skew the resulting concentration-velocity relation, as shown in Figure 12.5.

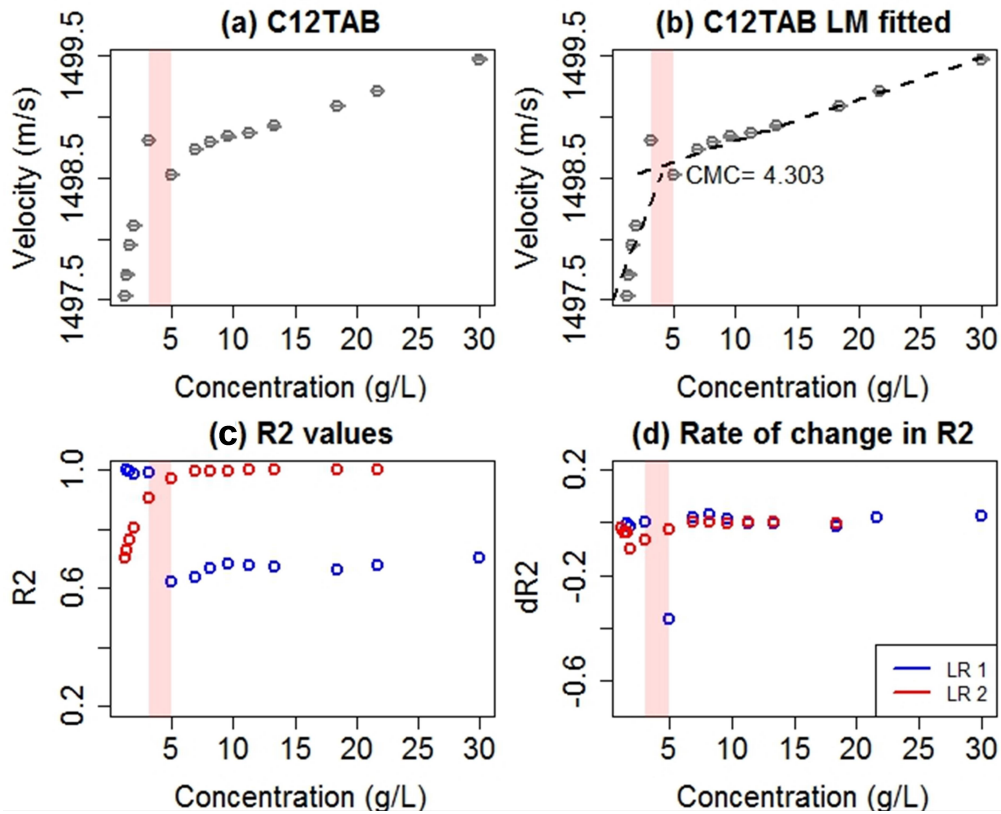


Figure 12.5: Estimation of the CMC for C_{12} TAB. Red shading indicates the CMC region estimation, dashed lines in plot (b) indicate the corresponding fitted regressions. Plots (c) and (d) indicate the changes in R^2 as more data is added to a regression model.

Figure 12.5 (a) illustrates the concentration-velocity profile for C_{12} TAB where every concentration point is an average of the first 7 measurements. Taking more points for velocity averaging did not affect the concentration-velocity relation, this will be illustrated for the ultrasonic characterisation of asphaltenes later. The (barely-visible) confidence intervals are very narrow and non-overlapping, indicating a very good measurement stability. The measurement mean standard deviation values are shown in Table 12.1. Plots (c) and (d) illustrate the change in the coefficient of deter-

mination (R^2) values as a function of increasing number of points in the monomeric (blue dots, LR1) and aggregated (red dots, LR2) linear regions (Zielinski *et al.*, 1986). For the former, a drop in the R^2 values is observed after ca. 3 g L^{-1} indicating that the data fit to a linear model declines as more points are added beyond that concentration. For the aggregated region, same applies to concentrations less than ca. 5 g L^{-1} . The 3-5 g L^{-1} region is marked by red shading, the final CMC=4.303 estimation was performed by regression intersection and is consistent with literature results (Zielinski *et al.*, 1986; Ray *et al.*, 2005) and the ‘transition region’ definition of the CMC (Atkins, 2014b).

12.1.2 *The critical micelle concentration estimation in cetyltrimethylammonium bromide aqueous solutions*

Figure 12.6 illustrates the CMC estimation of pure and binary (1/1 and 2/1 molar) C_{12}TAB and C_{14}TAB surfactants (Svalova *et al.*, 2017). The CMC, R^2 and mean standard deviation (SD) values are shown in Table 12.1. For full temperature-concentration profiles, correlation and R^2 diagnostic plots, see Appendix C.1. Every concentration measurement is an average of ca. 7-20 points. Plots (a,b) and the corresponding R^2 values (Table 12.1) provide good evidence of linearity between velocity and surfactant concentration, and the CMC values correspond to previous measurements (Zielinski *et al.*, 1986; Ray *et al.*, 2005; Sun *et al.*, 2005; Xi & Guo, 2008). Plots (c,d) illustrate multiple micellarisation in CTAB mixtures, with a strong indication of the primary critical micelle concentration (CMC_1); the secondary critical micelle concentration (CMC_2) may be highlighted by taking a (natural) log-transformation as shown in plots (e,f). Similar results were found by Ray *et al.* (2005) illustrating multiple micellarisation of C_nTAB surfactants using tensiometric, conductometric and other methods.

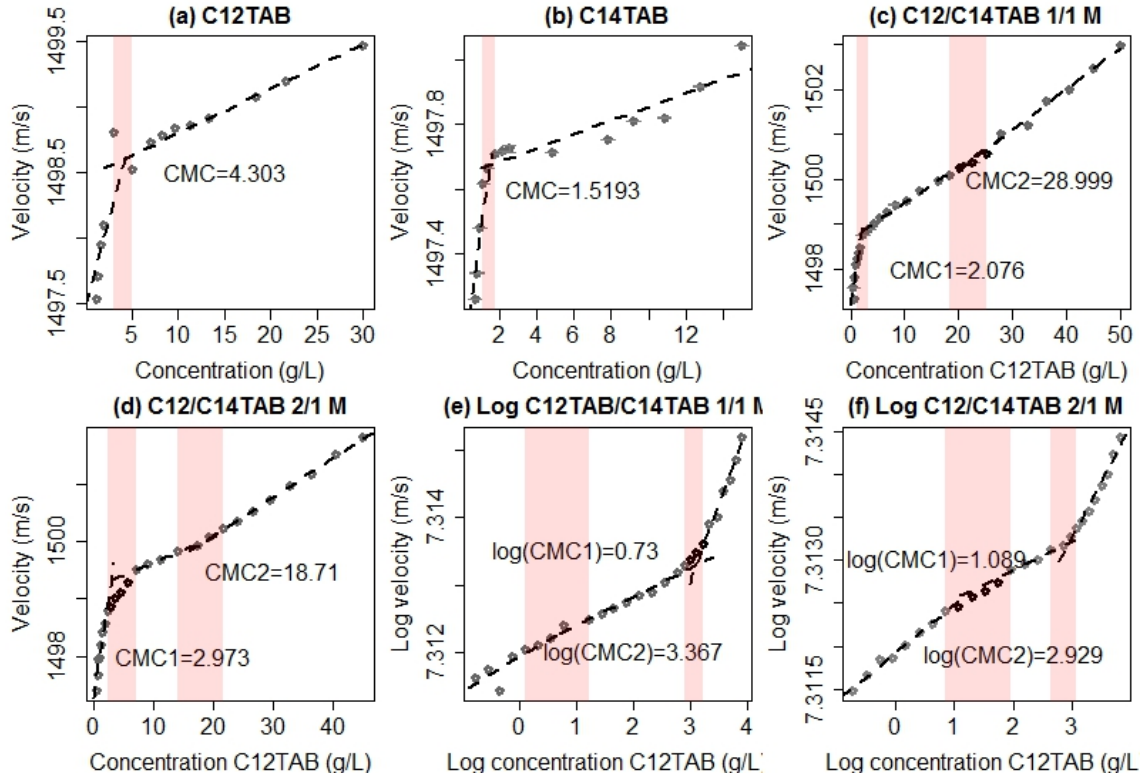


Figure 12.6: Concentration-velocity measurements of CTAB pure and mixed aqueous solutions (Svalova *et al.*, 2017). In (c-f), CMC1 and CMC2 are primary and secondary micelle formation respectively. Black points indicate data that were not included in regression estimation.

Name	SD	CMC ₁ g L ⁻¹	CMC ₂ g L ⁻¹	R^2_{mono}	R^2_{aggr}	R^2_{inter}
C ₁₂ TAB	3.7×10^{-4}	4.31	NA	0.62	0.97	NA
C ₁₄ TAB	7.5×10^{-4}	1.52	NA	0.80	0.84	NA
C ₁₂ /C ₁₄ TAB 1/1 M	7.7×10^{-4}	2.08	29.00	0.74	0.98	0.98
C ₁₂ /C ₁₄ TAB 2/1 M	4.9×10^{-4}	2.97	18.71	0.94	0.999	0.98

Table 12.1: Summary of CTAB concentration-velocity data (Svalova *et al.*, 2017). Mean sample standard deviation is denoted SD, subscripts of R^2 refer to models fitted in the estimated monomer (mono), aggregated (aggr) and CMC₁-CMC₂ intermediate (inter) regions.

12.2 Ultrasonic Characterisation of Asphaltenes

Asphaltene measurements were taken over a longer period of time, whereby the instrument was allowed to equilibrate for 3-4 min before a measurement, and on average 100 velocity measurements were taken per concentration. Figure 12.7 illustrates

the full time-temperature velocity profile for the E1 asphaltene. Time breaks, e.g. in plots (i) and (r), were caused by the re-initialisation of the instrument, possibly due to a propagating air bubble or another artifact. It was later found that a greater number of measurements does not improve the final concentration-velocity profile given that velocities are averaged over the same time period and outliers are treated prior to final inference. The author has discovered that due to the time-velocity gradients mentioned earlier, most stable velocity profiles (and narrow velocity confidence intervals) are achieved when only up to 20 measurements are used for an averaged velocity estimation. Speculatively, this is due to time gradients arising during continuous velocity measurements.

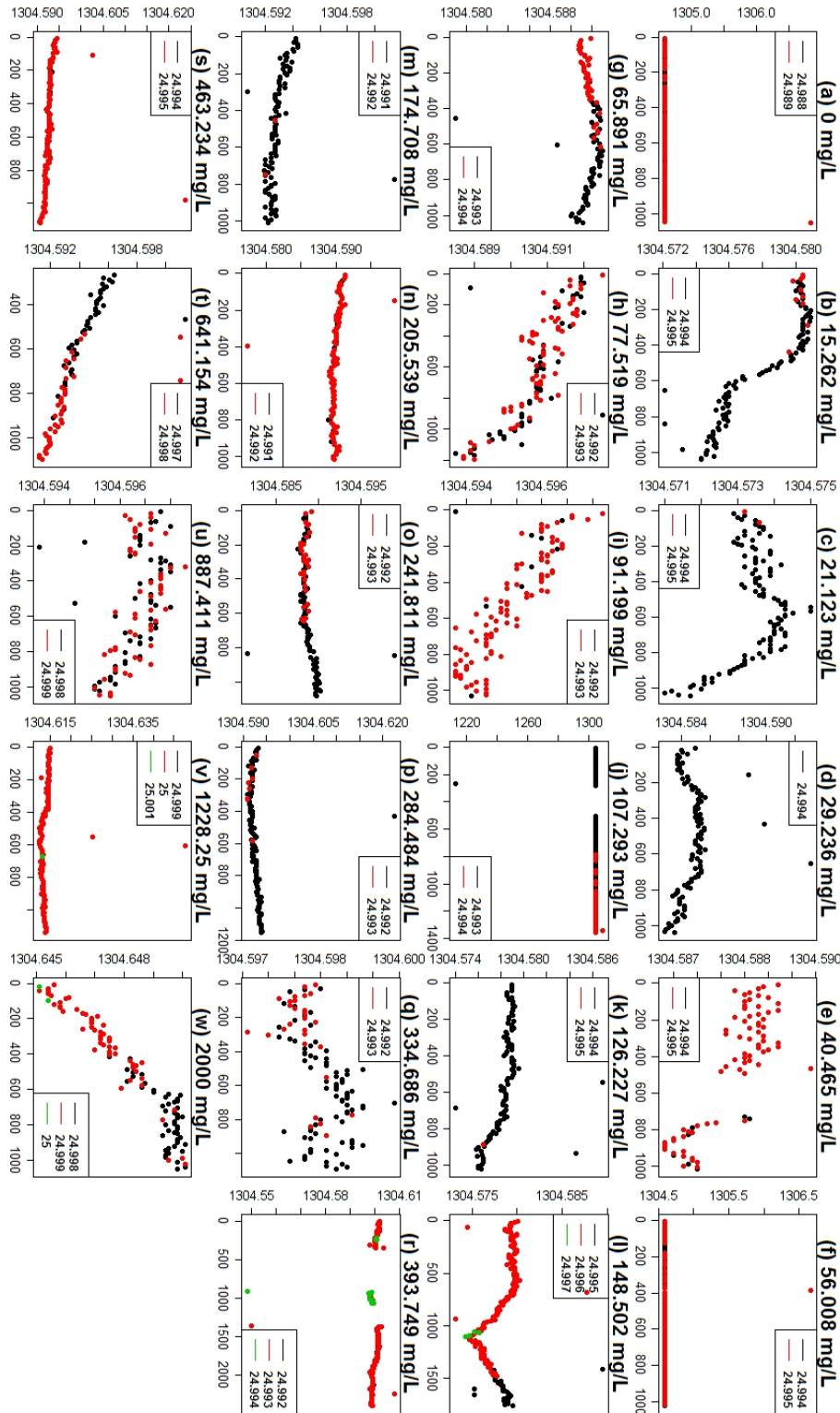


Figure 12.7: Time versus velocity (m s^{-1}) plots of E1 asphaltene ultrasonic measurements. Titles indicate E1 concentration, legends indicate measurement temperature in $^{\circ}\text{C}$.

12.2.1 Pre-processing of velocity data

Due to longer time series, all asphaltene data was treated to remove extreme outliers (Figure 12.9, in plot (b) note the change in velocity range). This section describes the treatment performed on all asphaltene samples, using the velocity measurements of the E1 284.48 mg L⁻¹ sample (Figure 12.7(p)) as an example.

Recall that Resoscan simultaneously measures velocity, attenuation and temperature of a sample (Section 8.2). Given a time-velocity profile for a particular concentration, two underlying models/dependencies were considered, whereby the variation in velocity change was explained by single (M₁) or multiple (M₂) linear regressions:

$$\begin{aligned} M_1 : \quad & \text{velocity} \sim \beta_0 + \beta_1 \times \text{time} + \varepsilon, \\ M_2 : \quad & \text{velocity} \sim \beta_0 + \beta_1 \times \text{time} + \beta_2 \times \text{temperature} + \beta_3 \times \text{attenuation} + \varepsilon, \\ & \text{where } \varepsilon \sim N(0, \sigma^2), \quad \sigma^2 - \text{residual variance.} \end{aligned}$$

The two models are interpreted that the variation in velocity values are explained by the change in time alone (M₁) or the change in time, temperature and attenuation (M₂). It is assumed that increases in attenuation are due to scattering effects from temperature fluctuations, trace amounts of dissolved air and temporal effects/microscopic toluene evaporation (Povey, 1997*d*) (inducing a shift in concentration). Noteworthy, the typical time gradients observed (β_1 in M₁ and M₂) were of the order of 10⁻⁷ to 10⁻⁶ which is respectively five and four orders of magnitude smaller than the velocity variation due to changes in asphaltene concentration (Andreatta *et al.*, 2005*a*). Given a time-velocity profile, the two regression models were fitted and their residual distribution calculated. If a residual lied outside the 95% two-sided confidence interval, the corresponding data point was removed.

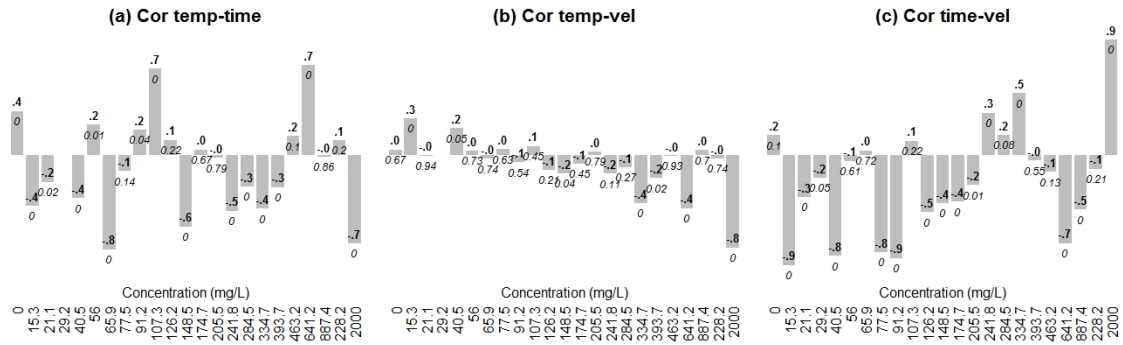


Figure 12.8: Correlation plots of E1 asphaltene ultrasonic measurements. Temperature and velocity are abbreviated as ‘temp’ and ‘vel’ respectively. Labels in bold and italic indicate Pearson’s correlation coefficient and their p -values respectively.

The fitted regression models and their R^2 values are illustrated in Figure 12.9 (c), for M_2 the adjusted R^2 value was used as the latter is more appropriate for multiple linear models. The R^2 and $R^2_{adjusted}$ are denoted R2 and R2a respectively, the residual distributions are illustrated in plot (d). Evidently, M_2 explains a greater proportion of the outliers than M_1 , as the former accounts for variation caused by temperature and attenuation as opposed to time effects only, this is also reflected in a narrower residual/outlier distribution (plot (d)). In plot (c), the triangles and crosses mark the identified extreme outliers following M_1 and M_2 respectively, and the high outlier at ca. 400 s was removed by fitting M_1 but not M_2 . Similar results were observed for other measurements. In conclusion, M_1 was used to process and eliminate extreme outliers in all asphaltene data in order to remove strong effects caused by temperature and attenuation.

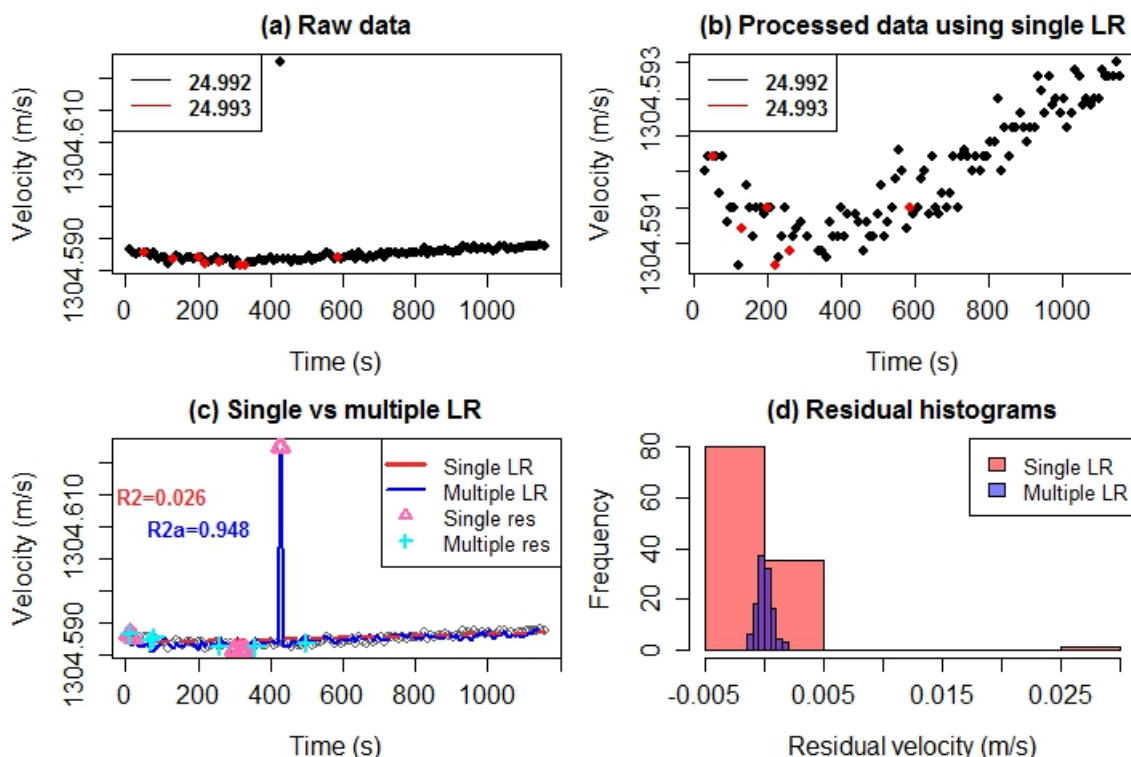


Figure 12.9: Time (s) versus velocity (m s^{-1}) plot of E1 asphaltene ultrasonic measurements, the 284.48 mg L^{-1} sample, Figure 12.7 (p). In all plots, ‘linear regression’ is abbreviated ‘LR’. In plots (a,b) the legend indicates measurement temperature in $^{\circ}\text{C}$, in plot (c) ‘res’ abbreviates residuals obtained from single (LR1) and multiple (LR2) linear models.

Figure 12.10 illustrates the effect of outlier removal and velocity averaging over different time intervals on the final concentration-velocity relation and confidence intervals. Once outliers are removed it is unnecessary to use long time series of velocity measurements which seem to have no improvement of the concentration-velocity relation but significantly increase the confidence intervals. The latter is plausible due to time gradients, as indicated in Figure 12.8 (c).

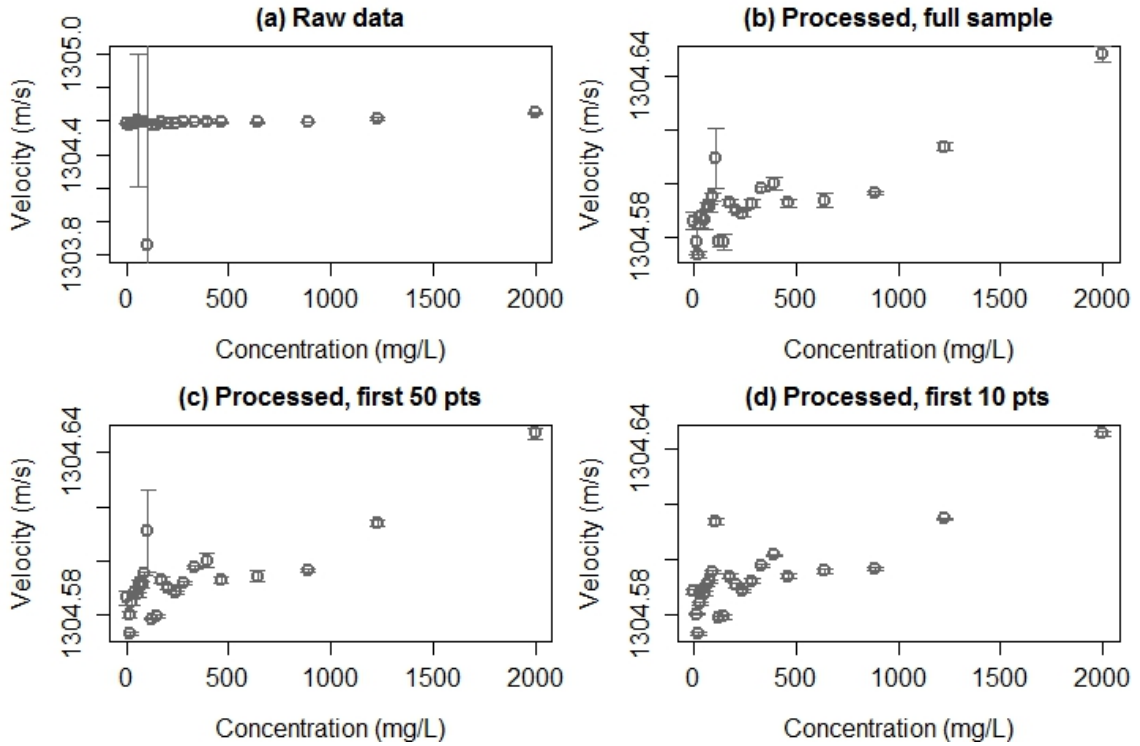


Figure 12.10: Effect of outlier removal and averaging over different time intervals for E1 asphaltene.

In Svalova *et al.* (2017) full-sample averaging was used as the authors were unaware of the impact of longer time series on the confidence intervals, and for consistency this will be followed here as well. Again, this will not affect the critical nanoaggregation region estimation but will widen the 95% confidence intervals.

12.2.2 Constrained optimisation of the CNR

The constrained optimisation scheme (Section 8.3) was used in order to estimate the critical nanoaggregation region (CNR). The use of weighted penalties for R^2 was designed to estimate the aggregation onset (CNR_1) and end (CNR_2). For a given velocity-concentration profile, the monomeric boundary CNR_1 was estimated by fitting regressions recursively from the lowest to the highest concentration and selecting the regression with the largest R_p^2 . The aggregated boundary CNR_2 was estimated in the same fashion, except fitting regressions recursively from the highest concentration to the lowest. The change in the R^2 and R_p^2 values, together with the penalty weights is given in Tables 12.2 and C.1 for E1 asphaltene and C.2-C.7 for the remaining samples, the estimated CNR are given in Table 12.3. For E1, R^2

is (almost) monotonically decreasing as more points are added to the aggregated region model, which is not entirely useful for our purposes. This rationalises the use of a length-based penalty P_1 . For both CNR boundaries, the R^2 and R_p^2 values through the first few points were set to -5 to avoid the automatic selection of a very early onset of CNR_1 and a very late onset of CNR_2 . This did not contradict the literature estimations of the CNAC (Mullins, 2011).

Conc.	P_1	w_2P_2	P_2	w_3P_3	P_3	R^2	R_p^2
21.12	0.58	0.01	1.38×10^{-3}	0.052	5.21×10^{-5}	-5	-5.00
29.24	0.5	0.15	0.015	0.431	4.31×10^{-4}	-5	-5.00
40.47	0.45	0.11	0.011	0.224	2.24×10^{-4}	0.039	-0.740
56.01	0.41	0	0	0.026	2.62×10^{-5}	0.13	-0.305
65.89	0.38	0	0	0.052	5.24×10^{-5}	0.34	-0.091
77.52	0.35	0	0	2.00×10^{-3}	2.00×10^{-6}	0.437	0.082
91.20	0.33	0	0	0.012	1.18×10^{-5}	0.571	0.226
107.29	0.32	0.129	0.013	0.066	6.61×10^{-5}	0.7	0.189
126.23	0.3	0.28	0.028	0.117	1.17×10^{-4}	0.229	-0.467
148.5	0.29	0.2	0.02	0.069	6.87×10^{-5}	0.05	-0.504
174.71	0.28	0	0	3.30×10^{-3}	3.30×10^{-6}	0.082	-0.199
205.54	0.27	0	0	8.80×10^{-3}	8.8×10^{-6}	0.081	-0.195
241.81	0.26	0	0	9.90×10^{-3}	9.90×10^{-6}	0.068	-0.201
284.48	0.25	0	0	1.40×10^{-3}	1.40×10^{-6}	0.088	-0.164
334.69	0.24	0	0	4.70×10^{-3}	4.70×10^{-6}	0.157	-0.09
393.75	0.24	0	0	2.50×10^{-3}	2.50×10^{-6}	0.237	-1.00×10^{-3}
463.23	0.23	0	0	8.00×10^{-3}	8.00×10^{-6}	0.209	-0.028
641.15	0.22	0	0	8.10×10^{-3}	8.10×10^{-6}	0.18	-0.052
887.41	0.22	0	0	5.10×10^{-3}	5.10×10^{-6}	0.185	-0.039

Table 12.2: Constrained nanoaggregation region estimation of E1 asphaltene, monomeric boundary selection using constrained optimisation, $w_2 = 10, w_3 = 1000$. Concentration indicated in mg L^{-1} . The length, outlier and slope penalties are abbreviated P_1, P_2 and P_3 respectively. Grey shading indicates concentrations with the highest R^2 and R_p^2 .

The change in penalties (from Tables 12.2 and C.1) with increasing concentration is illustrated for E1 asphaltene in Figure 12.11. Plots (b,d) illustrate the weighted penalties used in the R_p^2 calculation, red shading indicates the estimated CNR. The aggregation region is marked by a sharp decrease in the R^2 values for both,

monomeric and aggregated boundaries (plot (a)). The outlier and slope penalties have a maximum at the CNR and decline afterwards. Note that the length penalty (purple circles in plot (b), P_1) is always monotonically decreasing (Section 8.3). With the E1 sample, the inference using R_p^2 is only marginally different to that using ordinary R^2 , except the monomeric region is estimated to occur at a lower concentration due to larger outliers (blue triangles, P_2) and stronger change in regression slope (magenta crosses, P_3). Naturally, $R_p^2 < R^2$ for all measurements.

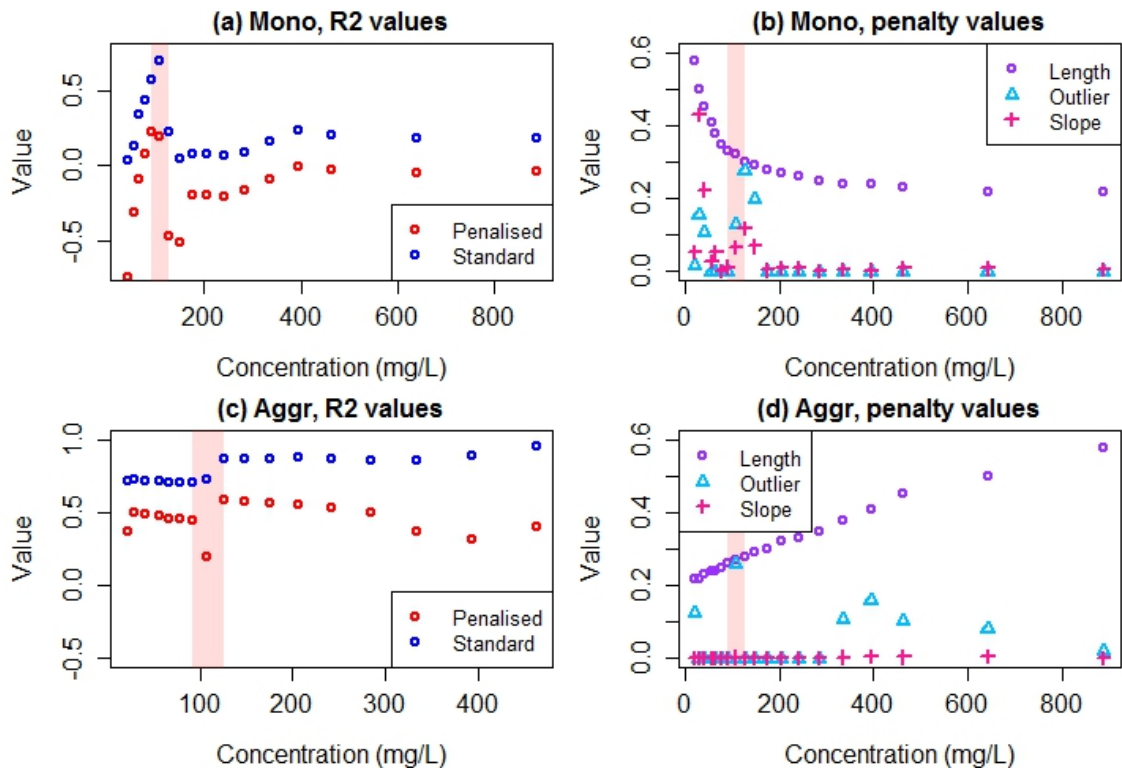


Figure 12.11: Linear model selection criteria in the CNR estimation for E1 asphaltene.

The penalty weights in the constrained optimisation scheme (Section 8.3) were chosen such that $w_i P_i, i = 2, 3$ were on a meaningful scale, e.g. 10^{-2} - 10^{-1} , and no weighted penalties exceed unity. For E1 asphaltene, $w_2 = 10$ and $w_3 = 1000$, which was used in the majority of other cases.

What follows illustrates that the CNR estimation was robust through changes in the penalty weights, as shown in Figure 12.12. The later is a series of bar plots, and whereby only one bar is shown (plots (c,d)) the change in penalty weights did not affect the choice of a CNR boundary. Firstly, w_2 was varied from 1 to 100 with a stepsize of 1, w_3 fixed at 10^3 and the distributions of CNR_1 and CNR_2 are shown

in Figure 12.12(a,c). To follow, the outlier penalty weight was fixed, $w_2 = 10$, and w_3 was varied from 10 to 10^4 with a step size of 10; the resulting CNR distributions are illustrated in plots (b,d). The final CNR_1 and CNR_2 estimation was a weighted average of the two iterations, Table 12.3. The bar plots for samples E3 and E4 are shown in Figures C.18 and C.19. For the sample E2, the weight search above did not generate other CNR estimations than in Table 12.3, thus the plot is omitted.

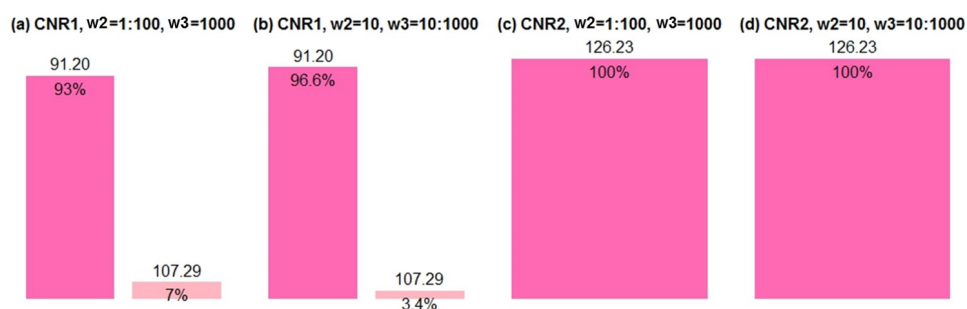


Figure 12.12: Barplot of the CNR_1 and CNR_2 (mg L^{-1}) estimation of E1 asphaltene as a function of varying penalty weights. In plots (b) and (d) a single bar is drawn indicating that no other values have been estimated.

Optimisation diagnostics for the remaining asphaltene samples are shown in Appendix C.2.

12.2.3 Results of the asphaltene CNR estimation

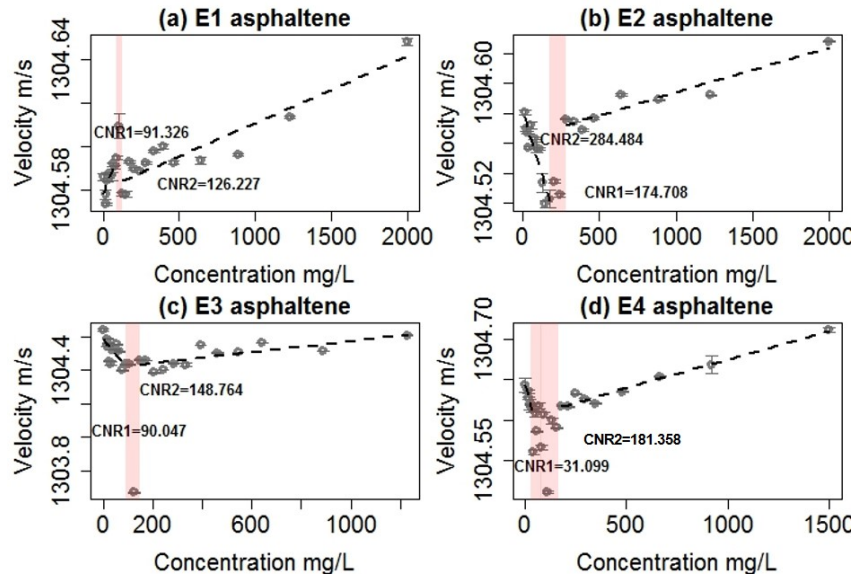


Figure 12.13: Concentration-velocity measurements of asphaltene-toluene mixtures. Dashed lines illustrate estimated linear models using constrained optimisation, CNR1 and CNR2 refer to the onset and decline of the critical nanoaggregation region respectively.

Figure 12.13 illustrates ultrasonic velocity measurements of four asphaltene samples with linear models superimposed. Every concentration measurement is an average of 60-100 points, the confidence intervals represent the mean \pm standard deviation. Piecewise regression models indicated by dashed lines were fitted using the constrained optimisation scheme. In general, the four plots suggest that at either ends of asphaltene concentration range the association with ultrasonic velocity is linear, and the CNR is indicated by large outliers and a change in regression slope. The width of the CNR (Δ CNR) and the velocity difference between the monomeric and aggregated linear models (Δu) are highly-variable across the samples which will be addressed further in Discussion (Chapter 14) by looking at the principal component analysis of combined asphaltene ultrasonic and geochemical data. Note that the inter-measurement change in the speed of sound is larger than the confidence intervals in the majority of cases. Noteworthy, in (Svalova *et al.*, 2017) the upper boundary of the sample E4 CNR has been estimated at a different value- this will also be addressed in Discussion.

Name	CNR ₁	CNR ₂	Δ CNR	Δu	R_{mono}^2	R_{aggr}^2	Total R_p^2
E1	91.33	126.23	34.90	1.70×10^{-2}	2.25×10^{-1}	5.90×10^{-1}	8.16×10^{-1}
E2	174.71	284.48	106.78	5.30×10^{-2}	5.33×10^{-1}	5.47×10^{-1}	1.08
E3	90.05	148.76	58.72	2.70×10^{-2}	1.06×10^{-1}	3.37×10^{-1}	4.44×10^{-1}
E4	31.10	181.36	150.26	5.00×10^{-3}	4.30×10^{-1}	6.40×10^{-1}	1.07

Table 12.3: Regression penalised R^2 values of asphaltene concentration-velocity data. Total R_p^2 denotes the sum of R_{mono}^2 and R_{aggr}^2 , Δ CNR denotes the CNR (mg L^{-1}) width, Δu denotes the velocity jump. Subscripts of CNR denote the onset₁ and decline₂ of aggregation. Penalised R^2 subscripts refer to estimated models in the monomer and aggregate regions.

Chapter 13. Empirical Bayesian Inference of Asphaltene Nanoaggregation

13.1 Model Calibration with Synthetic Data

13.1.1 *One changepoint model*

A synthetic data set \mathbf{y} following specification in Equation (9.5) is illustrated in Figure 13.1 and has parameter values:

$$\begin{aligned} \alpha_1 &= 150, & \beta_1 &= 0.5, & \sigma_1^2 &= 6, & \alpha_2 &= 250, \\ \sigma_2^2 &= 20, & \gamma &= 60 & \mathbf{x} &= e^i, & i &= 3, 3.01, \dots 5. \end{aligned} \quad (13.1)$$

Note that the segments of x are exponential which reflects our experimental data (Svalova *et al.*, 2017). Figure 13.1 (a) illustrates the full synthetic data set, plot (b) is a 10-point discretised set (only every 10th point from the original data set retained) used to assess prediction accuracy in conditions of low data availability. In the anal-

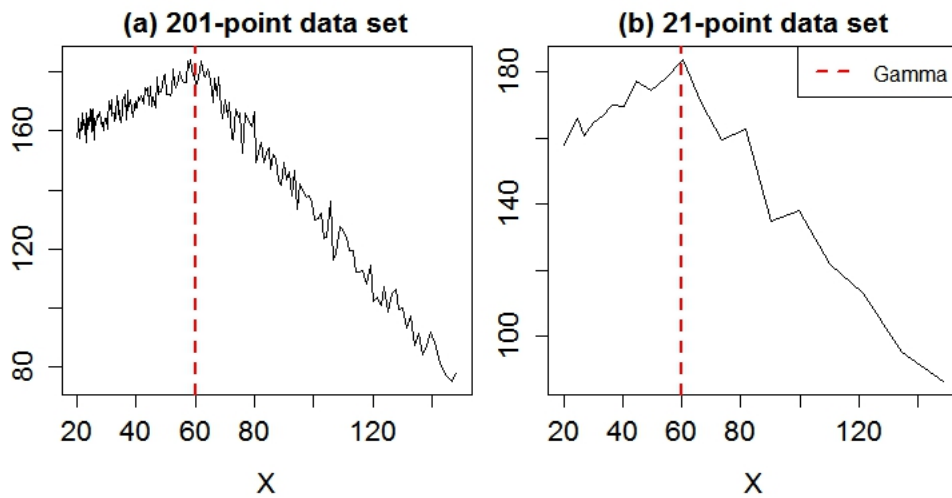


Figure 13.1: Synthetic data for testing the single-changepoint model following (13.1).

ysis to follow, the main parameter(s) of interest is the changepoint γ (equivalently, γ_1 and γ_2 assuming the bridge model) as it would represent the critical nanoaggregation concentration (region).

Prior to analysing the MCMC results, what follows details the burn-in period selection. In order to obtain reliable posterior estimates, the initial convergence period (burn-in) needs to be discarded. Brooks *et al.* (2011) (p. 19) suggests that if an MCMC chain starts near its equilibrium, discarding long series of draws may be unnecessary. Regarding the present data, Figure D.1 illustrates the MCMC chains for γ (or γ_1 for a bridge model) in different settings, e.g. synthetic data assuming a single-changepoint (plots (a,b)) and bridge (plots (c,d)) models and E1 sample data assuming both models (single and bridge in plots (e) and (f) respectively). It can be seen that the chain behaviour, such as the mixing efficiency and the onset of equilibrium is varied across the different scenarios, and in some cases (e.g. plots (b,e)) may require a generous burn-in. Noteworthy, the Figure illustrates draws using a Metropolis-Hastings scheme (Lee, 2012, p.317), which has less efficient mixing than a Gibbs sampler (Lee, 2012, p.294) that is used for the parameters for whom the marginal conditional posterior distributions are available. In most cases throughout this study, the chains were run for 10^6 iterations, discarding the first 50% as burn-in (Brooks *et al.*, 2011, p. 163, although they dealt with much lower numbers). Although the latter strategy may appear overcautious, running simulations for such a long period of iterations ensured smoothness of the obtained conditional marginal posterior distributions that would be unlikely to change with more iterations. Additionally, the short computation times per run (on the order of minutes) made this affordable. Plots (e) and (f) may also reveal that the mixing of the sampler is more efficient assuming a bridge model, although plot (f) reveals an interesting sampling ‘ceiling’, this will be discussed in Section 13.2.

To estimate the conditional marginal posterior distributions of the changepoint in the synthetic data following Equations (13.1), an MCMC sampler was run for 10^6 iterations discarding the initial 50% as a burn-in. Parameter priors were centred at the parameter true values, standard deviations were set at 0.2 times prior mean, the γ prior was Normal (Gaussian). The M-H step for γ used a Normal proposal centred at the current chain value and had a standard deviation of 30, and had a constraint such that $\gamma^{\text{candidate}}$ was at least two data points away from the sample data boundaries. The chain mixing was efficient for all parameters updated via Gibbs step, trace plots and posterior marginal conditional distributions are provided in Figures D.2

(201-point data), D.3 (21-point data) and D.4 respectively. Figure 13.2 illustrates chain mixing for γ using the two data sets and compares sampler efficiency between 10^5 and 10^6 iterations (first half discarded) whereby in the latter case the sample space exploration is significantly better and the sampler appears to have converged. Evidently, using a smaller data set does not strongly reduce the accuracy of γ estimation as the marginal conditional posterior means in plots (b) and (d) are very similar.

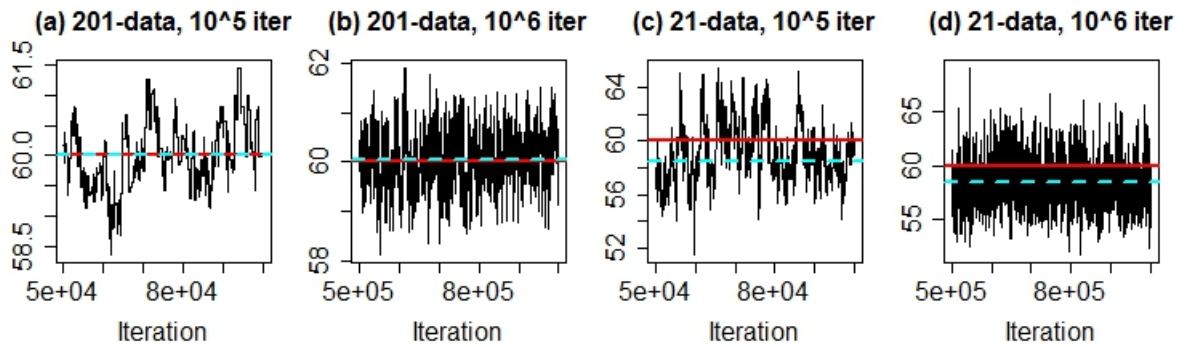


Figure 13.2: MCMC traces of γ conditional marginal posterior using 201-point and 21-point data sets (abbreviated 201-data and 21-data respectively), prior mean is set at the true parameter value. Solid red and dashed cyan lines indicate prior and posterior means respectively.

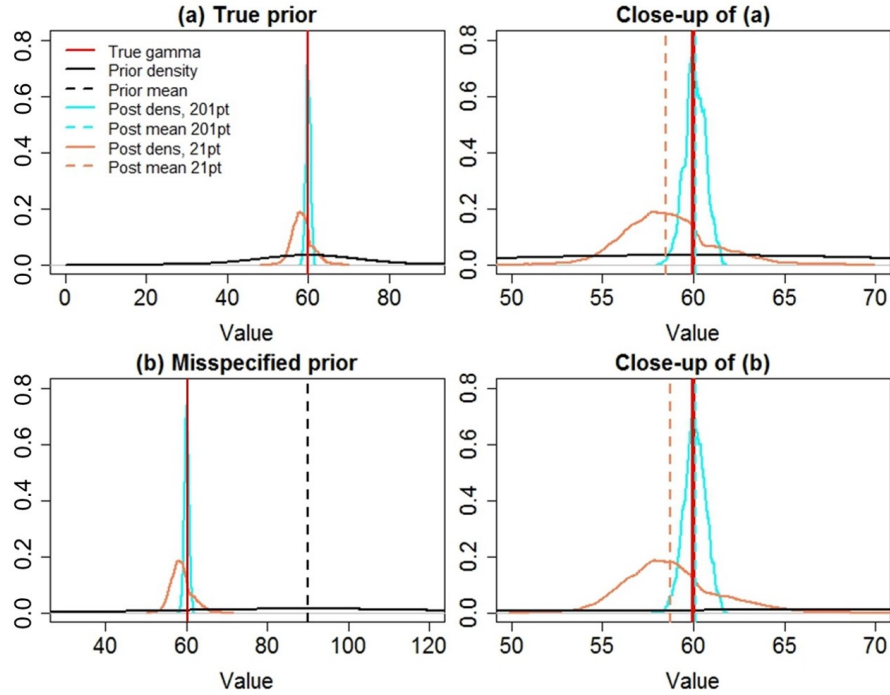


Figure 13.3: Posterior density plots of γ assuming a one-changepoint model using synthetic data. The densities are based on the final 50% of 10^6 iterations.

Figure 13.3 (a,b) and Figure D.4 illustrates posterior densities of γ and the remaining parameters respectively. Overall, there is a dramatic decrease in the parameter variance for most of the variables, including γ . Plot (a) in Figure 13.3 illustrates that there is a marginal reduction in the accuracy of the posterior γ mean using a smaller data set, however it is not significant to negatively influence the inference about the changepoint. For α_1, β_1 and α_2 (Figure D.4 plots (a,b,d)), a dramatic decrease in variance is observed using either of the data sets. Both posterior mean estimations are close to the prior means (true parameter values). Using a smaller data set in this case did not negatively affect the posterior estimation although the variance is somewhat greater. Importantly, this suggests that a 10-fold decrease in data quantity does not significantly reduce the quality of the MCMC posterior estimation. Therefore the scheme can be applied to the asphaltene velocity data. The posterior densities of σ_1^2 and σ_2^2 see a smaller decrease in variance from the prior than for the remaining parameters. For σ_1^2 especially, using a 21-point data set yields a very accurate posterior estimate.

The proposed MCMC scheme is also robust against prior misspecification. The prior means were scaled by 1.5 (offset by 50%) and standard deviations set at at 0.5 times

the prior mean. Figure 13.4 illustrates the posterior γ chain mixing for the two data sets showing that (surprisingly) the sampler is more efficient in exploring the sample space when the smaller data set is used. The prior mean for γ was set at 90 and outside the range of the Markov chain. The conditional marginal posterior densities of γ are near-identical to the true prior mean case, as illustrated in Figure 13.3(b). The posterior densities and trace plots of the remaining parameters were very similar to the true prior case, thus are omitted.

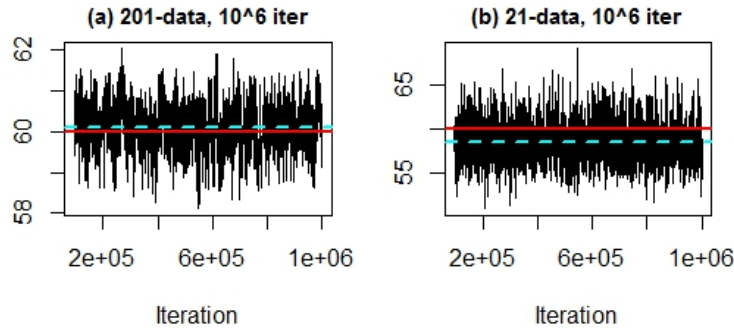


Figure 13.4: MCMC trace of γ posterior density using 201-point and 21-point data sets, prior mean is set at 1.5 times true parameters value. Solid red and dashed cyan lines indicate true γ and posterior mean respectively. The prior γ mean of is beyond the plot range.

To confirm that the models perform well and test the posterior model fit in sample data predictive distributions were simulated (10^4 draws) using conditional marginal posterior mean parameters estimations, from which the mean squared error (MSE), mean average error (MAE) and Pearson correlation (with corresponding p -values) between the observed and predictive values was calculated (Fawcett *et al.*, 2017). The diagnostic quantities are summarised in Table 13.1 for the 201-point and 21-point data sets, for priors centred at true and misspecified parameter means. The information criteria indicate that posterior fits are very similar for both runs. The MAE and MSE are lower for the larger data sets which is expected. The correlation between synthetic data and predictive distribution is very strong in all cases. Additionally, to ensure that the MCMC draws are independent, the partial autocorrelation function (PACF) (Gelman & Lopes, 2006) was calculated for both data sets and the were very low. The results were near-identical for the two data sets, therefore only one result is shown (Figure D.5).

Data	MAE	MSE	Cor ρ , p -value
201-point, true	-0.02	11.33	0.99, 2.2×10^{-16}
201-point, missp	-0.02	11.31	0.99, 2.2×10^{-16}
21-point, true	-0.05	11.75	0.99, 2.2×10^{-16}
21-point, missp	-0.07	11.64	0.99, 2.2×10^{-16}

Table 13.1: Posterior diagnostic criteria for assessing single-changepoint model fit. Posterior runs based on true and misspecified prior means are marked accordingly. Correlation (Cor) is calculated for the association between true and predicted values (Fawcett *et al.*, 2017). Information is calculated on 10^6 draws from posterior distributions discarding the initial 5×10^5 as burn-in.

13.1.2 Two-changepoint model with a Brownian bridge

The Brownian bridge scheme was tested using synthetic data (Figure 13.5) following the specification

$$\alpha_1 = 150, \quad \beta_1 = 0.5, \quad \sigma_1^2 = 6, \quad \alpha_2 = 350, \quad \beta_2 = -1, \\ \sigma_2^2 = 20, \quad \gamma_1 = 60, \quad \gamma_2 = 90, \quad \kappa = 10 \quad \text{and} \quad \mathbf{x} = e^i, i = 3, 3.01, \dots 5. \quad (13.2)$$

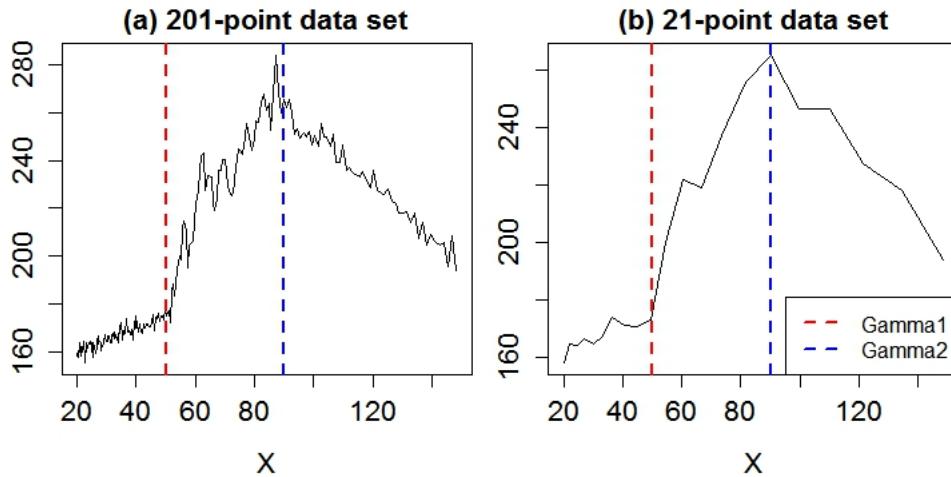


Figure 13.5: Synthetic data for testing the Brownian bridge model following (13.2).

Due to the nature of γ_1 and γ_2 their priors are ‘in reality’ correlated. It will be shown later with the sample data that for the estimated CNR widths and using very wide prior distributions, the posterior draws of γ_1 and γ_2 are only weakly correlated. However, the introduction of correlated priors (or a joint bivariate prior) may be the next step of this investigation. The MCMC sampler was run for 10^6

iterations discarding the initial 50% as a burn-in. As with the previous model, the scheme was firstly run with parameter means at true parameter values, standard deviation as before. During the M-H steps, Normal proposals were used for γ_1 and γ_2 , centred at current sampler value with a standard deviation of 30. An additional condition added in the changepoint proposal forced the bridge segment is at least two points long, whereby $\gamma_1^{\text{candidate}} < \gamma_2^{\text{current}}$, and equivalently $\gamma_2^{\text{candidate}} > \gamma_1^{\text{current}}$. Prior distributions were Normal (standard deviation of 30) for both changepoints. The remaining parameters were updated using a Gibbs mechanism.

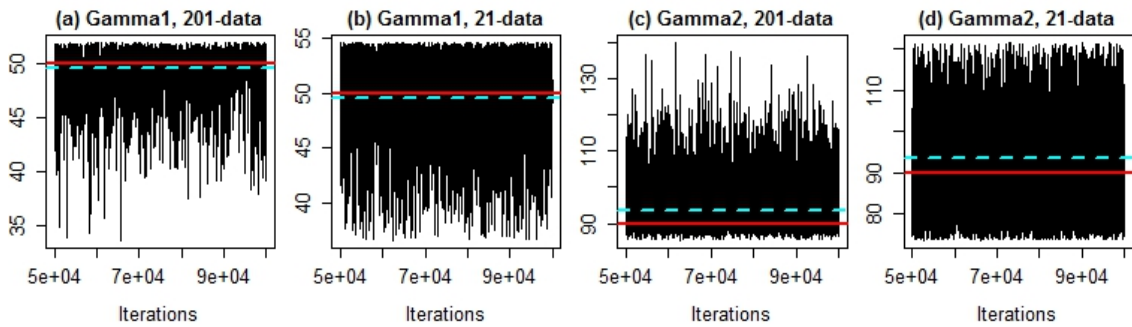


Figure 13.6: MCMC traces of γ_1 and γ_2 posterior densities using 201-point and 21-point data sets, prior mean is set at the true parameter value. Solid red and dashed cyan lines indicate prior and posterior means respectively.

Figure 13.6 illustrates MCMC traces for γ_1 and γ_2 , Figure D.6 illustrates trace plots for the 21-point data set posterior parameter estimations. The use of 201-point data set produced very similar traces, thus the plots are omitted. The posterior estimation of the changepoints is consistent with the prior means. In all plots, the Markov chains appear to have an upper/lower boundary which is consistent with the sharp change between the bridge and regression segments in Figure 13.5. These boundaries are less strong for the larger data set which illustrates the advantage of using more data.

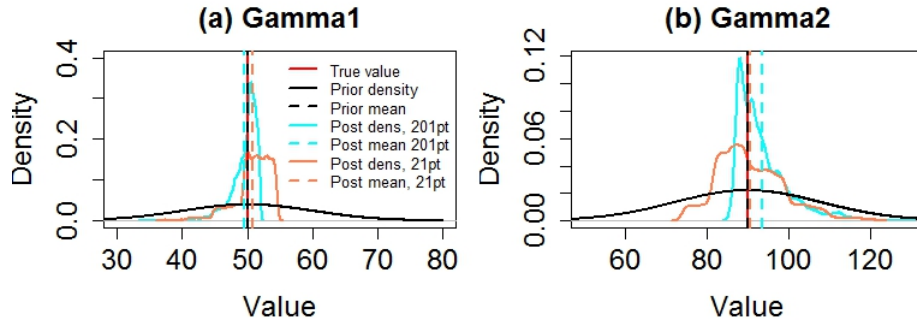


Figure 13.7: Plots of marginal conditional posterior posterior densities of γ_1 and γ_2 , prior means are set at true parameter values.

Figure 13.7 illustrates the posterior densities for the two changepoints, which illustrate a decrease in the variance of γ_1 and γ_2 . Apparent is the lack of smoothness of the densities, which can be explained as follows. As a new candidate value of either of the changepoints is proposed, the data is compartmentalised into regression and bridge segments and the posterior distribution of a changepoint will have local minima and maxima which correspond to the data point locations- as there are not too many plausible changepoint locations. This roughness is not too pronounced with synthetic data, however will become very strong when inference with the sample data is performed, especially for the the bridge model. Figure D.7 illustrates posterior densities and posterior means from the simulation, ordinary least squares estimates are also shown. For all parameters posterior means are consistent with true parameter values. In conclusion, using the two data sets gives very similar posterior mean values, although the variance is greater with the smaller set. Similarly to the above, the bridge model was tested with prior means at 1.5 times true parameter value and prior variances at 0.5 times prior mean. Figure 13.8 illustrates the posterior densities of the two changepoints which are very similar to Figure 13.7, the remaining plots are omitted. Overall, assuming the two underlying models, the testing has illustrated that the MCMC scheme provides consistent parameters estimation despite misspecified priors with an offset of 50% from their true parameter values. Table 13.2 provides performance diagnostics for both data sets and prior (mis-) specifications.

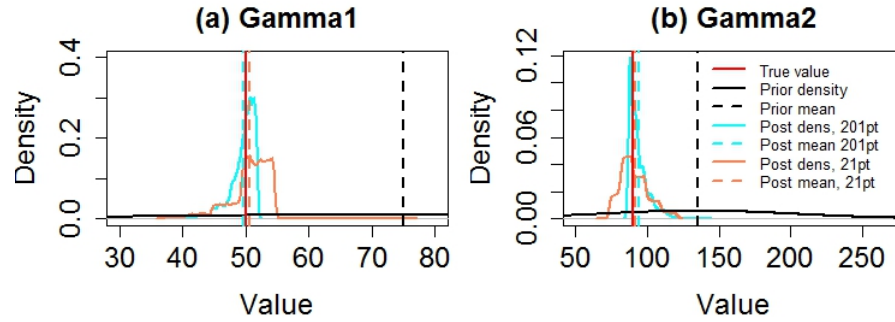


Figure 13.8: Marginal conditional posterior densities of γ_1 and γ_2 , prior means set at 1.5 times true parameter values.

Data	MAE	MSE	Cor ρ , p -value
201-point, true	5.06	115.98	0.95, 2.20×10^{-16}
201-point, miss	5.74	131.19	0.94, 2.20×10^{-16}
21-point, true	8.14	194.49	0.93, 1.51×10^{-7}
21-point, miss	7.91	183.62	0.94, 9.66×10^{-8}

Table 13.2: Posterior diagnostic criteria for assessing Brownian bridge model fit. Posterior runs based on true and misspecified prior means are marked accordingly. Correlation (Cor) is calculated for the association between true and predicted values (Fawcett *et al.*, 2017). Information is calculated on 10^5 draws from posterior distributions discarding the initial 5×10^4 as burn-in.

The MSE values are quite large due to the high stochasticity of the bridge segment. This is plausible as the expectation of the values along the bridge are given only by its trajectory and not by the Brownian uncertainty (Equation (9.19) in Section 9.2.2). The correlation between posterior predictive distributions and synthetic data is > 0.8 for all data sets. The PACF plots in Figure D.8 show low values for all parameters.

13.2 Experimental Data

13.2.1 Prior elicitation

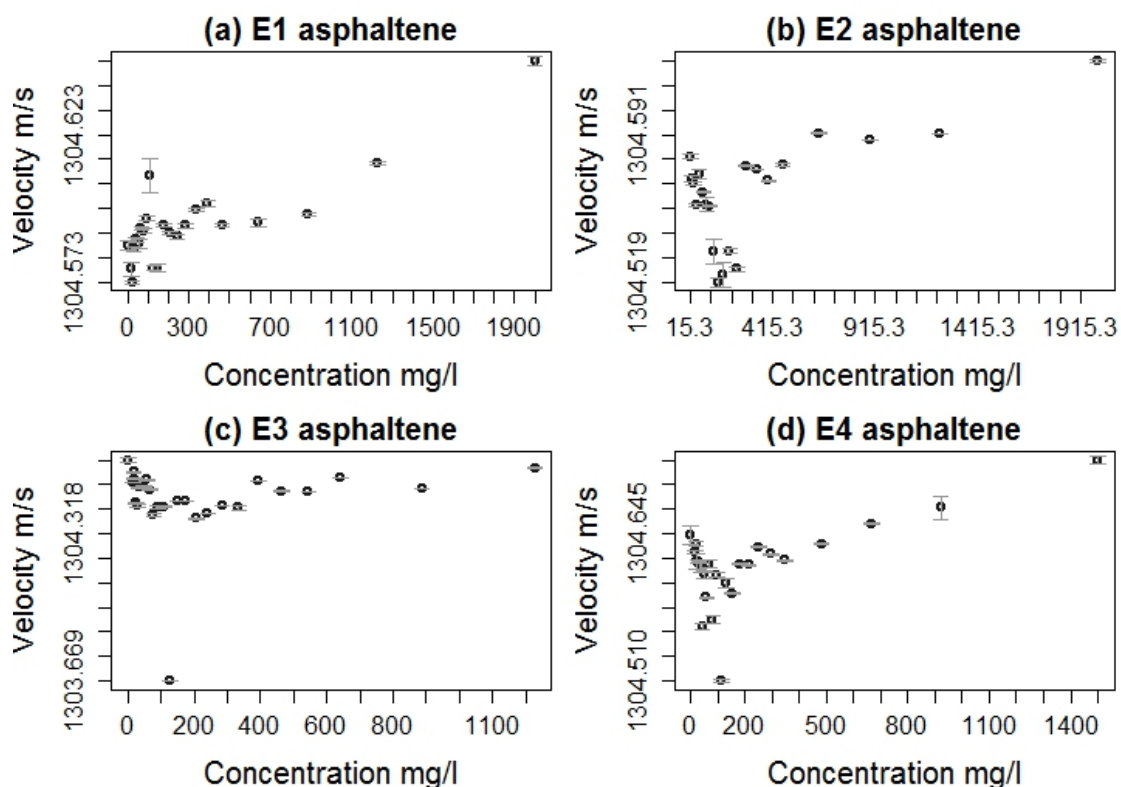


Figure 13.9: Velocity characterisation of asphaltene aggregation in E1-E4 asphaltenes (Svalova *et al.*, 2017).

Priors for the regression coefficients were performed using the constrained optimisation data, Tables 12.2, C.1 and C.2-C.7. The variation in regression coefficients before 100 mg L^{-1} (Mullins, 2011) was interpreted as representative of the coefficient variation in the monomeric region and that after 100 mg L^{-1} as variation in the aggregated region. The coefficient distributions and fitted prior densities are shown in Figure 13.10.

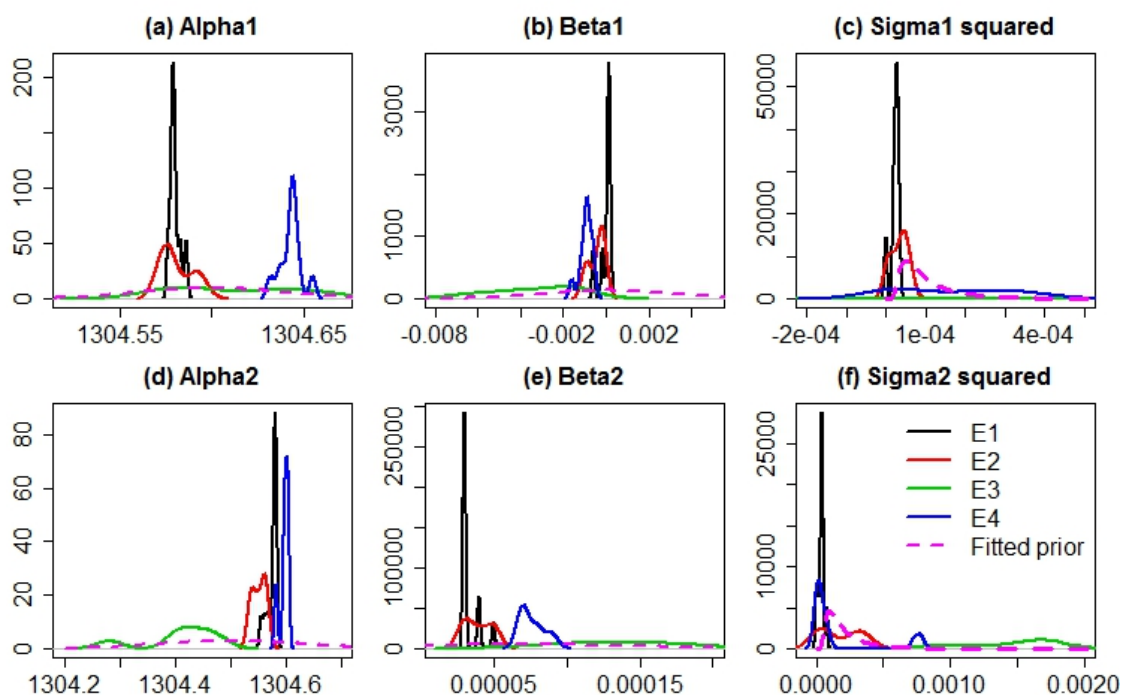


Figure 13.10: Densities of the parameters assuming a one-changepoint model with $\gamma = 100$ using data from constrained optimisation.

The illustrated plots are multimodal and in many cases the variation in regression parameters, e.g. plots (a) and (f), does not overlap. Additionally, for E3, due to an extreme outlier at ca. 110 mg L^{-1} the parameter densities are extremely wide. The corresponding prior formalisms have included this variation where possible and are as follows:

$$\begin{aligned} \alpha_1 &\sim N(1304.6, 0.13^2), & \beta_1 &\sim N(0, 0.003^2), & \sigma_1^2 &\sim IGa(2.01, 1.5 \times 10^{-4}), \\ \alpha_2 &\sim N(1304.5, 0.13^2), & \beta_2 &\sim N(0.7 \times 10^{-4}, 0.8 \times 10^{-8}), & \sigma_2^2 &\sim IGa(2.03, 3 \times 10^{-4}). \end{aligned} \quad (13.3)$$

What follows will compare the fit of the single-changepoint and bridge models to the asphaltene data to assess the plausibility of a critical nanoaggregation point versus a range.

13.2.2 One changepoint model

An MCMC scheme was run for the estimation of the critical nanoaggregate concentration in the asphaltene samples E1-E4 assuming a one-changepoint regression model. The scheme was run for 10^6 iterations, discarding the first half as a burn-in.

The prior distribution for γ was $\gamma \sim N(100, 50^2)$, which is consistent with literature (Mullins, 2011). Although the standard deviation of 50 is quite large, this was chosen so that the M-H update explores the sample space efficiently. The proposal kernel for γ was also Normal with a standard deviation of $v = 30$ and truncated above zero. The proposal mechanism included an additional condition such that no linear region is less than two points long. A search over a range of $v \in [1, 2, \dots, 40]$ was performed in order to ensure no correlation with the information criteria and posterior MAE/MSE.

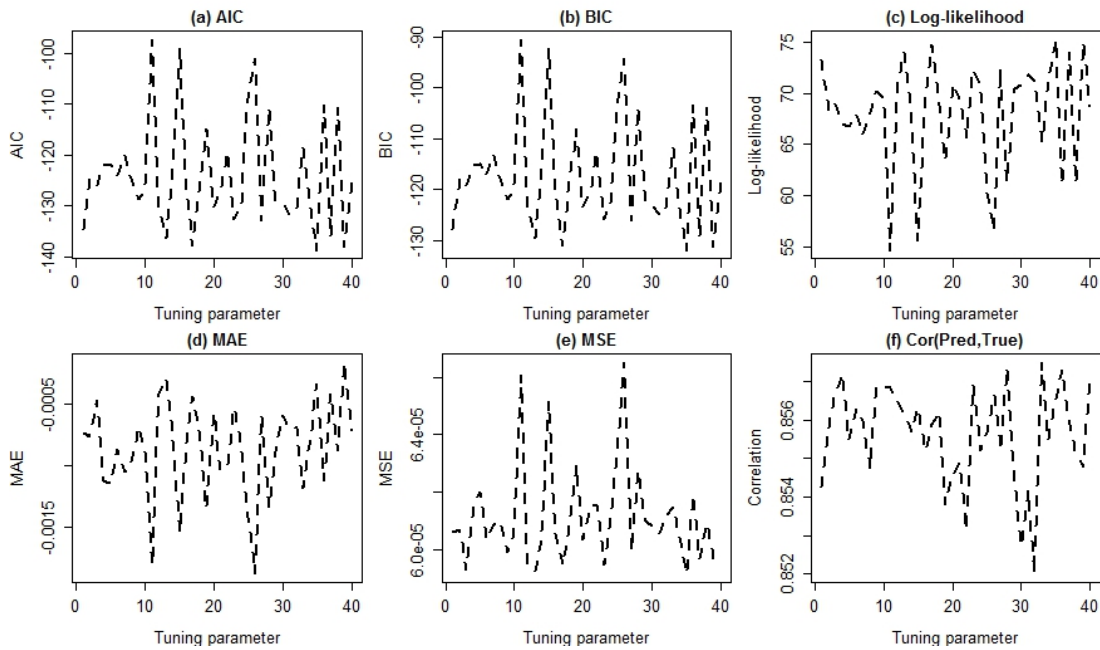


Figure 13.11: Variation of posterior single changepoint model performance with the change in tuning parameter v using E1 asphaltene data.

Figure 13.12 illustrates the MCMC draws from the γ conditional posterior distributions. A typical output trace for the remaining parameters is shown for E1 in Figure D.9. The mixing in the four plots looks satisfactory, except the ‘ceiling’ in plot (c) which is consistent with the large outlier (Figure 13.9(c)) which compartmentalises the sample.

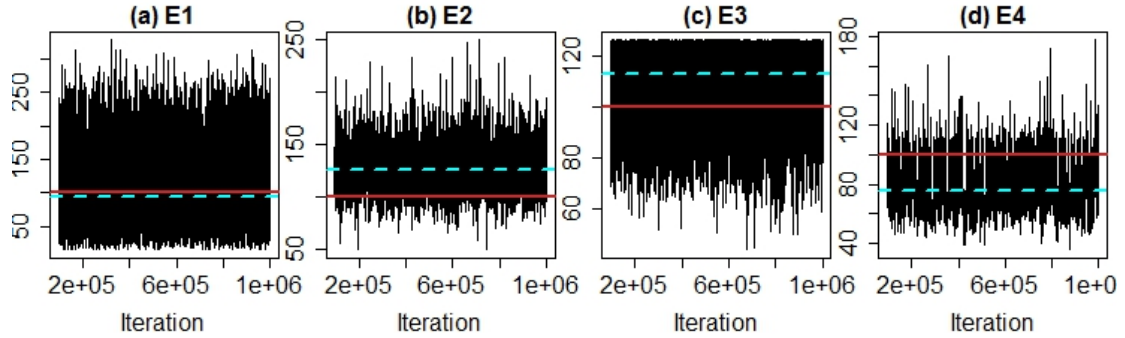


Figure 13.12: Trace plots of 10^6 MCMC iterations of the γ conditional marginal posterior distribution, first 50% discarded as a burn-in. Solid red and dashed cyan lines indicate prior and posterior means respectively.

Figure 13.13 illustrates the conditional marginal posterior densities of γ for E1-E4, again an example of densities for the remaining parameters is shown for E1 in Figure D.10. A strong indication of a dominant posterior mode emerges in all of the samples, although there are second modes. The slight multimodality arises due to data scarcity giving rise to the posterior mode instability. This multimodality is only apparent for the γ conditional marginal posteriors as they are samples through a H-M update- those sampled by a Gibbs samples are smooth and unimodal, as shown in Figure D.10. Finally, no significant partial autocorrelations were observed beyond lag 2 for any of the γ traces, as indicated in Figure 13.14 and for all of the model parameters of E1 (Figure D.11).

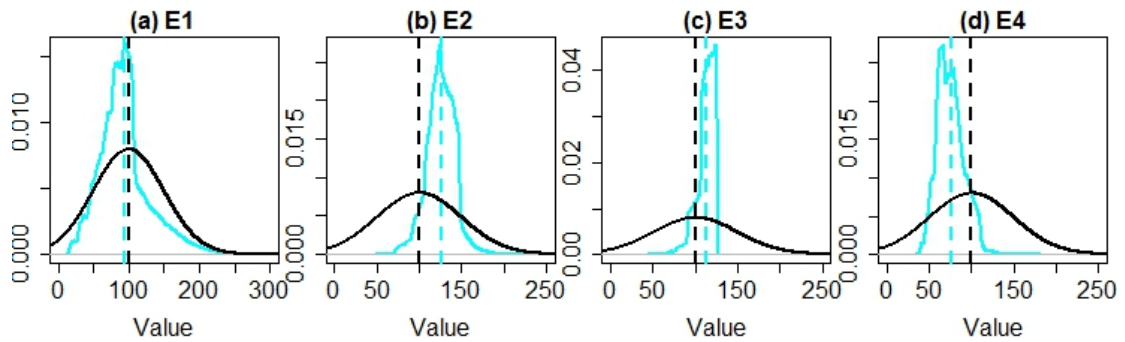


Figure 13.13: Density plots of the conditional marginal posterior distributions of γ . Black solid and dashed lines represent prior density and mean respectively, cyan solid and dashed lines represent posterior density and mean respectively.

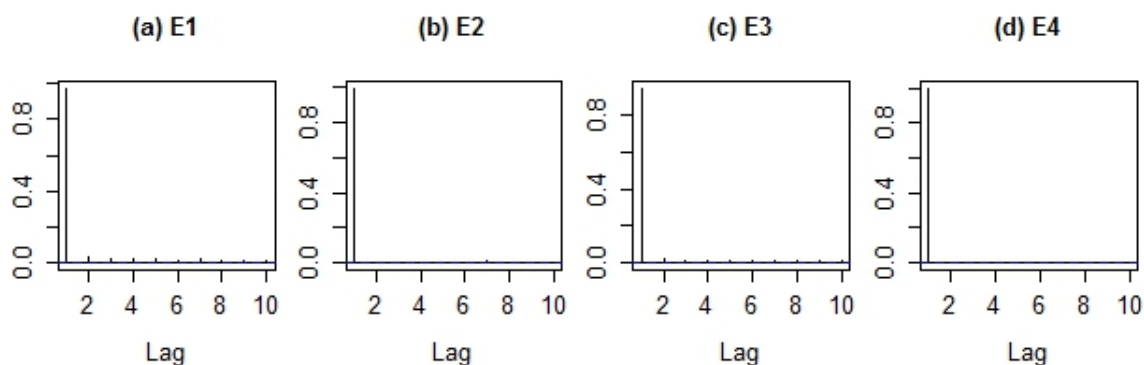


Figure 13.14: Partial autocorrelation plots of the MCMC draws from γ conditional marginal posterior distribution.

13.2.3 *Brownian bridge model*

Figure 13.15 illustrates the trace plots for γ_1 and γ_2 whereby good mixing is observed for all samples. For γ_1 , the posterior modes have diverged from the prior means for the majority of the samples, whereas for γ_2 the posterior means remained close to prior means. As previously, in E3 a ‘ceiling’ is observed for the γ_1 and γ_2 boundaries which is consistent with the outlier in the sample. For E4, however, a lower boundary for the γ_2 trace is also observed, which may reflect the velocity values in the sample. None of the correlations between the draws from the γ_1 and γ_2 were strong, with only E1 having a value of 0.46, the remaining correlations were below 0.2.

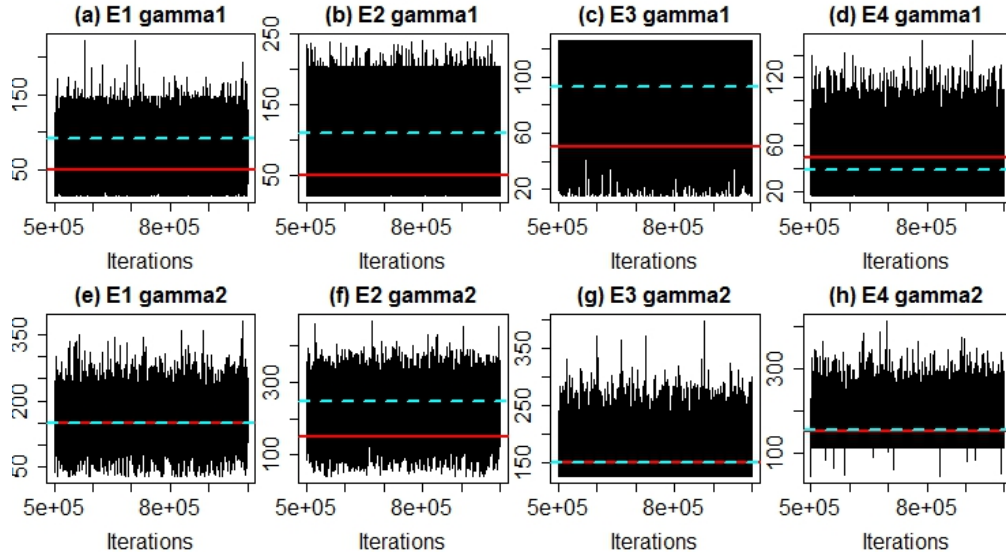


Figure 13.15: Trace plots of 10^6 MCMC iterations of the γ_1 and γ_2 conditional marginal posterior distribution, first 50% discarded as a burn-in. Solid red and dashed cyan lines indicate prior and posterior means respectively.

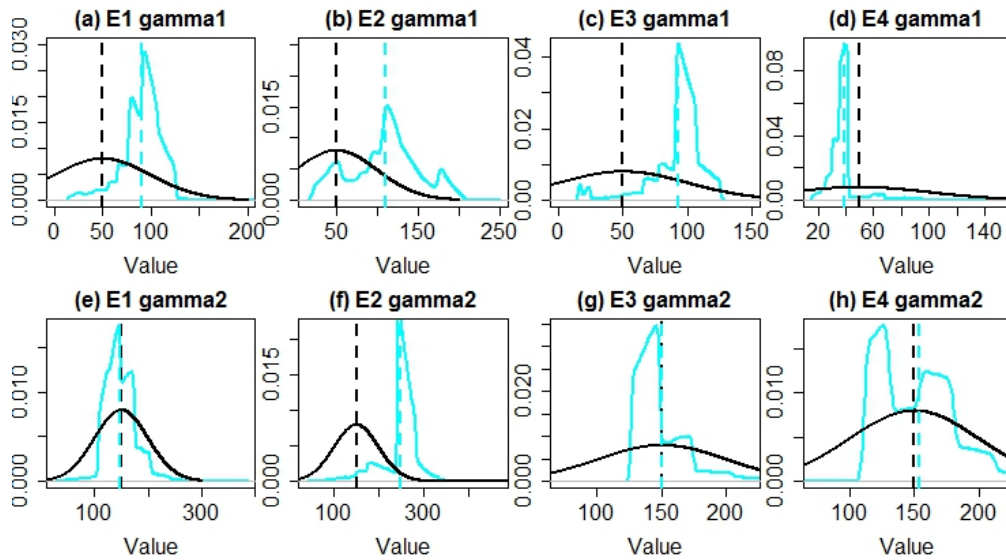


Figure 13.16: Density plots of the conditional marginal posterior distributions of γ_1 and γ_2 . Black solid and dashed lines represent prior density and mean respectively, cyan solid and dashed lines represent posterior density and mean respectively.

Figure 13.16 illustrates the posterior densities of γ_1 and γ_2 , whereby multimodality is observed. The MCMC scheme was run for 2×10^6 iterations for E1 and no change in the posterior densities was observed, thus it is presumed that the distributions are stationary. None of the partial autocorrelations for the γ_1 and γ_2 draws were significant, and similar results were found for all samples. The trace plots, densities and partial autocorrelation plots are provided for E1 as an example (Figures D.12- D.14).

13.2.4 Model comparison

Figures 13.17 and 13.18 illustrate the predictive distributions for the four samples that were generated from 10^4 draws based on posterior parameter means for the single changepoint and bridge models. For the former, the predictive distributions provide a good fit for the samples E1, E2 and E3, however for E4 the slope in the aggregated region appears to be estimated erroneously. As β_2 is defined as $(\alpha_1 - \alpha_2 + \beta_1\gamma)/\gamma$, a misestimation of any of the other regression parameters will lead to errors in the aggregated region slope. To test that this was not a computational/algebraic error, an MCMC scheme was run for E4 using priors that were based on the regression coefficient variation of E4 only, and a good fit can be observed in plot (c). The choice of prior distributions, therefore, may need to be re-considered to include more variation. This may also highlight the need of not forcing an intersection between the two regressions to allow more flexibility around the aggregation region.

For the bridge model, a much better fit can be observed (Figure 13.18). The introduction of the bridge segment has removed the constraint of regression intersection and has allowed a much greater flexibility. The variation around the regression intersection is much better accounted for by the Brownian bridge variance (Section 9.2.2). In sample E2 (plot (b)), the critical nanoaggregation region boundaries estimated by γ_1 and γ_2 are similar to those using constrained optimisation (Section 12.2).

What follows illustrates diagnostics (Fawcett *et al.*, 2017) in order to assess whether a single-changepoint or a Brownian bridge model better fits the asphaltene velocity data. Predictive distributions were generated by using marginal conditional posterior means and simulating 10^4 values from which the mean average error (MAE) and mean squared error (MSE) were calculated, as well as the correlation between observed and predicted values (Fawcett *et al.*, 2017) (Table 13.3). Figure 13.19 plots predictive versus observed values and illustrates the ‘perfect prediction’ line. The

Figure suggests that the bridge model provides a better fit to the data whereby the points that are included in the monomeric/aggregation segments follow the line of fit well. The deviation of the data points included in the bridge segment is to be expected as the mean of the bridge will be the drift between its two end-points whilst the variance along the bridge is quite high (Section 9.2.2). In general, the MAE and MSE are also lower for the bridge model. Strikingly, the variation in the sample E4 has been explained much better by the bridge model as well. The overall improvement in fit facilitates by the bridge model adds to the argument that asphaltenes form aggregates over a regions of concentrations.

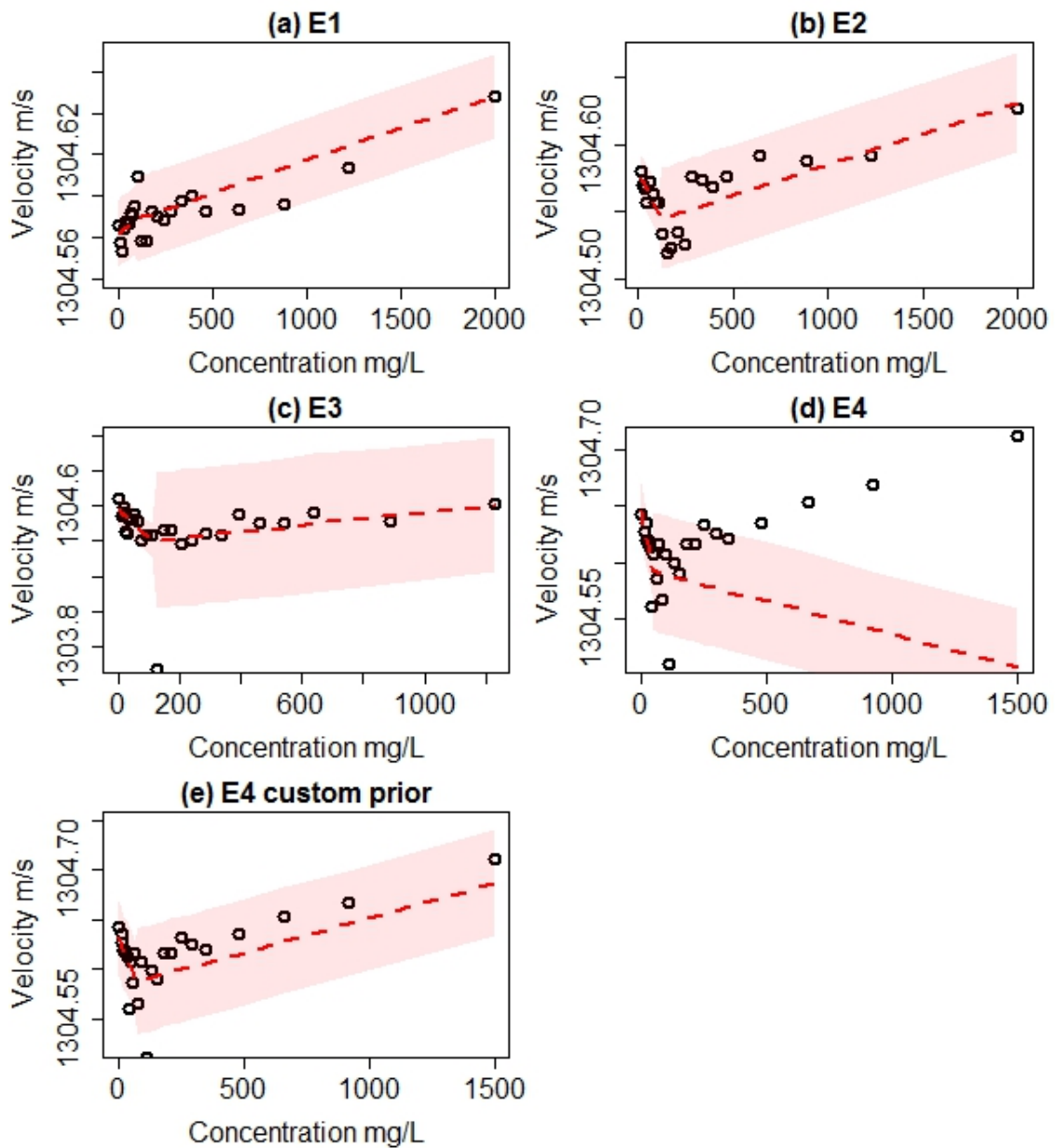


Figure 13.17: Predictive distributions of E1-E4 assuming the single changepoint underlying model, red lines indicate the model means, red shading indicates the 95% predictive intervals.

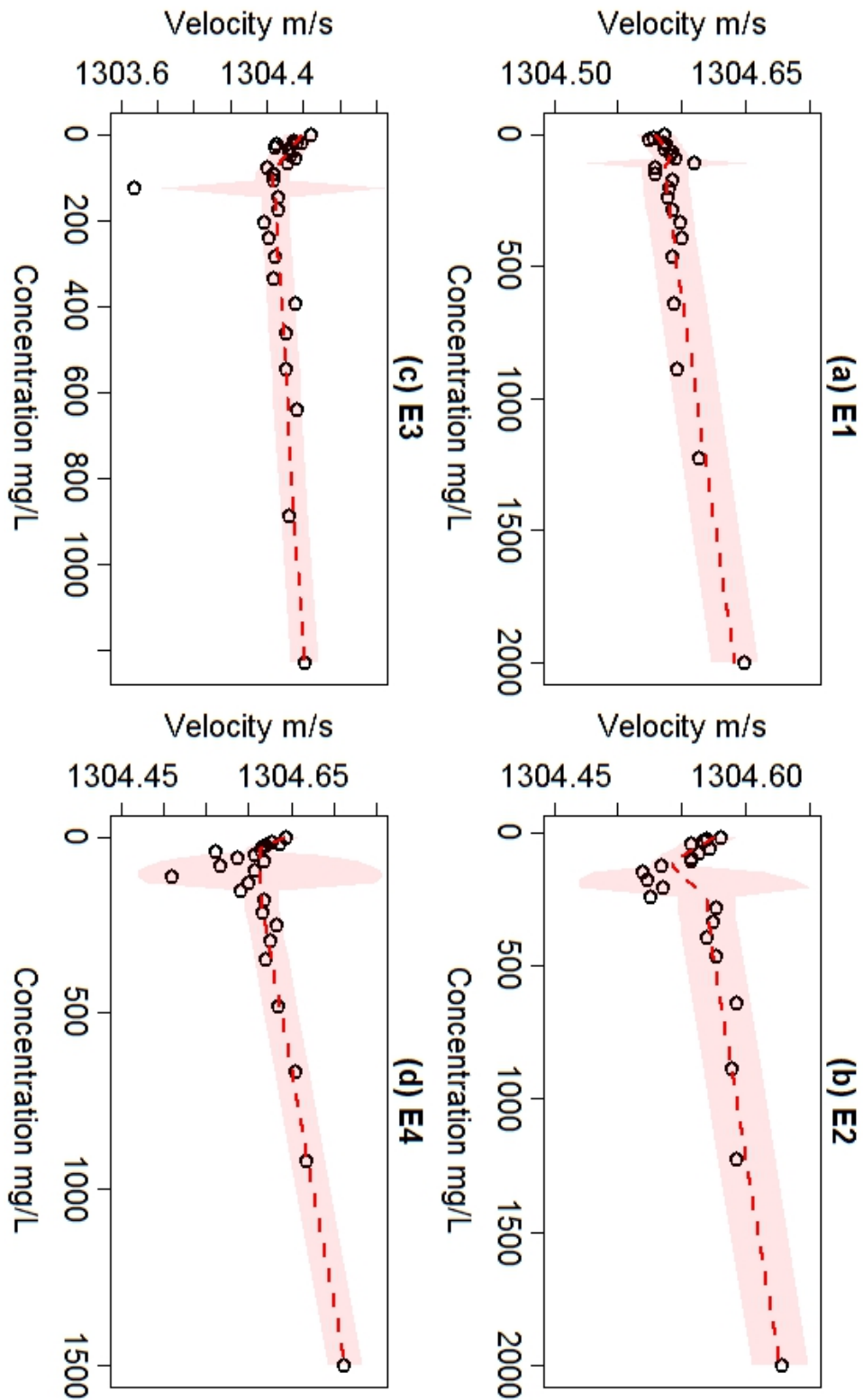


Figure 13.18: Predictive distributions of γ_1 and γ_2 , red shading indicates the 95% predictive intervals.

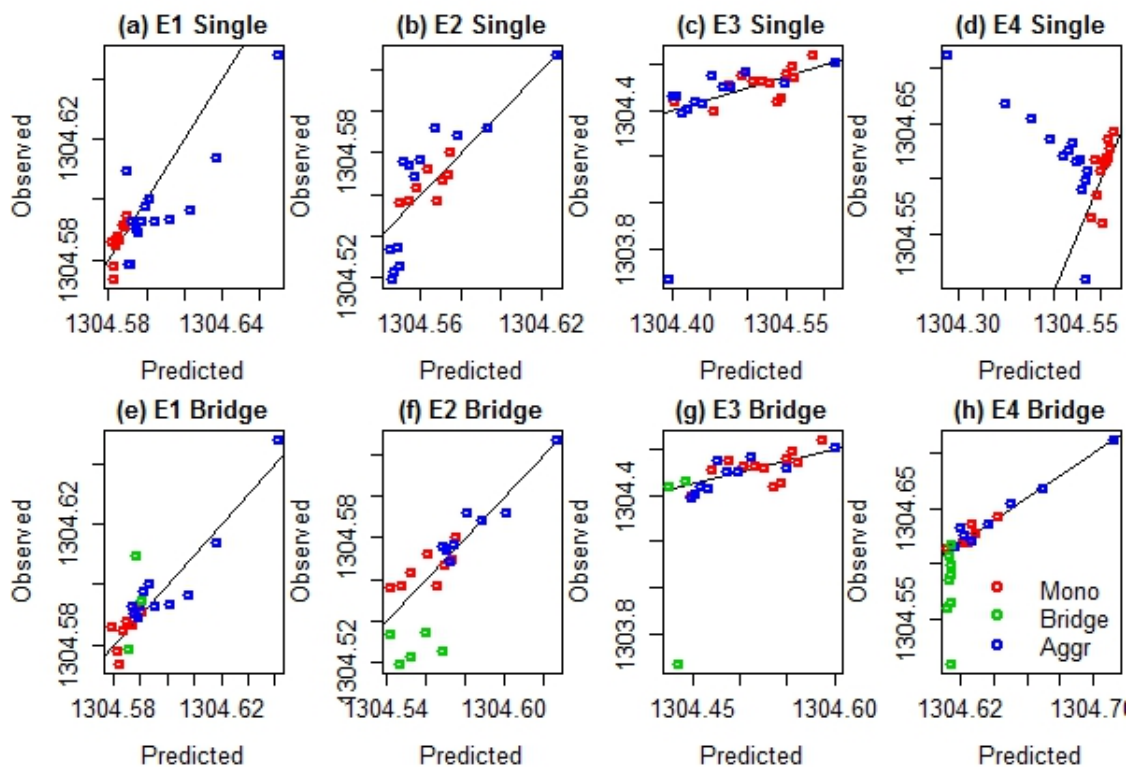


Figure 13.19: Plots of predicted versus observed quantities of E1-E4 asphaltenes, using the single changepoint (Single) and Brownian bridge (Bridge) models. The black line indicates the ‘Observed=Predicted’ regression.

Sample	MAE	MSE	Cor (ρ, p)
E1 single	-1.93E-03	6.83E-04	0.86, 1.86×10^{-7}
E1 bridge	8.01E-04	4.98E-05	0.88, 2.59×10^{-4}
E2 single	3.22E-04	2.19E-04	0.82, 4.34×10^{-6}
E2 bridge	-4.12E-03	2.52E-04	0.81, 8.80×10^{-6}
E3 single	-1.6E-02	2.19E-02	0.53, 4.18×10^{-3}
E3 bridge	-2.79E-02	2.35E-02	0.51, 6.82×10^{-2}
E4 single	2.68E-02	3.67E-02	-0.38, 0.06×10^{-3}
E4 bridge	-1E-02	6.88E-04	0.77, 6.14×10^{-6}

Table 13.3: Diagnostics for comparing the fit of the single-changepoint and bridge models to data, based on (Fawcett *et al.*, 2017).

Chapter 14. General Discussion

What follows draws on the results and discussions in previous Chapters in an attempt to explain how the variation in asphaltene geochemistry affects its nanoaggregation. In Svalova *et al.* (2017), principal component analysis (PCA) was performed on the variables

- ΔCNR - the width of the nanoaggregation region, $\Delta\text{CNR} = \text{CNR}_1 - \text{CNR}_2$,
- Δu - the velocity difference corresponding to CNR_1 and CNR_2 ,
- R_p^2 - the total penalised coefficient of determination of regressions in the monomeric and aggregated regions,
- Percentage of medium fatty acid methyl esters (FAMEs) out of total FAMEs,
- Percentage of long FAMEs out of total FAMEs.

In the following, these results will be revisited and improved as recent analysis brought to light new data and corrections. To begin, a clarification on the offset (CNR2) of E4 nanoaggregation needs to be highlighted, which is 181.358 instead of 81.358. This mistake was on the author's behalf and this change will affect the distribution of the four samples in the principal components. Although this was unfortunate, the re-analysis highlighted the need for more data, whereby a change in one data point would have a lesser implication on the remaining analysis. Secondly, the α -branched FAME data could aid in the understanding of the impact of steric hindrance arising from aliphatic branching to nanoaggregation. Thirdly, the discovery of benzoic acid methyl ester (BAME) is consistent with the possible archipelago structure of asphaltenes which also may have an impact on nanoaggregation.

The % of FAME compounds (based on peak heights) in relation to the total peak heights was calculated from their corresponding total ion chromatograms (TIC), and % of α -branched acids and BAME from their diagnostic partial ion chromatograms (as in Chapter 11.2) in relation to the total peak heights in the TIC. The relative

abundances of FAMEs were calculated from GC-MS runs in the selected ion monitoring (SIM) mode as the latter offered a better resolution (the compound retention times were confirmed from their corresponding full scan runs). The information on the branched and benzene acid compounds in the SIM mode was not available, thus their abundances were identified from scan runs (implying a lower resolution). The use of peak heights as opposed to peak areas was thought to be more appropriate for the relative abundance calculation due to the associated errors in variable baseline widths and heights and deformation of peaks due to coelution, whilst for the peak height data only the baseline non-uniformity would carry an error. Further, when the % abundance of FAMEs (and α, ω -*di*-fatty acid *di*-methyl esters) was compared between peak height-based and area-based calculations, virtually no difference was observed and the correlation between the two quantities was 0.99. On the other hand, when the two abundances were calculated for the branched compounds, their % abundance decreased by a factor of 10 when calculated using peak areas.

	V ₁	V ₂	V ₃	V ₄	V ₅	V ₆	V ₇	V ₈
V ₂	-0.1, 0.9							
V ₃	0.7, 0.3	0.1, 0.9						
V ₄	-1.0, 0.0	0.3, 0.7	-0.8, 0.2					
V ₅	0.7, 0.3	0.6, 0.4	0.5, 0.5	-0.6, 0.5				
V ₆	-0.1, 0.9	-0.2, 0.8	-0.8, 0.2	0.3, 0.7	-0.1, 0.9			
V ₇	0.2, 0.8	0.1, 0.9	-0.5, 0.5	-0.0, 1.0	0.4, 0.6	0.9, 0.1		
V ₈	0.6, 0.4	-0.4, 0.6	-0.1, 0.9	-0.5, 0.5	0.3, 0.7	0.7, 0.3	0.8, 0.2	
V ₉	-0.0, 1.0	1.0, 0.0	0.2, 0.8	0.2, 0.8	0.7, 0.4	-0.3, 0.7	0.1, 1.0	-0.4, 0.6

Table 14.1: Correlation matrix of the variables used in PCA, every cell illustrates a Pearson correlation ρ , followed by its corresponding p -value. Variable abbreviations are V₁– Δ CNR, V₂– Δu , V₃– R_p^2 , V₄– medium FAMEs, V₅– long FAMEs, V₆– α -methyl FAMEs, V₇– α -ethyl FAMEs, V₈– α -propyl FAMEs, V₉– BAME.

The correlation matrix of the nine variables used in PCA is displayed in Table 14.1, the ρ and p values are shown to one decimal place (there were no absolute correlations to two decimal places) and variables are abbreviated V₁₋₉ for compactness. Strong correlations (ca. > 0.7) are between e.g. Δ CNR and Δu , and Δ CNR and the abundance of medium FAMEs. In regards to the newly-introduced variables, striking is the very strong correlation between BAME and Δu , whilst the α -methylated

FAMEs are only weakly/moderately correlated with the remaining variables. To illustrate the impact of introducing α -branched FAMEs and BAME, PCA was first performed on V_{1-5} (Figure 14.1(a)) analogous to the original analysis in Svalova *et al.* (2017), then V_{1-8} (Figure 14.1(b)) introducing the branched acids and, finally, V_{1-9} (Figure 14.2) to add the BAME data.

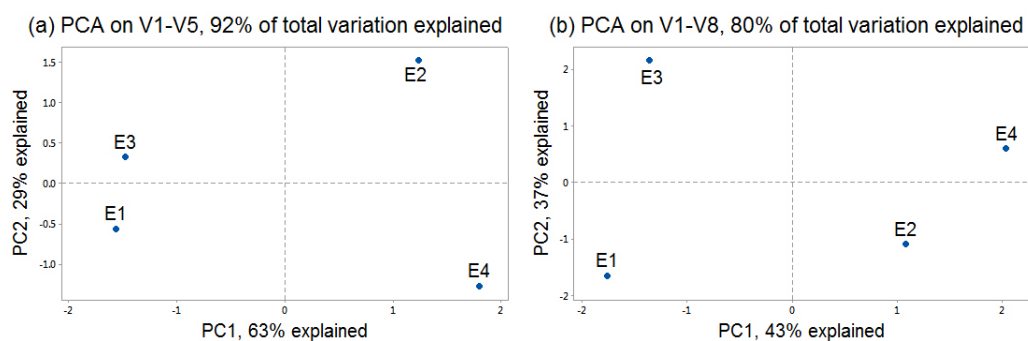


Figure 14.1: Sample separation based on the first two principal components. Loadings for plots (a) and (b) are given in Tables 14.2 and 14.3 respectively.

Variable	PC ₁	PC ₂	PC ₃	PC ₄	PC ₅
ΔCNR	0.542	-0.135	0.357	0.264	0.700
Δu	0.043	0.824	-0.162	-0.404	0.361
R_p^2	0.476	-0.032	-0.834	0.273	-0.052
M FAME	-0.528	0.293	-0.075	0.764	0.215
L FAME	0.447	0.465	0.381	0.329	-0.575

Table 14.2: Loadings of the principal components in Figure 14.1(a). Medium and long FAMES are abbreviated M FAME and L FAME.

Variable	PC ₁	PC ₂	PC ₃	PC ₄	PC ₅	PC ₆	PC ₇	PC ₈
ΔCNR	0.531	0.089	-0.069	0.138	-0.376	-0.499	-0.527	-0.132
Δu	0.005	-0.136	0.771	0.388	-0.298	-0.102	0.217	0.299
R_p^2	0.426	-0.353	-0.056	-0.572	-0.413	0.290	0.178	0.277
M FAME	-0.515	-0.000	0.239	-0.591	-0.238	-0.474	-0.032	-0.216
L FAME	0.419	0.055	0.495	-0.217	0.350	0.164	0.059	-0.614
$\alpha\text{-C}_1$ FAME	-0.147	0.557	0.005	0.081	-0.589	0.485	-0.002	-0.281
$\alpha\text{-C}_2$ FAME	0.061	0.543	0.262	-0.313	0.269	0.093	-0.383	0.554
$\alpha\text{-C}_3$ FAME	0.263	0.491	-0.164	-0.050	0.020	-0.400	0.702	0.082

Table 14.3: Loadings of the principal components in Figure 14.1(b). The α -methyl, α -ethyl and α -propyl FAMES are abbreviated $\alpha\text{-C}_1$, $\alpha\text{-C}_2$ and $\alpha\text{-C}_3$ FAME respectively. Blue indicates principal component loadings analogous to Table 14.2.

The author assumes that steric hindrance (Section 2.1) induced by longer asphaltene side-chains impacts potentially ‘slows down’ and complicates, the nanoaggregation process which is reflected in the velocity fluctuations observed in the CNR. This assumption will be key in the interpretation of PCA that follows. The ‘original’ PCA (Figure 14.1(a) and Table 14.2) has contrasted E1 and E3 versus E2 and E4 in PC₁. The width of the nanoaggregation region has the greatest contribution to PC₁ and is strongly related to R_p^2 . This may imply that as ΔCNR increases, the ‘noisy’ data within the CNR is excluded from the linear model which improves the R_p^2 . The long FAME compounds are also positively related to ΔCNR which may imply that the longer asphaltene side-chains induce higher velocity fluctuations which forces the ΔCNR to increase. Interestingly, the medium FAMES are strongly contrasted to the earlier variables, including long FAMES, although the correlation between medium and long FAMES is only moderate (Table 14.1). At a risk of overinterpreting, this

may imply that the velocity fluctuations induced by medium FAMEs are not strong enough to increase the ΔCNR but nevertheless decrease R_p^2 . The polarity between medium and long FAMEs is carried through the following analysis as well. In PC_2 , Δu has a very strong positive weight and is positively related to long FAMEs, suggesting that the long asphaltene side chains are related to the ‘height’ of the nanoaggregation region too, though not as strongly as to ΔCNR .

The introduction of the α -branched FAMEs to PCA is shown in Figure 14.1(b) and Table 14.3. The sample division in PC_1 is very similar to the previous analysis, both in the way the samples are located (Figure 14.1(b)) and in the loadings of the first five variables, whilst giving the branched FAMEs (very) small loads 14.3. In contrast, PC_2 changed the direction of the relation between E2 and E4 and further separated E1 from E3, positioning the samples according to their source. This change is reflected in the component’s loadings (Table 14.3) whereby the weight of Δu is reduced from 0.824 to -0.136 and the greatest weights are given to the branched FAMEs. The strongest contrast here is between R_p^2 and the branched compounds, which would be interpreted that an increase in the asphaltene side-chain branching also complicates the nanoaggregation process, thus decreases the fit of the linear models. Therefore, the introduction of the new variables has improved the explanation of nanoaggregation in the samples, as E1-E4 are now divided according to their velocity response in PC_1 and structural features in PC_2 .

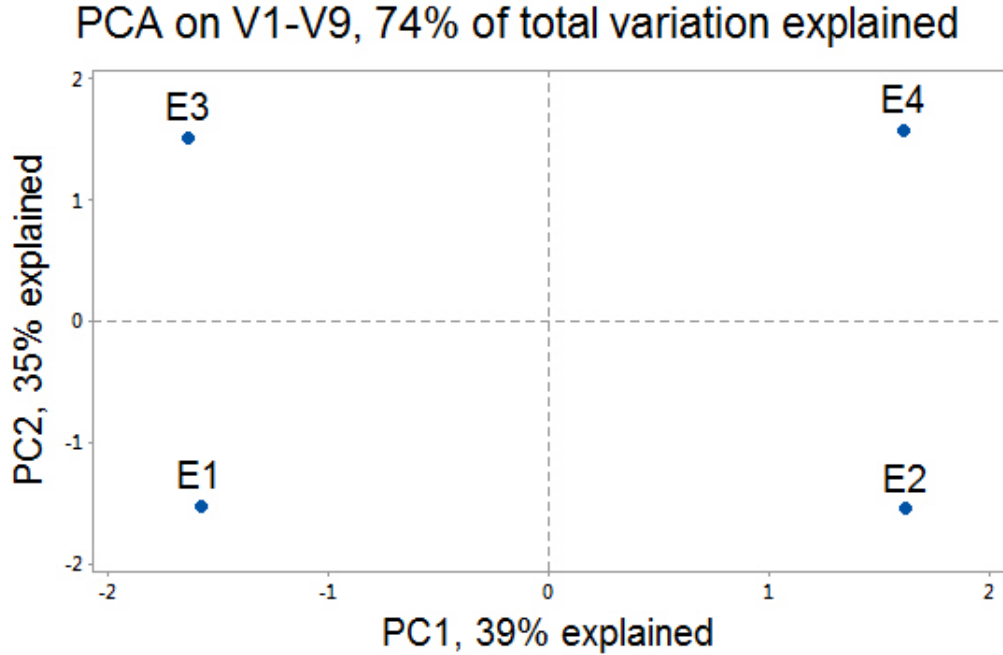


Figure 14.2: Sample separation based on the first two principal components (Table 14.4).

Variable	PC1	PC2	PC3	PC4	PC5	PC6	PC7	PC8	PC9
ΔCNR	0.493	0.218	0.064	0.190	-0.013	0.024	-0.120	0.732	-0.345
Δu	0.105	-0.308	-0.528	-0.579	-0.199	0.194	-0.394	0.192	0.104
R_p^2	0.466	-0.201	0.226	-0.182	-0.221	0.324	0.620	0.024	0.345
M FAME	-0.474	-0.177	-0.227	-0.061	-0.058	-0.395	0.505	0.522	0.042
L FAME	0.447	0.025	-0.360	-0.205	0.158	-0.472	0.290	-0.353	-0.414
$\alpha\text{-C}_1$ FAME	-0.235	0.459	-0.246	-0.014	-0.540	0.396	0.234	-0.123	-0.393
$\alpha\text{-C}_2$ FAME	-0.004	0.431	-0.417	0.003	0.634	0.327	0.178	0.083	0.304
$\alpha\text{-C}_3$ FAME	0.157	0.536	-0.054	-0.036	-0.386	-0.461	-0.139	-0.006	0.551
BAME	0.159	-0.321	-0.498	0.740	-0.199	0.046	-0.006	-0.090	0.162

Table 14.4: Loadings of the principal components in Figure 14.2. Abbreviation key is in Table 14.1.

Figure 14.2 illustrates PCA performed on all of the variables in Table 14.1 whereby the introduction BAME has improved the separation of samples, especially in PC₂, whereby the four are now ‘perfectly’ separated according to their source and velocity response (Table 14.4). The loadings are quite similar to the previous PCA and BAME does not have too strong of a weight in PC₁ or PC₂. In conclusion, new

structural data (branched acids and BAME) obtained from RICO has not strongly affected the inference of PC_1 and built on the sample separation in PC_2 by introducing new asphaltene features that may affect nanoaggregation. The neat separation of the samples according to their velocity response in PC_1 and structural data in PC_2 can suggest that there is indeed a relation between asphaltene architecture and their nanoaggregation behaviour.

Conclusions

Chapter 15. Conclusions

This work aimed to contribute to improving oil spill remediation practice by investigating the problem of asphaltene nanoaggregation. A literature review has highlighted the breadth of investigation that is directed towards asphaltene science. Fundamentally, what the asphaltenes are, still remains to be somewhat of a debate as different precipitation and separation techniques yield asphaltene fractions with different physico-chemical properties. A closer look at the asphaltene molecules appears to confirm that although many molecules have a polyaromatic hydrocarbon core – side chain structure (Mullins, 2011), a significant proportion of the molecules can be quite different (Schuler *et al.*, 2015, 2017) and the molecular heterogeneity of the asphaltenes is vast. In particular, some included only the longer aliphatic chains, whilst the others-only the polycyclic aromatic cores. The properties of the asphaltene fraction depend on the separation method and only a sub-fraction of the asphaltenes is surface-active (Wu, 2003; Czarnecki & Moran, 2005; Czarnecki, 2009), as opposed to the entire fraction (McLean & Kilpatrick, 1997*b*; Kilpatrick & Spiecker, 2001; Sjöblom *et al.*, 2001). In water-in-oil emulsions, the surface active portion of the asphaltenes self-associates and tend to sit on the water-oil boundary forming a rigid skin around water droplets (Gonzales & Middea, 1988; McLean *et al.*, 1998; Jeribi *et al.*, 2002), which is said to be one of the main petroleum emulsion/mousse stabilisation mechanisms. Experimental work (Svalova *et al.*, 2017) included oxidation experiments (Peng *et al.*, 1999), ultrasonic characterisation of asphaltenes (Andreatta *et al.*, 2005*a*) and maltene analysis (Peters *et al.*, 2005*a,b,c,d*). The oxidation experiments performed on model compounds revealed that the procedure is reliable to analyse straight-chain and α -branched medium-chain fatty acid methyl esters. Some inference about the archipelago compounds can also be performed by analysing the benzoic acid methyl esters. This is in contrast to the previous results whereby archipelago compounds were suggested to be inferred from the abundance of *di*-fatty acid *di*-methyl ester (Peng *et al.*, 1999). As it is highly-unlikely that the long *di*-fatty acid *di*-methyl esters are representative of the

‘original’ asphaltene structure, a better understanding of our experimental method is required. If the relative abundance of the latter compound is representative of that of the archipelago compounds, the proportion of the non-island molecules is extremely low, as previously reported (Schuler *et al.*, 2015, 2017). Ultrasonic characterisation was used as a novel method in asphaltene science that presented the advantages of high sensitivity to molecular rearrangements, probing of opaque samples without dilution and ease in implementation. Ultrasonic characterisation studies highlighted the non-linear nature of the asphaltene aggregation concentration point/region as the analysed samples exhibited high variation in the aggregation behaviour.

The analysis and modeling of combined asphaltene geochemical and velocity data revealed that there is a relationship between asphaltene structure obtained from oxidation studies, e.g. a higher degree of side-chain branching, and the size of the nanoaggregation region. However, more data is needed to test this relation. Additionally, a Bayesian modelling exercise was performed in order to test the assumptions of a critical nanoaggregation concentration point versus a region, and the latter was supported.

The limitations of the analysis and inference presented in this investigation are as follows. Firstly, the number of samples used in ultrasonic characterisation is fairly small, and the PCA analysis presented should be treated as an indication of a relation between asphaltene nanoaggregation and structure. Secondly, the limitations of RICO (Peng *et al.*, 1999; Strausz *et al.*, 1999a), such as volatility losses, call for a further understanding of how to make this experimental procedure more robust and reliable, or turn to other methods of understanding asphaltene structure. Thirdly, velocity measurements can be strongly affected by air bubbles and other artifacts (Povey, 1997a) and in future it would be advantageous to compare the findings with nuclear magnetic resonance (NMR) measurements (Ali *et al.*, 1990; Freed *et al.*, 2009; Lisitza *et al.*, 2009) and rheological studies (Rane *et al.*, 2012, 2013, 2015). The reported advantage of sound over light spectroscopic techniques could also be tested experimentally (Aske *et al.*, 2004; Oh & Deo, 2007; Yudin & Anisimov, 2007). Finally, within the greater context of oil spills this project has focused on the niche of asphaltene nanoaggregation, which is both very broad and narrow. An asphaltene ‘molecule’ doesn’t really exist as the asphaltene fraction as an agglomeration of multiple subfractions, not all of whom include aromatics (Schuler *et al.*, 2017). A given asphaltene sample will not only depend on the parent hydrocarbons but also the separation method. Thus, when measuring nanoaggregation in an as-

phaltene sample, one measures aggregation of a very broad class of molecules. Therefore, further directions of this research could be as follows. Asphaltene subfractions could be determined on the basis of e.g. saturation/aromaticity and surface activity (Gawrys *et al.*, 2005; Stanford *et al.*, 2007a; Kilpatrick, 2012; Rocha *et al.*, 2016). Nanoaggregation, then, could be measured in asphaltenes precipitated with different solvents, e.g. $n\text{-C}_5$ - $n\text{-C}_7$ (lighter solvent precipitates a greater amount of the asphaltenes with $n\text{-C}_7$ yielding the heaviest compounds) (Frakman *et al.*, 1990; Peng *et al.*, 1997; Strausz *et al.*, 1999a), and in samples of varying surface activity. These results could be compared with nanoaggregation in petroleum, whereby a deasphalted crude could be doped with different weight asphaltene subfractions. The results should then be related to asphaltene film thickness/surface activity in oil/water emulsions. Surface rheological studies (Fan *et al.*, 2010; Kilpatrick, 2012) currently do and they could add a great depth of understanding the dynamics of asphaltene subfraction aggregation. This could be compared against molecular dynamic simulations (Kuznicki *et al.*, 2008, 2009; Sedghi *et al.*, 2013; Teklebrhan *et al.*, 2014; Yang *et al.*, 2015a) and statistical models, e.g. involving the percolation theory (Sheu, 1996). Next, the water in oil emulsions should be studied. Again, petroleum is highly complex and to fully understand the interaction between the asphaltenes and the remaining compound fractions, in a variety of oils, would be a very burdensome task. Most studies focus on petroleum waxes and asphaltenes, whereby some report that the presence of waxes (Thompson *et al.*, 1985) and/or the interaction of the two is important (Bridie *et al.*, 1980), whilst others focus on the asphaltene ‘skin’ formation (Singh *et al.*, 1999; Yarranton *et al.*, 2000b; Khristov *et al.*, 2000; Jestin *et al.*, 2007; Mullins, 2011; Rane *et al.*, 2012, 2013). Increasingly, it seems that both the formation of asphaltene films at the O/W surface and the interaction with waxes is important (Sjoblom *et al.*, 2003; Jestin *et al.*, 2007), otherwise one obtains an incomplete picture regarding the stability of WOE. Petroleum indigenous acidity as well as water salinity should always be considered, as the interaction between the polar groups in the asphaltenes and the naphthenic acid in the maltene fraction in petroleum could create greater forces than those between the asphaltenes and water, this, however, is speculative. A greater understanding of factors impacting nanoaggregation and stability of water-in-oil emulsions could then be used to select a remediation strategy that targets specifically the WOE stabilisation mechanism, and reduce the environmental impacts of spills and remediation.

References

- ABBOTT, G. D., LEWIS, C. & MAXWELL, J. R. 1985 Laboratory models for aromatization and isomerization of hydrocarbons in sedimentary basins. *Nature* **318**, 651–653.
- ABBOTT, G. D. & POVEY, M. J. W. 2012 The acoustic spectroscopy of asphaltene aggregation in petroleum. In *International Symposium of Ultrasound in the Control of Industrial Processes (UCIP)*. Madrid, Spain: IOP Publishing.
- ACEVEDO, S., BORGES, B., QUINTERO, F., PISCITELLY, V. & GUTIERREZ, L. B. 2005 Asphaltenes and other natural surfactants from Cerro Negro crude oil. Stepwise adsorption at the water/toluene interface: Film formation and hydrophobic effects. *Energy & Fuels* **19**, 1948–1953.
- ACEVEDO, S., CASTILLO, J., FRENANDEZ, A., GONCALVES, S. & RANAUDO, M. A. 1998 A study of multilayer adsorption of asphaltenes on glass surfaces by photothermal surface deformation. Relation of this adsorption to aggregate formation in solution. *Energy & Fuels* **12**, 386–390.
- ACEVEDO, S., RANAUDO, M. A., ESCOBAR, G., GUTIERREZ, L. & ORTEGA, P. 1995 Adsorption of asphaltenes and resins on organic and inorganic substrates and their correlation with precipitation problems in production well tubing. *Fuel* **74**, 595–598.
- ACEVEDO, S., RANAUDO, M. A., GARCIA, C., CASTILLO, J. & FRENANDEZ, A. 2003 Adsorption of asphaltenes at the toluene-soloca interface: a kinetic study. *Energy & Fuels* **17**, 257–261.
- ADEBAJO, M. O., FROST, R. L., KLOPROGGE, J. T., CARMODY, O. & KOKOT, S. 2003 Porous materials for oil spill cleanup: a review of synthesis and absorbing properties. *Journal of Porous Materials* **10**, 159–170.

- AECKERSBERG, F., RAINEY, F. A. & WIDDEL, F. 1998 Growth, natural relationships, cellular fatty acids and metabolic adaptation of sulfate-reducing bacteria that utilize long-chain alkanes under anoxic conditions. *Archives of Microbiology* **170**, 361–369.
- AINGH, A., VAN HAMME, J. D. & WARD, O. P. 2007 Surfactants in microbiology and biotechnology: Part 2. Application aspects. *Biotechnology Advances* **25**, 99–121.
- AITKEN, C. M., JONES, D. M. & LARTER, S. R. 2004 Anaerobic hydrocarbon biodegradation in deep subsurface oil reservoirs. *Nature* **431**, 291–294.
- ALBA, E. 1992 Method and apparatus for determining particle size distribution and concentration in a suspension using ultrasonics. Patent No. US 5121629.
- ALBOUDWAREJ, H., BECK, J., SVRCEK, W. & YARRANTON, H. 2002 Sensitivity of asphaltene properties to separation techniques. *Energy & Fuels* **16**, 462–469.
- ALEXANDER, R., KAGI, R. & WOODHOUSE, G. W. 1981 Geochemical correlation of Windalia oil and extracts of winning group (Cretaceous) potential source rocks, Barrow Subbasin, Western Australia. *American Association of Petroleum Geologists Bulletin* **65**, 235–250.
- ALEXANDER, R., KAGI, R. I., ROWLAND, S. J., SHEPPARD, P. N. & CHIRILA, T. V. 1985 The effects of thermal maturity on distributions of dimethylnaphthalenes and trimethylnaphthalenes in some ancient sediments and petroleum. *Geochimica et Cosmochimica Acta* **49**, 385–395.
- ALEXANDER, R., KAGI, R. I. & SHEPPARD, P. N. 1983 Relative abundance of dimethylnaphthalene isomers in crude oils. *Journal of Chromatography* **267**, 367–372.
- ALI, L. H., AL-GHANNAM, K. A. & AL-RAWI, J. M. 1990 Chemical structure of asphaltenes in heavy crude oils investigated by n.m.r. *Fuel* **69**, 519–521.
- ALIMOHAMMADI, S., J., S. A. & NIKOOEE, E. 2017 Estimation of asphaltene precipitation in light, medium and heavy oils: experimental study and neural network modeling. *Neural Computing and Applications* **28**, 679–694.

- ALLEGRA, J. R. L. & HAWLEY, S. A. 1972 Attenuation of sound in suspensions in emulsions: theory and experiments. *Journal of the Acoustical Society of America* **51**, 1545–1564.
- ALLEN, A. A., MABILE, N. J., JAEGER, D. & COSTANZO, D. 2011 The use of controlled burning during the gulf of Mexico Deepwater Horizon MC-252 oil spill response. In *Proceedings of the 2011 International Oil Spill Conference*, , vol. 1, p. 194.
- ALMGREN, M. & LOFROTH, J.-E. 1981 Determination of micelle aggregation numbers and micelle fluidities from time resolved fluorescence quenching. *Journal of Colloid and Interface Science* **81**, 486–499.
- ALMGREN, M. & LOFROTH, J.-E. 1982 Effects of polydispersity on fluorescence quenching in micelles. *The Journal of Chemical Physics* **76**, 2734–2743.
- ALVAREZ, G., JESTIN, J., ARGILLIER, J. F. & LANGEVIN, D. 2009 Small-angle neutron scattering study of crude oil emulsions: structure of the oil-water interface. *Langmuir* **25**, 3985–3990.
- ALVES, D. R., CARNEIRO, J. S., OLIVEIRA, I. F., FACANHA, F., SANTOS, A. F., DARIVA, C., FRANCESCHI, E. & FORTUNY, M. 2014 Influence of the salinity on the interfacial properties of a Brazilian crude oil-brine systems. *Fuel* **118**, 21–26.
- AMIN, S. J., ALAMDARI, A., MEHRANBOD, N., AYATOLLAHI, S. & NIKOOEE, E. 2010 Prediction of asphaltene precipitation: Learning from data at different conditions. *Energy & Fuels* **24**, 4046–4053.
- ANDERSEN, S. I. & BIRDI, K. S. 1991 Aggregation of asphaltenes as determined by calorimetry. *Journal of Colloid and Interface Science* **142**, 497–502.
- ANDERSON, S. I. & BIRDI, K. S. 1991 Aggregation of asphaltenes as determined by calorimetry. *Journal of Colloid and Interface Science* **142**, 497–502.
- ANDO, T. 2007 Bayesian predictive information criterion for the evaluation of hierarchical Bayesian and empirical Bayes models. *Biometrika* **94**, 443–458.

- ANDREATTA, G., BOSTROM, N. & MULLINS, O. C. 2005a High-Q ultrasonic determination of the critical nanoaggregate concentration of asphaltenes and the critical micelle concentration of standard surfactants. *Langmuir* **21**, 2728–2736.
- ANDREATTA, G., BOSTROM, N. & MULLINS, O. C. 2007 9. ultrasonic spectroscopy of asphaltene aggregation. In *Asphaltenes, heavy oils and petroleumics* (ed. O. C. Mullins, E. Y. Sheu, A. Hammami & A. G. Marshall), pp. 231–258. New York: Springer Science + Business Media.
- ANDREATTA, G., GONCALVES, C. C., BUFN, G., BOSTROM, N., QUINTELLA, C. M., ARTEAGA-LARIOS, F., PEREZ, E. & MULLINS, O. C. 2005b Nanoaggregates and structure-function relations in asphaltenes. *Energy & Fuels* **19**, 1282–1289.
- ANIANSOON, E. G., WALL, S. N., ALMGREN, A., HOFFMAN, H., KEILMAN, I., ULBRICHT, W., ZANA, R., LANG, J. & TONDRE, C. 905-922 Theory of the kinetics of micellar equilibria and quantitative interpretation of chemical relaxation studies of micellar solutions of ionic surfactants. *Journal of Physical Chemistry* **80**.
- ANISIMOV, M. A., YUDIN, I. K., NIKITIN, V., NIKOLAENKO, G., CHERNOUTSAN, A., TOULHOAT, H., FROT, D. & BRIOLANT, Y. 1995 Asphaltene aggregation in hydrocarbon solutions studied by photon correlation spectroscopy. *Journal of Physical Chemistry* **99**, 9576–9580.
- ANNWEILER, E., MATERNA, A., SAFINOWSKI, M., KAPPLER, A., RICHNOW, H. H., MICHAELIS, W. & MECKENSTOCK, R. U. 2000 Anaerobic degradation of 2-methylnaphthalene by a sulfate-reducing enrichment culture. *Applied and Environmental Microbiology* **66**, 5329–5333.
- APARNA, A., SRINIKETHAN, G. & HEDGE, S. 2011 Effect of addition of biosurfactant produced by *Pseudomonas ssp.* on biodegradation of crude oil. In *International Proceedings of Chemical, Biological & Environmental Engineering*, , vol. 6, pp. 71–75. Singapore.
- AQUINO-OLIVOS, M. A., ANDERSEN, S. I. & LIRA-GALEANA, C. 2003 Comparisons between asphaltenes from the dead and live-oil samples of the same crude oils. *Petroleum Science and Technology* **21**, 1017–1041.

- ARDITTY, S., SCHMITT, V., GIEMANSKA-KAHN, J. & LEAL-CALDERON, F. 2004 Materials based on solid-stabilized emulsions. *Journal of Colloid and Interface Science* **275**, 659–664.
- AREFYEV, O. A., MAKUSHINA, V. M. & PETROV, A. A. 1980 Asphaltenes as indicators of the geochemical history of oil. *International Geology Review* **24**, 723–728.
- ASKE, N., KALLEVIK, H. & SJÖBLOM, J. 2001 Determination of saturate, aromatic, resin, and asphaltenic (SARA) components in crude oils by means of infrared and near-infrared spectroscopy. *Energy & Fuels* **15**, 1304–1312.
- ASKE, N., ORR, R., SJOBLOM, J., KALLEVIK, H. & OYE, G. 2004 Interfacial properties of watercrude oil systems using the oscillating pendant drop. Correlations to asphaltene solubility by near infrared spectroscopy. *Journal of Dispersion Science and Technology* **25**, 263–275.
- ATKINS, P. W. 2014a *Atkins' physical chemistry*, 10th edn., chap. 16. Oxford: Oxford University Press.
- ATKINS, P. W. 2014b *Atkins' physical chemistry*, 10th edn., chap. 17. Oxford: Oxford University Press.
- BADRE, S., GONCALVES, C. C., NORINAGA, K., GUSTAVSON, G. & MULLINS, O. C. 2006 Molecular size and weight of asphaltene and asphaltene solubility fractions from coals, crude oils and bitumen. *Fuel* **85**, 1–11.
- BAELUM, J., BORGLIN, S., CHAKRABORTY, R., FORTNEY, J. L., LAMENDELLA, R., MASON, O. U., AUER, M., ZEMLA, M., BILL, M., CONRAD, M. E., MALFATTI, S. A., TRINGE, S. G., HOLMAN, H.-Y., HAZEN, T. C. & JANSSON, J. K. 2012 Deep-sea bacteria enriched by oil and dispersant from the Deepwater Horizon spill. *Environmental Microbiology* **14**, 2405–2416.
- BAILEY, N. L., KROUSE, H. R., EVANS, C. R. & ROGERS, M. A. 1973 Alteration of crude oil by waters and bacteria - evidence from geochemical and isotopic studies. *American Association of Petroleum Geologists Bulletin* **57**, 1276–1290.
- BARRE, L., JESTIN, J., MORISSET, A., PALERMO, T. & SIMON, S. 2009 Relation between nanoscale structure of asphaltene aggregates and their macroscopic solution properties. *Oil & Gas Science and Technology* **64**, 617–628.

- BARRE, L., SIMON, S. & PALERMO, T. 2008 Solution properties of asphaltenes. *Langmuir* **24**, 3709–3717.
- BASTIN, E. 1926 Microorganisms in oilfields. *Science* **63**, 21–24.
- BATCHELOR, G. K. 1976 Brownian diffusion of particles with hydrodynamic interaction. *Journal of Fluid Mechanics* **74**, 1–29.
- BAUER, P. E., DUNLAP, N. K., ARSENIYADIS, S., WATT, D. S., SEIFERT, W. K. & MOLDOWAN, J. M. 1983 Synthesis of biological markers in fossil fuels. 1. 17.alpha. and 17.beta. isomers of 30-norhopane and 30-normoretane. *The Journal of Organic Chemistry* **48**, 4493–4497.
- BAUGET, F., LANGEVIN, D. & LENORMAND, R. 2001 Dynamic surface properties of asphaltenes and resins at the oil/air interface. *Journal of Colloid and Interface Science* **239**, 501–508.
- BEACH, F., PEAKMAN, T. M., ABBOTT, G. D., SLEEMAN, R. & MAXWELL, J. R. 1989 Laboratory thermal alteration of triaromatic steroid hydrocarbons. *Organic Geochemistry* **14**, 109–111.
- BEHAR, F. & PELET, R. 1984 Characterisation of asphaltenes by pyrolysis and chromatography. *Journal of Analytical and Applied Pyrolysis* **7**, 121–135.
- BERR, S. S. & JONES, R. M. 1988 Effect of added sodium and lithium chlorides on intermicellar interactions and micellar size of aqueous dodecyl sulfate aggregates as determined by small-angle neutron scattering. *Langmuir* **4**, 1247–1251.
- BERRIDGE, S. A., THEW, M. T. & LORISTON-CLARKE, A. G. 1968 The formation and stability of emulsions of water in crude petroleum and similar stocks. *Journal of the Institute of Petroleum* **54**, 333–357.
- BERTSEKAS, D. P. 1982 *Constrained optimization and Lagrange multiplier methods*. Massachusetts: Athena Scientific.
- BETANCOURT, S. S., VENTURE, T. G., POMERANTZ, A. E., VILORIA, O., DUBOST, F. X., ZUO, J., MONSON, G., BUSTAMANTE, D., PURCELL, J. M., NELSON, R. K., RODGERS, R. P., REDDY, C. M., MARSHALL, A. G. & MULLINS, O. C. 2009 Nanoaggregates of asphaltenes in a reservoir crude oil and reservoir connectivity. *Energy & Fuels* **23**, 1178–1188.

- BHATTACHARYA, R. & WAYMIRE, E. 1990 *Stochastic processes with applications (Wiley series in probability and mathematical statistics. Applied probability and statistics)*. New York: Wiley.
- BIKKY, K. 2012 Effect of salinity on interfacial tensions of model and crude oil systems. Master's thesis, University of Calgary, Calgary, Alberta, Canada.
- BINKS, B. P. 2002 Particles as surfactant similarities and differences. *Current Opinion in Colloid and Interface Science* **7**, 21–41.
- BINKS, B. P., MEUNIER, J., ABILLON, O. & LANGEVIN, D. 1989 Measurement of film rigidity and interfacial tensions in several ionic surfactant-oil-water microemulsion systems. *Langmuir* **5**, 415–421.
- BLANC, P. & CONNAN, J. 1994 Preservation, degradation and destruction of trapped oil. In *The Petroleum System - From Source to Trap* (ed. L. B. Magoon & W. G. Dow), pp. 237 – 247. Tulsa, OK: American Association of Petroleum Geologists.
- BLÖCHL, E., RACHEL, R., BURGGRAF, S., HAFENBRADL, D., JANNASCH, H. W. & STETTER, K. O. 1997 *Pyrolobus fumarii*, gen. and sp. nov., represents a novel group of archaea, extending the upper temperature limit for life to 113 °C. *Extremophiles* **1**, 14–21.
- BOBRA, M., FINGAS, M. & TENNYSON, E. 1992 When oil spills emulsify. *Chemtech* **22**, 343–348.
- BODUSZYNSKI, M. M. 1988 Composition of heavy petroleums. 2. Molecular characterization. *Energy & Fuels* **2**, 597–613.
- BOLEF, D. I. & MILLER, J. G. 1971 High-frequency continuous wave ultrasonics. In *Physical Acoustics* (ed. P. W. Mason & R. N. Thurston), , vol. 8, pp. 95–201. Academic Press.
- BOREHAM, C. J., HOPE, J. M. & HARTUNG-KAGI, B. 2001 Understanding source, distribution and preservation of Australian natural gas: A geochemical perspective. *Australian Petroleum Exploration Association Journal* **41**, 523–547.

- BORTON, D., PINKSTON, D. S., HURT, M. R., TAN, X., AZYAT, K., SCHERER, A., TYKWINSKI, R., GRAY, M., QIAN, K. & KENTTÄMAA, H. I. 2010 Molecular structures of asphaltenes based on the dissociation reactions of their ions in mass spectrometry. *Energy & Fuels* **24**, 5548–5559.
- BOST, F. D., FRONTERA-SUAU, R., McDONALD, T. J., PETERS, K. E. & MORRIS, P. J. 2001 Aerobic biodegradation of hopanes and norhopanes in Venezuelan crude oils. *Organic Geochemistry* **32**, 105–114.
- BOUHADDA, Y., BORMANN, D., SHEU, E. Y., BENEDEDOUCH, D., KRALLAFA, A. & DAAOU, M. 2007 Characterization of Algerian Hassi-Messaoud asphaltene structure using Raman spectrometry and X-ray diffraction. *Fuel* **86**, 1855–1864.
- BOWDEN, S. A., FARRIMOND, P., SNAPE, C. E. & LOVE, G. D. 2006 Compositional differences in biomarker constituents of the hydrocarbon, resin, asphaltene and kerogen fractions: An example from the Jet Rock (Yorkshire, UK). *Organic Geochemistry* **37**, 369–383.
- BP 2010 *Deepwater Horizon* accident investigation report. September 2010. *Tech. Rep.*. BP.
- BRAY, E. E. & EVANS, E. D. 1961 Distribution of *n*-paraffins as a clue to recognition of source beds. *Geochimica et Cosmochimica Acta* **22**, 2–15.
- BRIDIE, A. J., WANDERS, T. H. W., ZEGVELD, W. & VAN DER HEIJDE, H. B. 1980 Formation, prevention and breaking of sea water in crude oil emulsions ‘chocolate mousses’. *Marine Pollution Bulletin* **11**, 343–348.
- BROOKS, S., GELMAN, A., JONES, G. L. & MENG, X.-L. 2011 *Handbook of Markov Chain Monte Carlo*. Boston: Chapman & Hall/CRC.
- BUCH, L., GROENZIN, H., BUENROSTRO-GONZALEZ, E., ANDERSEN, S. I., LIRA-GALEANA, C. & MULLINS, O. C. 2003 Effect of hydrotreatment on asphaltene fractions. *Fuel* **82**, 1075–1084.
- BUCKLEY, J. S., WANG, J. & CREEK, J. L. 2007 Solubility of the least-soluble asphaltenes. In *Asphaltenes, heavy oils and petroleomics* (ed. O. C. Mullins, E. Y. Sheu, A. Hammami & A. G. Marshall), pp. 189–203. New York: Springer Science + Business Media.

- BUENROSTRO-GONZALEZ, E., GROENZIN, H., LIRA-GALEANA, C. & MULLINS, O. C. 2001 The overriding chemical principles that define asphaltenes. *Energy & Fuels* **15**, 972978.
- BUNGER, J. W. & LI, N. C. 1981 *Chemistry of Asphaltenes*. Washington, D.C.: American Chemical Society (ACS).
- BURY, R., TREINER, C., CHEVALET, J. & MAKAYSSI, A. 1991 Peculiar solubilization thermodynamics of pentan-1-ol in mixed surfactant solutions of benzyldimethyltetradecylammonium chloride and trimethyltetradecylammonium chloride: a calorimetric investigation. *Analytica Chimica Acta* **251**, 69–77.
- CAHN, R. S., INGOLD, C. & PRELOG, V. 1966 Specification of molecular chirality. *Angewandte Chemie International Edition* **5**, 385–415.
- CARMODY, O., FROST, R., XI, Y. & KOKOT, S. 2007 Adsorption of hydrocarbons on organo-clays - implications for oil spill remediation. *Journal of Colloid and Interface Science* **305**, 17 – 24.
- CAROLL, B. J. 1976 The stability of emulsions and mechanisms of emulsions breakdown. *Surface and Colloid Science* **9**, 1–65.
- CASSANI, F. & EGLINTON, G. 1986 Organic geochemistry of Venezuelan extra-heavy oils 1. Pyrolysis of asphaltenes: a technique for the correlation and maturity evaluation of crude oils. *Chemical Geology* **56**, 167–183.
- CASSANI, F., GALLANGO, O., TALUKDAR, S., VALLEJOS, C. & EHRMANN, U. 1988 Methylphenanthrene maturity index of marine source rock extracts and crude oils from the Maracaibo Basin. *Organic Geochemistry* **13**, 73–80.
- CHALLIS, R., POVEY, M. J. W., MATHER, M. & HOLMES, A. 2005 Ultrasound techniques for characterising colloidal dispersions. *Reports on Progress in Physics* **68**, 1541–1637.
- CHARRIÉ-DUHAUT, A., LEMOINE, S., ADAM, P., CONNAN, J. & ALBRECHT, P. 2000 Abiotic oxidation of petroleum bitumens under natural conditions. *Organic Geochemistry* **31**, 977–1003.

- CHEN, S. H. 1986 Small angle neutron scattering studies of the structure and interaction in micellar and microemulsion systems. *Annual Review of Physical Chemistry* **37**, 351–399.
- CHEVALIER, Y., GERMANAUD, L. & LE PERCHEC, P. 1988 Micellar properties of zwitterionic phosphobetaine amphiphiles in aqueous solution: influence of the interchange distance. *Colloid Polymer Science* **266**, 441.
- CHEVALIER, Y. & ZEMB, T. 1990 The structure of micelles and microemulsions. *Reports on Progress in Physics* **53**, 279.
- CHILINGARIAN, G. V. & YEN, T. F. 1978 *Bitumens, Asphalts and Tar Sands*. New York: Elsevier.
- CHOI, H. M. & CLOUD, R. M. 1992 Natural sorbents in oil spill cleanup. *Environmental Science & Technology* **26**, 772–776.
- CHOSSON, P., CONNAN, J., DESSORT, D. & LANAU, C. 1992 In vitro biodegradation of steranes and terpanes: a clue to understanding geological situations. In *Biological Markers in Sediments and Petroleum* (ed. J. M. Moldowan, P. Albrecht & R. P. Philp), pp. 320–349. Englewood Cliffs, NJ: Prentice-Hall.
- CHOSSON, P., LANAU, C., CONNAN, J. & DESSORT, D. 1991 Biodegradation of refractory hydrocarbon biomarkers from petroleum under laboratory conditions. *Nature* **351**, 640–642.
- CHOW, W. C. 2009 Brownian bridge. *Wiley interdisciplinary reviews: computational statistics* **1**, 325–332.
- CLAYDEN, J., GREEVES, N., WARREN, S. & WOTHERS, P. 2001 Stereochemistry. In *Organic chemistry*. Oxford: Oxford University Press.
- CLINT, J. H. 1992a Adsorption at liquid interfaces. In *Surfactant aggregation*, pp. 13–32. New York: Chapman and Hall.
- CLINT, J. H. 1992b Adsorption on solids. In *Surfactant Aggregation*, pp. 192–221. New York: Chapman and Hall.
- CLINT, J. H. 1992c General phase behaviour of surfactants. In *Surfactant aggregation*, pp. 147–172. New York: Chapman and Hall.

- CLINT, J. H. 1992*d* Micelle formation. In *Surfactant aggregation*, pp. 82–127. New York: Chapman and Hall.
- CLINT, J. H. 1992*e* Mixed-micelle formation. In *Surfactant aggregation*, pp. 130–146. New York: Chapman and Hall.
- CLINT, J. H. 1992*f* Nature of surfactants. In *Surfactant Aggregation*, pp. 1–12. New York: Chapman and Hall.
- COATES, J. D., ANDERSON, R. T. & LOVLEY, D. R. 1996 Oxidation of polycyclic aromatic hydrocarbons under sulfate-reducing conditions. *Applied and Environmental Microbiology* **62**, 1099–1101.
- CONNAN, J. 1984 Biodegradation of crude oils in reservoirs. In *Advances in Petroleum Geochemistry* (ed. J. Brooks & D. H. Welte), , vol. 1, pp. 299–335. London: Academic Press.
- CORKILL, J. M., GEMMELL, K. W., GOODMAN, J. F. & WALKER, T. 1969 Influence of charge on the micelle size of a zwitterionic surface-active agent. *Transactions of the Faraday Society* **64**, 1817–1824.
- COSGROVE, T. & ZASADZINSKI, J. A. 1998 Seeing is believing: the role of microscopy in determining morphology and kinetics of colloids - overview. *Current Opinion in Colloid & Interface Science* **3**, 123–124.
- CZARNECKI, J. 2009 Stabilization of water in crude oil emulsions. Part 2. *Energy & Fuels* **23**, 1253–1257.
- CZARNECKI, J. & MORAN, K. 2005 On the stabilization mechanism of water-in-oil emulsions in petroleum systems. *Energy & Fuels* **19**, 2074–2079.
- DALING, P. S., BRANDVIK, P. J., MACKAY, D. & JOHANSEN, O. 1990 Characterization of crude oils for environmental purposes. *Oil and Chemical Pollution* **7**, 199–224.
- DAUGHNEY, C. J. 2000 Sorption of crude oil from a non-aqueous phase onto silica: the influence of aqueous pH and wetting sequence. *Organic Geochemistry* **31**, 147–158.
- DAVIES, J. T. & RIDEAL, E. K. 1963 *Interfacial Phenomena*. New York and London: Academic Press.

- DAVIS, Z. 2009 Nanoelectro mechanical systems (nems). Course notes for 33321 Nano-2: Nanosystems Engineering, Technical University of Denmark.
- DE, T. K. & MAITRA, A. 1997 Particle engineering of drug loaded nanoparticles and their potential drug-targeting applications. In *Handbook of surface and colloid science* (ed. K. S. Birdi). New York: CRC Press.
- DEKKING, F. M., KRAAIKAMP, C., LOPUHAÄ, H. P. & MEESTER, L. E. 2005 *A modern introduction to probability and statistics: understanding why and how*. London: Springer.
- DEL GROSSO, V. A. 1966 NRL Report 6409, 9. 8. *Tech. Rep.*. Naval Research Laboratory, Washington.
- DEMBICKI, H. J. & MATHIESEN, M. D. 1994 Biomarkers from asphaltene pyrolysis; an additional tool for oil correlation. In *Annual Meeting of the American Association of Petroleum Geologists*. Denver, CO.
- DESAI, J. & DESAI, A. 1993 Production of biosurfactants. In *Biosurfactants*, 1st edn. (ed. N. Kosaric), , vol. 48, pp. 65–97. New York, NY: Marcel Dekker.
- DICHARRY, C., ARLA, D., SINQUIN, A., GRACIA, A. & BOURIAT, P. 2006 Stability of water/crude oil emulsions based on interfacial dilatational rheology. *Journal of Colloid and Interface Science* **297**, 785–791.
- DICKINSON, E., KRUIZENGA, F., POVEY, M. J. W. & VAN DER MOLEN, M. 1993 Crystallization in oil-in-water emulsions containing liquid and solid droplets. *Colloids and Surfaces A: Physicochemical and Engineering Aspects* **81**, 273–279.
- DICKINSON, E., MA, J. & POVEY, M. J. W. 1996 Crystallization kinetics in oil-in-water emulsions containing a mixture of solid and liquid droplets. *Journal of the Chemical Society, Faraday Transactions* **92**, 1213–1215.
- DIDYK, B. M., SIMONEIT, B. T., BRASSELL, S. C. & EGLINTON, G. 1978 Organic geochemical indicators of palaeoenvironmental conditions of sedimentation. *Nature* **272**, 216–222.
- DUDASOVA, D., SIMON, S., HEMMINGSEN, P. & SJÖBLOM, J. 2008 Study of asphaltenes adsorption onto different minerals and clays. Part 1. Experimental

- adsorption with UV depletion detection. *Colloids and Surfaces A: Physicochemical and Engineering Aspects* **317**, 1–9.
- DURHAM, G. B. & GALLANT, R. A. 2002 Numerical techniques for maximum likelihood estimation of continuous-time diffusion. *Journal of Business & Economic Statistics* **20**, 297–316.
- DZIEGIELEWSKA, E. & ADAMCZAK, M. 2013 Evaluation of waste products in the synthesis of surfactants by yeasts. *Chemical Papers* **67**, 1113–1122.
- DZOU, L. I., HOLBA, A. G., RAMÓN, J. C., MOLDOWAN, J. M. & ZINNIKER, D. 1999 Application of new diterpane biomarkers to source, biodegradation and mixing effects on Central Llanos Basin oils, Colombia. *Organic Geochemistry* **30**, 515–534.
- EDWARDS, K. J., BOND, P. L., GIHRING, T. M. & BANFIELD, J. F. 2000 An archaeal iron-oxidizing extreme acidophile important in acid mine drainage. *Science* **287**, 1796–1799.
- EDWARDS, K. R., LEPO, J. E. & LEWIS, M. A. 2003 Toxicity comparison of bio-surfactants and synthetic surfactants used in oil spill remediation to two estuarine species. *Marine Pollution Bulletin* **46**, 1309–1316.
- EGGERS, F. & FUNCK, T. 1973 Ultrasonic measurements with milliliter liquid samples in the 0.5-100 MHz range. *Review of Scientific Instruments* **33**, 969–977.
- EGLINTON, G. & CALVIN, M. 1967 Chemical fossils. *Scientific American* **216**, 32–43.
- EKWALL, P., MANDELL, L. & SOLYOM, P. 1971 The aqueous cetyl trimethylammonium bromide solutions. *Journal of Colloid and Interface Science* **35**, 519 – 528.
- EKWEOZOR, C. M. 1985 Characterisation of the non-asphaltene products of mild chemical degradation of asphaltenes. *Organic Geochemistry* **10**, 1053–1058.
- ELEY, D. D., HEY, M. J. & SYMONDS, J. D. 1988 Emulsions of water in asphaltene-containing oils 1. Droplet size distribution and emulsification rates. *Colloids and Surfaces* **32**, 87–101.

- ELEY, D. D., HEY, M. J., SYMONDS, J. D. & WILLISON, J. M. 1976 Electron micrography of emulsions of water in crude petroleum. *Journal of Colloid and Interface Science* **54**, 462–466.
- ELSHARKAWY, A. M., YARRANTON, H. W., AL-SAHHAF, T. & FAHIM, M. 2008 Water in crude oil emulsions in the Burgan oilfield: effects of oil aromaticity, resins to asphaltenes content ($R/(R+A)$), and water pH. *Journal of Dispersion Science and Technology* **29**, 224–229.
- ENSMINGER, A., JOLY, G. & ALBRECHT, P. 1978 Rearranged steranes in sediments and crude oils. *Tetrahedron Letters* **19**, 1575–1578.
- EPSTEIN, P. S. & CARHART, R. R. 1953 The absorption of sound in suspensions and emulsions. I. Water fog in air. *Journal of the Acoustical Society of America* **52**, 553–565.
- EY 2017 Global oil and gas tax guide. Electronic resource. Ernst & Young, [https://www.ey.com/Publication/vwLUAssets/ey-oil-and-gas-tax-pdf/\\$File/ey-oil-and-gas-tax-pdf.pdf](https://www.ey.com/Publication/vwLUAssets/ey-oil-and-gas-tax-pdf/$File/ey-oil-and-gas-tax-pdf.pdf).
- EYSSAUTIER, J., LEVITZ, P., ESPINAT, D., JESTIN, J., GUMMEL, J., GRILLO, I. & BARRE, L. 2011 Insight into asphaltene nanoaggregate structure inferred by small angle neutron and X-ray scattering. *Journal of Physical Chemistry* **115**, 6827–6837.
- FABRE, H., KAMENKA, N. AND KHAN, A., LINDBLOM, G., LINDMAN, B. & TIDDY, G. T. 1980 Self-diffusion and NMR studies of chloride and bromide ion binding in aqueous hexadecyltrimethylammonium salt solutions. *The Journal of Physical Chemistry* **84** (25), 3428–3433.
- FAN, P., KING, J. D. & CLAYPOOL, G. E. 1987 Characteristics of biomarker compounds in Chinese crude oils. In *Petroleum Geochemistry and Exploration in the Afro-Asian Region* (ed. R. K. Kumar, P. Dwivedi, V. Banerjee & V. Gupta), pp. 197–202. Rotterdam.
- FAN, Y., SIMON, S. & SJÖBLOM, J. 2010 Interfacial shear rheology of asphaltenes at oilwater interface and its relation to emulsion stability: Influence of concentration, solvent aromaticity and nonionic surfactants. *Colloids and Surfaces A: Physicochemical and Engineering Aspects* **366**, 120–128.

- FAWCETT, L., THORPE, N., MATTHEWS, J. & KREMER, K. 2017 A novel Bayesian hierarchical model for road safety hotspot prediction. *Accident Analysis and Prevention* **99**, 262–271.
- FENDLER, J. H. & FENDLER, E. J. 1975 *Catalysis in Micellar and Macromolecular Systems*. New York: Academic Press.
- FENISTEIN, D. & BARRÉ, L. 2001 Experimental measurement of the mass distribution of petroleum asphaltene aggregates using ultracentrifugation and small-angle X-ray scattering. *Fuel* **80**, 283–287.
- FENISTEIN, D., BARRE, L. & FROT, D. 2000 From aggregation to occlusion of asphaltenes: a structural description by radiation scattering techniques. *Oil & Gas Science & Technology* **55**, 123–128.
- FINGAS, M., FIELDHOUSE, B. & MULLIN, J. 1994 Studies of water-in-oil emulsions and techniques to measure emulsion treating agents. In *Proceedings of the Arctic Marine Oilspill Program Technical Seminar*, p. 213244. Environment Canada, Ottawa, Ontario.
- FISHER, S. J., ALEXANDER, R., ELLIS, L. & KAGI, R. I. 1996b The analysis of dimethylphenanthrenes by direct deposition gas chromatography-Fourier transform infrared spectroscopy (GC-FTIR). *Polycyclic Aromatic Compounds* **9**, 257–264.
- FISHER, S. J., ALEXANDER, R., KAGI, R. I. & OLIVER, G. A. 1998 Aromatic hydrocarbons as indicators of biodegradation in North Western Australian reservoirs. In *Sedimentary Basins of Western Australia: West Australian Basins Symposium* (ed. P. G. Purcell & R. R. Purcell), pp. 185–194. WA Branch, Perth, Australia: Petroleum Exploration Society of Australia.
- FONTEVECCHIA, A. February 5, 2013 BP fighting a two front war as macondo continues to bite and production drops. Retrieved from <https://www.forbes.com/sites/afontevetchia/2013/02/05/bp-fighting-a-two-front-war-as-macondo-continues-to-bite-and-production-drops/#3db359fd458c>.
- FORDEDAL, H., SCHILDBERG, Y., SJBLÖM, J. & VOLLE, J.-L. 1996 Crude oil emulsions in high electric fields as studied by dielectric spectroscopy. Influence of

- interaction between commercial and indigenous surfactants. *Colloids and Surfaces A: Physicochemical and Engineering Aspects* **106**, 33–47.
- FOSSEN, M., KALLEVIK, H., KUNDSSEN, K. D. & SJÖBLOM, J. 2007 Asphaltenes precipitated by a two-step precipitation procedure. 1. Interfacial tension and solvent properties. *Energy & Fuel* **21**, 1030–1037.
- FOSSEN, M., KALLEVIK, H., KUNDSSEN, K. D. & SJÖBLOM, J. 2011 Asphaltenes precipitated by a two-step precipitation procedure. 2. Physical and chemical characteristics **25**, 3552–3567.
- FRAKMAN, Z., IGNASIAK, T. M., LOWN, E. M. & STRAUZ, O. P. 1990 Oxygen compounds in Athabasca asphaltene. *Energy & Fuels* **4**, 263–270.
- FRAKMAN, Z., IGNASIAK, T. M., MONTGOMERY, D. S. & STRAUZ, O. P. 1988 Nitrogen compounds in Athabasca asphaltene: The vanadyl porphyrins. *AOSTRA J. Research* **4** (3), 171–179.
- FRANZETTI, A., CAREDDA, P., RUGGERI, C., LA COLLA, P., TAMBURINI, E., PAPACCHINI, M. & BESTETTI, G. 2009 Potential applications of surface active compounds by *Gordonia sp.* strain BS29 in soil remediation technologies. *Chemosphere* **75**, 810–807.
- FRASCH-MELNIK, S. 2011 Fat crystals stabilised double emulsions. PhD thesis, University of Birmingham.
- FREED, D. E., LISITZA, N. V., SEN, P. N. & SONG, Y. Q. 2009 A study of asphaltene nanoaggregation by NMR. *Energy & Fuels* **23**, 1189–1193.
- FRIBERG, S. E. 2007 Micellization. In *Asphaltenes, heavy oils and petroleomics* (ed. O. C. Mullins, E. Y. Sheu, A. Hammani & A. G. Marshall), pp. 189–203. New York: Springer Science + Business Media.
- FRIBERG, S. E., ALBAWAB, A. & ABDOH, A. A. 2007 Surface active inverse micelles. *Colloid and Polymer Science* **285**, 1625–1630.
- FRIBERG, S. E., MULLINS, O. C. & SHEU, E. Y. 2005 Surface activity of an amphiphilic association structure. *Journal of Dispersion Science and Technology* **26** (4), 513–515.

- GAFONOVA, O. V. & YARRANTON, H. W. 2001 The stabilization of water-in-hydrocarbon emulsions by asphaltenes and resins. *Journal Colloid and Interface Science* **241**, 469–478.
- GAMERMAN, D. & LOPES, H. F. 2006 *Gibbs Sampling*, 2nd edn. Boca Raton: Taylor & Francis.
- GARROTT, R. A., EBERHARDT, L. L. & BURN, D. M. 1993 Mortality of sea otters in Prince William Sound following the Exxon Valdez oil spill. *Marine Mammal Science* **9**, 343–359.
- GAWRYS, K. L., BLANKENSHIP, G. A. & KILPATRICK, P. K. 2005 On the distribution of chemical properties and aggregation of solubility fractions in asphaltenes. *Energy & Fuels* **20**, 705–714.
- GAWRYS, K. L., BLANKENSHIP, G. A. & KILPATRICK, P. K. 2006 Solvent entrainment in and occlusion of asphaltenic aggregates probed by small-angle neutron scattering. *Langmuir* **22**, 4487–4497.
- GAWRYS, K. L. & KILPATRICK, P. K. 2005 Asphaltene aggregates are polydisperse oblate cylinders. *Journal of Colloid and Interface Science* **288**, 325–334.
- GELBART, W. M., BEN-SHAUL, A. & ROUX, D. 1989 *Micelles, Membranes, Microemulsions, and Monolayers*. New York: Springer-Verlag.
- GEORGES, J. & CHEN, J. W. 1986 Micellization study of sodium dodecyl sulfate in water and microemulsion systems by conductivity and counterion-activity measurements. *Journal of Colloid and Interface Science* **113**, 143–156.
- GETTINS, J., JOBLING, P. L., WALSH, M. F. & WYN-JONES, E. 1980 Ultrasonic relaxation of surfactants in water and deuterium oxide solutions. *Journal of the Chemical Society, Faraday Transactions 2* **76**, 794–802.
- GIBBS, J. W. 1948 *On the Equilibrium of Heterogeneous Substances*, , vol. 1. Yale University Press.
- GONZALES, G. & MIDDEA, A. 1988 The properties of the calcite-solution interface in the presence of adsorbed resins or asphaltenes. *Colloids and Surfaces* **33**, 217–229.

- GOODWIN, N. S., PARK, P. D. & RAWLINSON, T. 1983 Crude oil biodegradation. In *Advances in Organic Geochemistry 1981* (ed. M. Bjoroy, C. Albrecht, C. Cornford, K. De Groot, G. Eglinton, E. Galimov, D. Leythaeuser, R. Pelet, J. Rullkötter & G. Speers), pp. 650–658. New York: John Wiley & Sons.
- GOUAL, L. & FIROOZABADI, A. 2002 Measuring asphaltenes and resins, and dipole moment in petroleum fluids. *American Institute of Chemical Engineers Journal* **48**, 2646–2663.
- GOUAL, L. & SEDGHI, M. 2015 Role of ion-pair interactions on asphaltene stabilization by alkylbenzenesulfonic acids. *Journal of Colloid and Interface Science* **440**, 23–31.
- GOUAL, L., SEDGHI, M., WANG, X. & ZHU, Z. 2014 Asphaltene aggregation and impact of alkylphenols. *Langmuir* **30**, 5394–5403.
- GOUAL, L., SEDGHI, M., ZENG, H., MOSTOWFI, F., MCFARLANE, R. & MULLINS, O. C. 2011 On the formation and properties of asphaltene nanoaggregates and clusters by DC-conductivity and centrifugation. *Fuel* **90**, 2480–2490.
- GOUGH, M. A. & ROWLAND, S. J. 1990 Characterization of unresolved complex mixtures of hydrocarbons in petroleum. *Nature* **344**, 648–650.
- GRANTHAM, P. J. 1986 The occurrence of unusual C27 and C29 sterane predominances in two types of oman crude oil. *Organic Geochemistry* **9**, 1–10.
- GRANTHAM, P. J., LIJMBACK, G. M. & POSTHUMA, J. 1988 Origin of crude oils in Oman. *Journal of Petroleum Geology* **11**, 61– 80.
- GRAY, M. R., TYKWINSKI, R. R., STRYKER, J. M. & TAN, X. 2011 Supramolecular assembly model for aggregation of petroleum asphaltenes. *Energy & Fuels* **25**, 3125–3134.
- GROENZIN, H. & MULLINS, O. C. 1999 Asphaltene molecular size and structure. *Journal of Physical Chemistry A* **103**, 1123711245.
- GROENZIN, H. & MULLINS, O. C. 2000 Molecular sizes of asphaltenes from different origin. *Energy & Fuels* **14**, 677–684.

- GROENZIN, H. & MULLINS, O. C. 2007 Asphaltene molecular size and weight by time-resolved fluorescence depolarization. In *Asphaltenes, Heavy Oils and Petroleomics* (ed. O. C. Mullins, E. Y. Sheu, A. Hammami & A. G. Marshall). New York: Springer.
- GROENZIN, H., MULLINS, O. C., ESER, S., MATHEWS, J., YANG, M. G. & JONES, D. 2003 Molecular size of asphaltene solubility fractions. *Energy and Fuels* **17**, 498–503.
- DEL GROSSO, V. A. & MADER, C. W. 1972 Velocity of sound in pure water. *Journal of the Acoustical Society of America* **52**, 1442–1445.
- GUERRA, R., ANDREWS, A. B., MULLINS, O. C. & SEN, P. N. 2007 Comparison of asphaltene molecular diffusivity of various asphaltenes by fluorescence correlation spectroscopy. *Fuel* **86**, 20162020.
- GUNNARSON, G., JOHNSON, B. & WENNERSTORM, H. 1980 Surfactant association into micelles: an electrostatic approach. *The Journal of Physical Chemistry* **84**, 3114–3121.
- HABDAS, P. & WEEKS, E. R. 2002 Video microscopy of colloidal suspensions and colloidal crystals. *Current Opinion in Colloid & Interface Science* **7**, 196–203.
- HALWACHI, A., HASSAN, K., YAKOVLEV, D. S. & BOEK, E. S. 2012 Systematic optimization of asphaltene molecular structure and molecular weight using the quantitative molecular representation approach. *Energy & Fuels* **26**, 6177–6185.
- HARAYAMA, S., KOK, M. & NEIDLE, E. L. 1992 Functional and evolutionary relationships among diverse oxygenases. *Annual Reviews of Microbiology* **46**, 565–601.
- HARAYAMA, S. & TIMMIS, K. N. 1989 Catabolism of aromatic hydrocarbons by pseudomonas. In *Genetics of Bacterial Diversity* (ed. D. A. Hopwood & K. Charter), pp. 151–174. New York: Academic Press.
- HARBOTTLE, D., CHEN, Q., MOORTHY, K., WANG, L., XU, S. & LIU, Q. 2014 Problematic stabilizing films in petroleum emulsions: shear rheological response of viscoelastic asphaltene films and the effect on drop coalescence. *Langmuir* **30**, 6730–6738.

- HARING, M. M. 1926 Colloid and capillary chemistry (Freundlich, Herbert). *Journal of Chemical Education* **3**.
- HARTLEY, G. S. 1936 *Aqueous solutions of paraffin chain salts*. Paris: Herman & Cie.
- HAYASHI, S. & IKEDA, S. 1980 Micelle size and shape of sodium dodecyl sulfate in concentrated sodium chloride solutions. *The Journal of Physical Chemistry* **84**, 744–751.
- HAYTER, J. B. & PENFOLD, J. 1981 Self-consistent structural and dynamic study of concentrated micelle solutions. *Journal of the Chemical Society (Faraday Transactions 1)* **77**, 1851.
- HAZLEHURST, T. A., HARLEN, O. G., HOLMES, M. J. & POVEY, M. J. W. 2014 Multiple scattering in dispersions, for long wavelength thermoacoustic solutions. *Journal of Physics: Conference Series* **498**, 1–8.
- HEAD, I. M., JONES, D. M. & LARTER, S. R. 2003 Biological activity in the deep subsurface and the origin of heavy oil. *Nature* **426**, 344–352.
- HIRATO, T., KOYAMA, K., TANAKA, T., AWAKURA, Y. & MAJIMA, H. 1991 Demulsification of water-in-oil emulsion by an electrostatic coalescence method. *Materials Transactions* **52**, 257–263.
- HOFFMANN, C. F., MACKENZIE, A. S., LEWIS, C. A., MAXWELL, J. R., OUDIN, J. L., DURAND, B. & VANDENBROUCKE, M. 1984a A biological marker study of coals, shales, and oils from the Mahakam Delta, Kalimantan, Indonesia. *Chemical Geology* **42**, 1–23.
- HOFFMANN, C. F., MACKENZIE, A. S., LEWIS, C. A. MAXWELL, J. R., OUDIN, J. L., DURAND, B. & VANDENBROUCKE, M. 1984b A biological marker study of coals, shales, and oils from the Mahakam Delta, Kalimantan, Indonesia. *Chemical Geology* **42**, 1–23.
- HOFFMANN, C. F. & STRAUZ, O. P. 1986 Bitumen accumulation in Grosmont Platform Complex, Upper Devonian, Alberta, Canada. *American Association of Petroleum Geologists Bulletin* **70**, 1113–1128.

- HOIER, L. & WHITSON, C. 2001 Compositional grading, theory and practice. *SPE Reservoir Evaluation & Engineering* **4**, 525–535.
- HORSTAD, I., LARTER, S. & MILS, N. A. 1992 Quantitative model of biological petroleum degradation within the brent group reservoir in the gulfaks field, norwegian north sea. *Organic Geochemistry* **19**, 107–117.
- HORTAL, A. R., HURTADO, P. M., MARTÍNEZ-HAYA, B. & MULLINS, O. C. 2007 Molecular weight distributions of coal and petroleum asphaltenes from laser desorption ionization experiments. *Energy & Fuels* **21**, 2863–2868.
- HORVÁTH-SZABÓ, G., MASLIYAH, J. H., ELLIOTT, J. W., YARRANTON, H. W. & CZARNECKI, J. 2005 Adsorption isotherms of associating asphaltenes at oil/water interfaces based on the dependence of interfacial tension on solvent activity. *Journal of Colloid and Interface Science* **283**, 5–17.
- HOSSEINI-DASTGERDI, Z., TABATABEJ-NEJAD, S. A. R., KHODAPANAH, E. & SAHAREI, E. 2015 A comprehensive study on mechanism of formation and techniques to diagnose asphaltene structure; molecular and aggregates: a review. *Asia-Pacific Journal of Chemical Engineering* **10**, 1–14.
- HU, Y. F. & GUO, T. M. 2001 Effect of temperature and molecular weight of *n*-alkane precipitants on asphaltene precipitation. *Fluid Phase Equilibria* **192**, 13–25.
- HUGHES, W. B., HOLBA, A. G. & PZOU, I. P. 1995 The ratios of dibenzothiophene to phenanthrene and pristane to phytane as indicators of depositional environment and lithology of petroleum source rocks. *Geochimica et Cosmochimica Acta* **59**, 3581–3598.
- HUMMEL, D. O. 1999 *Handbook of surfactant analysis: chemical, physico-chemical, and physical methods*. New York: John Wiley.
- HUNTER, R. J. 1987 *Foundations of colloid science*, , vol. 1. Oxford: Oxford University Press.
- HUNTER, R. J. 2001 Nature of colloidal dispersions. In *Foundations of colloid science*. New York: Oxford University Press.

- IGNASIAK, T. M., KOTLYAR, L., SAMMAN, N., MONTGOMERY, D. S. & STRAUZ, O. P. 1983 Preparative gel permeation chromatography of Athabasca asphaltene and the relative polymer-forming propensity of the fractions. *Fuel* **62**, 363–369.
- ISRAELACHVILI, J. 1987 Physical properties of surfactant self-association into micelles, vesicles and microemulsions droplets. In *Surfactants in Solution* (ed. K. L. Mittal & P. Bothorel), , vol. 4, p. 3. New York: Plenum.
- ISRAELACHVILI, J. N. 1974 The nature of van der Waals forces. *Contemporary Physics* **15**, 159–178.
- ITOPF 2017 Oil tanker spill statistics 2016. *Tech. Rep.*. The international tanker owners pollution federation limited.
- JARVIS, J. M., ROBBINS, W. K., CORILO, Y. E. & RODGERS, R. P. 2015 Novel method to isolate interfacial material. *Energy & Fuels* **29**, 7058–7064.
- JERIBI, M., ALMIR-ASSAD, B., LANGEVIN, D., HENAUT, I. & ARGILLIER, J. F. 2002 Adsorption kinetics of asphaltenes at liquid interfaces. *Journal of Colloid and Interface Science* **256**, 268–272.
- JESTIN, J., SIMON, S., ZUPANCIC, L. & BARRE, L. 2007 A small angle neutron scattering study of the adsorbed asphaltene layer in water-in-hydrocarbon emulsions: structural description related to stability. *Langmuir* **23**, 10471–10478.
- JILLAVENKATESA, A., DAPKUNAS, S. J. & LUM, L.-S. H. 2001 Particle size characterization. *NIST Special Publication* **960**, 1.
- JOBSON, A., COOK, F. D. & WESTLAKE, D. S. 1972 Microbial utilization of crude oil. *Applied Microbiology* **23**, 1082–1089.
- JONES, D. M., DOUGLAS, A. G. & CONNAN, J. 1987 Hydrocarbon distributions in crude oil asphaltene pyrolyzates. 1. Aliphatic compounds. *Energy & Fuels* **1**, 468–476.
- JONES, D. M., HEAD, I. M., GRAY, N. D., ADAMS, J. J., ROWAN, A. K., AITKEN, C. M., BENNETT, B., HUANG, H., BROWN, A., BOWLER, B. F., OLDENBURG, T., ERDMANN, M. & LARTER, S. R. 2008 Crude-oil biodegradation via methanogenesis in subsurface petroleum reservoirs. *Nature* **451**.

- KATO, S., NOMURA, H., HONDA, H., ZIELINSKI, R. & IKEDA, S. 1988 Ultrasonic relaxation study of the exchange process of surfactant monomer with micelle in aqueous solutions of alkyltrimethylammonium bromides. *Journal of Physical Chemistry* **75**, 2305–2310.
- KHRISTOV, K., TAYLOR, S. D., CZARNECKI, J. & MASLIYAH, J. 2000 Thin liquid film technique - application to water-oil-water bitumen emulsion films. *Colloids and Surfaces A* **174**, 183–196.
- KILLOPS, S. D. & AL-JUBOORI, M. A. 1990 Characterization of the unresolved complex mixture (UCM) in the gas chromatograms of biodegraded petroleums. *Organic Geochemistry* **15**, 147–160.
- KILPATRICK, P. K. 2012 Water-in-crude oil emulsion stabilization: review and unanswered questions. *Energy & Fuels* **26**, 4017–4026.
- KILPATRICK, P. K. & SPIECKER, P. M. 2001 Asphaltene emulsions. In *Encyclopedic Handbook of Emulsion Technology* (ed. J. Sjoblom), pp. 707–730. New York: Marcel Dekker.
- KIM, Y. H., WASAN, D. T. & BREEN, P. J. 1993 A study of dynamic interfacial mechanisms for demulsification of water-in-oil emulsions. *Colloids and Surfaces A: Physicochemical and Engineering Aspects* **95**, 235–247.
- KIMBLER, O. K., REED, R. L. & SILBERBERG, I. H. 1966 Physical characteristics of natural films formed at crude oil-water interfaces. *Society of Petroleum Engineers Journal* **6**, 153–165.
- KLEIN, G. C., ANGSTRÖM, A., RODGERS, R. P. & MARSHALL, A. G. 2006a Use of saturates/aromatics/resins/asphaltenes (SARA) fractionation to determine matrix effects in crude oil analysis by electrospray ionization Fourier transform ion cyclotron resonance mass spectrometry. *Energy & Fuels* **20** (2), 668–672.
- KLEIN, G. C., KIM, S., RODGERS, R. P. & MARSHALL, A. G. 2006b Mass spectral analysis of asphaltenes. i. Compositional differences between pressure-drop and solvent-drop asphaltenes determined by electrospray ionization Fourier transform ion cyclotron resonance mass spectrometry. *Energy & Fuels* **20**, 1965–1972.

- KOCH, K.-R. 2007 *Introduction to Bayesian statistics*, 2nd edn. Berlin ; New York: Springer.
- KOKAL, S. 2005 Crude-oil emulsions: A state-of-the-art review. *SPE Production and Facilities* **20**, 5–13.
- KRAFFT, F. 1899 Ueber die krystallisationsbedingungen colloïdaler salzlösungen. *Berichte der deutschen chemischen Gesellschaft* **32**, 1596–1608.
- KRATOHVIL, J. P. 1980 Comments on some novel approaches for the determination micellar aggregation numbers. *Journal of Colloid and Interface Science* **75**, 271–275.
- KRAWCZYK, M. A., WASAN, D. T. & SHETTY, C. S. 1991 Chemical demulsification of petroleum emulsions using oil-soluble demulsifiers. *Industrial and Engineering Chemistry Research* **30**, 367–375.
- KRISTENSEN, K. 2010 Theory and application of ultrasound diagnostics of aqueous solutions. Master's thesis, Department of Micro- and Nanotechnology, Technical University of Denmark.
- KROPP, K. G., DAVIDOVA, I. A. & SUFLITA, J. M. 2000 Anaerobic oxidation of *n*-dodecane by an addition reaction in a sulfate-reducing bacterial enrichment culture. *Applied and Environmental Microbiology* **66**, 5393–5398.
- KUO, L.-C. 1994 An experimental study of crude oil alteration in reservoir rocks by water washing. *Organic Geochemistry* **21**, 465–479.
- KUZNICKI, T., MASLIYAH, J. H. & BHATTACHARJE, S. 2008 Molecular dynamics study of model molecules resembling asphaltene-like structures in aqueous organic solvent systems. *Energy and Fuels* **22**, 2379–2389.
- KUZNICKI, T., MASLUYAH, J. H. & BHATTACHARJEE, S. 2009 Aggregation and partitioning of model asphaltenes at toluene-water interfaces: molecular dynamics simulations. *Energy and Fuels* **23**, 5027–5035.
- LA MESA, C. 1990 Dependence of critical micelle concentrations on intensive variables: a reduced variable analysis. *The Journal of Physical Chemistry* **94**, 271.

- LARTER, S., KOOPMANS, M. P. & HEAD, I., E. A. 2000 Biodegradation rates assessed geologically in a heavy oilfield - implications for a deep, slow (large) biosphere. In *GeoCanada 2000 - The Millennium Geoscience Summit*. Calgary, Alberta.
- LAUGHLIN, R. G. 1978*a* Relative hydrophobicities among surfactant hydrophilic groups. *Advances in Liquid Crystals* **3**, 99–148.
- LAUGHLIN, R. G. 1978*b* Solvation and structural requirements of surfactant hydrophilic groups. *Advances in Liquid Crystals* **3**, 41–98.
- LAURENDEAU, N. M. 2005 *Statistical Thermodynamics: Fundamentals and Applications*, chap. Appendix N. Cambridge: Cambridge University Press.
- LEE, P. M. 2012 *Bayesian Statistics: An Introduction*, 4th edn. Chichester: John Wiley & Sons.
- LEE, R. F. 1999 Agents which promote and stabilize water-in-oil emulsions. *Spill Science and Technology Bulletin* **5**, 117–126.
- LICHTENTHALER, R. G. & DALING, P. S. 1985 Aerial application of dispersants comparison of slick behaviour of chemically treated versus non-treated slicks. In *1985 Oil Spill Conference*, pp. 471–478. American Petroleum Institute, Washington, DC.
- LINDMAN, B., PUYAL, M.-C., KAMENKA, N., BRUN, B. & GUNNARSSON, G. 1982 Micelle formation in ionic surfactants: Tracer self-diffusion studies and theoretical calculations for sodium *p*-octylbenzenesulphonate. *Journal of Physical Chemistry* **86**, 1702–1711.
- LISITZA, N. V., FREED, D. E., SEN, P. N. & SONG, Y.-Q. 2009 Study of asphaltene nanoaggregation by nuclear magnetic resonance (NMR). *Energy & Fuels* **23**, 1189–1193.
- LITTMAN, W. 1997 Application of surface active agents in petroleum production. In *Surface and colloid chemistry* (ed. K. S. Birdi). New York: CRC Press, Boca Raton.
- LIU, Z., LIU, J., ZHU, Q. & WU, W. 2012 The weathering of oil after the Deepwater Horizon oil spill: insights from the chemical composition of the oil

- from the sea surface, salt marshes and sediments. *Environmental Research Letters* **7**, 1–14.
- LLOYD, P. & BERRY, M. V. 1967 Wave propagation through an assembly of spheres. Part IV. Relations between different scattering theories. *Proceedings of the Physical Society* **91**, 678–688.
- LOH, W., TEIXEIRA, L. C. & LEE, L. T. 2004 Isothermal calorimetric investigation of the interaction of poly(_N-isopropylacrylamide) and ionic surfactants. *The Journal of Physical Chemistry B* **108**, 31963201.
- LONDON, F. 1930 Zur theorie und systematik der molekularkräfte. *Zeitschrift für Physik* **63**, 245–279.
- LOUGHLIN, T. R. 2013 *Marine mammals and the Exxon Valdez*. Academic Press.
- MA, A., SHUICHANG, Z. & ZHANG, D. 2008 Ruthenium-ion-catalyzed oxidation of asphaltenes of heavy oils in Lunnan and Tahe oilfields in Tarim Basin, NW China. *Organic Geochemistry* **39**, 1502–1511.
- MACKAY, D. 1987 Formation and stability of water-in-oil emulsions. *Tech. Rep. DIWO Report No. 1*. IKU, Trondheim, Norway.
- MACKAY, G. M., MCLEAN, A. Y., BETANCOURT, O. J. & JOHNSON, B. D. 1973 Formation of water-in-oil emulsions subsequent to an oil spill. *Journal of the Institute of Petroleum* **59**, 164–172.
- MACKENZIE, A. S. 1984 Application of biological markers in petroleum geochemistry. In *Advances in Petroleum Geochemistry* (ed. J. Brooks & D. H. Welte), , vol. 1, pp. 115–214. London: Academic Press.
- MACKENZIE, A. S., HOFFMANN, C. F. & MAXWELL, J. R. 1981 Molecular parameters of maturation in the Toarcian shales, Paris Basin, France 3. changes in aromatic steroid hydrocarbons. *Geochimica et Cosmochimica Acta* **45**, 1345–1355.
- MACKENZIE, A. S., PATIENCE, R. L., MAXWELL, J. R., VANDENBROUCKE, M. & DURAND, B. 1980 Molecular parameters of maturation in the Toarcian shales, Paris Basin, France i. Changes in the configuration of acyclic isoprenoid alkanes, steranes, and triterpanes. *Geochimica et Cosmochimica Acta* **44**, 1709–1721.

- MACKOR, E. L. 1951 A theoretical approach of the colloid-chemical stability of dispersions in hydrocarbons. *Journal of Colloid Science* **6**, 492–495.
- MACKOR, E. L. & VAN DER WAALS, J. H. 1952 The statistics of the adsorption of rod-shaped molecules in connection with the stability of certain colloidal dispersions. *Journal of Colloid Science* **7**, 535–550.
- MAGOT, M., CONNAN, J. & CROLET, J.-L. 1994 Les bactéries des gisements pétroliers. *Recherche* **228**, 936–937.
- MAKKAR, R. S., CAMEOTRA, S. S. & BANAT, I. M. 2011 Advances in utilization of renewable substrates for biosurfactant production. *Applied Microbiology and Biotechnology* **1**, 1–5.
- MANSUY, R. & YOR, M. 2007 *Aspects of Brownian motion (Universitext)*. Berlin; London: Springer.
- MARCHANT, R. & BANAT, I. M. 2012 Microbial biosurfactants: challenges and opportunities for future exploitation. *Trends in Biotechnology* **11**, 558–565.
- MARTINEZ-HAYA, B., HORTAL, A. R., HURTADO, P. M., LOBATO, M. D. & PEDROSA, J. M. 2007 Laser desorption/ionization determination of molecular weight distributions of polyaromatic carbonaceous compounds and their aggregates. *The Journal of Mass Spectrometry* **42**, 701–713.
- MASLIYAH, J., XU, Z., NANDAKUMAR, K., YEUNG, A. & CZARNECKI, J. 2002 Emulsion studies associated with bitumen recovery from Canadian oil sands: part i. In *Proceedings of the 3rd International Conference on Petroleum Phase Behavior and Fouling*. New Orleans, LA.
- MASON, T. & PETERS, D. 2002 1 - an introduction to the uses of power ultrasound in chemistry. In *Practical Sonochemistry (Second Edition)*, Second edition edn., pp. 1–48. Woodhead Publishing.
- MASTERSON, W. D., DZOU, L. I., HOLBA, A. G., FINCANNON, A. L. & ELLIS, L. 2000 Evidence for biodegradation and evaporite fractionation on west sak, kumaruk and prudhoe bay field areas, north slope, alaska. *Organic Geochemistry* **32**, 411–441.

- MCCAFFREY, M. A., LEGARRE, H. A. & JOHNSON, S. J. 1996 Using biomarkers to improve heavy oil reservoir management; an example from the Cymric Field, Kern County, California. *American Association of Petroleum Geologists Bulletin* **80**, 898–913.
- MCKENNA, A. M., MARSHALL, A. G. & RODGERS, R. P. 2013 Heavy petroleum composition. 4 Asphaltene compositional space. *Energy and Fuels* **27**, 12571267.
- MCKENNA, A. M., PURCELL, J. M., RODGERS, R. P. & MARSHALL, A. G. 2009 Identification of vanadyl porphyrins in a heavy crude oil and raw asphaltene by atmospheric pressure photoionization fourier transform ion cyclotron resonance (FT-ICR) mass spectrometry. *Energy & Fuels* **23**, 2122–2128.
- MCKIRDY, D. M., ALDRIDGE, A. K. & YPMA, P. M. 1983 A geochemical comparison of some crude oils from Pre-Ordovician carbonate rocks. In *Advances in Organic Geochemistry 1981* (ed. M. Bjoroy, C. Albrecht, C. Cornford, K. De Groot, G. Eglinton, E. Galimov, D. Leythaeuser, R. Pelet, J. Rullkötter & G. Speers), pp. 99–107. New York: John Wiley & Sons.
- MCLEAN, J. D. & KILPATRICK, P. K. 1997a Effects of asphaltene aggregation in model heptane-toluene mixtures on stability of water-in-oil emulsions. *Journal of Colloid and Interface Science* **196**, 56–59.
- MCLEAN, J. D. & KILPATRICK, P. K. 1997b Effects of asphaltene solvency on stability of water-in-crude-oil emulsions. *Journal of Colloid and Interface Science* **189**, 242–253.
- MCLEAN, J. D., SPEICKER, P. M., SULLIVAN, A. P. & KILPATRICK, P. K. 1998 The role of petroleum asphaltenes in the stabilization of water-in-oil emulsions. In *Structures and dynamics of asphaltenes* (ed. O. C. Mullins & E. Y. Sheu), pp. 377–422. New York: Plenum Press.
- MELVOLD, R. W., GIBSON, S. C. & SCARBERRY, R. 1988 Sorbents for liquid hazardous substance cleanup and control. *Tech. Rep.*. Noyes Data Corp, Park Ridge, N.J., U.S.A.
- METTLER TOLEDO 1999 *Operating Instructions, Mettler Toledo MT/UMT Balances*. Mettler Toledo GmbH.

- MIGET, R. J., OPPENHEIMER, C. H., KATOR, H. I. & LAROCK, D. A. 1969 Microbial degradation of normal paraffin hydrocarbons in crude oil. In *Proceedings of the Joint Conference on Prevention and Control of Oil Spills*, pp. 327–331. Washington, DC: American Petroleum Institute.
- MILLER, D. D. 1996 Video- and computer-enhanced light microscopy of three-dimensional colloidal structures. *Current Opinion in Colloid & Interface Science* **1**, 243–249.
- MILNER, C. D., ROGERS, M. A. & EVANS, C. R. 1977a Petroleum transformations in reservoirs. *Journal of Geochemical Exploration* **7**, 101–153.
- MILNER, C. D., ROGERS, M. A. & EVANS, C. R. 1977b Petroleum transformations in reservoirs. *Journal of Geochemical Exploration* **7**, 101–153.
- MOHAMMED, R. A., BAILEY, A. I., LUCKHAM, P. F. & TAYLOR, S. E. 1993 Dewatering of crude oil emulsions 2. Interfacial properties of the asphaltic constituents of crude oil. *Colloids and Surfaces A: Physicochemical and Engineering Aspects* **80**, 237–242.
- MOLDOWAN, J. M., FAGO, F. J. & CARLSON, R. K. 1991 Rearranged hopanes in sediments and petroleum. *Geochimica et Cosmochimica Acta* **55**, 3333–3353.
- MOLDOWAN, J. M. & FAGO, J. F. 1986 Structure and significance of a novel rearranged monoaromatic steroid hydrocarbon in petroleum. *Geochimica et Cosmochimica Acta* **50**, 343–351.
- MOLDOWAN, J. M., LEE, C. Y., SUNDARARAMAN, P., SALVATORI, T., ALAJBEG, A., GJUKIC, B. & DEMAISON, G. J. 1992 Source correlation and maturity assessment of select oils and rocks from the Central Adriatic Basin (Italy and Yugoslavia). In *Biological Markers in Sediments and Petroleum*, pp. 370–401. Englewood Cliffs, NJ: Prentice-Hall.
- MOLDOWAN, J. M., PETERS, K. E., CARLSON, R. K., SCHOELL, M. & ABU-ALI, M. A. 1994b Diverse applications of petroleum biomarker maturity parameters. *Arabian Journal for Science and Engineering* **19**, 273–298.
- MOLDOWAN, J. M., SEIFERT, W. K. & GALLEGOS, E. J. 1985 Relationship between petroleum composition and depositional environment of petroleum source rocks. *American Association of Petroleum Geologists Bulletin* **69**, 1255–1268.

- MOLDOWAN, J. M., SUNDARARAMAN, P. & SCHOELL, M. 1986a Sensitivity of biomarker properties to depositional environment and/or source input in the Lower Toarcian of S. W. Germany. *Organic Geochemistry* **10**, 915–926.
- MOLDOWAN, J. M., SUNDARARAMAN, P. & SCHOELL, M. 1986b Sensitivity of biomarker properties to depositional environment and/or source input in the Lower Toarcian of S.W. Germany. *Organic Geochemistry* **10**, 915–926.
- MOSTOWFI, F., INDO, K., MULLINS, O. C. & MCFARLANE, R. 2009 Asphaltene nanoaggregates studied by centrifugation. *Energy & Fuels* **23** (3), 1194–1200.
- MUKHERJEE, S. & KUSHNICK, A. P. 1988 Effect of demulsifiers on interfacial properties governing crude oil demulsification. In *Symposium On Advances in Oil Field Chemistry Presented Before the Division of Petroleum Chemistry*. Toronto: American Chemical Society.
- MULLINS, O. C. 2010 The modified yen model. *Energy and Fuels* **24**, 2170–2207.
- MULLINS, O. C. 2011 The asphaltenes. *Annual Reviews in Analytical Chemistry* **4**, 393–418.
- MULLINS, O. C., SABBAH, H., EYSSAUTIER, J., POMERANTZ, A., BARRÉ, L., ANDREWS, A., RUIZ-MORALES, Y., MOSTOWFI, F., MCFARLANE, R., GOUAL, L., LEPKOWICZ, R., COOPER, T., ORBULESCU, J., LEBLANC, R., EDWARDS, J. & ZARE, R. 2012 Advances in asphaltene science and the Yen-Mullins model. *Energy & Fuel* **26**, 3986–4003.
- MULLINS, O. C., SHEU, E. Y. & EDS 1998 *Structures and Dynamics of Asphaltenes*. New York: Plenum.
- MULLINS, O. C., SHEU, E. Y., HAMMAMI, A. & MARSHALL, A. G. 2007 *Asphaltenes, heavy oils and petroleomics*. New York: Springer.
- MURGICH, J., ABANERO, J. A. & STRAUZ, O. P. 1999 Molecular recognition in aggregates formed by asphaltene and resin molecules from the athabasca oil sand. *Energy & Fuels* **13**, 278–286.
- MUSA, R. S. 1958 Two-crystal interferometric method for measuring ultrasonic absorption coefficients in liquids. *The Journal of the Acoustical Society of America* **30**, 215–219.

- NABHOLZ, J. V., MILLER, P. & ZEEMAN, M. 1993 Environmental risk assessment of new chemicals under the Toxic Substances Control Act (TSCA). In *Section Five: Environmental Toxicology and Risk Assessment* (ed. W. G. Landis, J. S. Hughes & M. A. Lewis), pp. 40–55. American Society for Testing and Materials, Philadelphia, PA.
- NALWAYA, V., TANTAYAKOM, V., PIUMSOMBOON, P. & FOGLER, S. 1999 Studies on asphaltenes through analysis of polar fractions. *Industrial and Engineering Chemistry Research* **38**, 964–972.
- NAPPER, D. H. & HUNTER, R. J. 1983 Hydrosols. In *M.T.P. International Review of Science* (ed. M. Kerker), 2, vol. 7, pp. 161–213. London and Boston: Butterworths.
- NES, W. R. & MCKEAN, M. L. 1977 *Biochemistry of Steroids and Other Isoprenoids*. Baltimore: University Park Press.
- NIST 2005 *NIST/EPA/NIH Mass Spectral Library (NIST 05) and NIST Mass Spectral Search Program (Version 2.0d)*. U.S. Department of Commerce, Technology Administration, National Institute of Standards and Technology, Standard Reference Data Program, Gaithersburg, MD 20899.
- NORTON, J., FRYER, P. & NORTON, I. T. 2013 Formulation engineering of food emulsions. In *Formulation engineering of foods*, pp. 82–106. Chichester: Wiley-Blackwell.
- NYTOFT, H. P. & BOJESEN-KOEFOED, J. A. 2001 $17\alpha,21\alpha(\text{h})$ -hopanes: natural and synthetic. *Organic Geochemistry* **32**, 841–856.
- OCHENDUSZKO, A. & BUCKIN, V. 2010 Real-time monitoring of heat-induced aggregation of β -lactoglobulin in aqueous solutions using high-resolution ultrasonic spectroscopy. *International Journal of Thermophysics* **31**, 113–130.
- ODDEN, W., BARTH, T. & TALBOT, M. R. 2002 Compound-specific carbon isotope analysis of natural and artificially generated hydrocarbons in source rocks and petroleum fluids from offshore Mid-Norway. *Organic Geochemistry* **33**, 47–65.
- OH, K. & DEO, M. D. 2007 Near-infrared spectroscopy to study asphaltene aggregation in solvents. In *Asphaltenes, Heavy Oils and Petroleomics* (ed. O. C.

- Mullins, E. Y. Sheu, A. Hammami & A. G. Marshall), pp. 469–488. New York: Springer.
- OPEC 2018 Electronic resource. https://www.opec.org/opec_web/en/publications/202.htm.
- ORBULESCU, J., MULLINS, O. C. & LEBLANC, R. M. 2010a Surface chemistry and spectroscopy of UG8 asphaltene Langmuir film. Part 1. *Langmuir* **26**, 15257–15264.
- ORBULESCU, J., MULLINS, O. C. & LEBLANC, R. M. 2010b Surface chemistry and spectroscopy of UG8 asphaltene Langmuir film. Part 2. *Langmuir* **26**, 15265–15271.
- OVALLES, C., ROGEL, E., MOIR, M. & THOMAS, L. 2011 *Characterization of heavy crude oil, their fractions, and hydrovisbroken products by the asphaltene solubility fraction method*, vol. 26.
- PALLASER, R. J. 2000 Recognising biodegradation in gas/oil accumulations through the $\delta^{13}\text{C}$ composition of gas components. *Organic Geochemistry* **31**, 1363–1373.
- PALMER, S. E. 1983 Porphyrin distributions in degraded and non-degraded oils from Colombia. In *The 186th National Convention of the American Chemical Society*. Washington, DC.
- PALMER, S. E. 1984 Effect of water washing on C_{15+} hydrocarbon fraction of crude oils from northwest Palawan, Philippines. *American Association of Petroleum Geologists Bulletin* **68**, 137–149.
- PALMER, S. E. 1993 Effect of biodegradation and water washing on crude oil composition. In *Organic Geochemistry* (ed. M. H. Engel & S. A. Macko), pp. 511–533. New York: Plenum Press.
- PARRA, J., GUINEA, J., MANRESA, M., MERCADE, R. M., COMELLAS, F. & BOSCH, M. 1989 Chemical characterization and physicochemical behavior of biosurfactants. *Journal of the American Oil Chemists' Society* **66**, 141–145.
- PATIENCE, R. L., YON, D. A., RYBACK, G. & MAXWELL, J. R. 1980 Acyclic isoprenoid alkanes and geochemical maturation. In *Advances in Organic Geochemistry 1979* (ed. A. G. Douglas & J. R. Maxwell), pp. 287–294. New York: Pergamon Press.

- PAUCHARD, V., RANE, J. P. & BANERJEE, S. 2014 Asphaltene-laden interfaces form soft glassy layers in contraction experiments: a mechanism for coalescence blocking. *Langmuir* **30**, 12795–12803.
- PEÑA, A. A., HIRSAKI, G. J. & MILLER, C. A. 2005 Chemically induced destabilization of water-in-crude oil emulsions. *Industrial & Engineering Chemistry Research* **44**, 1139–1149.
- PENG, P., FU, J. & SHENG, G. 1999 Ruthenium-ions-catalyzed oxidation of an immature asphaltene: Structural features and biomarker distribution. *Energy and Fuels* **13**, 266–277.
- PENG, P., MORALES-IZQUIERDO, A., HOGG, A. & STRAUZ, O. P. 1997 Molecular structure of athabasca asphaltene: sulfide, ether, and ester linkages. *Energy & Fuels* **11**, 1171–1187.
- PETERS, K. E. 2000 Petroleum tricyclic terpanes: predicted physicochemical behavior from molecular mechanics calculations. *Organic Geochemistry* **31**, 497–507.
- PETERS, K. E., CLARK, M. E., DAS GUPTA, U., MCCAFFREY, M. A. & LEE, C. Y. 1995 Recognition of an infracambrian source rock based on biomarkers in the Bagehwala-1 oil, India. *American Association of Petroleum Geologists Bulletin* **79**, 1481–1494.
- PETERS, K. E. & MOLDOWAN, J. M. 1991 Effects of source, thermal maturity, and biodegradation on the distribution and isomerization of homohopanes in petroleum. *Organic Geochemistry* **17**, 47–61.
- PETERS, K. E. & MOLDOWAN, J. M. 1993 *The Biomarker Guide. Interpreting Molecular Fossils in Petroleum and Ancient Sediments*. Englewood Cliffs, NJ: Prentice-Hall.
- PETERS, K. E., MOLDOWAN, J. M., SCHOELL, M. & HEMPKINS, W. B. 1986 Petroleum isotopic and biomarker composition related to source rock organic matter and depositional environment. *Organic Geochemistry* **10**, 17–27.
- PETERS, K. E., MOLDOWAN, J. M. & SUNDARARAMAN, P. 1990 Effects of hydrous pyrolysis on biomarker thermal maturity parameters: Monterey phosphatic and siliceous members. *Organic Geochemistry* **15**, 249–265.

- PETERS, K. E., SNEDDEN, J. W., SULAEMAN, A., SARG, J. F. & ENRICO, R. J. 2000 A new geochemical-stratigraphic model for the Mahakam Delta and Makassar slope, Kalimantan, Indonesia. *American Association of Petroleum Geologists Bulletin* **84**, 12–44.
- PETERS, K. E., WALTERS, C. C. & MOLDOWAN, J. M. 2005a Biodegradation parameters. In *The Biomarker Guide*, 2nd edn., , vol. 2, pp. 645–708. Cambridge: Cambridge University Press.
- PETERS, K. E., WALTERS, C. C. & MOLDOWAN, J. M. 2005b Geochemical screening. In *The Biomarker Guide*, 2nd edn., , vol. 1, pp. 72–118. Cambridge: Cambridge University Press.
- PETERS, K. E., WALTERS, C. C. & MOLDOWAN, J. M. 2005c Maturity-related biomarker parameters. In *The Biomarker Guide*, 2nd edn., , vol. 2, pp. 608–640. Cambridge: Cambridge University Press.
- PETERS, K. E., WALTERS, C. C. & MOLDOWAN, J. M. 2005d Non-biomarker maturity parameters. In *The Biomarker Guide*, 2nd edn., , vol. 2, pp. 641–644. Cambridge: Cambridge University Press.
- PETERS, K. E., WALTERS, C. C. & MOLDOWAN, J. M. 2005e Organic chemistry. In *The Biomarker Guide*, 2nd edn., , vol. 1, pp. 18–44. Cambridge: Cambridge University Press.
- PETERS, K. E., WALTERS, C. C. & MOLDOWAN, J. M. 2005f Origin and preservation of organic matter. In *The Biomarker Guide*, 2nd edn., , vol. 1, pp. 3–17. Cambridge: Cambridge University Press.
- PETERS, K. E., WALTERS, C. C. & MOLDOWAN, J. M. 2005g Refinery oil assays. In *The Biomarker Guide*, 2nd edn., , vol. 1, pp. 119–135. Cambridge: Cambridge University Press.
- PETERS, K. E., WALTERS, C. C. & MOLDOWAN, J. M. 2005h Source- and age-related biomarker parameters. In *The Biomarker Guide*, 2nd edn., , vol. 2, pp. 483–607. Cambridge: Cambridge University Press.
- PETERSON, C. H., RICE, S. D., SHORT, J. W., ESLER, D., BODKIN, J. L., BALLACHEY, B. E. & IRONS, D. B. 2003 Long-term ecosystem response to the Exxon Valdez Oil Spill. *Science* **302**, 2082–2086.

- PHILP, R. P., BAKEL, A., GALVEZ-SINIBALDI, A. & LIN, L. H. 1988 A comparison of organosulphur compounds produced by pyrolysis of asphaltenes and those present in related crude oils and tar sands. *Organic Geochemistry* **13**, 915–926.
- PIATT, J. F., LENSINK, C. J., BUTLER, W., KENDZIOREK, M. & NYSEWANDER, D. R. 1990 Immediate impact of the ‘Exxon Valdez’ oil spill on marine birds. *The Auk* **107**, 387–397.
- PICHOT, R., SPYROPOULOS, F. & NORTON, I. T. 2009 Mixed-emulsifier stabilised emulsions: investigation of the effect of monoolein and hydrophilic silica particle mixtures on the stability against coalescence. *Journal of Colloid and Interface Science* **329**, 284–291.
- PICHOT, R., SPYROPOULOS, F. & NORTON, I. T. 2010 O/w emulsions stabilised by both low molecular weight surfactants and colloidal particles: the effect of surfactant type and concentration. *Journal of Colloid and Interface Science* **352**, 128–135.
- PIERCE, A. D. 1981 *Acoustics: An Introduction to its Physical Principles and Applications*. New York: McGraw-Hill.
- PINFIELD, V. J. 1996 Studies of creaming, flocculation and crystallization in emulsions: Computer modelling and analysis of ultrasound propagation. PhD thesis, Leeds University, UK.
- PIRNIK, M. P., ATLAS, R. & BARTHA, R. 1974 Hydrocarbon metabolism by *Brevibacterium erythrogenes*: normal and branched alkanes. *Journal of Bacteriology* **119**, 68–78.
- POTEAU, S., ARGILLIER, J. F., LANGEVIN, D., PINCET, F. & PEREZ, R. 2005 Influence of pH on stability and dynamic properties of asphaltene and other amphiphilic molecules at the oil-water interface. *Energy and Fuels* **19**, 1337–1341.
- POVEY, M. J. W. 1997a *Ultrasonic techniques for fluids characterisation*, chap. Water, pp. 11–45. California: Academic Press.
- POVEY, M. J. W. 1997b *Ultrasonic techniques for fluids characterisation*, chap. Introduction, pp. 1–10. California: Academic Press.

- POVEY, M. J. W. 1997c *Ultrasonic techniques for fluids characterisation*, chap. Scattering of Sound, pp. 91–140. California: Academic Press.
- POVEY, M. J. W. 1997d *Ultrasonic techniques for fluids characterisation*, chap. Multiphase media, pp. 47–90. California: Academic Press.
- POVEY, M. J. W. 2013 Ultrasound particle sizing: A review. *Particuology* **11**, 135–147.
- POVEY, M. J. W. 2017 Applications of ultrasonics in food science - novel control of fat crystallization and structuring. *Current Opinion in Colloid and Interface Science* **28**, 1–6.
- PRASAD, M., MOULIK, S. P., MACDONALD, A. & PALEPU, R. 2004 Self-aggregation of alkyl (C10-, C12-, C14-, and C16-) triphenyl phosphonium bromides and their 1:1 molar mixtures in aqueous medium: a thermodynamic study. *The Journal of Physical Chemistry B* **108**, 355–362.
- PRASAD, M., MOULIK, S. P. & PALEPU, R. 2005 Self-aggregation of binary mixtures of alkyltriphenylphosphonium bromides: a critical assessment in favor of more than one kind of micelle formation. *Journal of Colloid and Interface Science* **284**, 658–666.
- PRENDERGAST, D. P. & GSCHWEND, P. M. 2014 Assessing the performance and cost of oil spill remediation technologies. *Journal of Cleaner Production* **78**, 233–242.
- PUSKAR, A. 1982 *The Use of High Intensity Ultrasonics*. Amsterdam, The Netherlands: Elsevier Science.
- QIAO, P., HARBOTTLE, D., TCHOUKOV, P., MASLIYAH, J., SJÖBLOM, J., LIU, Q. & XU, Z. 2017a Fractionation of asphaltenes in understanding their role in petroleum emulsion stability and fouling. *Energy & Fuels* **31**, 3330–3337.
- QIAO, P., HARBOTTLE, D., TCHOUKOV, P., WANG, X. & XU, Z. 2017b Asphaltene subfractions responsible for stabilizing water-in-crude oil emulsions. Part 3. effect of solvent aromaticity. *Energy & Fuels* **31**, 9179–9187.
- R CORE TEAM 2015 *R: A Language and Environment for Statistical Computing*. R Foundation for Statistical Computing, Vienna, Austria.

- RADKE, M., LEYTHAEUSER, D. & TEICHMÜLLER, M. 1984 Relationship between rank and composition of aromatic hydrocarbons for coal of different origins. *Organic Geochemistry* **6**, 423–430.
- RADKE, M. & WELTE, D. H. 1983 The methylphenanthrene index (MPI): a maturity parameter based on aromatic hydrocarbons. In *Advances in Organic Geochemistry 1981* (ed. M. Bjoroy, C. Albrecht, C. Cornford, K. De Groot, G. Eglinton, E. Galimov, D. Leythaeuser, R. Pelet, J. Rullkötter & G. Speers), pp. 504–512. Chichester: Wiley & Sons.
- RADKE, M., WILLISCH, H., LEYTHAEUSER, D. & TEICH-MULLER, M. 1982*a* Aromatic components of coal: relation of distribution pattern to rank. *Geochimica et Cosmochimica Acta* pp. 1831–1848.
- RADKE, M., WILLISCH, H. & LEYTHAEUSER, D. 1982*b* Aromatic components of coal: relation of distribution pattern to rank. *Geochimica et Cosmochimica Acta* **46**, 1831–1848.
- RANE, J. P., HARBOTTLE, D., PAUCHARD, V., COUZIS, A. & BANJAREE, S. 2012 Adsorption kinetics of asphaltenes at the oil-water interface and nanoaggregation in the bulk. *Langmuir* **28**, 9986–9995.
- RANE, J. P., PAUCHARD, V., COUZIS, A. & BANJAREE, S. 2013 Interfacial rheology of asphaltenes at oil-water interface and interpretation of the equation of state. *Langmuir* **29**, 4750–4759.
- RANE, J. P., ZAKAR, S., PAUCHARD, V., MULLINS, O. C., CHRISTIE, D., ANDREWS, A. B., POMERANTZ, A. E. & BANJAREE, S. 2015 Applicability of the Langmuir equation of state for asphaltene adsorption at the oil-water interface: coal-derived, petroleum, and synthetic asphaltenes. *Energy & Fuels* **29**, 3584–3590.
- RATULOWSKI, J., FUEX, A. N., WESTRICH, J. E. & SIELER, J. J. 2003 Theoretical and experimental investigation of isothermal compositional grading. *SPE Reservoir Evaluation & Engineering* **6**, 168–175.
- RAY, G. B., CHAKRABORTY, I., GHOSH, S., MOULIK, S. P. & PALEPU, R. 2005 Self-aggregation of alkyltrimethylammonium bromides (C₁₀-, C₁₂-, C₁₄-, and

- C₁₆tab) and their binary mixtures in aqueous medium: a critical and comprehensive assessment of interfacial behavior and bulk properties with preference to two types of micelle formation. *Langmuir* **21**, 1095810967.
- REDDY, C. M., AREY, S. J., SEEWALD, J. S., SYLVA, S. P., LEMKAU, K. L., CARMICHAEL, C. A., MCINTYRE, C. P., FENWICK, J., VENTURA, G. T., VAN MOOY, B. S. & CAMILLI, R. 2012 Composition and fate of gas and oil released to the water column during the Deepwater Horizon oil spill. *Proceedings of the National Academy of Sciences of the United States of America* **109**, 20229–20234.
- REED, W. E. 1977 Molecular compositions of weathered petroleum and comparison with its possible source. *Geochimica et Cosmochimica Acta* **41**, 237–247.
- REYNOLDS, J. G., CORONADO, P. R. & HRUBESH, L. W. 2001 Hydrophobic aerogels for oil-spill cleanup? Intrinsic absorbing properties. *Energy Sources* **23**, 831–843.
- ROBERTS, D. 1996 Ultrasound analysis of particle size distribution. *Materials world* **4**, 12–14.
- ROCHA, J. A., BAYDAK, E. N., YARRANTON, H. W., SZTUKOWSKI, D. M., ALI-MARCANO, W., GONG, L., SHI, C. & ZENG, H. 2016 Role of aqueous phase chemistry, interfacial film properties, and surface coverage in stabilizing water-in-bitumen emulsions. *Energy & Fuels* **30**, 5240–5252.
- ROONEY, M. A., VULETCH, A. K. & GRIFFITH, C. E. 1998 Compound-specific isotope analysis as a tool for characterizing mixed oils: an example from the West of Shetlands area. *Organic Geochemistry* **29**, 241–254.
- ROSS, S. L. 1986 An experimental study of the oil spill treating agents that inhibit emulsification and promote dispersion. *Tech. Rep.* Report EE-87. Environment Canada, Ottawa, Ontario.
- RUBINSTEIN, I., SPYCKERELLE, C. & STRAUZ, O. P. 1979 Pyrolysis of asphaltenes: a source of geochemical information. *Geochimica et Cosmochimica Acta* **43**, 1–6.

- RUFINO, R. D., LUNA, J. M., CAMPOS TAKAKI, G. M. & SARUBBO, L. A. 2014 Characterization and properties of the biosurfactant produced by *Candida lipolytica* UCP 0988. *Electronic Journal of Biotechnology* **17**, 34–38.
- RUIZ-MORALES, Y. & MULLINS, O. C. 2009 Measured and simulated electronic absorption and emission spectra of asphaltenes. *Energy & Fuels* **23**, 1169–1177.
- RULLKÖTTER, J. & WENDISCH, D. 1982 Microbial alteration of 17 α (h)-hopane in Madagascar asphalts: removal of C-10 methyl group and ring opening. *Geochimica et Cosmochimica Acta* **46**, 1543–1553.
- RUSSELL, C. A., SNAPE, C. E., MEREDITH, W., LOVE, G. D., CLARKE, E. & MOFFATT, B. 2004 The potential of bound biomarker profiles released via catalytic hydrolysis to reconstruct basin charging history for oils. *Organic Geochemistry* **35**, 1441–1459.
- SABBAH, H., MORROW, A. L., POMERANTZ, A. E. & ZARE, R. N. 2011 Evidence for island structures as the dominant architecture of asphaltenes. *Energy & Fuels* **25**, 1597–1604.
- SCALAN, R. S. & SMITH, J. E. 1970 An improved measure of the odd-to-even predominance in the normal alkanes of sediment extracts and petroleum. *Geochimica et Cosmochimica Acta* **34**, 611–620.
- SCAMEHORN, J. F. 1986 Phenomena in mixed surfactant systems. In *ACS Symposium Series*. Washington, DC.
- SCHICK, M. J. 1962 Surface films of nonionic detergents: 1. Surface tension study. *Journal of Colloid Science* **17**, 801–813.
- SCHNEIDER, M., ANDREWS, A. B., MITRA-KIRTLEY, S. & MULLINS, O. C. 2007 Asphaltene molecular size from translational diffusion constant by fluorescence correlation spectroscopy. *Energy & Fuels* **21**, 2875–2882.
- SCHOELL, M., TESCHNER, M., WEHNER, H., DURAND, B. & OUDIN, J. L. 1983 Maturity related biomarker and stable isotope variations and their application to oil/source rock correlation in the Mahakam Delta, Kalimantan. In *Advances in Organic Geochemistry* (ed. M. Bjørøy, C. Albrecht & C. Cornford), pp. 156–163. New York: John Wiley & Sons.

- SCHOTT, H. 1962 Salting in of nonionic surfactants by complexation with inorganic salts. *Journal of Colloid and Interface Science* **43**, 150–155.
- SCHRAMM, L. L. 1992 Petroleum emulsions: basic principles. In *Emulsions: Fundamental and Applications in the Petroleum Industry* (ed. L. L. Schramm), pp. 1–49. Washington, D. C.: American Chemical Society.
- SCHULER, B., FATAYER, S., MEYER, G., ROGEL, E., MOIR, M., ZHANG, Y., HARPER, M. R., POMERANTZ, A. E., BAKE, K. D., WITT, M., PEÑA, D., KUSHNERICK, J. D., MULLINS, O. C., OVALLES, C., VAN DEN BERG, F. G. A. & GROSS, L. 2017 Heavy oil based mixtures of different origins and treatments studied by atomic force microscopy. *Energy & Fuels* **31** (7), 6856–6861.
- SCHULER, B., MEYER, G., PEÑA, D., MULLINS, O. C. & GROSS, L. 2015 Unraveling the molecular structures of asphaltenes by atomic force microscopy. *Journal of the American Chemical Society* **137**, 9870–9876.
- SCHULMAN, J. H. & LEJA, J. 1954 Control of contact angles at the oil-water-solid interfaces. emulsions stabilized by solid particles (baso_4). *Transactions of the Faraday Society* **50**, 598–605.
- SEDGHI, M., GOUAL, L., WELCH, W. & KUBELKA, J. 2013 Effect of asphaltene structure on association and aggregation using molecular dynamics. *Journal of Physical Chemistry B* **18**, 5765–5776.
- SEIFERT, W. K. & MOLDOWAN, J. M. 1978 Applications of steranes, terpanes and monoaromatics to the maturation, migration and source of crude oils. *Geochimica et Cosmochimica Acta* **42**, 77–95.
- SEIFERT, W. K. & MOLDOWAN, J. M. 1979 The effect of biodegradation on steranes and terpanes in crude oils. *Geochimica et Cosmochimica Acta* **43**, 111–126.
- SEIFERT, W. K. & MOLDOWAN, J. M. 1986 Use of biological markers in petroleum exploration. In *Methods in Geochemistry and Geophysics* (ed. R. B. Johns), , vol. 24, pp. 261–290. Amsterdam: Elsevier.
- SEIFERT, W. K., MOLDOWAN, J. M. & DEMAISON, G. J. 1984 Source correlation of biodegraded oils. *Organic Geochemistry* **6**, 633–643.

- SEIFERT, W. K., MOLDOWAN, J. M. & JONES, R. W. 1980 Application of biological marker chemistry to petroleum exploration. In *Proceedings of the Tenth World Petroleum Congress*, pp. 425–440. Philadelphia, PA: Heyden & Son, Inc.
- SHARMA, A., GROEZIN, H., TOMITA, A. & MULLINS, O. C. 2002*a* Probing order in asphaltenes and aromatic ring systems by HRTEM. *Energy & Fuels* **16**, 490–496.
- SHARMA, A., SCOTT, J. H., CODY, G. D., FOGEL, M. L., HAZEN, R. M., HEMLEY, R. J. & HUNTRESS, W. T. 2002*b* Microbial activity at gigapascal pressures. *Science* **295**, 1514–1516.
- SHETTY, C. S., NIKOLOV, A. D. & WASAN, D. T. 1992 Demulsification of water in oil emulsions using water soluble demulsifiers. *Journal of Dispersion Science and Technology* **13**, 121–133.
- SHEU, E. Y. 1996 Physics of asphaltene micelles and microemulsions- theory and experiment. *Journal of Physics: Condensation Matter* **8**, 125–141.
- SHEU, E. Y. 2002 Petroleum asphaltenes-properties, characterization, and issues. *Energy & Fuels* **16**, 74–82.
- SHEU, E. Y., DE TAR, M. M. & STORM, D. A. 1992 Interfacial properties of asphaltenes. *Fuel* **71**, 1277–1281.
- SHEU, E. Y., MULLINS, O. C. & EDS. 1995*a* *Asphaltenes: fundamentals and applications*. New York: Plenum Publishing, Co.
- SHEU, E. Y., STORM, D. A. & SHIELDS, M. B. 1995*b* Adsorption kinetics of asphaltenes toluene/acid solution interface. *Fuel* **74**, 1475–1479.
- SHUKLA, A., PRAKASH, A. & ROHANI, S. 2007 Particles settling studies using ultrasonic techniques. *Powder Technology* **177** (2), 102–111.
- SIFFERT, B., BOURGEOIS, C. & PAPIRER, E. 1984 Structure and wateroil emulsifying properties of asphaltenes. *Fuel* **63**, 834–837.
- ROCHA E SILVA, N. P., RUFINO, R. D., LUNA, J. M., SANTOS, V. A. & SARUBBO, L. A. 2014 Screening of pseudomonas species for biosurfactant production using low-cost substrates. *Biocatalysis and Agricultural Biotechnology* **3**, 132–139.

- SILVA, E. J. AND ROCHA E SILVA, N. P., RUFINO, R. D. AND LUNA, J. M., SILVA, R. O. & SARUBBO, L. A. 2014 Characterization of a biosurfactant produced by *Pseudomonas cepacia* CCT6659 in the presence of industrial wastes and its application in the biodegradation of hydrophobic compounds in soil. *Colloids and Surfaces B, Biointerfaces* **117**, 36–41.
- SIMON, S., JESTIN, J., PALERMO, T. & BARRE, L. 2009 Relation between solution and interfacial properties of asphaltene aggregates. *Energy and Fuels* **23**, 306–313.
- SINGH, S., MCLEAN, J. D. & KILPATRICK, P. K. 1999 Fused ring aromatic solvency in destabilising water-in-asphaltene-heptane-toluene emulsions. *Journal of Dispersion Science and Technology* **20**, 279–293.
- SINNINGHE DAMSTÉ, J. S., KENIG, F., KOOPMANS, M. P., KÖSTER, J., SCHOUTEN, S., HAYES, J. M. & DE LEEUW, J. W. 1995 Evidence for gammacerane as an indicator of water-column stratification. *Geochimica et Cosmochimica Acta* **59**, 1895–1900.
- SIROTA, E. B. 2005 Physical structure of asphaltenes. *Energy & Fuels* **19**, 1290–1296.
- SIROTA, E. B. & LIN, M. Y. 2007 Physical behavior of asphaltenes. *Energy & Fuels* **21**, 2809–2815.
- SJOBLOM, J., ASKE, N., AUFLEM, H., BRANDAL, O., HARVE, T. E., SAETHER, O., WESTVIK, A., JOHNSEN, E. E. & KALLEVIK, H. 2003 Our current understanding of water-in-crude oil emulsions. recent characterization techniques and high pressure performance. *Advances in Colloid and Interface Science* **100-102**, 399–473.
- SJÖBLOM, J., JOHNSEN, E., WESTVIK, A., ESE, M., DJUVE, J., AUFLEM, I. & KALLEVIK, H. 2001 Demulsifiers in the oil industry. In *Encyclopedic handbook of emulsion technology*. New York: Marcel Dekker.
- SJOBLOM, J., SIMON, S. & XU, Z. 2015 Model molecules mimicking asphaltenes. *Advances in Colloid and Interface Science* **218**, 1–16.
- SMIRNOVAS, V., WINTER, R., FUNCK, T. & DZWOLAK, W. 2005 Thermodynamic properties underlying the α -helix-to- β -sheet transition, aggregation and

- amyloidogenesis of polylysine as probed by calorimetry, densimetry, and ultrasound velocimetry. *The Journal of Physical Chemistry Letters B* **109**, 19043–19045.
- SMITH, A. E. & COIT, D. W. 1995 Constraint-handling techniques - penalty functions. In *Handbook of Evolutionary Computation* (ed. T. Baeck, D. Fogel & Z. Michalewicz). Bristol: Institute of Physics Publishing and Oxford University Press.
- SNAPE, C. E., BOLTON, C., DOSCH, R. G. & STEPHENS, H. P. 1989 High liquid yields from bituminous coal via hydrolysis with dispersed catalysts. *Energy & Fuels* **3**, 421–425.
- SNOWDON, L., VOLKMAN, J., ZHANG, Z., TAO, G. & LIU, P. 2016 The organic geochemistry of asphaltenes and occluded biomarkers. *Organic Geochemistry* **91**, 3–15.
- SOBRINHO, H. B., LUNA, J. M., RUFINO, R. D., PORTO, A. F. & SARUBBO, L. A. 2013 Biosurfactants: classification, properties and environmental applications. *Recent Developments in Biotechnology* **11**, 1–29.
- SOUZA, E. C., VESSONI-PENNA, T. C. & SOUZA OLIVEIRA, R. P. 2014 Biosurfactant-enhanced hydrocarbon bioremediation: an overview. *International Biodeterioration & Biodegradation* **89**, 88–94.
- SPEIGHT, J. G. 1999 *The Chemistry and Technology of Petroleum*. New York: Marcel Dekker.
- SPEIGHT, J. G. 2004 Petroleum asphaltenes. Part 1. Asphaltenes, resins and the structure of petroleum. *Oil & Gas Science and Technology* **59**, 467–477.
- SPIECKER, P. M., GAWRYS, K. L. & KILPATRICK, P. K. 2003 Aggregation and solubility behavior of asphaltenes and their subfractions. *Journal of Colloid and Interface Science* **267**, 178–193.
- STANFORD, L. A., RODGERS, R. P., MARSHALL, A. G., CZARNECKI, J. & WU, X. A. 2007a Compositional characterization of bitumen/water emulsion lms by negative- and positive-ion electrospray ionization and elddesorption/ionization Fourier transform ion cyclotron resonance mass spectrometry. *Energy & Fuels* **21**, 963–972.

- STANFORD, L. A., RODGERS, R. P., MARSHALL, A. G., CZARNECKI, J., WU, X. A. & TAYLOR, S. 2007*b* Detailed elemental compositions of emulsion interfacial material versus parent oil for nine geographically distinct light, medium, and heavy crude oils, detected by negative- and positive-ion electrospray ionization Fourier transform ion cyclotron resonance mass spectrometry. *Energy & Fuels* **21**, 973–981.
- STOUT, S. A. & WANG, Z. 2008 Diagnostic compounds for fingerprinting petroleum in the environment. In *Environmental Forensics*, , vol. 26, pp. 54–104. The Royal Society of Chemistry.
- STRASSNER, J. E. 1968 Effect of pH on interfacial films and stability of crude oil-water emulsions. *Journal of Petroleum Technology* **20**, 303–312.
- STRAUSZ, O. P. 2002 About the colloidal nature of asphaltenes and the MW of covalent monomeric units. *Energy & Fuels* **16**, 809–812.
- STRAUSZ, O. P., MOJELSKY, T. W., FARAJI, F. & LOWN, E. M. 1999*a* Additional structural details on Athabasca asphaltene and their ramifications. *Energy and Fuels* **13**, 207–227.
- STRAUSZ, O. P., MOJELSKY, T. W., FARAJI, F., LOWN, E. M. & PENG, P. 1999*b* Additional structural details on Athabasca asphaltene and their ramifications. *Energy & Fuels* **13**, 207–227.
- STRAUSZ, O. P., MOJELSKY, T. W., LOWN, E. M., KOWALEWSKI, I. & BEHAR, F. 1999*c* Structural features of Boscan and Duri asphaltenes. *Energy & Fuels* **13**, 228–247.
- STRUTT, J. W. 1896 *The theory of sound*, 2nd edn. London: Macmillan.
- SUN, D. Z., WANG, S. B., SONG, M. Z., WEI, X. L. & YIN, B. L. 2005 A microcalorimetric study of hostguest complexes of alpha-cyclodextrin with alkyl trimethyl ammonium bromides in aqueous solutions. *Journal of Solution Chemistry* **34**, 701–712.
- SVALOVA, A., PARKER, N. G., POVEY, M. J. W. & ABBOTT, G. D. 2017 Determination of asphaltene critical nanoaggregate concentration region using ultrasound velocity measurements. *Scientific Reports* **7**, 1–11.

- SZTUKOWSKI, D. M., JAFARI, M., ALBOUDWAREJ, H. & YARRANTON, H. W. 2003 Asphaltene self-association and water-in-hydrocarbon emulsions. *Journal of Colloid and Interface Science* **265**, 179–186.
- TANFORD, C. 1980 *The Hydrophobic Effect: Formation of Micelles and Biological Membranes*, 2nd edn. New York: John Wiley & Sons.
- TAULIER, N. & CHALIKIAN, T. V. 2001 Characterization of pH-induced transitions of β -lactoglobulin: Ultrasonic, densimetric, and spectroscopic studies. *Journal of Molecular Biology* **314**, 873–889.
- TAYLOR, P., BENNETT, B., JONES, M. & LARTER, S. 2001 The effect of biodegradation and water washing on the occurrence of alkylphenols in crude oils. *Organic Geochemistry* **32**, 341–358.
- TCHOUKOV, P., YANG, F., XU, Z., DABROS, T., CZARNECKI, J. & SJÖBLOM, J. 2014 Role of asphaltenes in stabilizing thin liquid emulsion films. *Langmuir* **30**, 3024–3033.
- TEAS, C., KALLIGEROS, S., ZANIKOS, F., STOURNAS, S., LOIS, E. & ANASTOPOULOS, G. 2001 Investigation of the effectiveness of absorbent materials in oil spills clean up. *Desalination* **140**, 259 – 264.
- TEKLEBRHAN, R. B., GE, L., BHATTACHARJEE, S., XU, Z. & SJOBLUM, J. 2014 Initial partition and aggregation of uncharged polyaromatic molecules at the oil-water interface: a molecular dynamics simulation study. *The Journal of Physical Chemistry B* **118**, 1040–1051.
- TEN HAVEN, H. L. & RULLKÖTTER, J. 1988 The diagenetic fate of taraxer-14-ene and oleanene isomers. *Geochimica et Cosmochimica Acta* **52**, 2543–2548.
- TF INSTRUMENTS 2007 *ResoscanTM- System Operations Manual*. TF Instruments GmbH.
- THINGSTAD, T. & PENDERUD, B. 1983 The formation of chocolate mousse from Statfjord crude oil and seawater. *Marine Pollution Bulletin* **14**, 214–216.
- THOMPSON, D. G., TAYLOR, A. S. & GRAHAM, D. E. 1985 Emulsification and demulsification related to crude oil production. *Colloids and Surfaces* **15**, 175–189.

- TISSOT, B., CALIFET-DEBYSER, Y., DEROO, G. & OUDIN, J. L. 1971 Origin and evolution of hydrocarbons in early Toarcian shales, Paris Basin, France. *American Association of Petroleum Geologists Bulletin* **55**, 2177–2193.
- TISSOT, B. P. & WELTE, D. H. 1984 *Petroleum Formation and Occurrence, 2nd Edition*. Berlin: Springer-Verlag.
- TOKIWA, F. 1972 Electrostatic and electrokinetic potentials of surfactant micelles in aqueous solutions. *Advance in Colloid and Interface Science* **3**, 389–424.
- TREINER, C., AMAR KHODJA, A. & FROMON, M. 1989 Counterion condensation on mixed anionic/nonionic surfactant micelles: Bjerrum's limiting condition. *Journal of Colloid and Interface Science* **128**, 416–421.
- TREINER, C. & MAKAYSSI, A. 1992 Structural micellar transition for dilute solutions of long chain binary cationic surfactant systems: a conductance investigation. *Langmuir* **8**, 794–800.
- TREJO, F., CENTENO, G. & ANCHEYTA, J. 2004 Precipitation, fractionation and characterization of asphaltenes from heavy and light crude oils. *Fuel* **83**, 2169–2175.
- TRENDEL, J.-M., GUILHEM, J., CRISP, P., REPETA, D., CONNAN, J. & ALBRECHT, P. 1990 Identification of two C-10 demethylated C₂₈ hopanes in biodegraded petroleum. *Journal of the Chemical Society, Chemical Communications* pp. 424–425.
- TURRO, N. J. & YETKA, A. 1978 Luminiscent probes for detergent solutions: a simple procedure for determination of the mean aggregation number of micelles. *Journal of the American Chemical Society* **100**, 5951.
- URICK, J. R. 1947 A sound velocity method for determining the compressibility of finely divided substances. *Journal of Applied Physics* **18**, 983–987.
- USEIA 2017 International projections to 2050. World total energy consumption by region and fuel. Electronic resource. U.S. Energy Information Administration, <https://www.eia.gov/analysis/projection-data.php#intlproj>.

- VARADARAJ, R. & BRONS, C. 2007 Molecular origins of heavy crude oil interfacial activity. Part 2: fundamental interfacial properties of model naphthenic acids and naphthenic acids separated from heavy crude oils. *Energy & Fuels* **21**, 199–204.
- VASHISTH, C., WHITBY, C. P., FORNASIERO, D. & RALSTON, J. 2010 Interfacial displacement of nanoparticles by surfactant molecules in emulsions. *Journal of Colloid and Interface Science* **349**, 537–543.
- VERRUTO, V. & KILPATRICK, P. K. 2008 Water-in-model oil emulsions studied by small-angle neutron scattering: interfacial thickness and composition. *Langmuir* **24**, 12807–12822.
- VOLKMAN, J. K., ALEXANDER, R., KAGI, R. I., ROWLAND, S. F. & SHEPARD, P. N. 1984 Biodegradation of aromatic hydrocarbons in crude oils from the Barrow Sub-basin of Western Australia. *Organic Geochemistry* **6**, 619–632.
- VOLKMAN, J. K., ALEXANDER, R., KAGI, R. I. & WOODHOUSE, G. W. 1983 Demethylated hopanes in crude oils and their application in petroleum geochemistry. *Geochimica et Cosmochimica Acta* **47**, 785–794.
- VAN DER WAALS, J. H. 1873 Over de continuïteit van den gas- en vloeistofoestand (On the continuity of the gas and liquid state). PhD thesis, University of Leiden.
- VAN DER WAARDEN, M. 1958 Stability of emulsions of water in mineral oils containing asphaltenes. *Kolloid-Zeitschrift und Zeitschrift für Polymere* **156**, 116–122.
- WALTERS, C. C. 1999 Oil-oil and oil-source rock correlations. In *Encyclopedia of Geochemistry* (ed. C. P. Marshall & R. W. Fairbridge), pp. 442 – 444. Dordrecht, the Netherlands: Kluwer Academic Publishers.
- WANG, S., LIU, J., ZHANG, L., MASLIYAH, J. & XU, Z. 2010 Interaction forces between asphaltene surfaces in organic solvents. *Langmuir* **26**, 183–190.
- WANG, Y., QIU, Y., LI, J., ZHAO, C. & SONG, Z. 2018 Low-intensity pulsed ultrasound promotes alveolar bone regeneration in a periodontal injury model. *Ultrasonics* **90**, 166–172.
- WANG, Z., FINGAS, M. F., SIGOUIN, L. & OWENS, E. H. 2001 Fate and persistence of long-termed spilled Metula oil in the marine salt marsh environment: degradation of petroleum biomarkers. In *Proceedings of the 2001 International*

- Oil Spill Conference, Tampa, Florida*, pp. 115–125. Washington, DC: American Petroleum Institute.
- WANG, Z., STOUT, S. A. & FINGAS, M. 2006 Forensic fingerprinting of biomarkers for oil spill characterization and source identification. *Environmental Forensics* **7**, 105–146.
- WARDROPER, A. K., HOFFMANN, C. F., MAXWELL, J. R., BARWISE, A. G., GOODWIN, N. S. & PARK, P. D. 1984 Crude oil biodegradation under simulated and natural conditions 2. Aromatic steroid hydrocarbons. *Organic Geochemistry* **6**, 605–617.
- WARR, G. G., GRIESER, F. & EVANS, D. F. 1986 Determination of micelle size and polydispersity by fluorescence quenching-experimental results. *Journal of the Chemical Society (Faraday Transactions 1)* **82**, 1829–1838.
- WASAN, D. T. 1992 Destabilization of water-in-oil emulsions. In *Emulsions - A Fundamental and Practical Approach* (ed. J. Sjöblom), pp. 283–295. Netherlands: Kluwer Academic Publishers.
- WATSON, N., HAZLEHURST, T., POVEY, M. J. W., VIEIRA, J., SUNDARA, R. & SANDOZ, J.-P. 2014 Can airborne ultrasound monitor bubble size in chocolate? *Journal of Physics: Conference Series* **498**, 1–13.
- WATTANA, P., FOGLER, H. S., YEN, A., GARCIA, M. D. & CARBOGNANI, L. 2005 Characterization of polarity-based asphaltene subfractions. *Energy & Fuels* **19**, 101–110.
- WENGER, L. M., DAVIS, C. L. & ISAKEN, G. H. 2002 Multiple controls on petroleum biodegradation and impact on oil quality. In *SPE Reservoir Evaluation and Engineering*, pp. 375–383. New Orleans, Louisiana: Society of Petroleum Engineers.
- WENGER, L. M. & ISAKSEN, G. H. 2002 Control of hydrocarbon seepage intensity on level of biodegradation in sea bottom sediments. *Organic Geochemistry* **33**, 1277–1292.
- WIDDEL, F. & RABUS, R. 2001 Anaerobic biodegradation of saturated and aromatic hydrocarbons. *Current Opinion in Biotechnology* **12**, 259–276.

- WILLIAMS, J. A., BJOROY, M., DOLCATER, D. L. & WINTERS, J. C. 1986 Biodegradation in South Texas Eocene oils effects on aromatics and biomarkers. *Organic Geochemistry* **10**, 451–461.
- WINTERS, J. C. & WILLIAMS, J. A. 1969 Microbiological alteration of crude oil in the reservoir. *American Chemical Society, Division of Petroleum Chemistry, New York Meeting Preprints* **14**, E22–E31.
- WOOD, A. B. 1941 *A Textbook of Sound*. London: Bell and Sons.
- WOOD, A. B. 1964 *A Textbook of Sound*, 3rd edn. London: Bell and Sons.
- WU, X. 2003 Investigating the stability mechanism of water-in-diluted bitumen emulsions through isolation and characterization of the stabilizing materials at the interface. *Energy & Fuels* **17**, 179190.
- XI, J. & GUO, R. 2008 Interactions of puerarin with micelles: pKa shifts and thermodynamics. *Journal of Solution Chemistry* **37**, 107–118.
- XIAOBO, Z., XIAOWEI, H. & POVEY, M. J. W. 2016 Non-invasive sensing for food reassurance. *Analyst* **141**, 1587–1610.
- XU, Y. M. 1995 Dynamic interfacial-tension between bitumen and aqueous sodium-hydroxide solutions. *Energy & Fuels* **9**, 148–154.
- YAMANE, A., SAKAKIBARA, K., HOSOMI, M. & MURAKAMI, A. 1997 Microbial degradation of petroleum hydrocarbons in estuarine sediment of Tama river in Tokyo urban area. *Water Science and Technology* **35**, 69–76.
- YANG, C., LIAO, Z., ZHANG, L. & CREUX, P. 2009 Some biogenic-related compounds occluded inside asphaltene aggregates. *Energy & Fuels* **23**, 820–827.
- YANG, F., TCHOUKOV, P., DETTMAN, H., TEKLEBRHAN, R., LIU, L. & DABROS, T. 2015a Asphaltene subfractions responsible for stabilizing water-in-crude oil emulsions. Part 2: molecular representations and molecular dynamics simulations. *Energy & Fuels* **29**, 4783–4794.
- YANG, F., TCHOUKOV, P., PENSINI, E., DABROS, T., CZARNECKI, J. & MASLIYAH, J. H. 2014 Asphaltene subfractions responsible for stabilizing water-in-crude oil emulsions. Part 1: interfacial behaviors. *Energy & Fuels* **28**, 6897–6904.

- YANG, F., WANG, T. & LI, M. 2015*b* The distribution of triaromatic steroids and oil group classification of ordovician petroleum systems in the Cratonic Region of the Tarim Basin, NW China. *Petroleum Science and Technology* **33**, 1794–1800.
- YARRANTON, H. W., ALBOUDWAREJ, H. & JAKHER, R. 2000*a* Investigation of asphaltene association with vapour pressure osmometry and interfacial tension measurements. *Industrial & Engineering Chemistry Research* **39**, 2916–2924.
- YARRANTON, H. W., HUSSEIN, H. & MASLIYAH, J. H. 2000*b* Water-in-hydrocarbon emulsions stabilized by asphaltenes at low concentrations. *Journal of Colloid and Interface Science* **228**, 52–63.
- YARRANTON, H. W. & MASLIYAH, J. H. 1996 Molar mass distribution and solubility modeling of asphaltenes. *American Institute of Chemical Engineers Journal* **42** (12), 3533–3543.
- YARRANTON, H. W., ORTIZ, D. P., BARRERA, D. M., BAYDAK, E. N., BARRÉ, L., FROT, D., EYSSAUTIER, J., ZENG, H., XU, Z., DECHAIINE, G., BECERRA, M., SHAW, J. M., MCKENNA, A. M., MAPOLELO, M. M., BOHNE, C., YANG, Z. & OAKE, J. 2013 On the size distribution of self-associated asphaltenes. *Energy & Fuels* **27**, 5083–5106.
- YEUNG, C. W., LAW, B. A., MILLIGAN, T. G., LEE, K., WHYTE, L. G. & GREER, C. W. 2011 Analysis of bacterial diversity and metals in produced water, seawater and sediments from an offshore oil and gas production platform. *Marine Pollution Bulletin* **62**, 2095–2105.
- YU, G., KARINSHAKA, K., HARWELLA, J. H., GRADYA, B. P., WOODSIDE, A. & GHOSH, M. 2014 Interfacial behavior and water solubility of various asphaltenes at high temperature. *Colloid and Interfacial Science A* **441**, 378–388.
- YUDIN, I. K. & ANISIMOV, M. A. 2007 Dynamic light scattering monitoring of asphaltene aggregation in crude oils and hydrocarbon solutions. In *Asphaltenes, Heavy Oils, and Petroleomics* (ed. O. C. Mullins, E. Y. Sheu, A. Hammami & A. G. Marshall). New York, NY: Springer.
- ZAJAC, G. W., SETHI, N. K. & JOSEPH, J. T. 1994 Molecular imaging of petroleum asphaltenes by scanning tunneling microscopy: Verification of structure from ^{13}C and proton NMR data. *Scanning Microscopy* **8**, 463–470.

- ZAMAN, M., BJORNDALLEN, N. & ISLAM, M. R. 2004 Detection of precipitation in pipelines. *Petroleum Science and Technology* **22**, 1119–1141.
- ZAPRYANOV, Z., MALHOTRA, A. K., ADERANGI, N. & WASAN, D. T. 1983 Emulsions stability: an analysis of the effect of bulk and interfacial properties on film mobility and drainage rate. *International Journal of Multiphase Flow* **9**, 105–129.
- ZENG, H., SONG, Y. Q., JOHNSON, D. L. & MULLINS, O. C. 2009 Critical nanoaggregate concentration of asphaltenes by low frequency conductivity. *Energy & Fuels* **23**, 1201–1208.
- ZHANG, D., HUANG, D. & LI, J. 1988 Biodegraded sequence of Karamay oils and semi-quantitative estimation of their biodegraded degrees in Junggar Basin, china. *Organic Geochemistry* **13**, 295–302.
- ZHANG, L. Y., XU, Z. & MASLIYAH, J. H. 2003 Langmuir and Langmuir-Blodgett films of mixed asphaltene and a demulsifier. *Langmuir* **19**, 9730–9741.
- ZHANG, Z., HOU, Z., YANG, C., MA, C., TAO, F. & XU, P. 2011 Degradation of *n*-alkanes and polycyclic aromatic hydrocarbons in petroleum by a newly isolated *Pseudomonas aeruginosa* DQ8. *Bioresource Technology* **102**, 4111–4116.
- ZHAO, J., LIAO, Z., CHROSTOWSKA, A., LIU, Q., ZHANG, L., GRACIAA, A. & CREUX, P. 2012 Experimental studies on the adsorption/occlusion phenomena inside the macromolecular structures of asphaltenes. *Energy & Fuels* **26**, 1746–1755.
- ZIELINSKI, R., IKEDA, S., NOMURA, H. & KATO, S. 1986 Adiabatic compressibility of alkyltrimethylammonium bromides in aqueous solutions. *Journal of Colloid and Interface Science* **119**, 398–408.
- ZUMBERGE, J. E. 1993 Organic geochemistry of Estancia Vieja Oils, Rio Negro Norte block. Correlation with other Neuquen Basin, Argentina, oils. In *Organic Geochemistry* (ed. M. H. Engel & S. A. Macko). New York: Plenum Press.

**Appendix A. Supplementary Material for Geochemical
Characterisation of Maltenes**

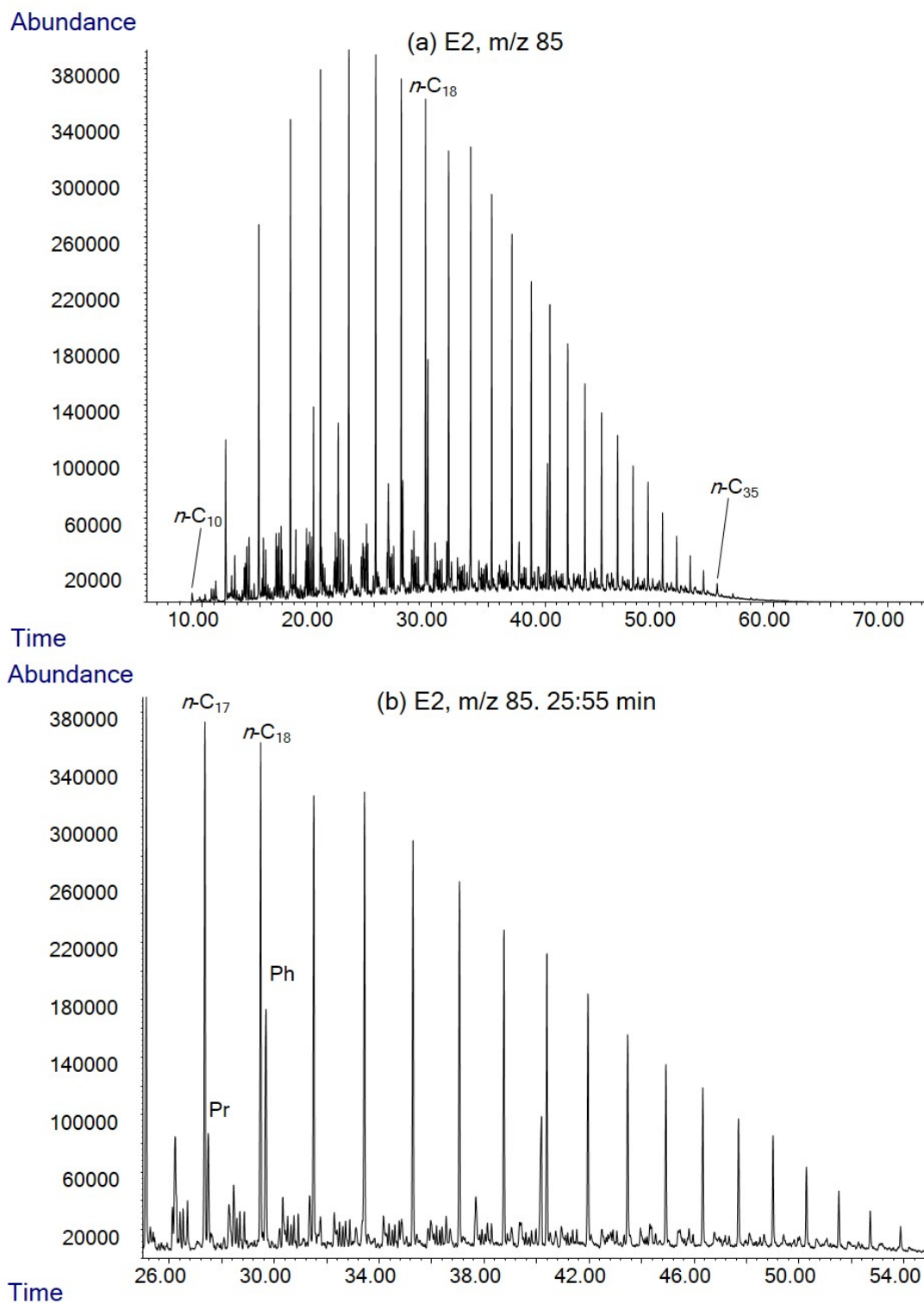


Figure A.1: Partial mass chromatograms of the E2 aliphatic fraction, showing the distributions of n -alkanes. Labels are listed in Table 10.2.

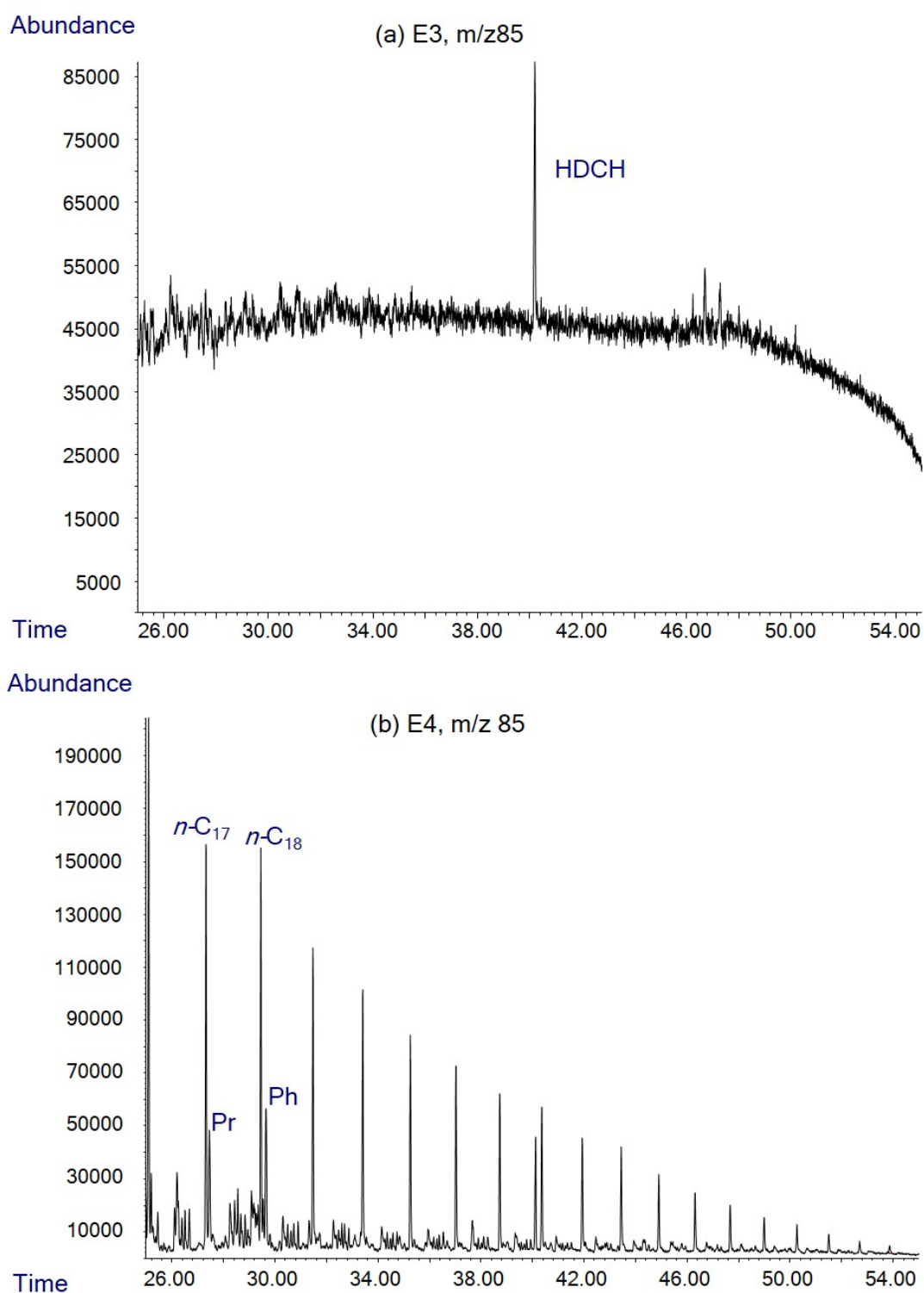


Figure A.2: Partial mass chromatograms of the E3 and E4 aliphatic fractions, showing the distributions of *n*-alkanes. Labels are listed in Table 10.2.

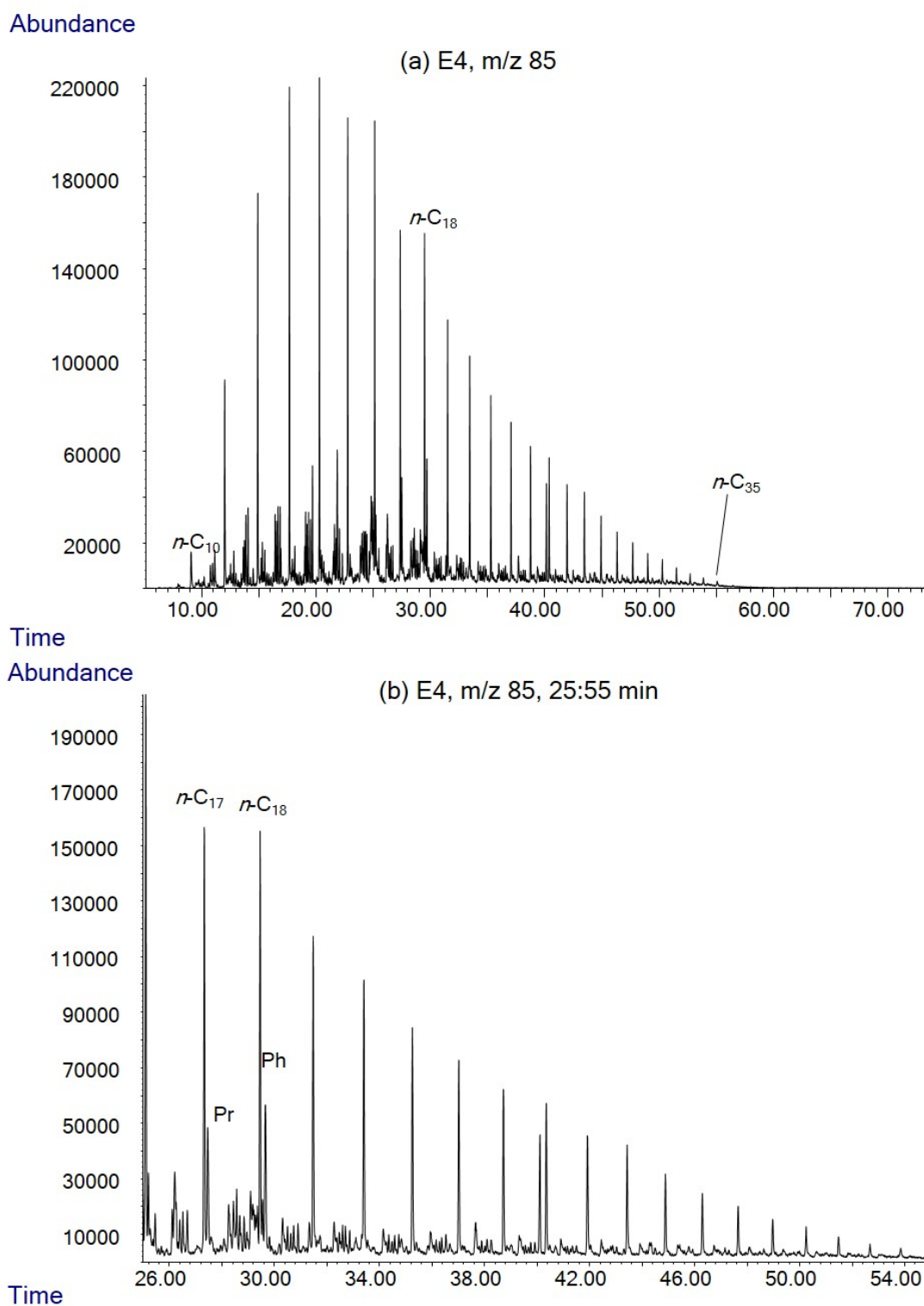


Figure A.3: Partial mass chromatograms of the E4 aliphatic fraction, showing the distributions of n -alkanes. Labels are listed in Table 10.2.

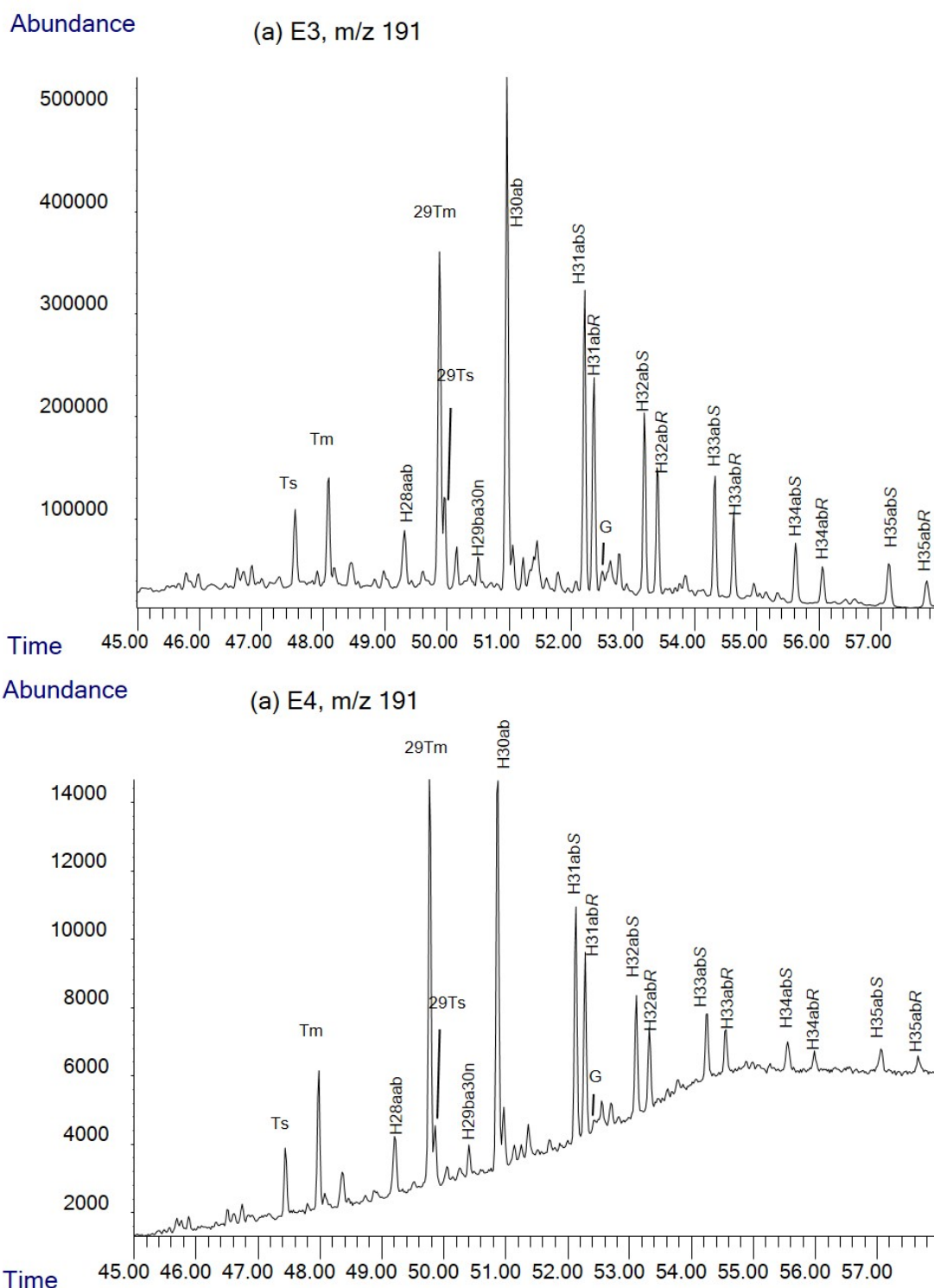


Figure A.4: Partial m/z 191 mass chromatograms of the E3 and E4 aliphatic fraction. Labels are listed in Table 10.2.

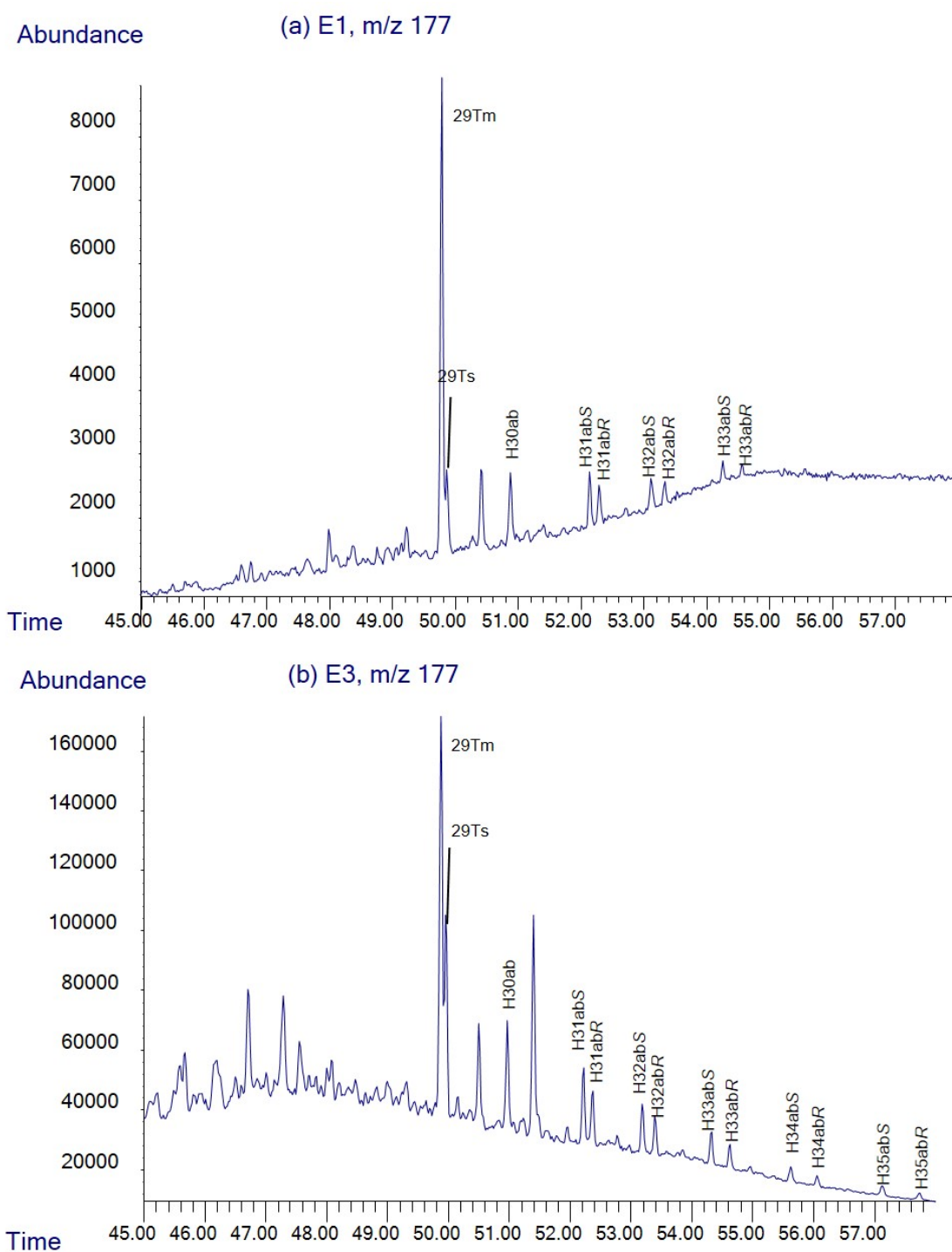


Figure A.5: Partial m/z 177 mass chromatograms of the E1 and E3 aliphatic fraction. Labels are listed in Table 10.2.

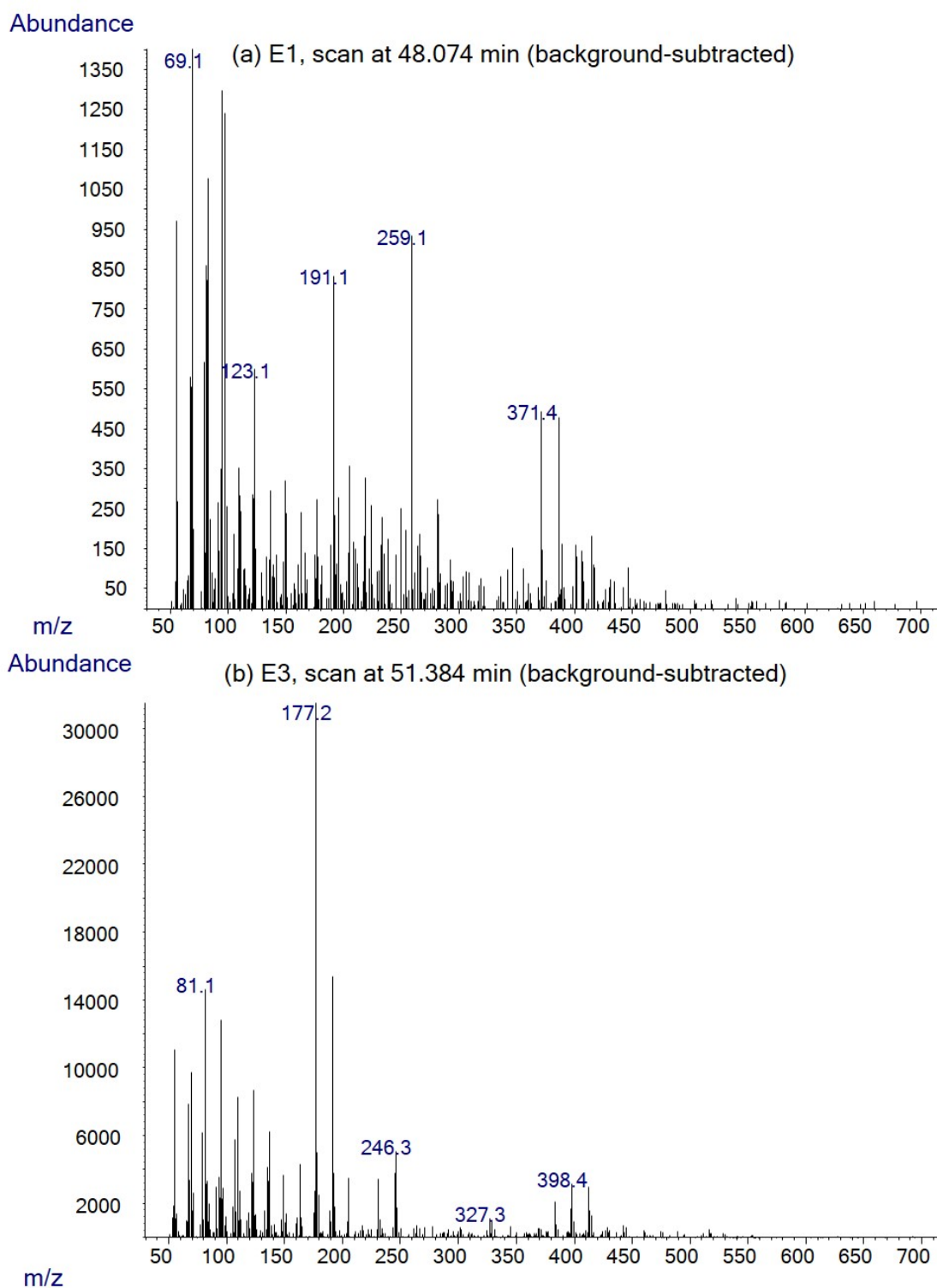


Figure A.6: Additional mass spectra for biodegradation assessment.

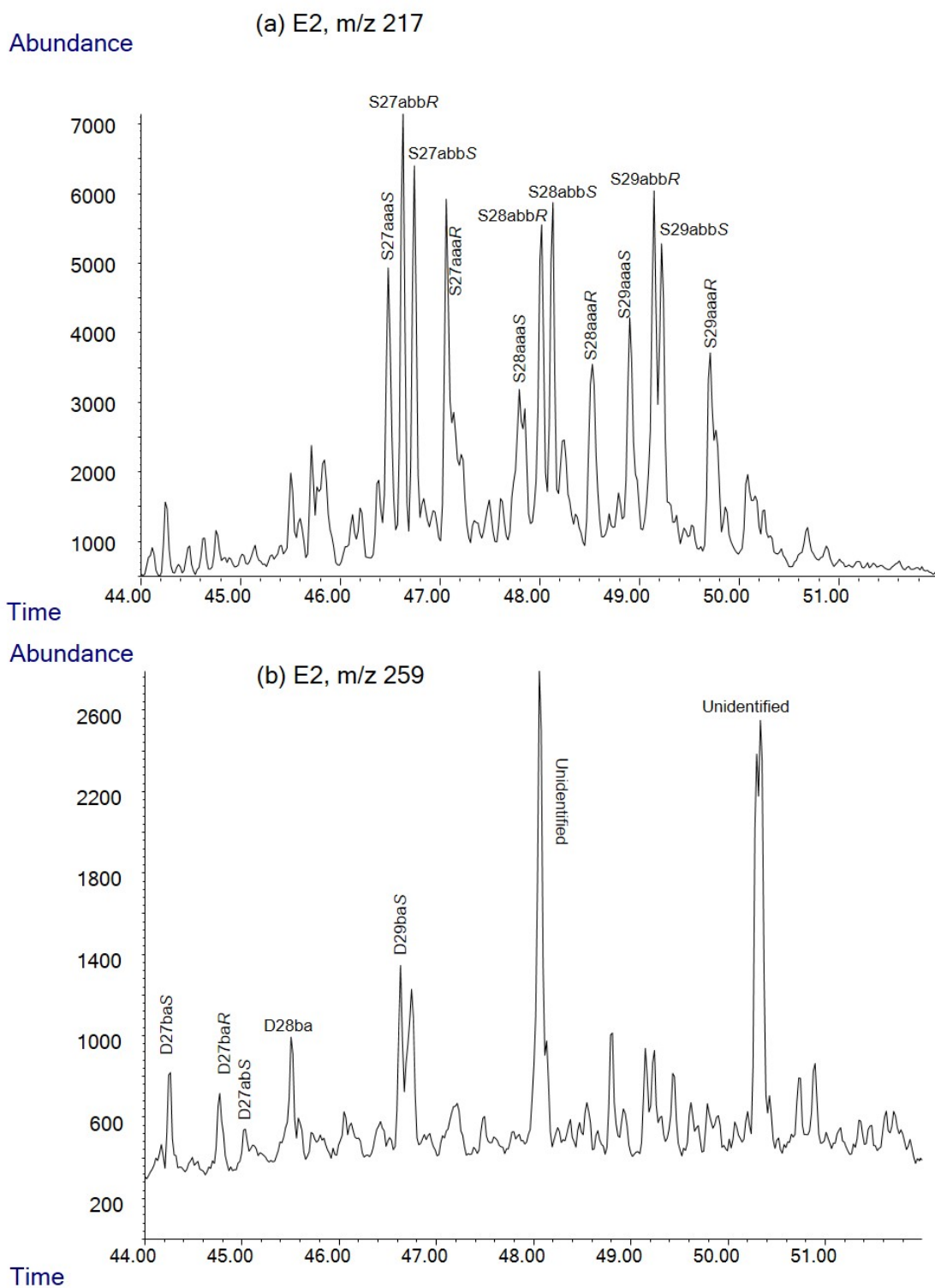


Figure A.7: Partial mass chromatograms of the E2 aliphatic fraction, showing sterane biomarkers. Labels are listed in Table 10.2.

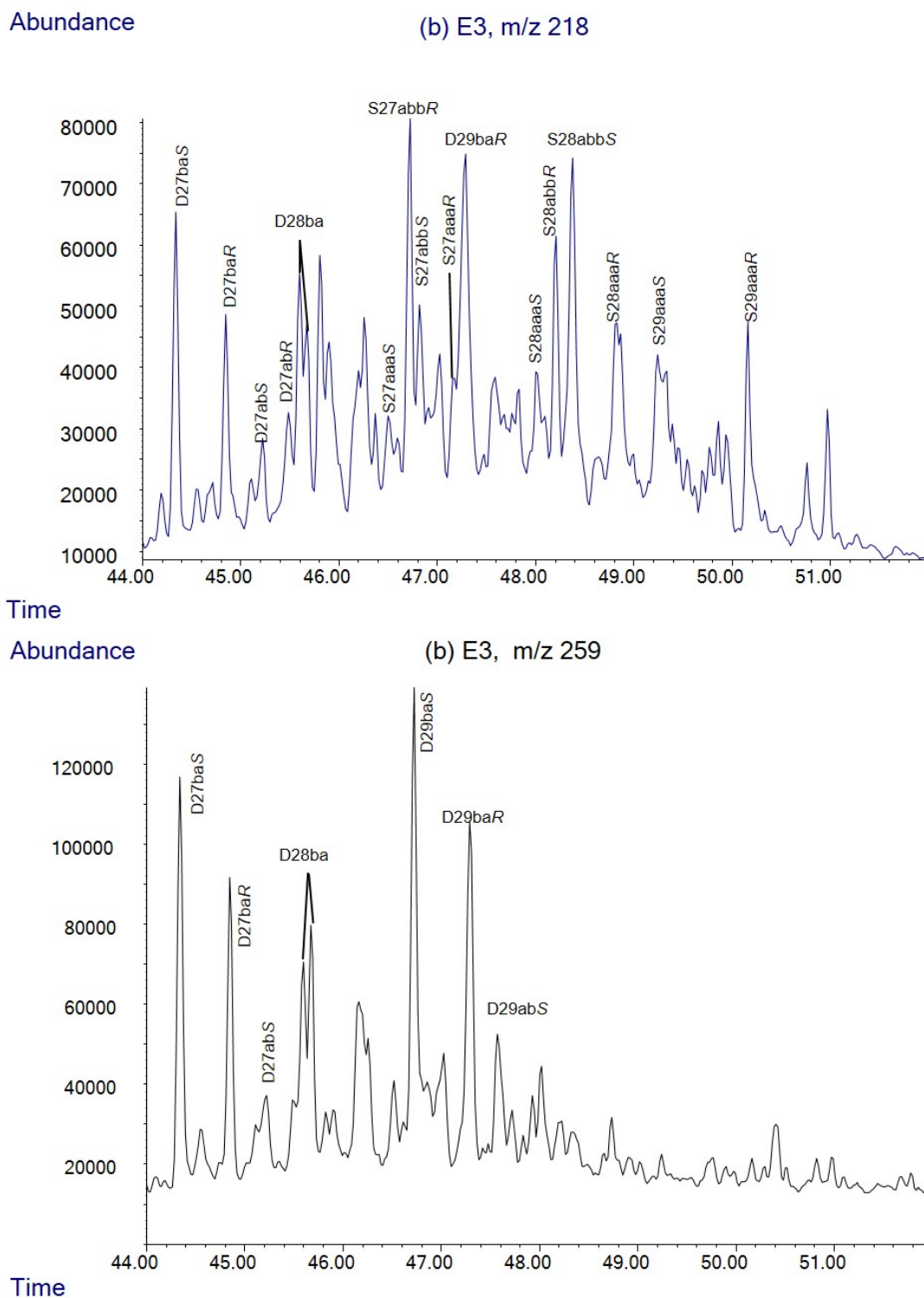


Figure A.8: Partial mass chromatograms of the E3 aliphatic fraction, showing sterane biomarkers. Labels are listed in Table 10.2.

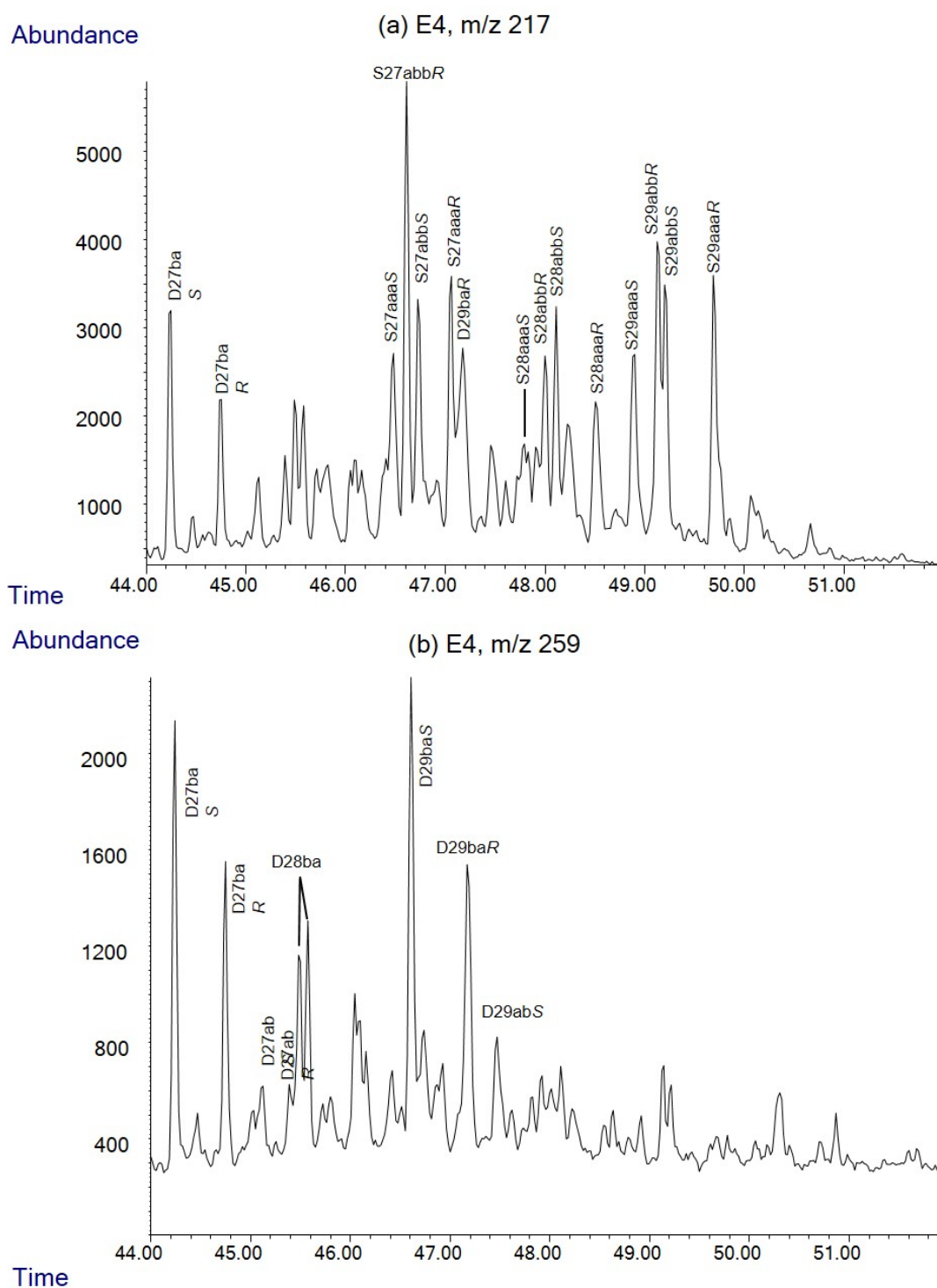


Figure A.9: Partial mass chromatograms of the E4 aliphatic fraction, showing sterane biomarkers. Labels are listed in Table 10.2.

Compound label	Compound name	Empirical formula
1N	Naphthalene	C ₁₀ H ₈
2N	2-MN	C ₁₁ H ₁₀
3N	1-MN	C ₁₁ H ₁₀
4N	2,6+2,7-DMN	C ₁₂ H ₁₂
5N	1,3+1,7-DMN	C ₁₂ H ₁₂
6N	1,6-DMN	C ₁₂ H ₁₂
7N	1,4+2,3-DMN	C ₁₂ H ₁₂
8N	1,5-DMN	C ₁₂ H ₁₂
9N	1,2-DMN	C ₁₂ H ₁₂
10N	1,3,7-TMN	C ₁₃ H ₁₄
11N	1,3,6-TMN	C ₁₃ H ₁₄
12N	1,4,6+,1,3,5-TMN	C ₁₃ H ₁₄
13N	2,3,6-TMN	C ₁₃ H ₁₄
14N	1,2-TMN	C ₁₃ H ₁₄
15N	1,6,7+1,2,6-TMN	C ₁₃ H ₁₄
16N	1,2,4-TMN	C ₁₃ H ₁₄
17N	1,2,5-TMN	C ₁₃ H ₁₄
18N	1,2,3-TMN	C ₁₃ H ₁₄
1P	Phenanthrene	C ₁₄ H ₁₀
2P	3-MP	C ₁₅ H ₁₂
3P	2-MP	C ₁₅ H ₁₂
4P	9-MP	C ₁₅ H ₁₂
5P	1-MP	C ₁₅ H ₁₂
6P	3,5+2,6-DMP	C ₁₆ H ₁₄
7P	2,7-DMP	C ₁₆ H ₁₄
8P	1,3+2,10+3,9+3,10-DMP	C ₁₆ H ₁₄
9P	2,5+2,9+1,6-DMP	C ₁₆ H ₁₄
10P	1,7-DMP	C ₁₆ H ₁₄
11P	2,3-DMP	C ₁₆ H ₁₄
12P	1,9+4,9+4,10-DMP	C ₁₆ H ₁₄
13P	1,8-DMP	C ₁₆ H ₁₄
14P	1,2-DMP	C ₁₆ H ₁₄

Table A.1: Compound table for naphthalene and phenanthrene compounds (Stout & Wang, 2008). Abbreviations MN, DMN and TMN refer to methylnaphthalene, dimethylnaphthalene and trimethylnaphthalene respectively. Abbreviations MP and DMP refer to methylphenanthrene and dimethylphenanthrene respectively.

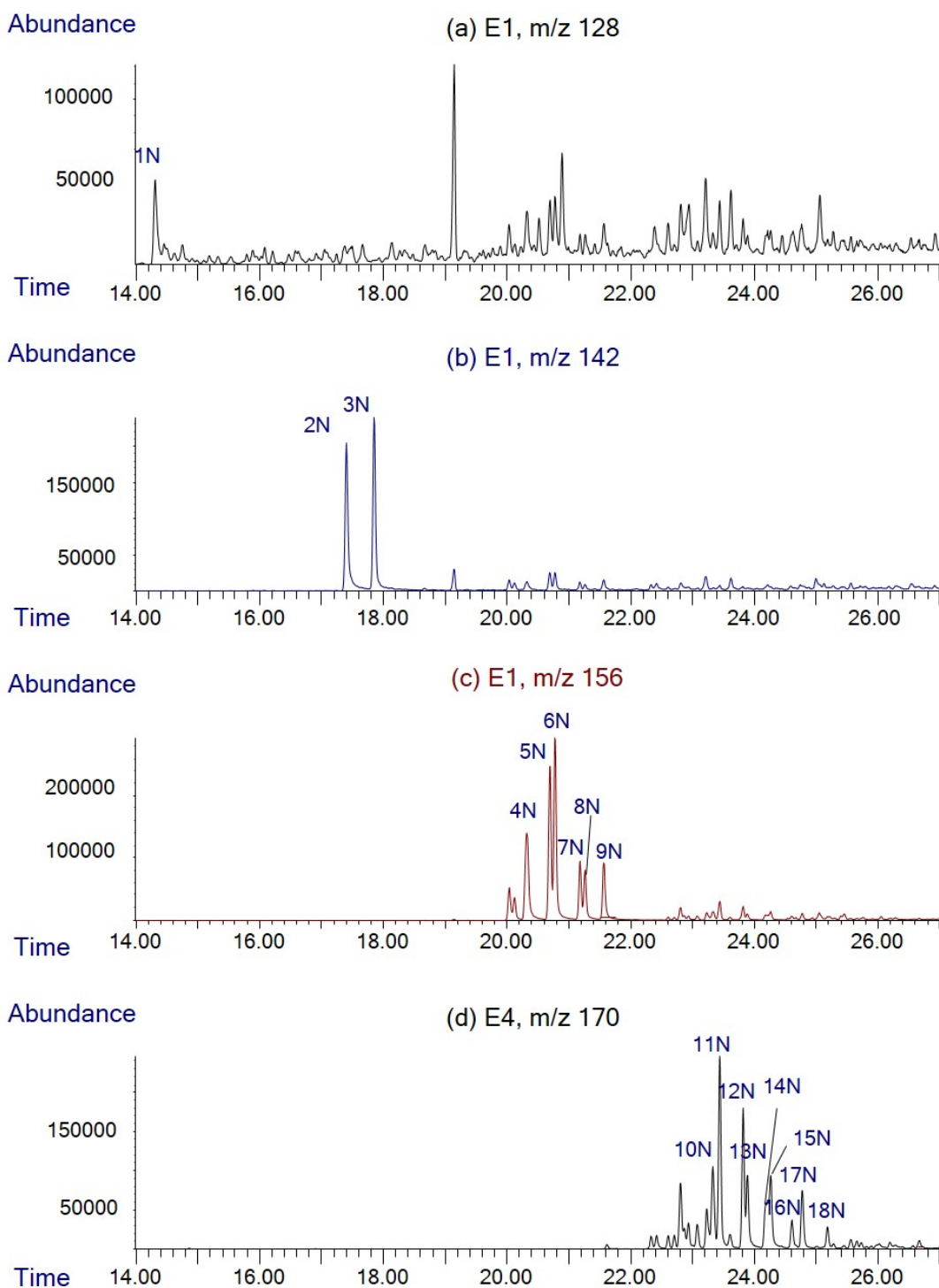


Figure A.10: Partial mass chromatograms of the E1 aromatic fraction, showing naphthalene biomarkers. Labels are listed in Table A.1.

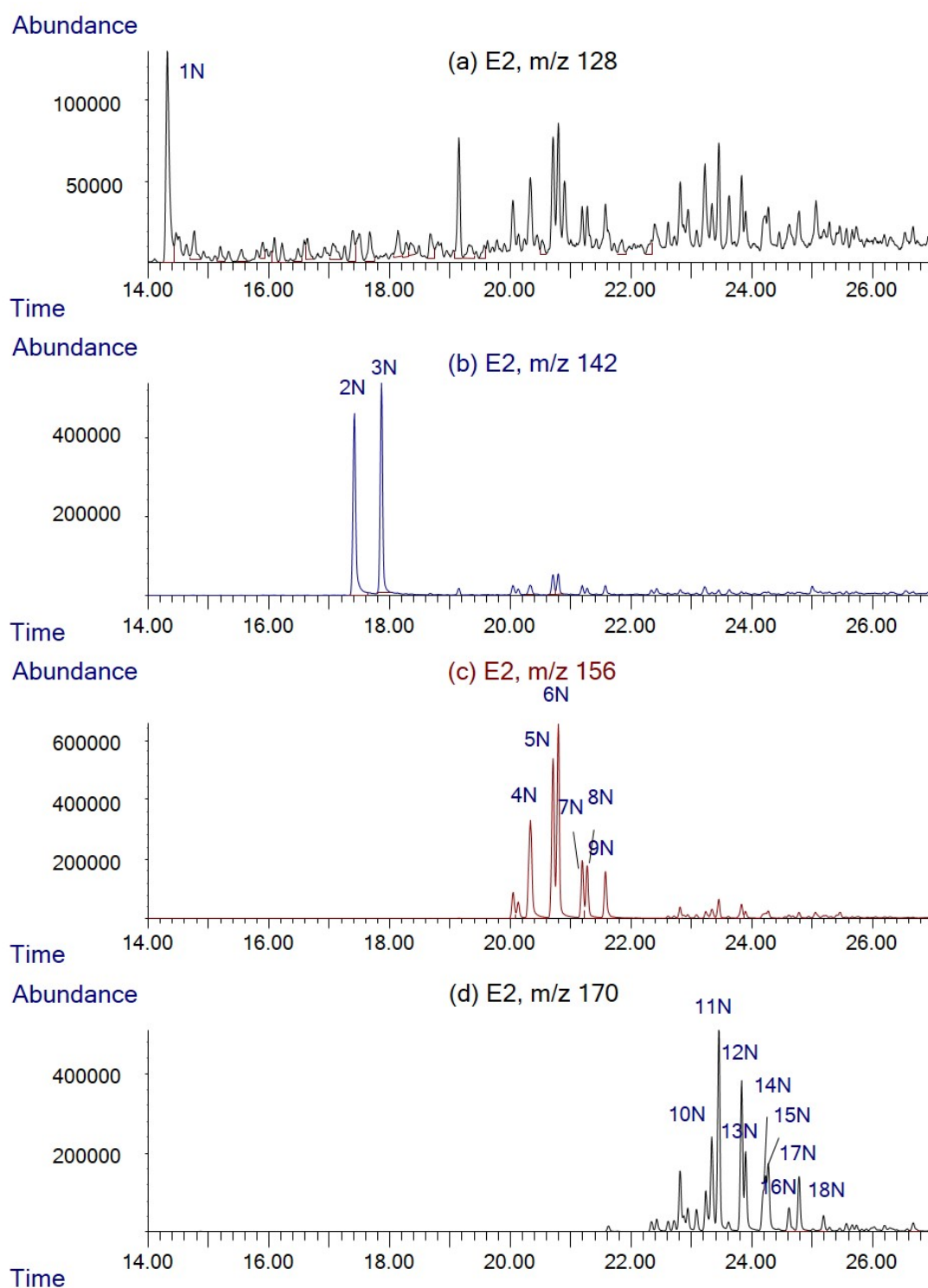


Figure A.11: Partial mass chromatograms of the E2 aromatic fraction, showing naphthalene biomarkers. Labels are listed in Table A.1.

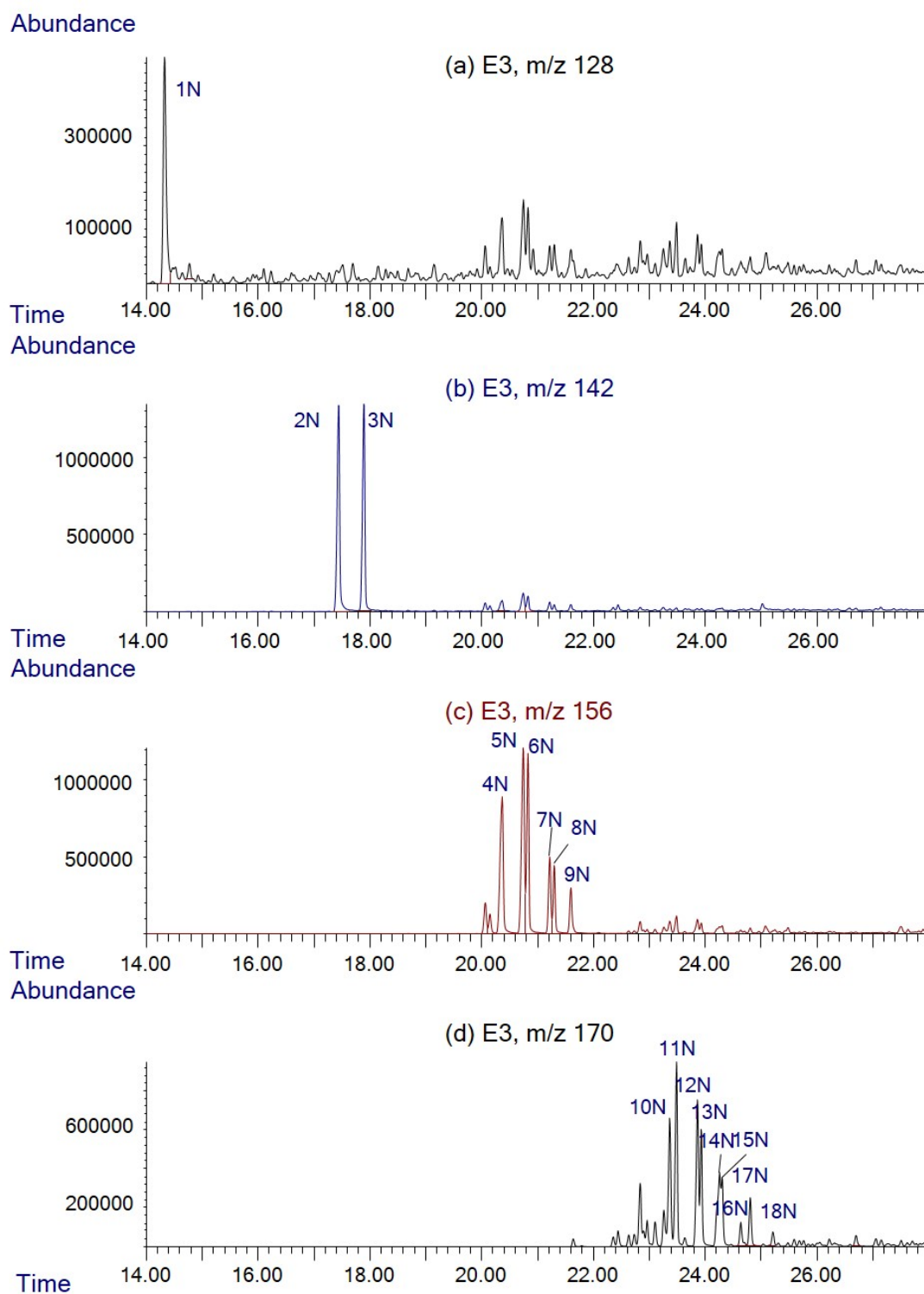


Figure A.12: Partial mass chromatograms of the E3 aromatic fraction, showing naphthalene biomarkers. Labels are listed in Table A.1.

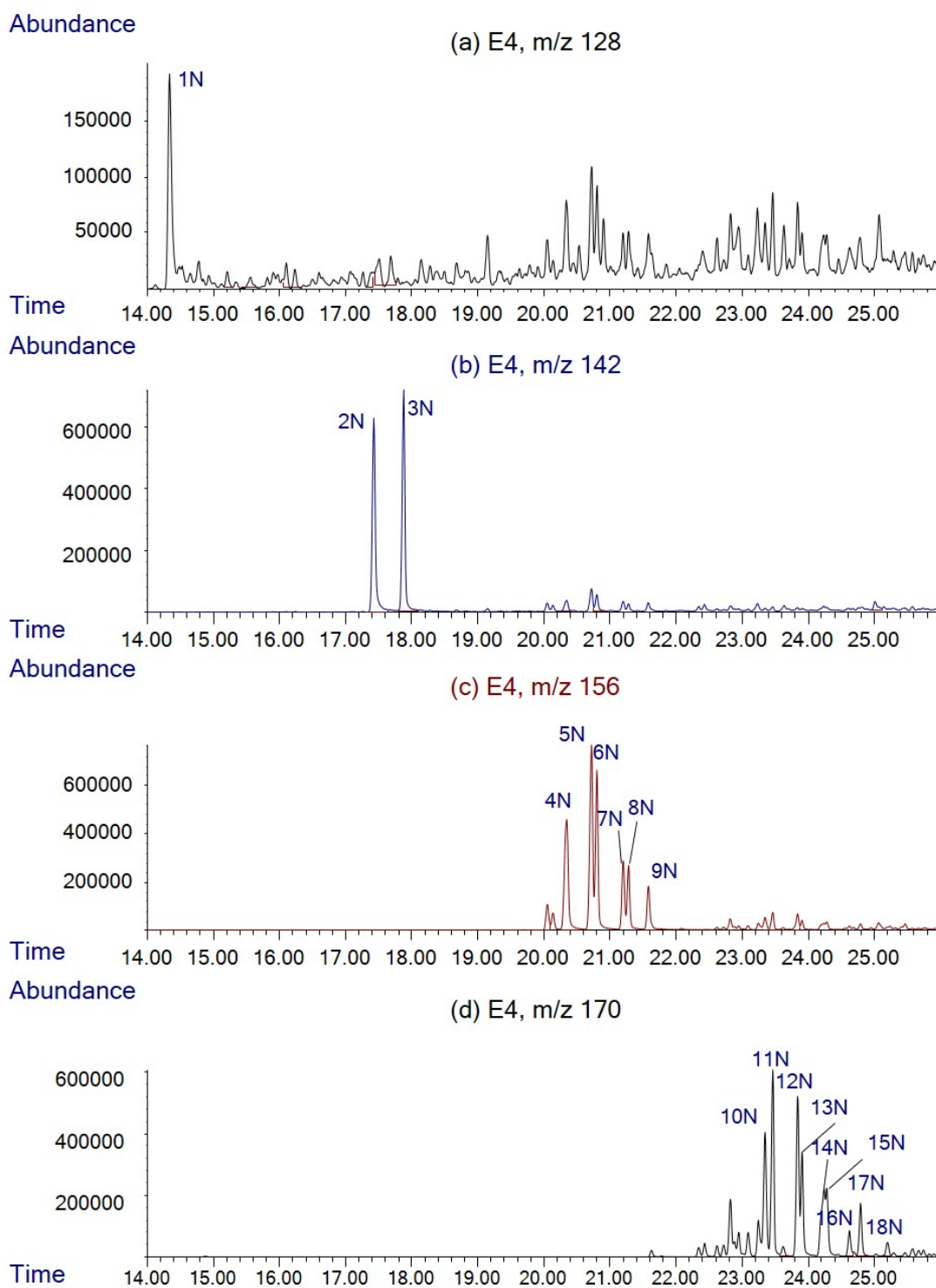


Figure A.13: Partial mass chromatograms of the E4 aromatic fraction, showing naphthalene biomarkers. Labels are listed in Table A.1.

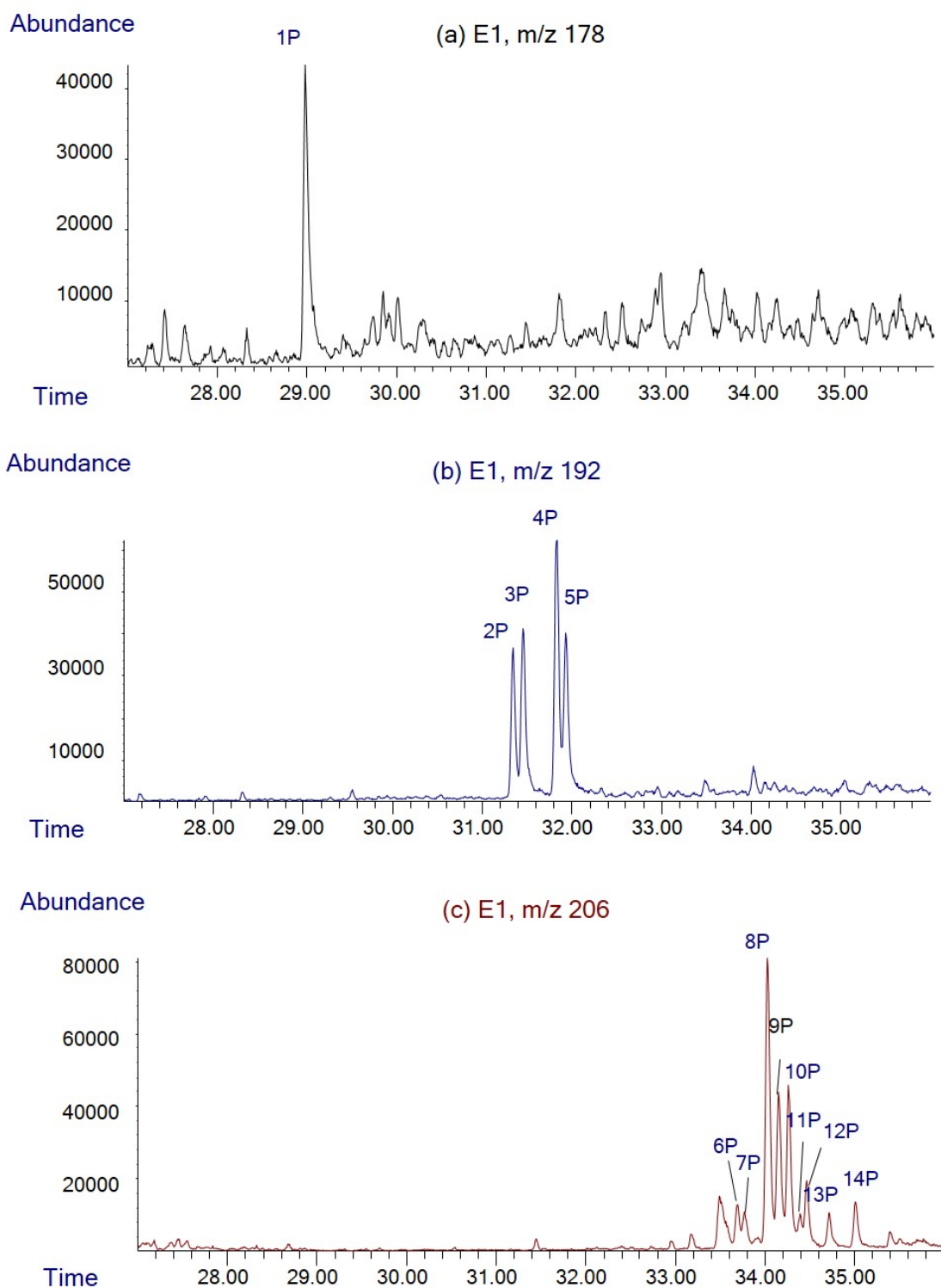


Figure A.14: Partial mass chromatograms of the E1 aromatic fraction, showing phenanthrene biomarkers. Labels are listed in Table A.1.

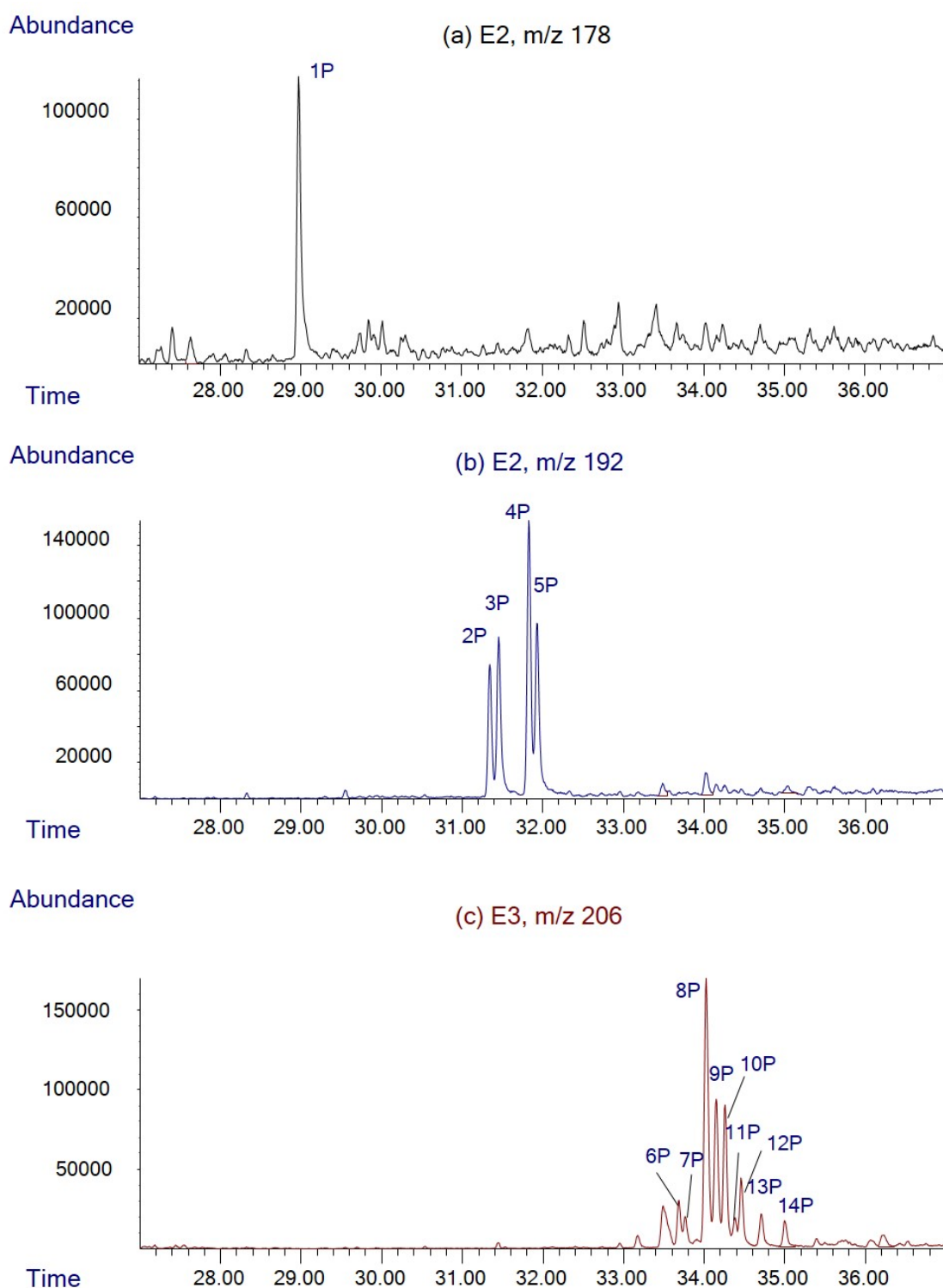


Figure A.15: Partial mass chromatograms of the E2 aromatic fraction, showing phenanthrene biomarkers. Labels are listed in Table A.1.

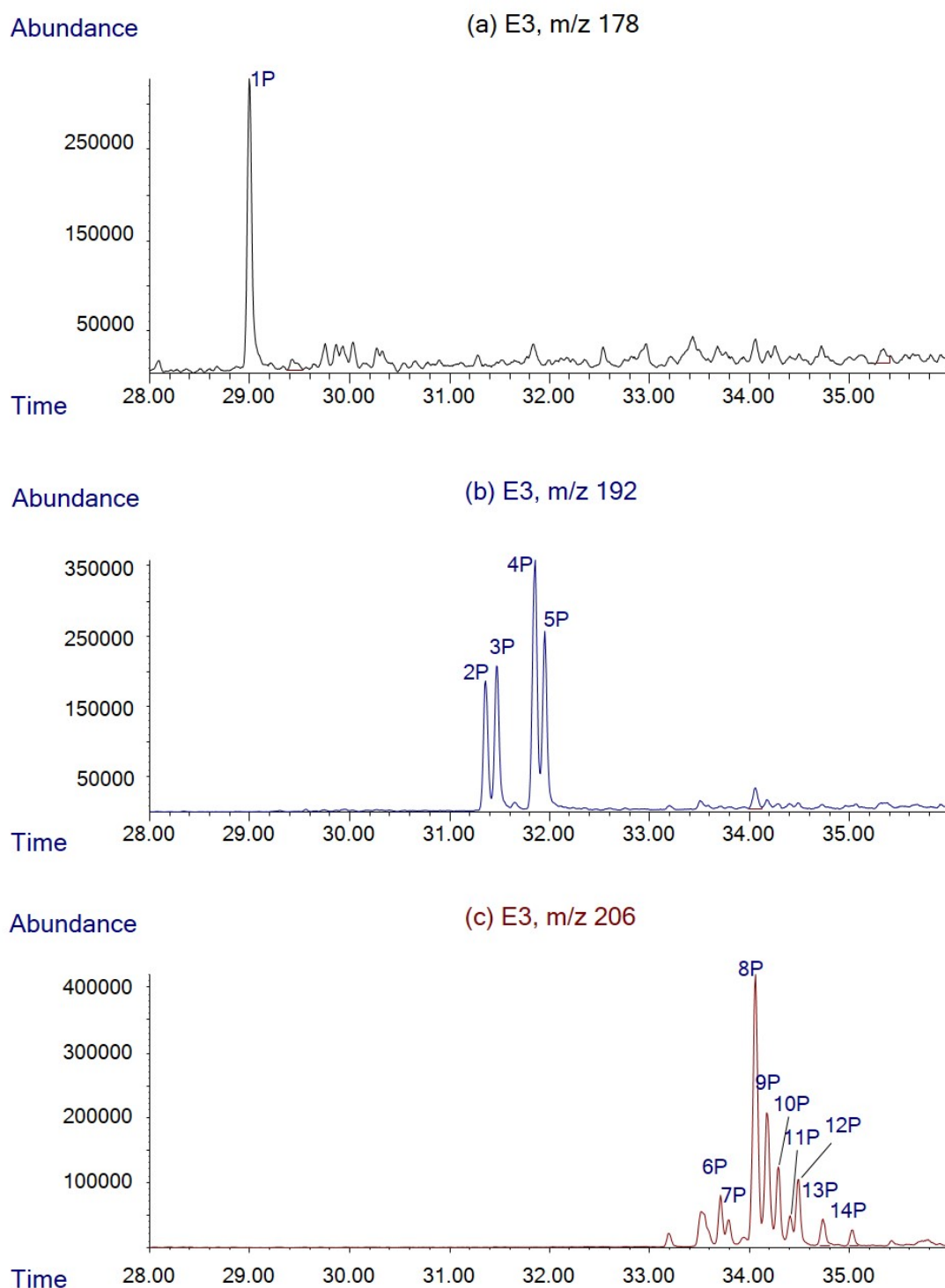


Figure A.16: Partial mass chromatograms of the E3 aromatic fraction, showing phenanthrene biomarkers. Labels are listed in Table A.1.

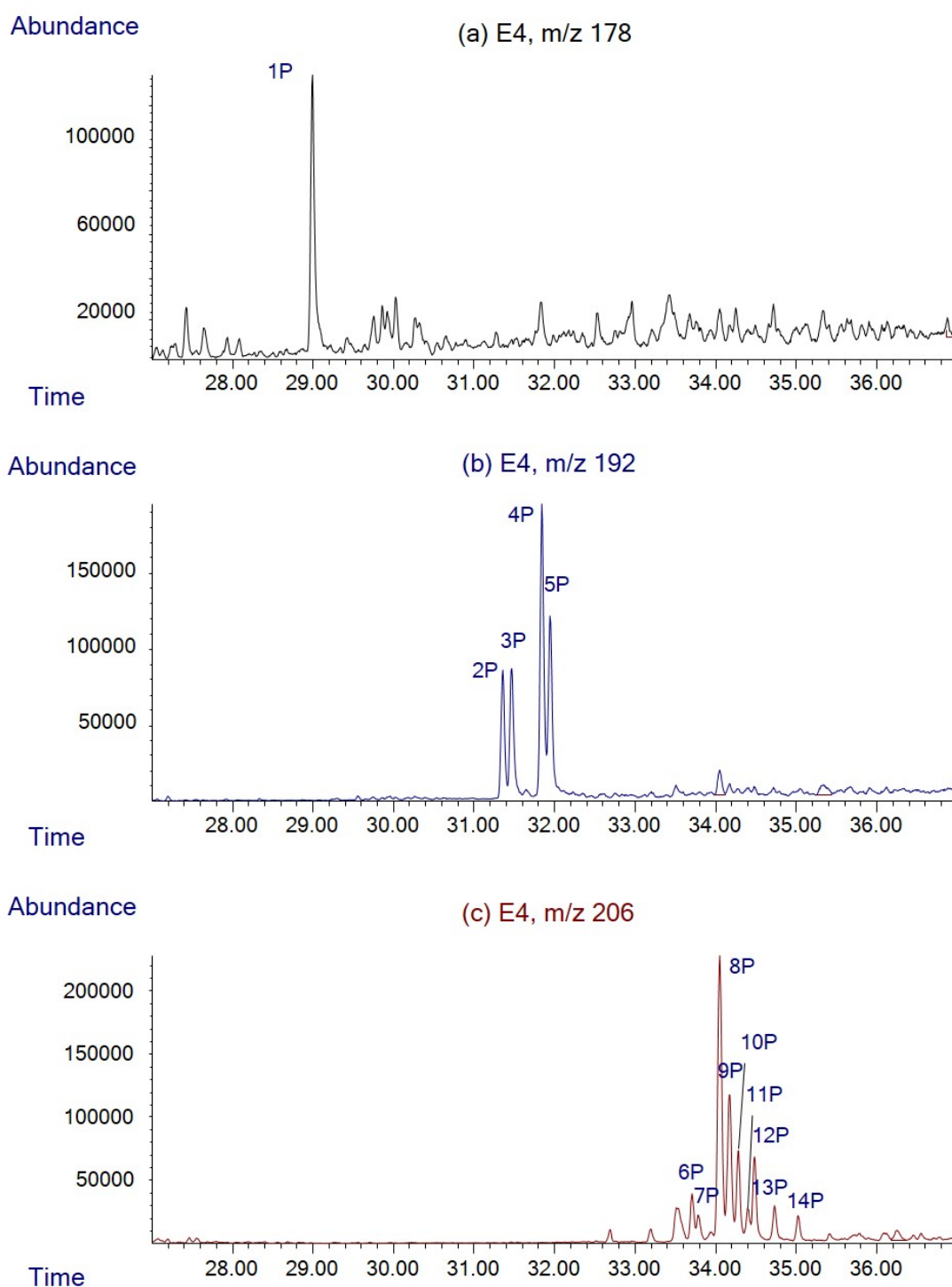


Figure A.17: Partial mass chromatograms of the E4 aromatic fraction, showing phenanthrene biomarkers. Labels are listed in Table A.1.

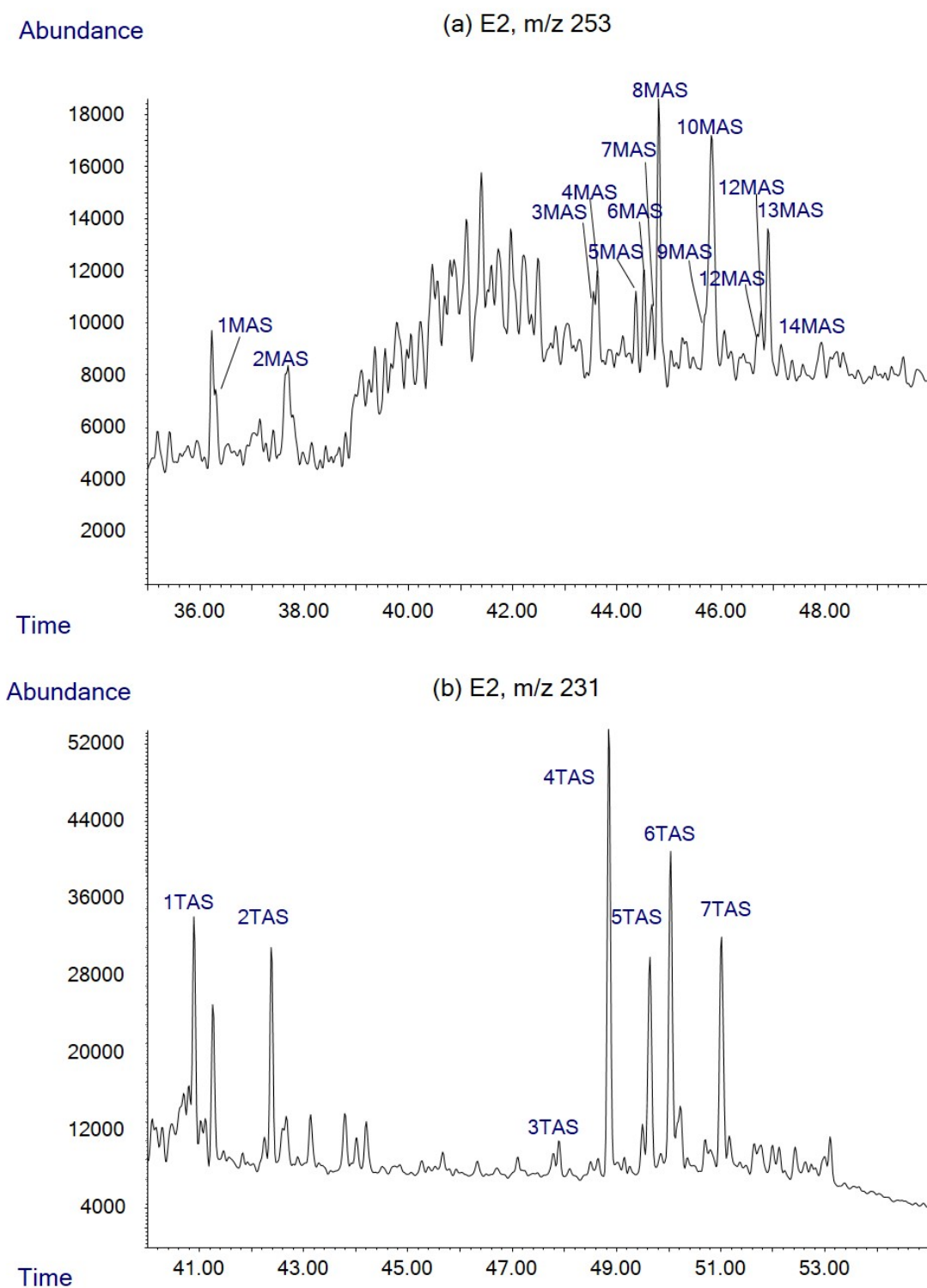


Figure A.18: Partial mass chromatograms of the E2 aromatic fraction, showing aromatic steroid biomarkers. Labels are listed in Table 10.3.

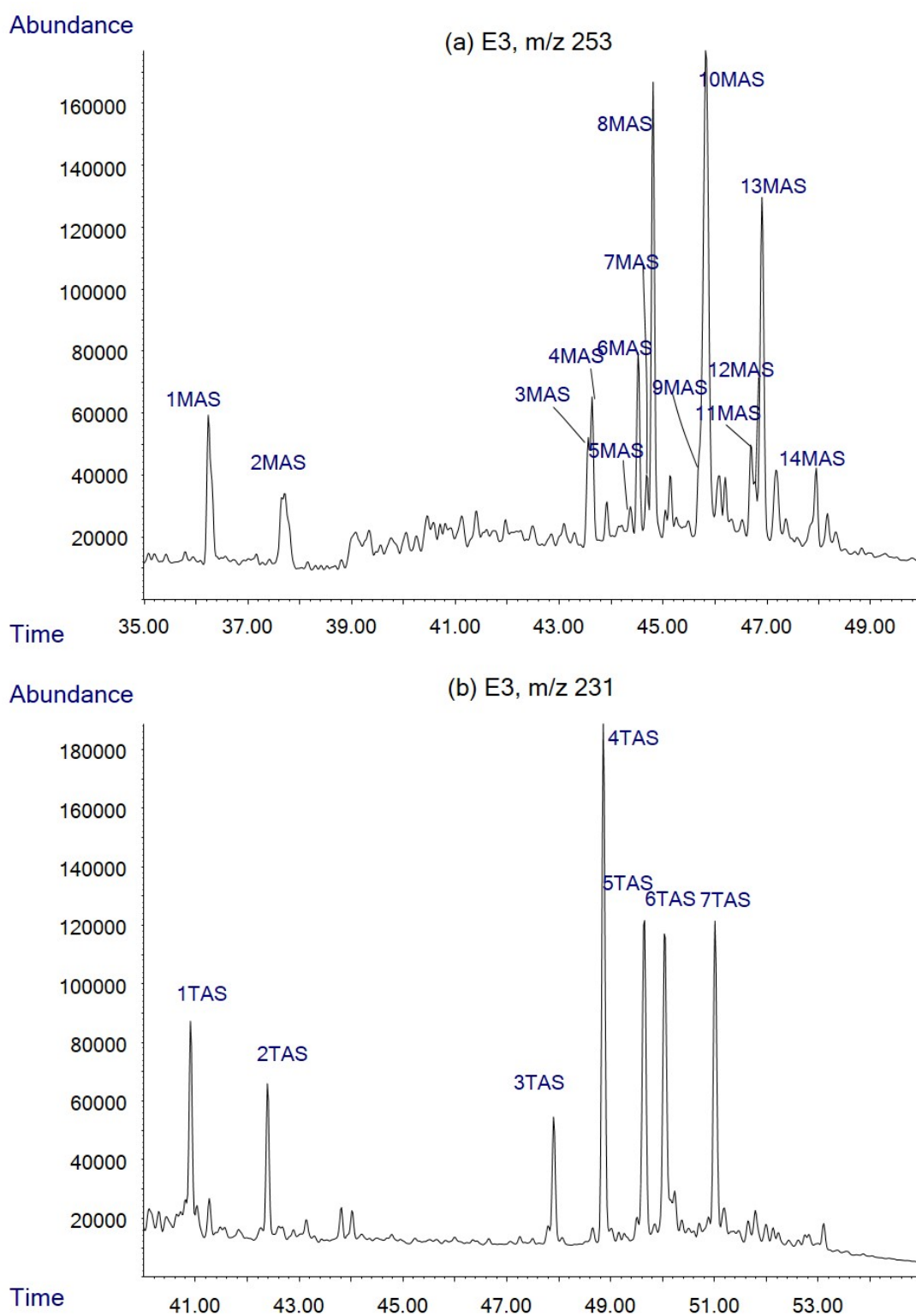


Figure A.19: Partial mass chromatograms of the E3 aromatic fraction, showing aromatic steroid biomarkers. Labels are listed in Table 10.3.

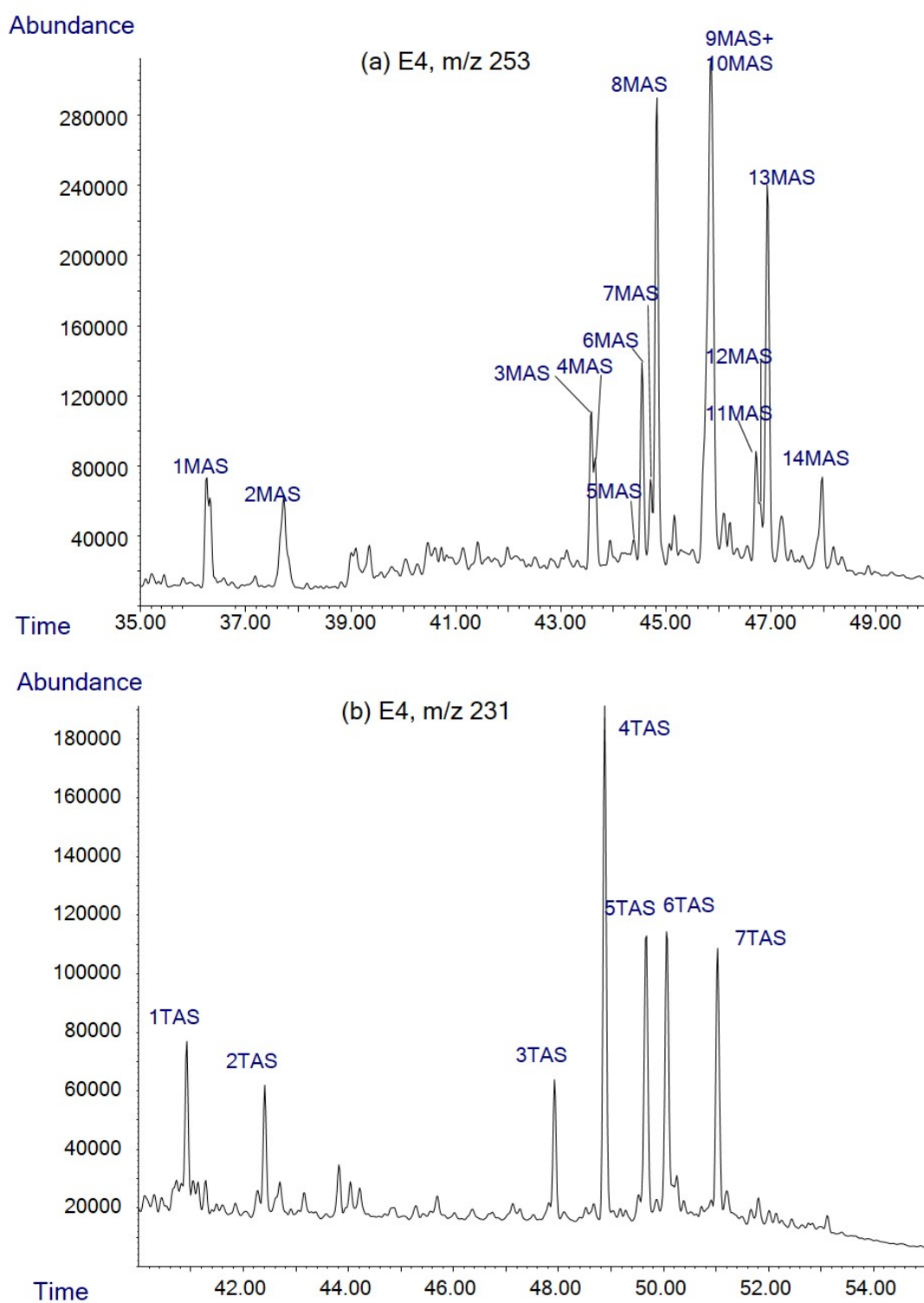


Figure A.20: Partial mass chromatograms of the E4 aromatic fraction, showing aromatic steroid biomarkers. Labels are listed in Table 10.3.

**Appendix B. Supplementary Material for Ruthenium Ion
Catalysed Oxidation of Asphaltenes**

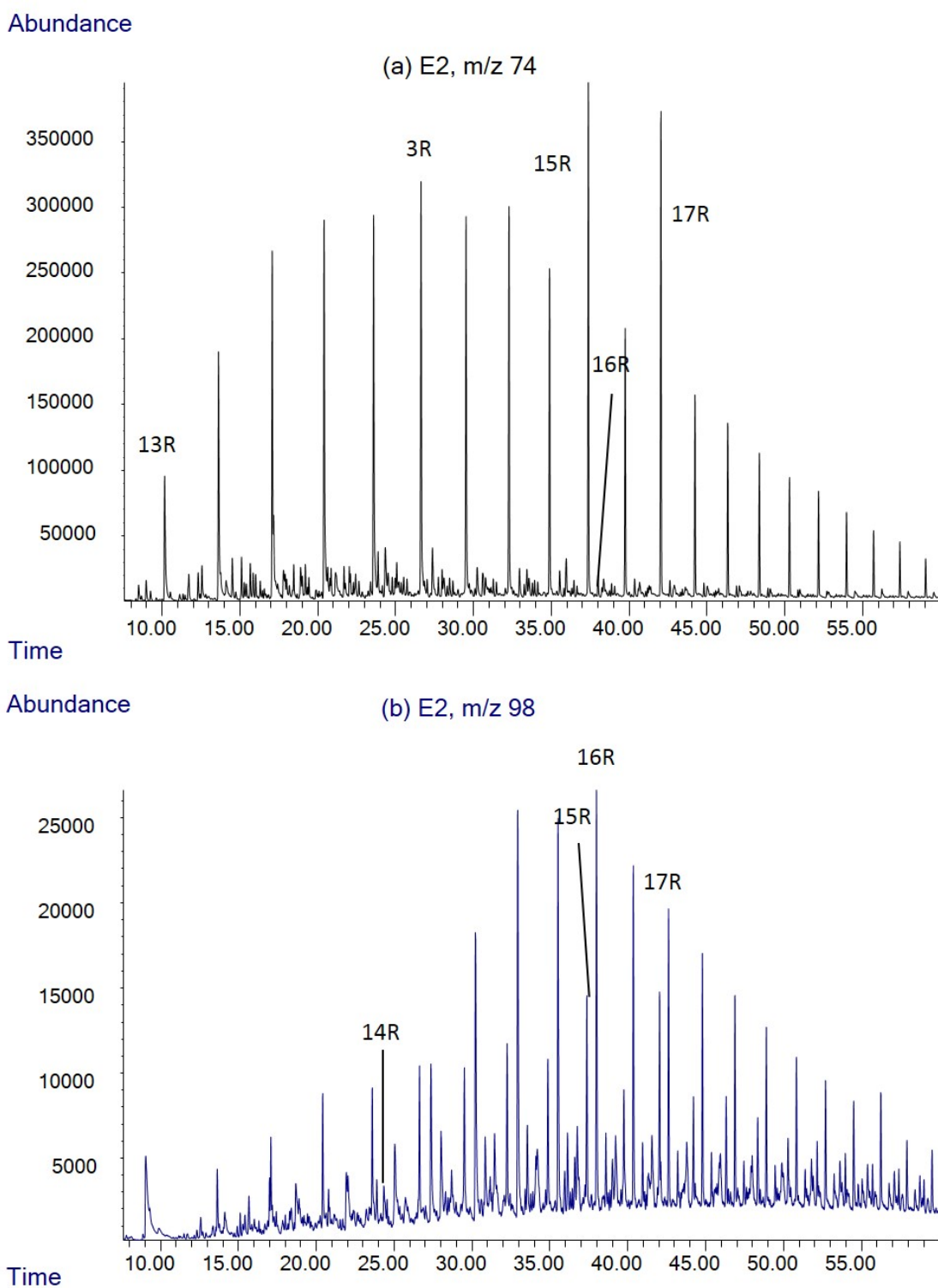


Figure B.1: Partial ion chromatograms of (a) *n*-alkanoic fatty acid and (b) α,ω -di-*n*-alkanoic di-fatty acid methyl esters of E2 asphaltene.

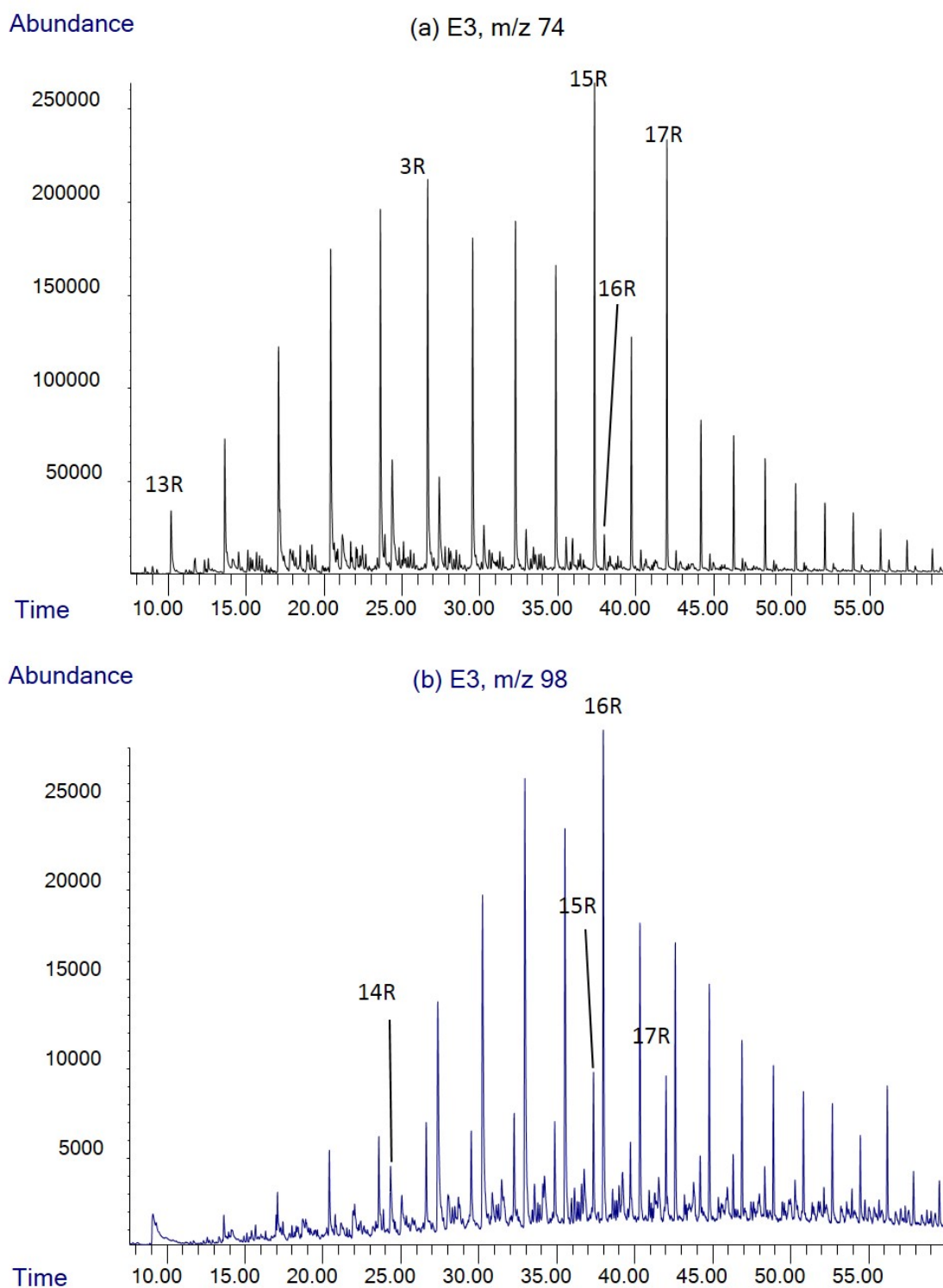


Figure B.2: Partial ion chromatograms of (a) *n*-alkanoic fatty acid and (b) α,ω -di-*n*-alkanoic di-fatty acid methyl esters of E3 asphaltene.

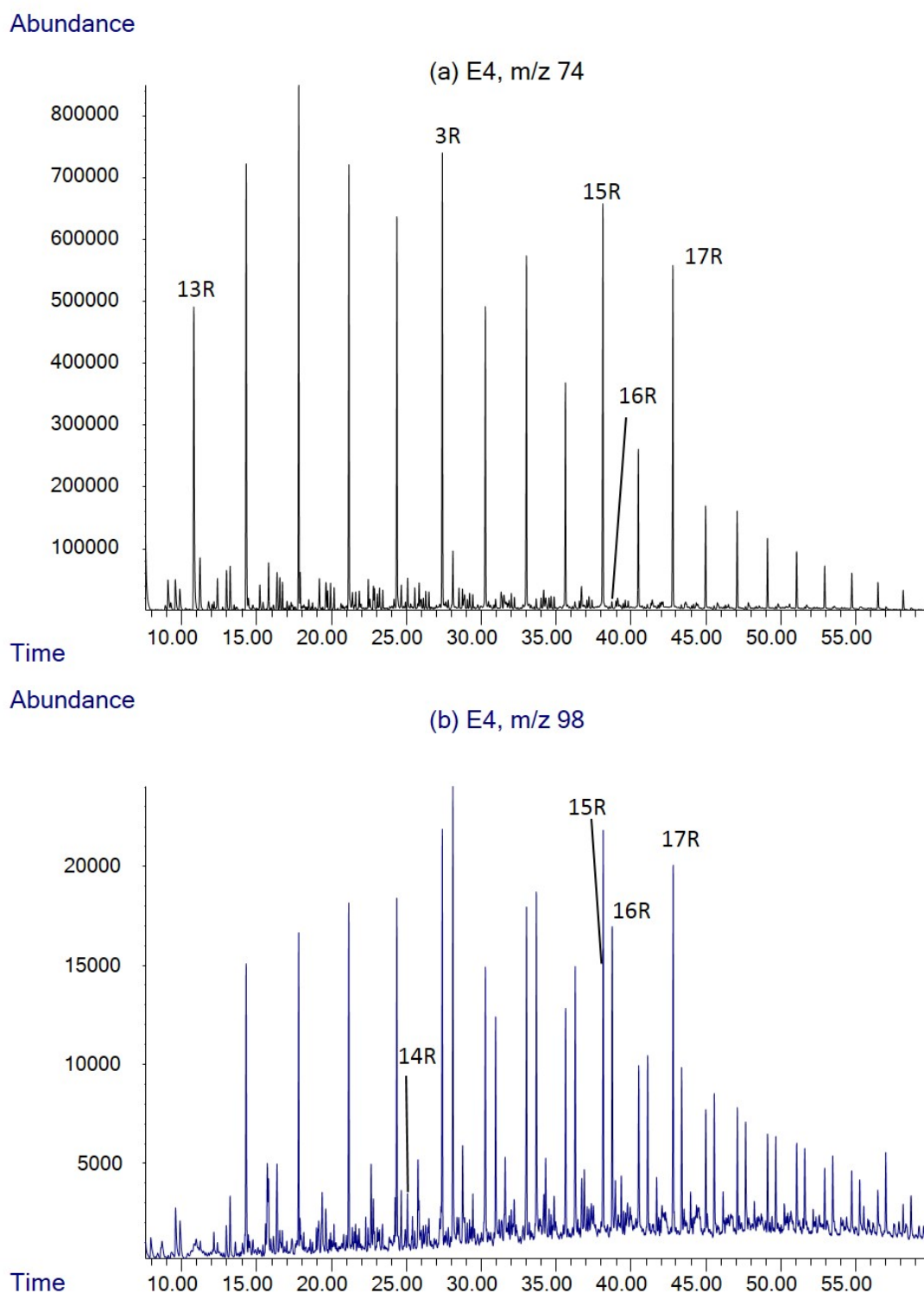


Figure B.3: Partial ion chromatograms of (a) *n*-alkanoic fatty acid and (b) α,ω -di-*n*-alkanoic di-fatty acid methyl esters of E4 asphaltene.

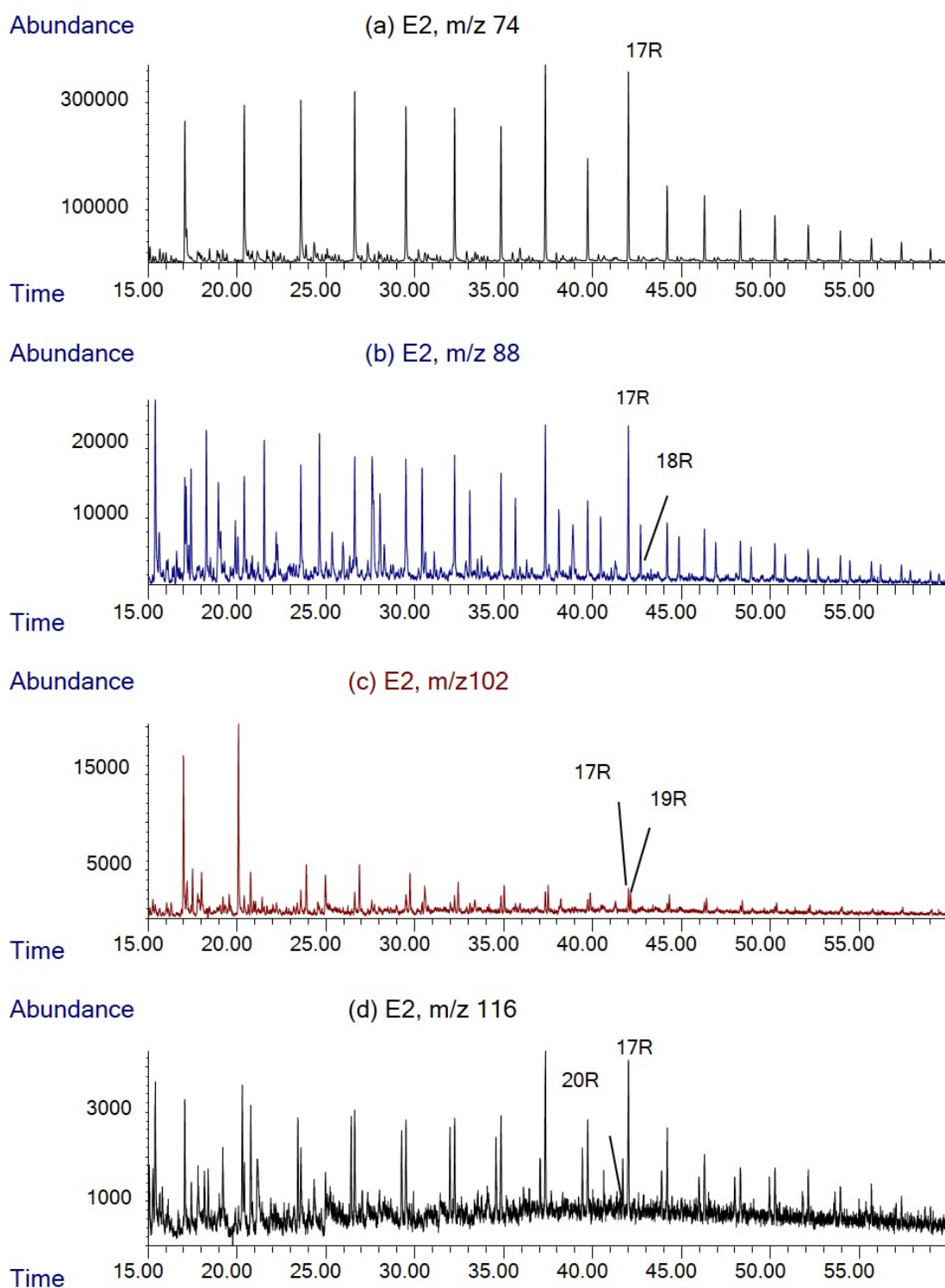


Figure B.4: Partial ion chromatograms of (a) *n*-alkanoic, (b) α -methyl-*n*-alkanoic, (c) α -ethyl-*n*-alkanoic and (d) α -propyl-*n*-alkanoic fatty acid methyl esters of E2 asphaltene.

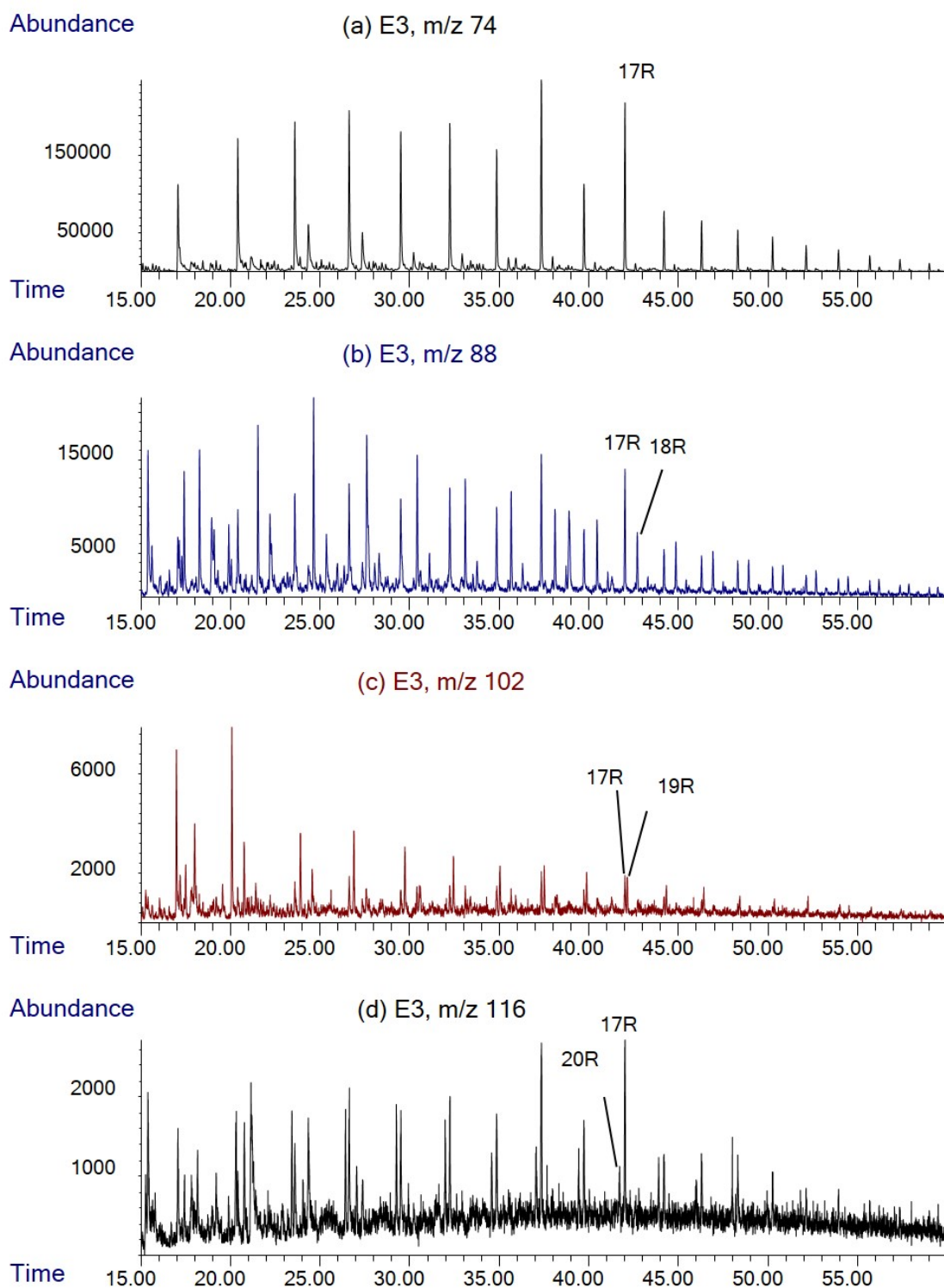


Figure B.5: Partial ion chromatograms of (a) *n*-alkanoic, (b) α -methyl-*n*-alkanoic, (c) α -ethyl-*n*-alkanoic and (d) α -propyl-*n*-alkanoic fatty acid methyl esters of E3 asphaltene.

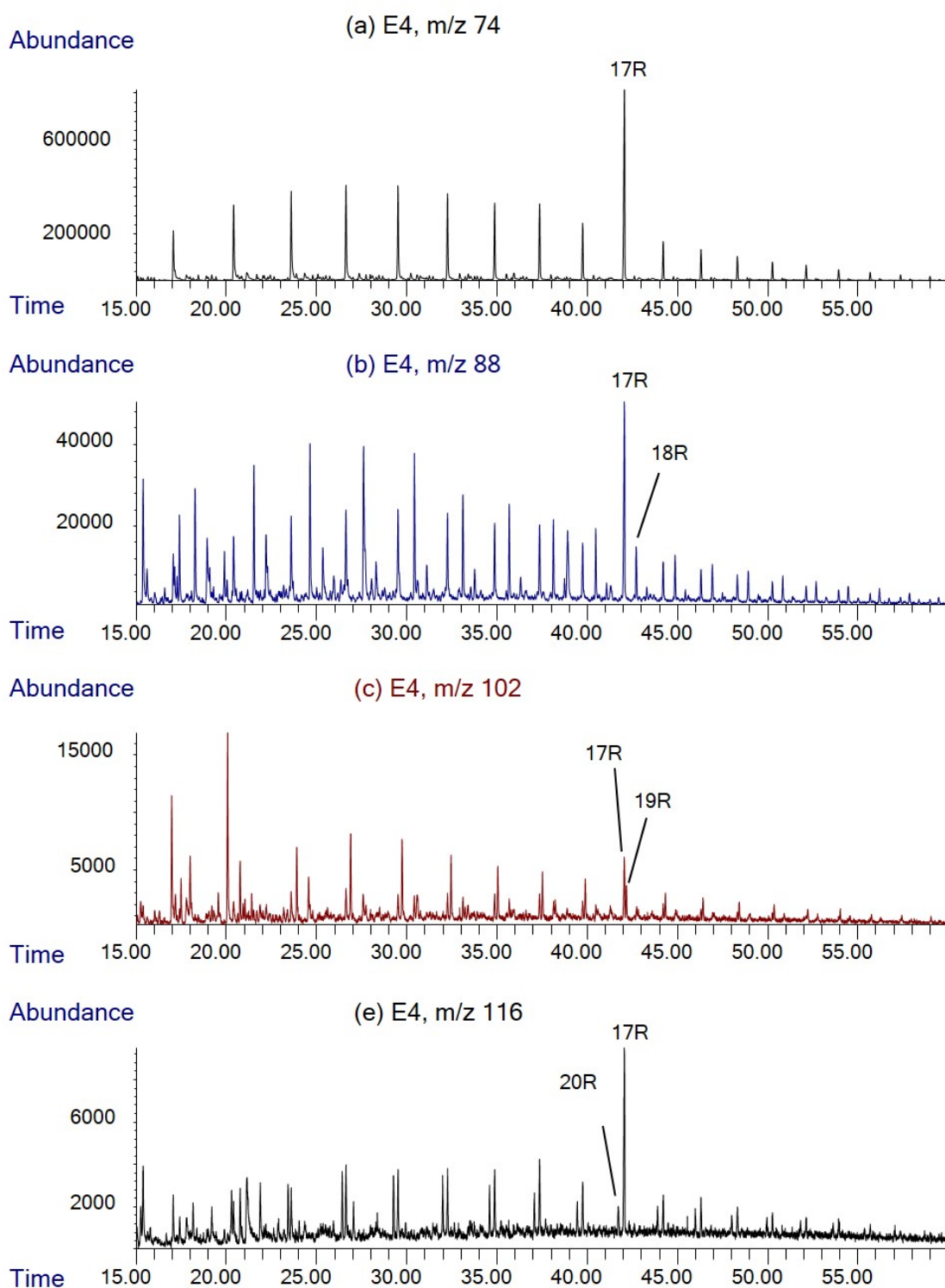


Figure B.6: Partial ion chromatograms of (a) *n*-alkanoic, (b) α -methyl-*n*-alkanoic, (c) α -ethyl-*n*-alkanoic and (d) α -propyl-*n*-alkanoic fatty acid methyl esters of E4 asphaltene.

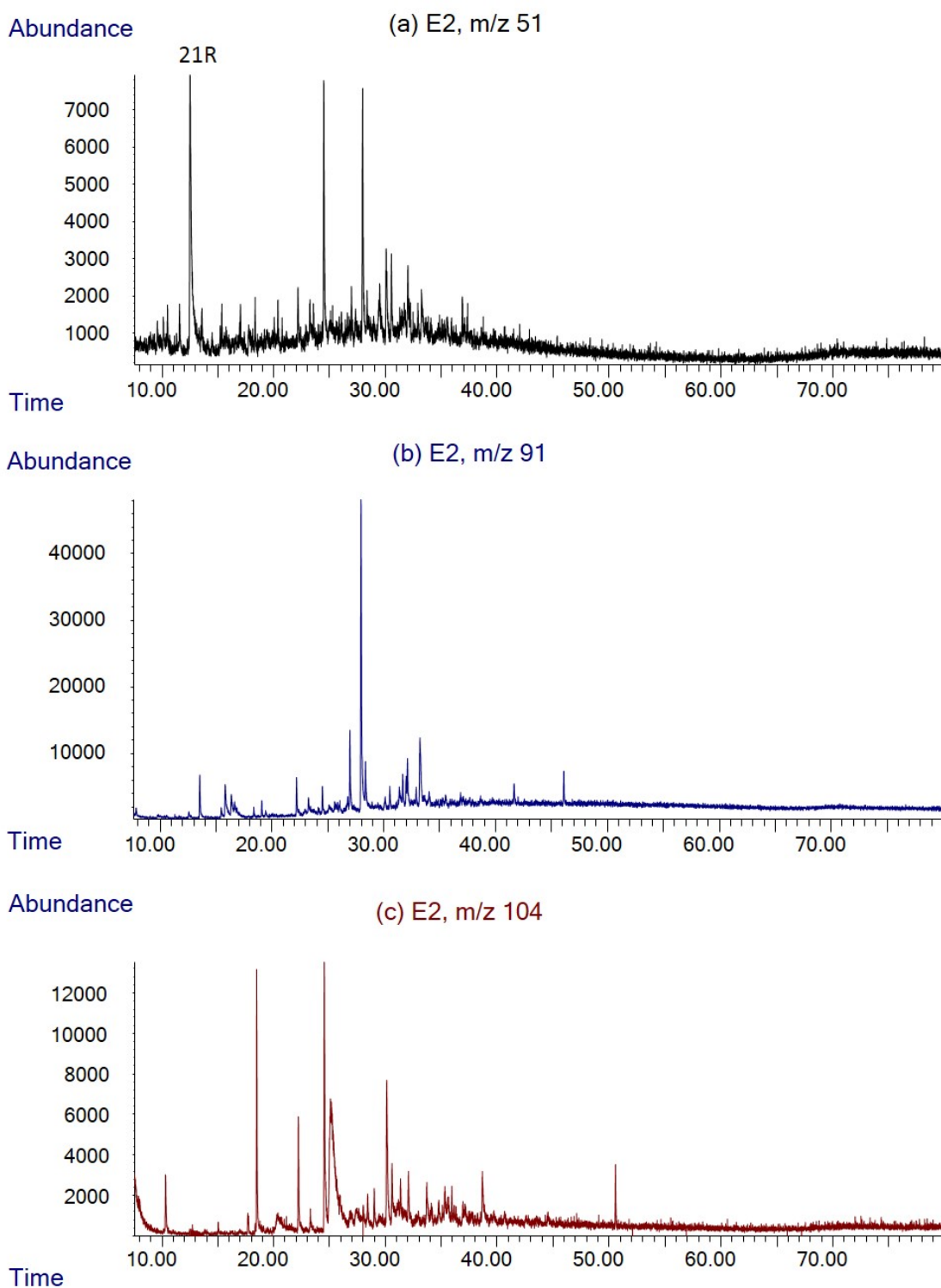


Figure B.7: Partial ion chromatograms for the identification of benzenealkyl acid methyl esters of E2 asphaltene.

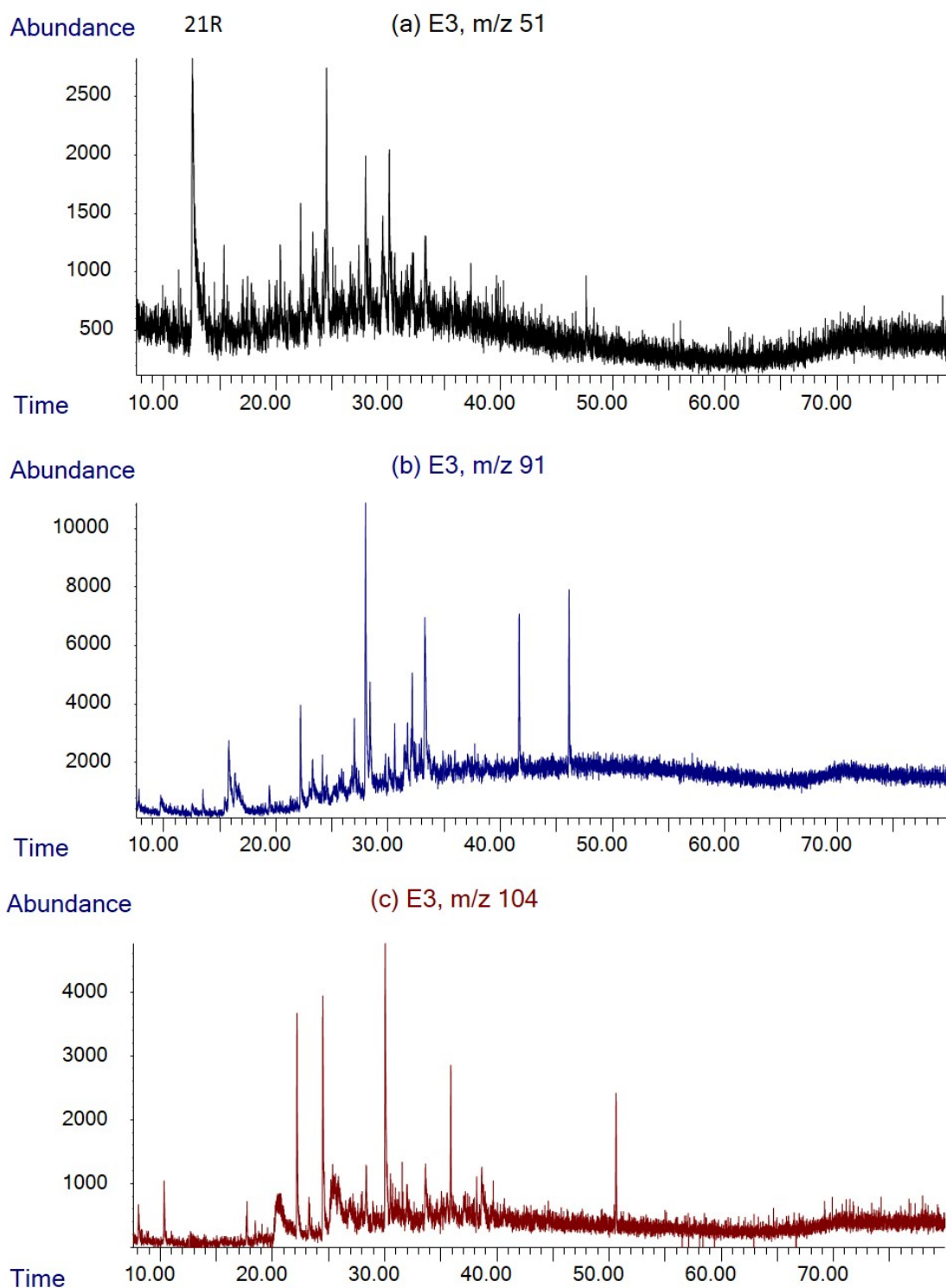


Figure B.8: Partial ion chromatograms for the identification of benzenealkyl acid methyl esters of E3 asphaltene.

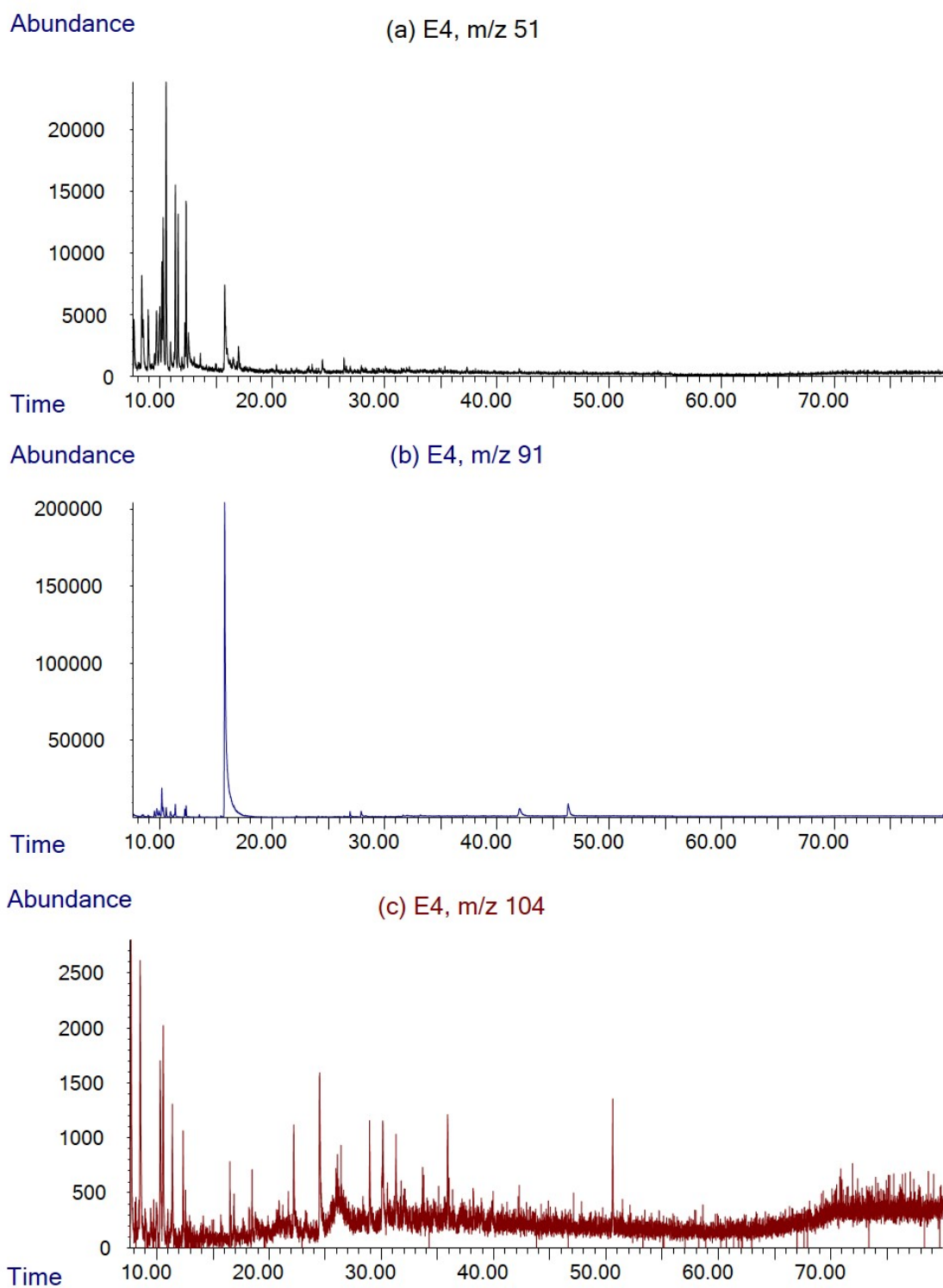


Figure B.9: Partial ion chromatograms for the identification of benzenealkyl acid methyl esters of E4 asphaltene.

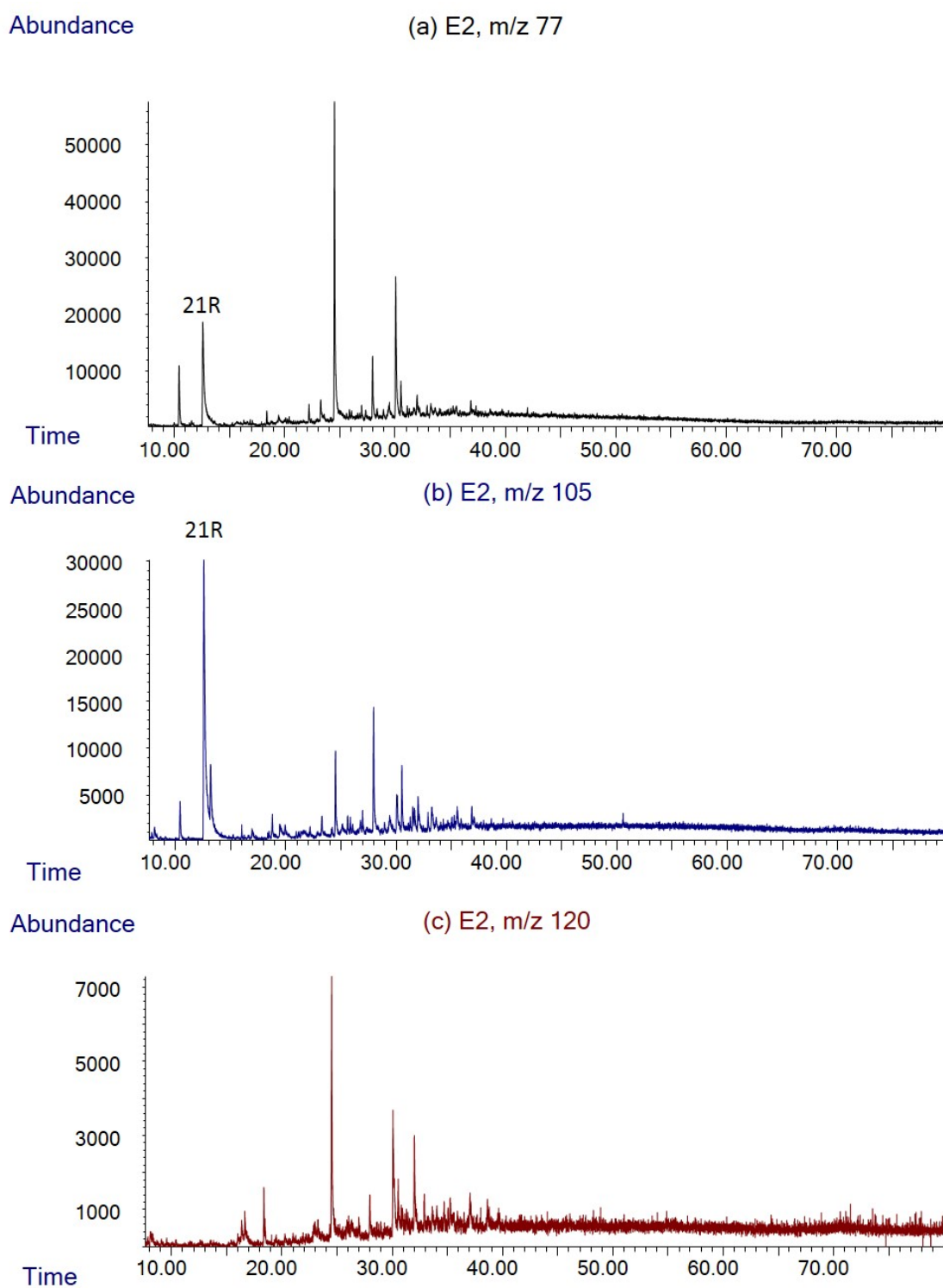


Figure B.10: Partial ion chromatograms for the identification of phenylalkylketones of E2 asphaltene.

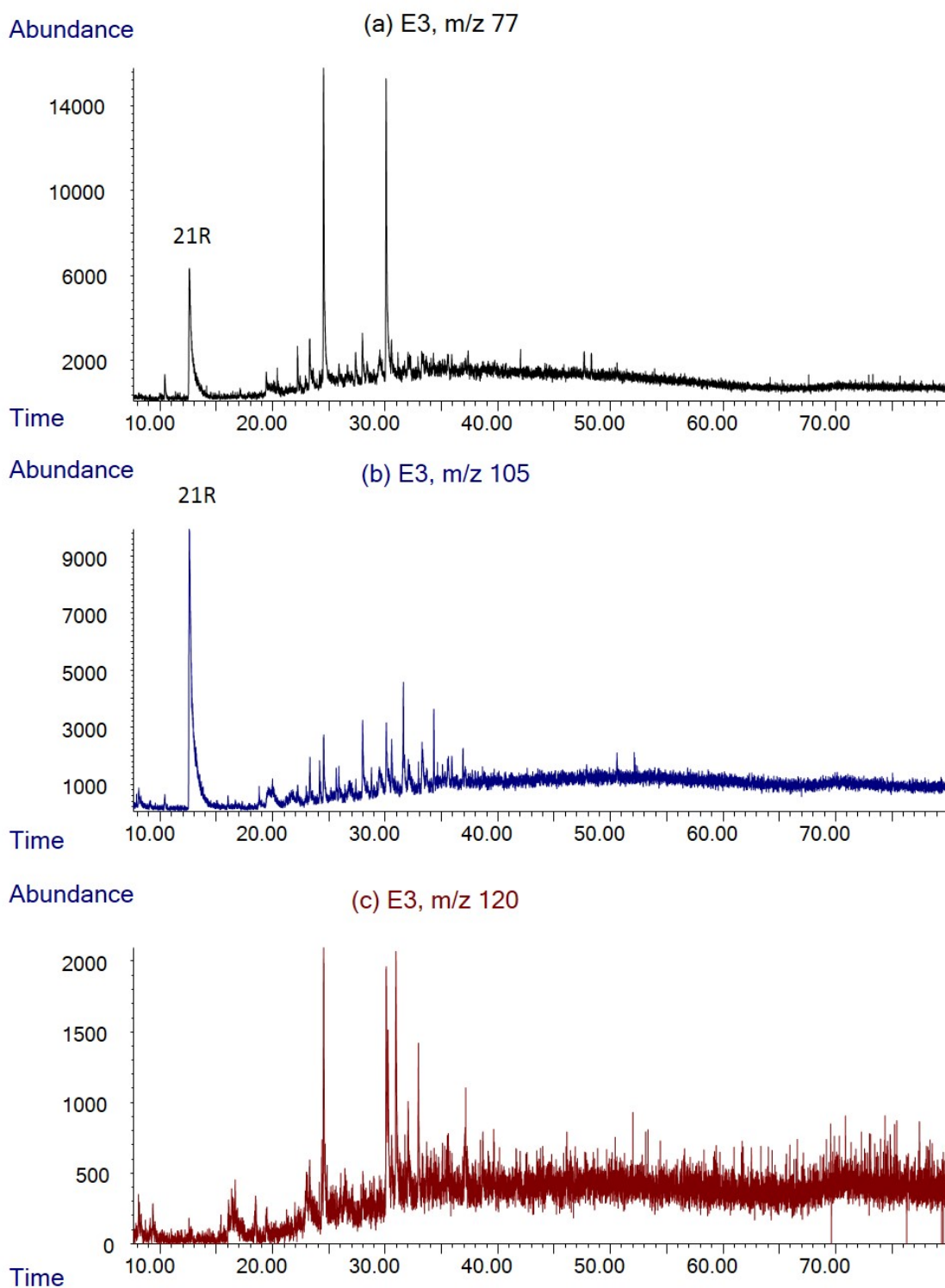


Figure B.11: Partial ion chromatograms for the identification of phenylalkylketones of E3 asphaltene.

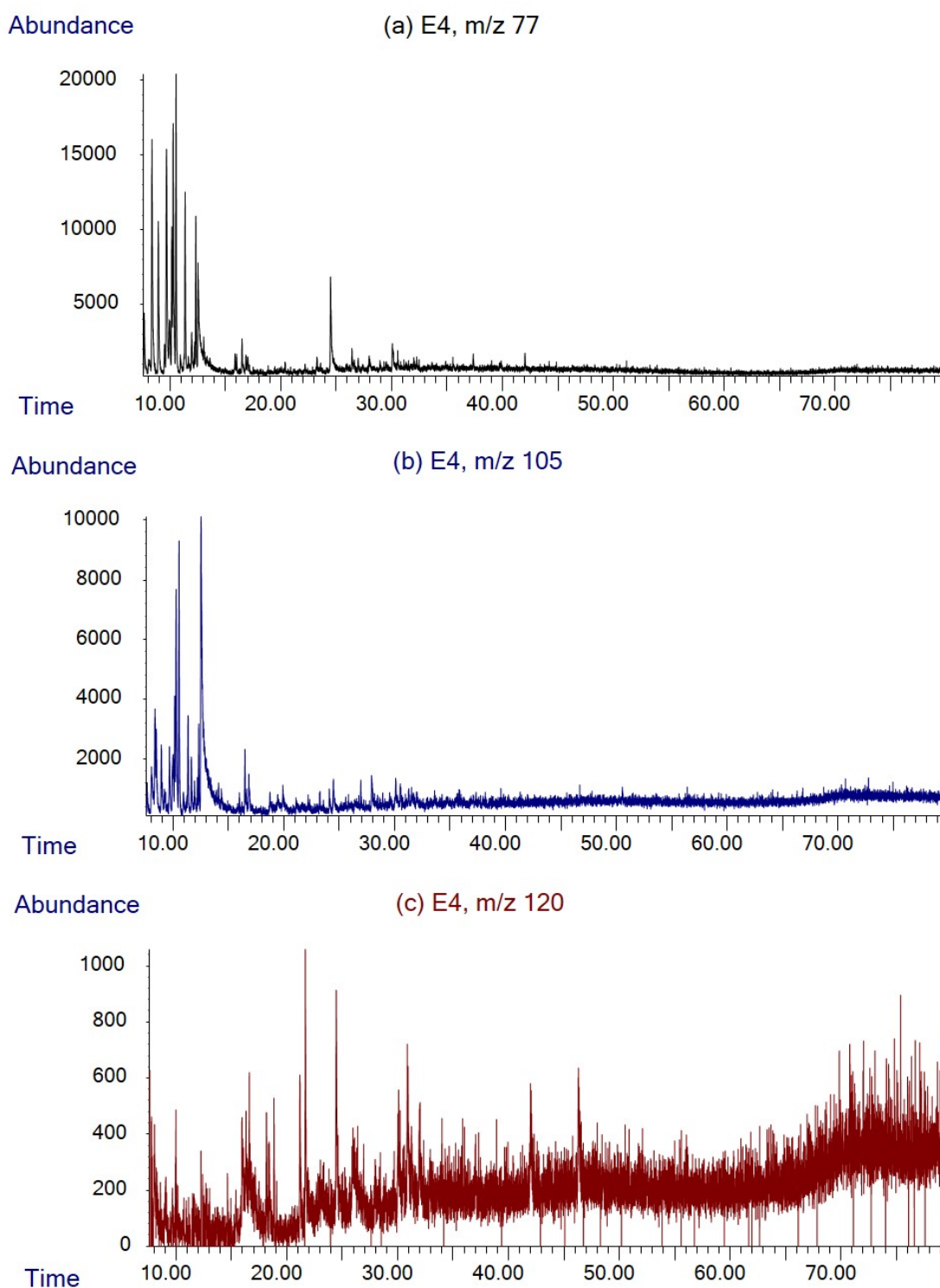


Figure B.12: Partial ion chromatograms for the identification of phenylalkylketones of E4 asphaltene.

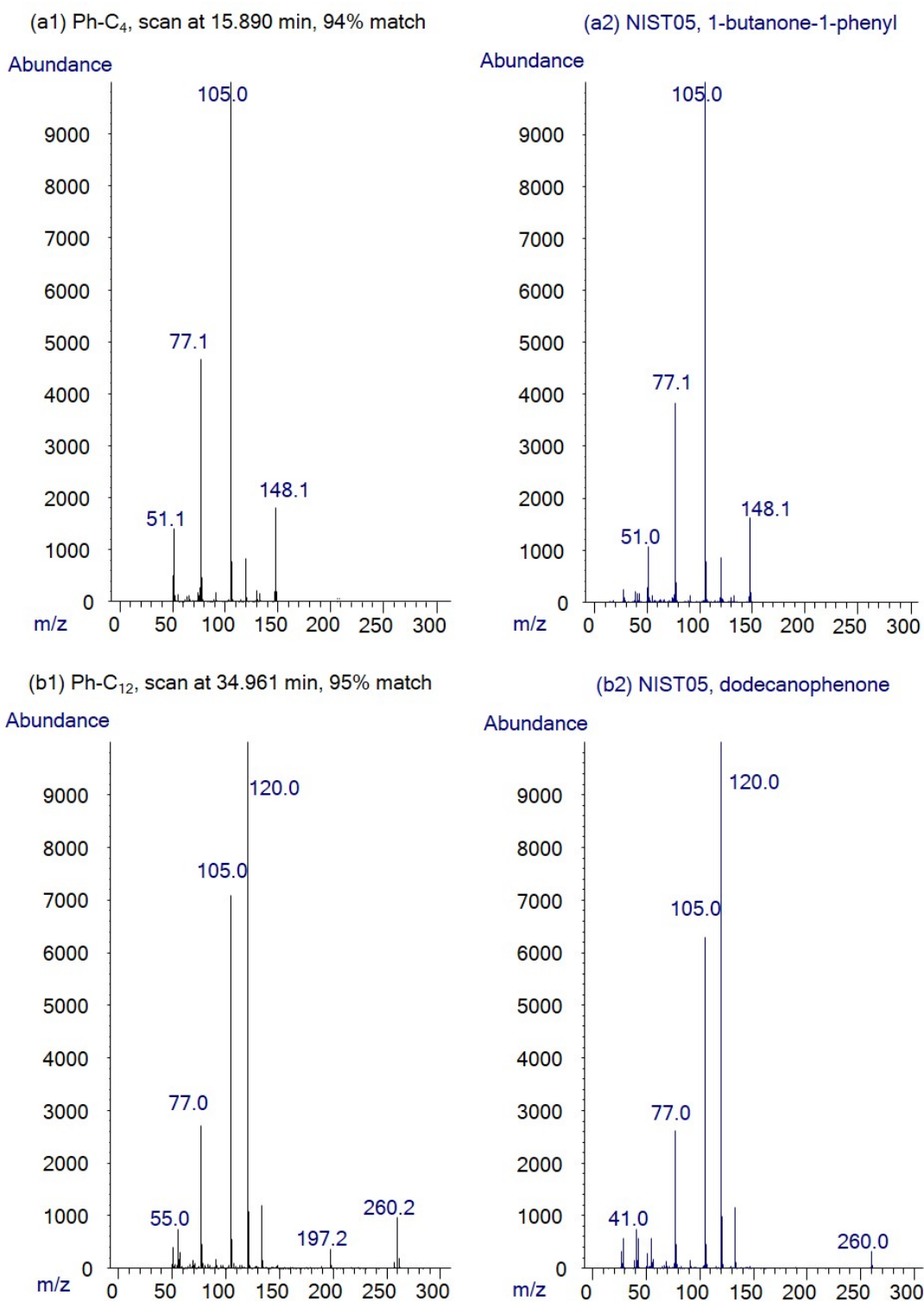


Figure B.13: Mass spectra of 1-butanone-1-phenyl.

Appendix B. Supplementary Material for Ruthenium Ion Catalysed Oxidation of Asphaltenes

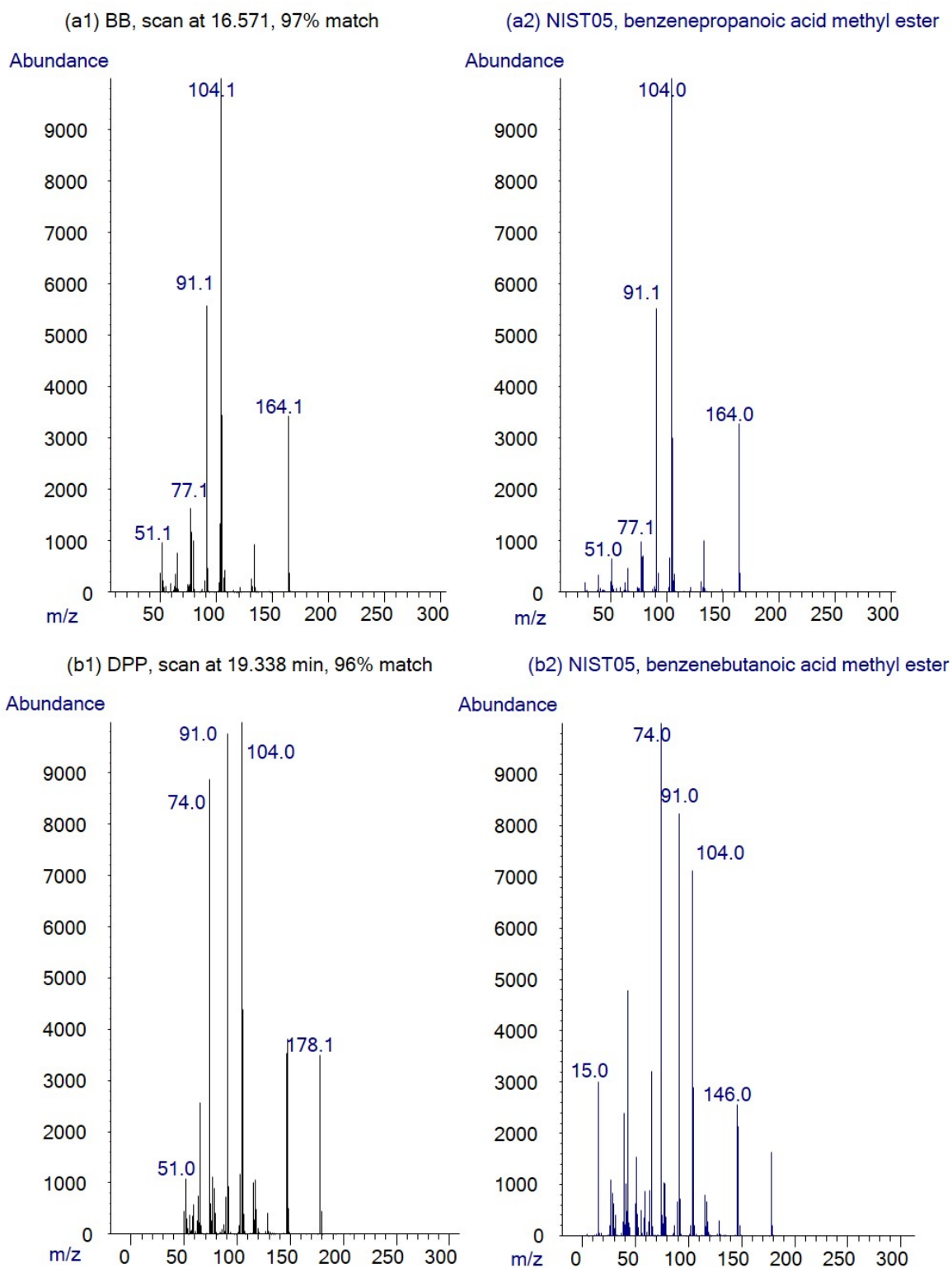


Figure B.14: Mass spectra of dodecanophenone.

Appendix C. Supplementary Material for Ultrasonic Characterisation Studies

C.1 Cetyltrimethylammonium bromide diagnostic data

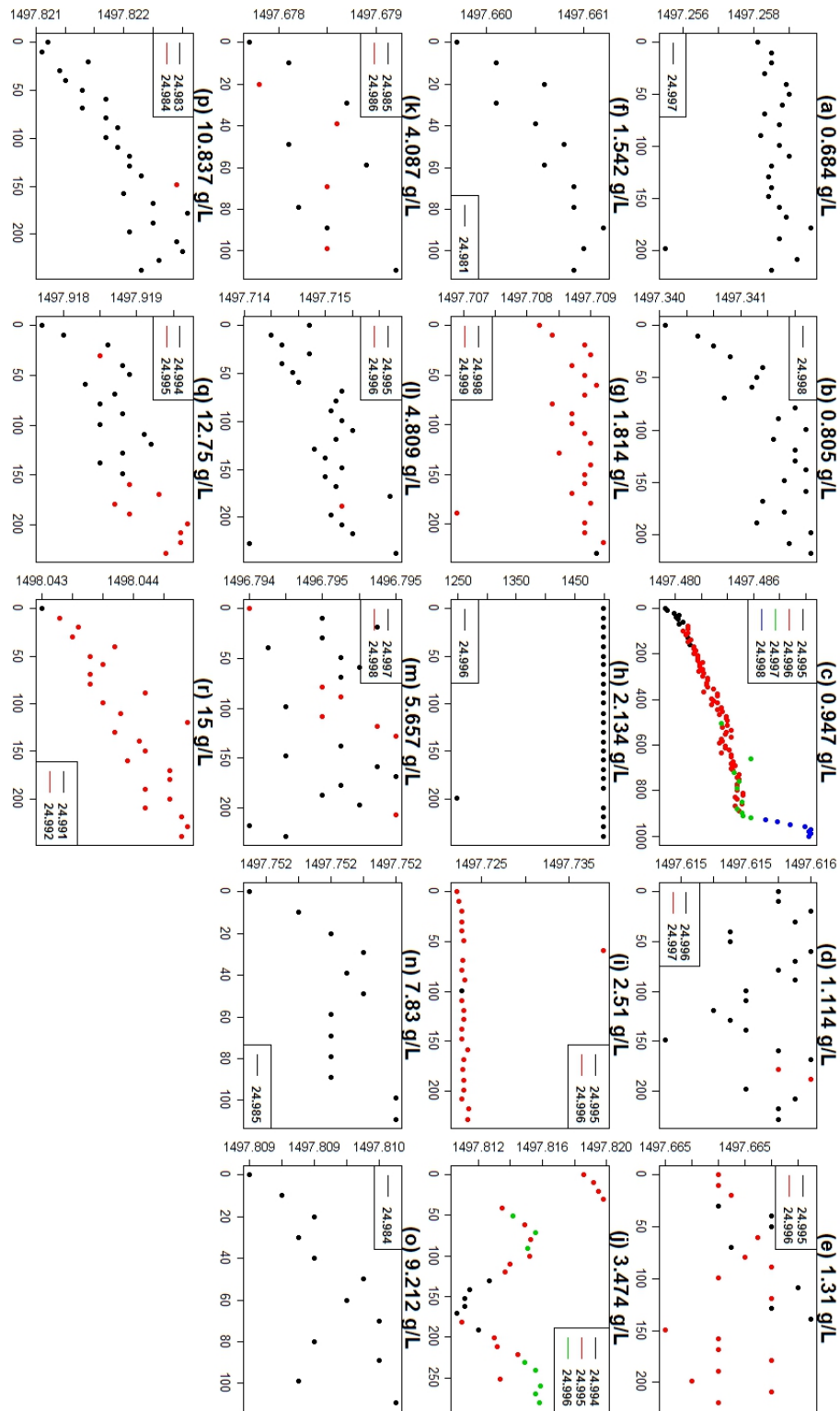


Figure C.1: Time (s) versus velocity (ms⁻¹) plots of C₁₄TAB ultrasonic measurements. Titles indicate C₁₄TAB concentration, legends indicate measurement temperature in °C.

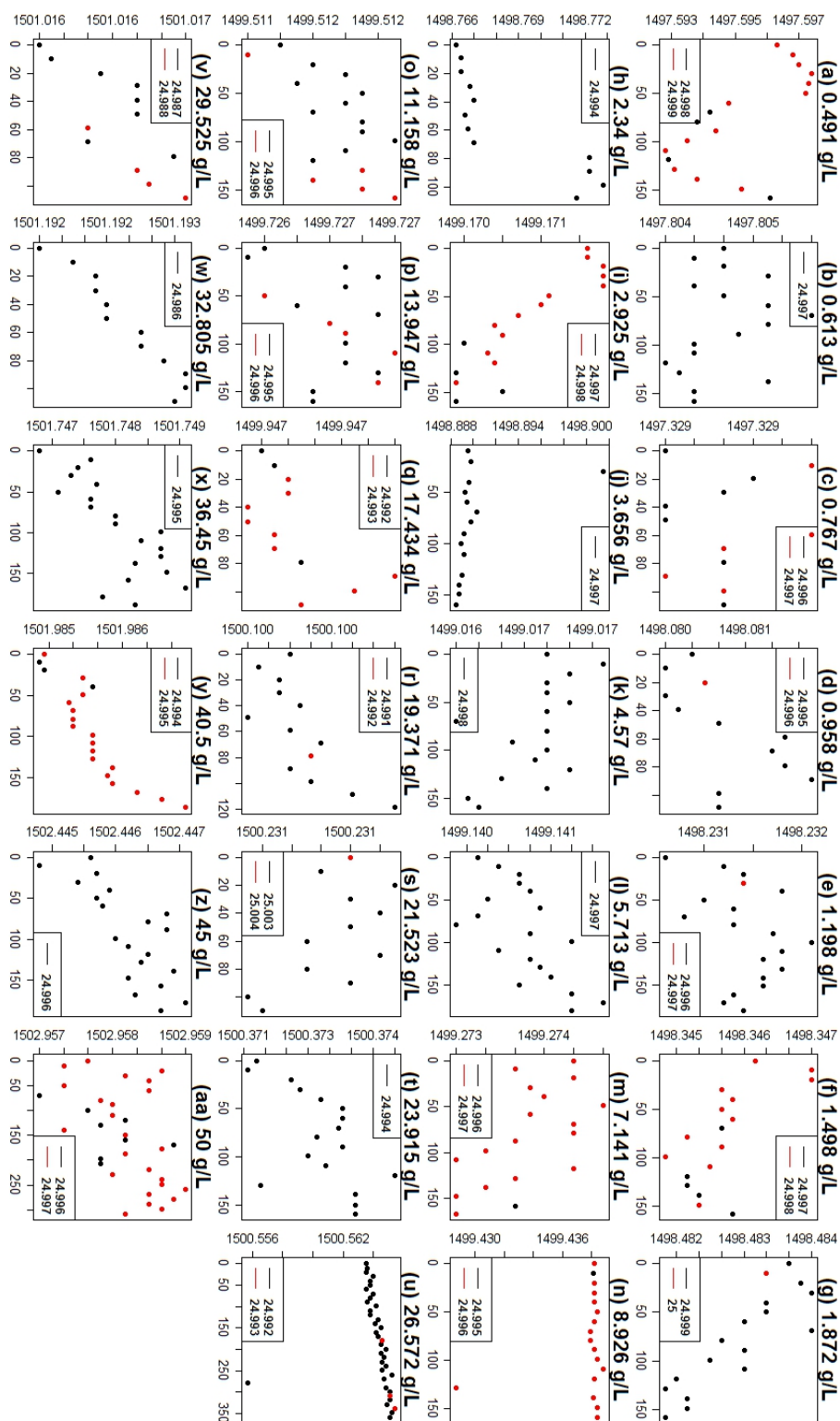


Figure C.2: Time (s) versus velocity (ms⁻¹) plots of C₁₂TAB/C₁₄TAB 1/1 M ultrasonic measurements. Titles indicate C₁₂TAB concentration, legends indicate measurement temperature in °C.

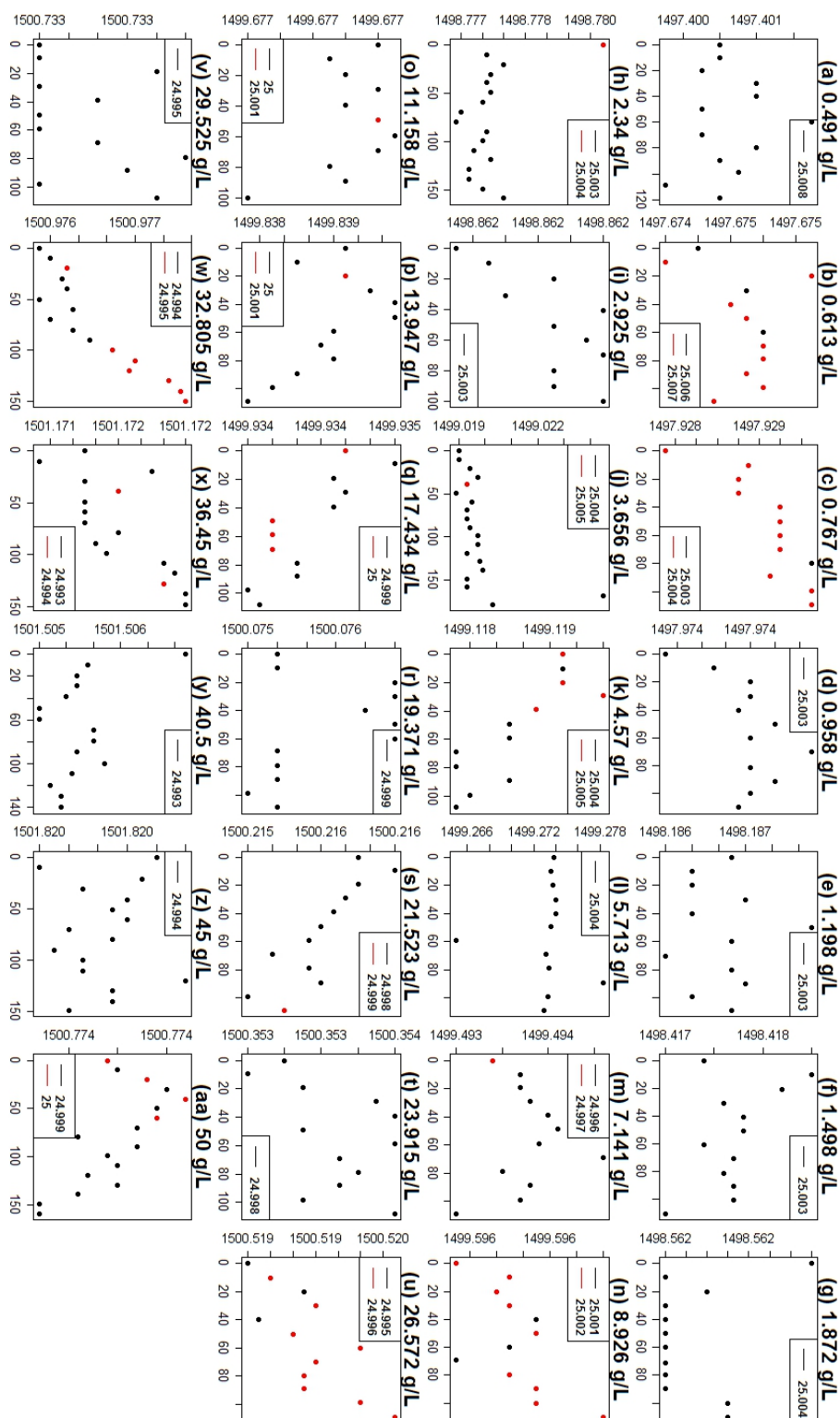


Figure C.3: Time (s) versus velocity (ms⁻¹) plots of C₁₂TAB/C₁₄TAB 2/1 M ultrasonic measurements. Titles indicate C₁₂TAB concentration, legends indicate measurement temperature in °C.

Appendix C. Supplementary Material for Ultrasonic Characterisation Studies

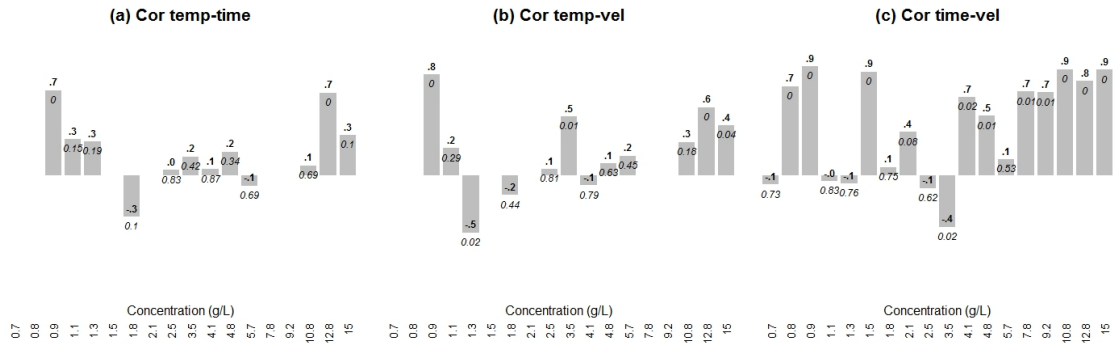


Figure C.4: Correlation plots of C₁₄TAB ultrasonic measurements. Temperature and velocity are abbreviated as ‘temp’ and ‘vel’ respectively. Pearson’s correlation and corresponding *p*-values are indicated in bold and italic respectively.

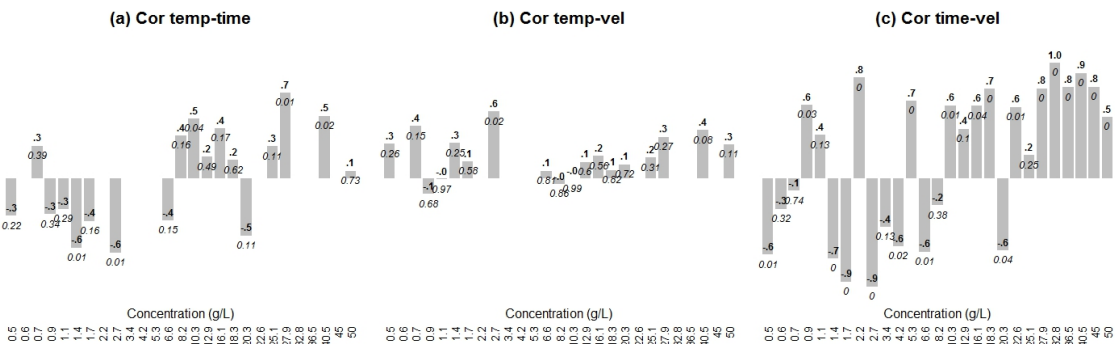


Figure C.5: Correlation plots of C₁₂TAB/C₁₄TAB 1/1 M ultrasonic measurements. Temperature and velocity are abbreviated as ‘temp’ and ‘vel’ respectively. Pearson’s correlation and corresponding *p*-values are indicated in bold and italic respectively.

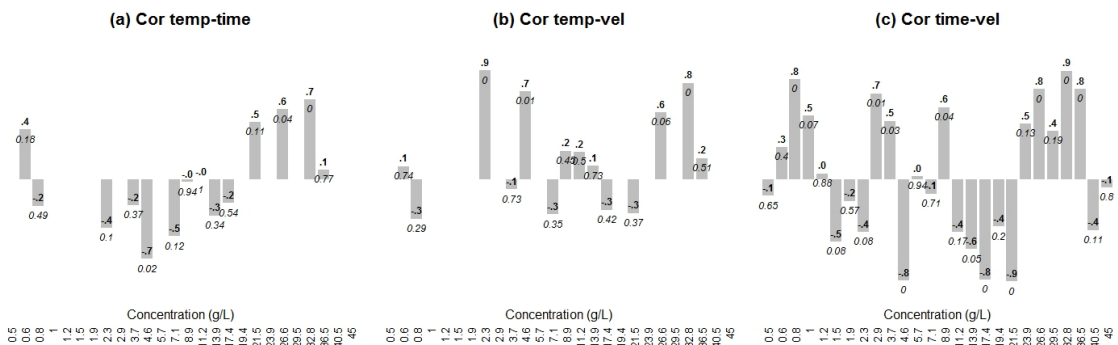


Figure C.6: Correlation plots of C₁₂TAB/C₁₄TAB 2/1 M ultrasonic measurements. Temperature and velocity are abbreviated as ‘temp’ and ‘vel’ respectively. Pearson’s correlation and corresponding *p*-values are indicated in bold and italic respectively.

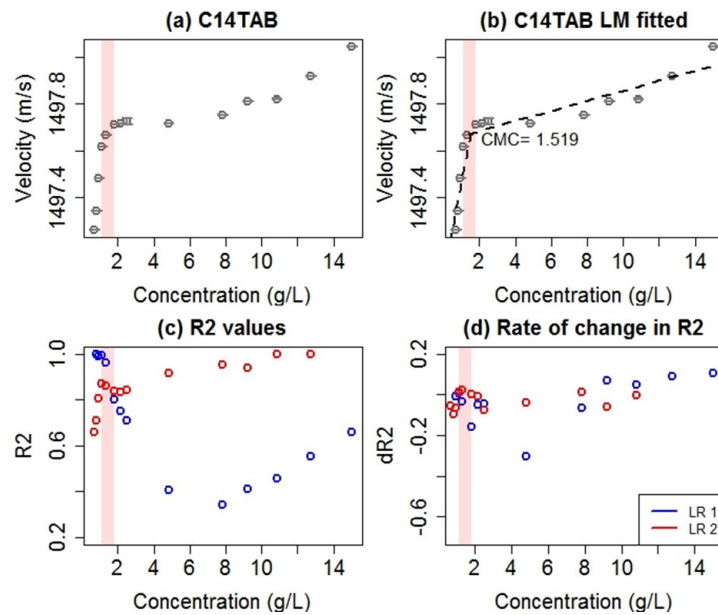


Figure C.7: Estimation of the CMC for C_{14} TAB. Red shading indicates the CMC region estimation, dashed lines in plots (b) and (c) indicate the corresponding fitted regressions.

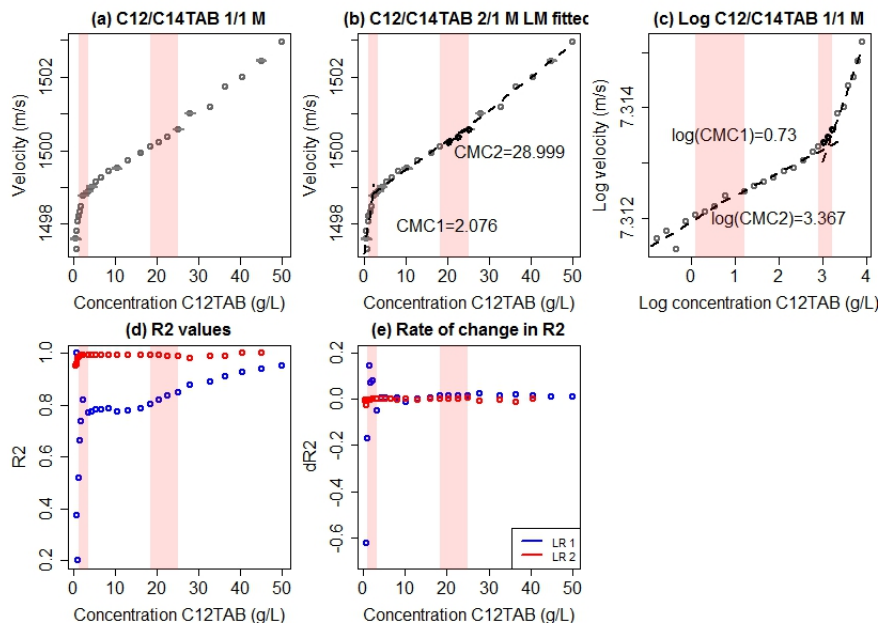


Figure C.8: Estimation of the CMC for C_{12} TAB/ C_{14} TAB 1/1 M. Red shading indicates the CMC region estimation, dashed lines in plot (b) and (c) indicate the corresponding fitted regressions.

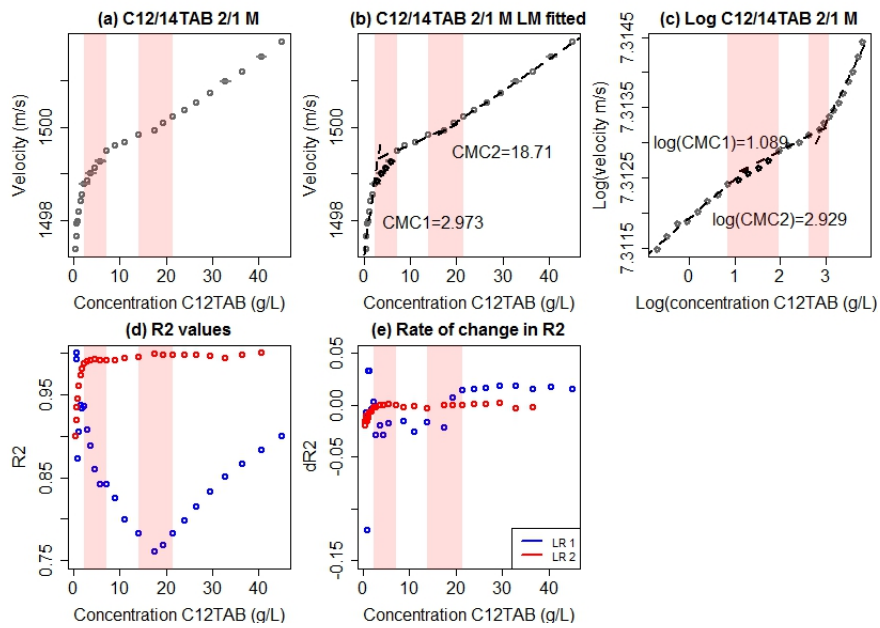


Figure C.9: Estimation of the CMC for $C_{12}TAB/C_{14}TAB$ 2/1 M. Red shading indicates the CMC region estimation, dashed lines in plot (b) indicate the corresponding fitted regressions.

C.2 Asphaltene diagnostic data

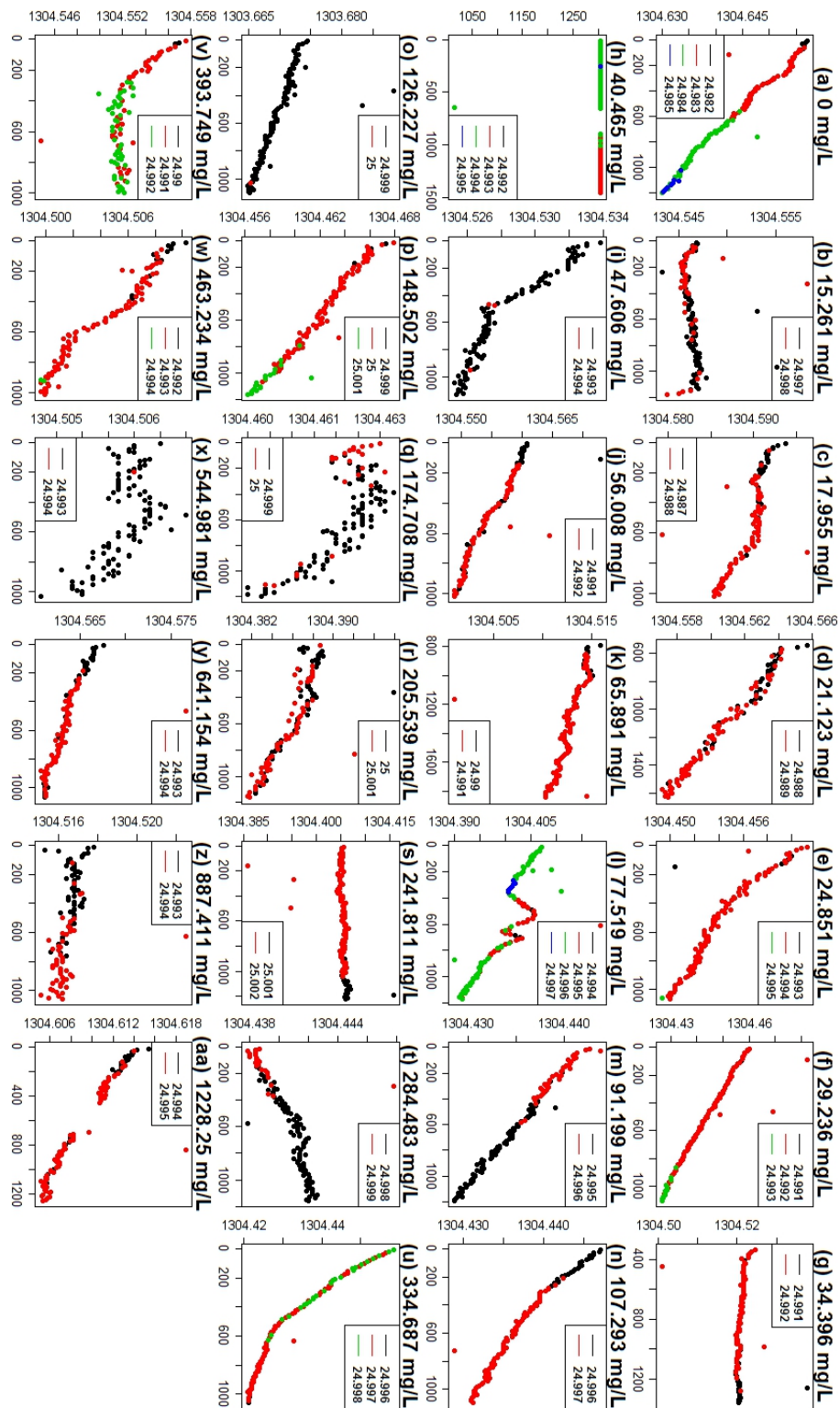


Figure C.11: Time versus velocity (m s^{-1}) plots of E3 asphaltene ultrasonic measurements. Titles indicate E3 concentration, legends indicate measurement temperature in $^{\circ}\text{C}$.

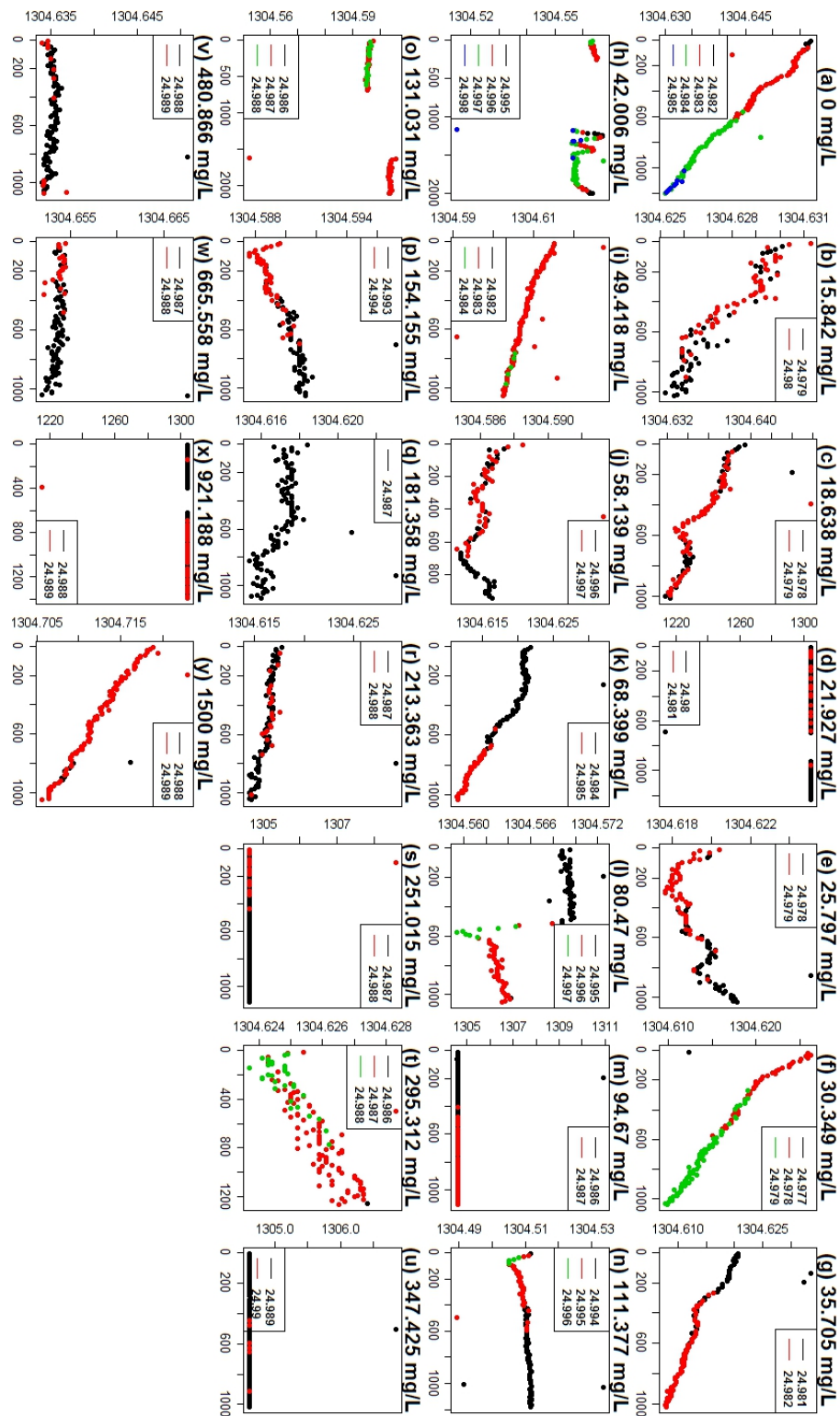


Figure C.12: Time versus velocity (m s^{-1}) plots of E4 asphaltene ultrasonic measurements. Titles indicate E4 concentration, legends indicate measurement temperature in $^{\circ}\text{C}$.

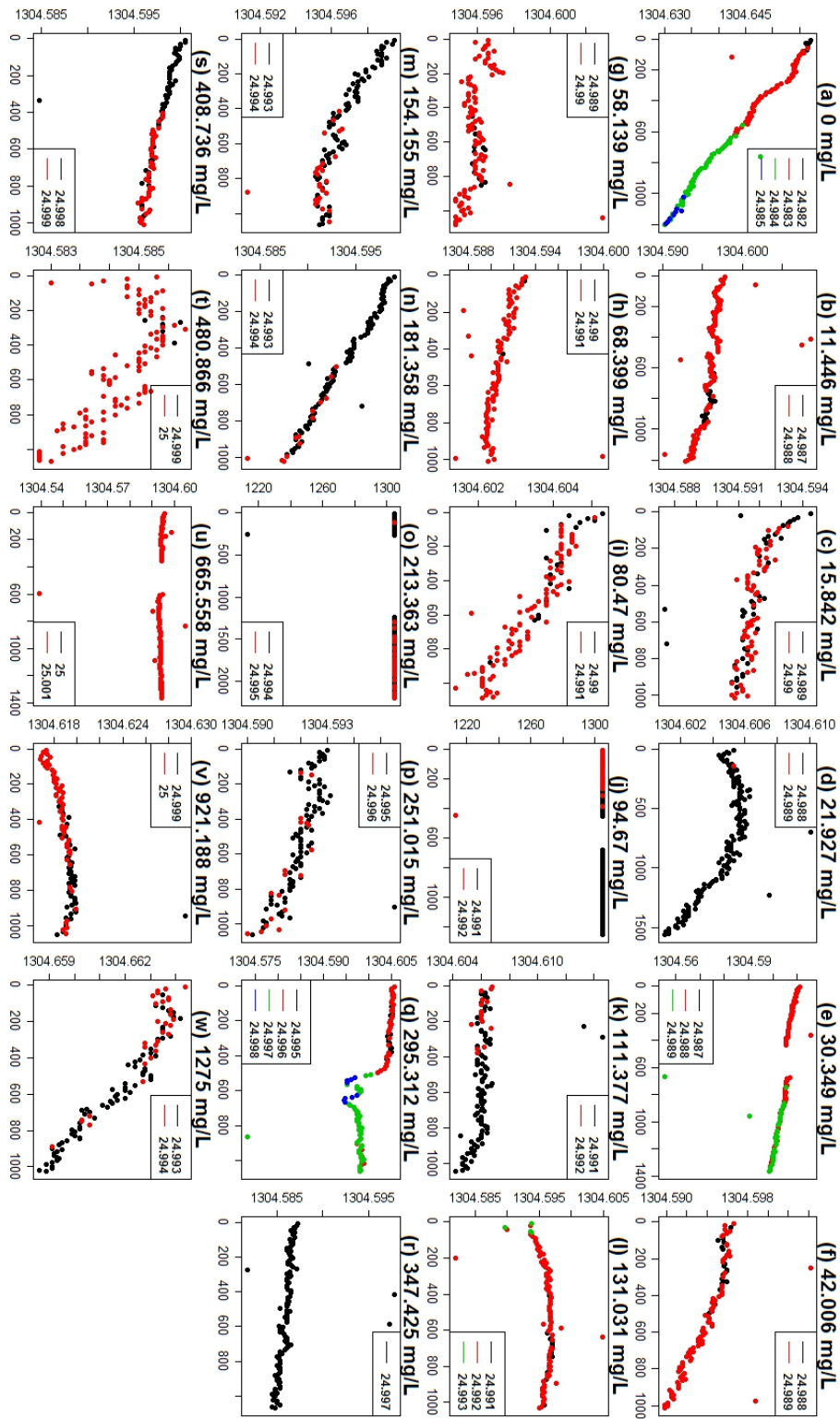


Figure C.13: Time versus velocity (m s^{-1}) plots of S1 asphaltene ultrasonic measurements. Titles indicate S1 concentration, legends indicate measurement temperature in $^{\circ}\text{C}$.

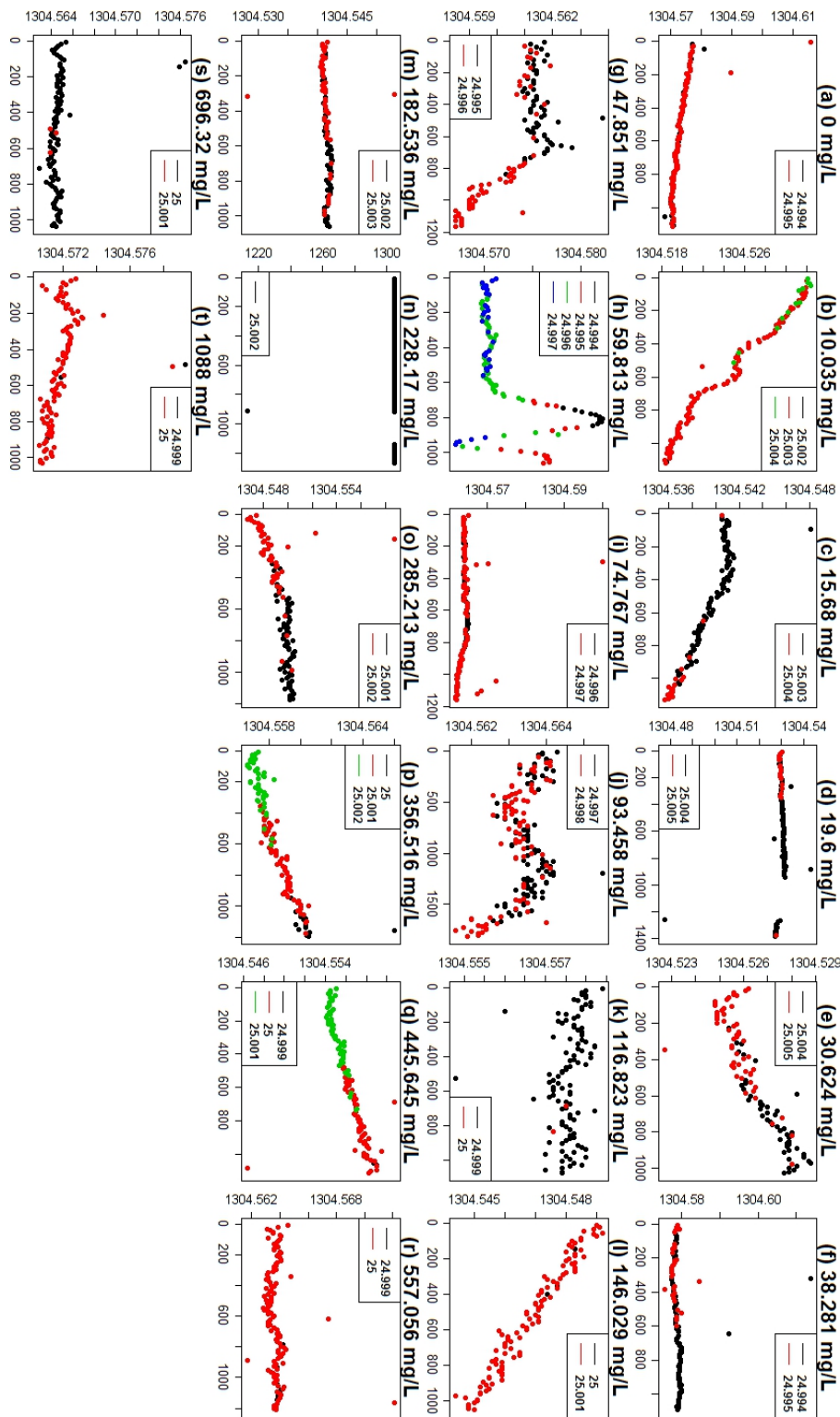


Figure C.14: Time versus velocity (m s^{-1}) plots of S3 asphaltene ultrasonic measurements. Titles indicate S3 concentration, legends indicate measurement temperature in $^{\circ}\text{C}$.

Appendix C. Supplementary Material for Ultrasonic Characterisation Studies

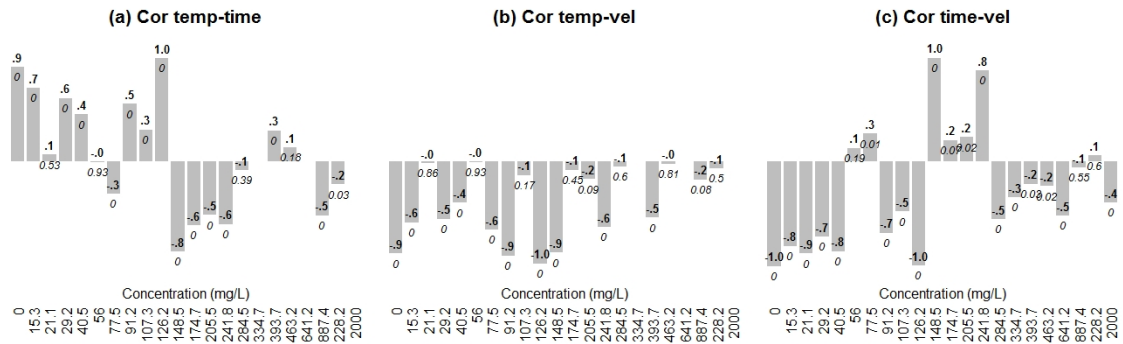


Figure C.15: Correlation plots of E2 asphaltene ultrasonic measurements. Temperature and velocity are abbreviated as 'temp' and 'vel' respectively. Pearson's correlation and corresponding p -values are indicated in bold and italic respectively.

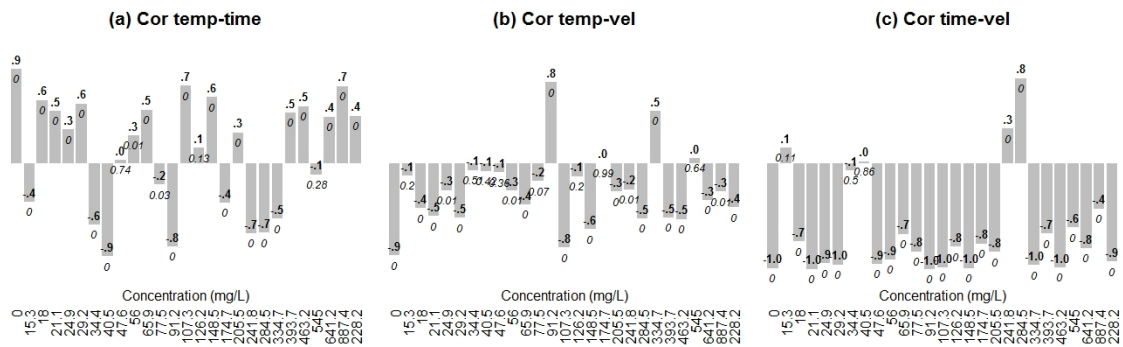


Figure C.16: Correlation plots of E3 asphaltene ultrasonic measurements. Temperature and velocity are abbreviated as 'temp' and 'vel' respectively. Pearson's correlation and corresponding p -values are indicated in bold and italic respectively.

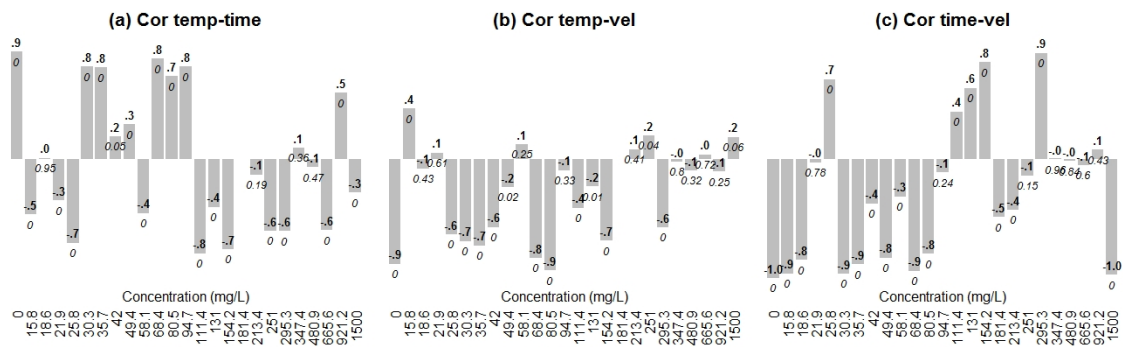


Figure C.17: Correlation plots of E4 asphaltene ultrasonic measurements. Temperature and velocity are abbreviated as 'temp' and 'vel' respectively. Pearson's correlation and corresponding p -values are indicated in bold and italic respectively.

Appendix C. Supplementary Material for Ultrasonic Characterisation Studies

Conc. (mg L ⁻¹)	P_1	w_2P_2	P_2	w_3P_3	P_3	R^2	R_p^2
21.123	0.220	0.126	0.013	9.00×10^{-4}	9.00×10^{-7}	0.720	0.375
29.236	0.220	0.000	0.000	1.00×10^{-4}	1.00×10^{-7}	0.724	0.501
40.465	0.230	0.000	0.000	1.00×10^{-4}	1.00×10^{-7}	0.717	0.488
56.008	0.240	0.000	0.000	1.00×10^{-4}	1.00×10^{-7}	0.712	0.477
65.891	0.240	0.000	0.000	4.00×10^{-4}	4.00×10^{-7}	0.705	0.462
77.519	0.250	0.000	0.000	4.00×10^{-4}	4.00×10^{-7}	0.708	0.458
91.199	0.260	0.000	0.000	9.00×10^{-4}	9.00×10^{-7}	0.708	0.449
107.293	0.270	0.257	0.026	2.80×10^{-3}	2.80×10^{-6}	0.725	0.198
126.227	0.280	0.000	0.000	8.00×10^{-4}	8.00×10^{-7}	0.868	0.590
148.502	0.290	0.000	0.000	1.20×10^{-3}	1.20×10^{-6}	0.865	0.576
174.708	0.300	0.000	0.000	9.00×10^{-4}	9.00×10^{-7}	0.867	0.565
205.539	0.320	0.000	0.000	4.00×10^{-4}	4.00×10^{-7}	0.875	0.558
241.811	0.330	0.000	0.000	1.00×10^{-4}	1.00×10^{-7}	0.870	0.536
284.484	0.350	0.000	0.000	8.00×10^{-4}	8.00×10^{-7}	0.859	0.505
334.686	0.380	0.106	0.011	2.60×10^{-3}	2.60×10^{-6}	0.855	0.368
393.749	0.410	0.159	0.016	4.70×10^{-3}	4.70×10^{-6}	0.886	0.314
463.234	0.450	0.103	0.010	4.00×10^{-3}	4.00×10^{-6}	0.959	0.406
641.154	0.500	0.080	0.008	4.20×10^{-3}	4.20×10^{-6}	-5.000	-5.000
887.411	0.580	0.020	0.002	1.50×10^{-3}	1.50×10^{-6}	-5.000	-5.000

Table C.1: Constrained nanoaggregation region estimation of E1 asphaltene, aggregated boundary selection using constrained optimisation. The length, outlier and slope penalties are abbreviated P_1 , P_2 and P_3 respectively. Grey shading indicates concentrations with the highest R^2 and R_p^2 .

Conc. (mg L ⁻¹)	P_1	w_2P_2	P_2	w_3P_3	P_3	R^2	R_p^2
29.236	0.580	0.132	0.013	0.986	9.86×10^{-4}	-5.000	-5.000
40.465	0.500	0.000	0.000	0.060	5.95×10^{-5}	-5.000	-5.000
56.008	0.450	0.287	0.029	0.642	6.42×10^{-4}	0.162	-1.214
77.519	0.410	0.000	0.000	0.048	4.77×10^{-5}	0.229	-0.227
91.199	0.380	0.000	0.000	0.025	2.53×10^{-5}	0.415	0.012
107.293	0.350	0.000	0.000	0.007	7.40×10^{-6}	0.516	0.155
126.227	0.330	0.190	0.019	0.095	9.48×10^{-5}	0.680	0.062
148.502	0.320	0.189	0.019	0.076	7.55×10^{-5}	0.782	0.201
174.708	0.300	0.000	0.000	0.005	5.10×10^{-6}	0.839	0.533
205.539	0.290	0.233	0.023	0.062	6.15×10^{-5}	0.779	0.195
241.811	0.280	0.157	0.016	0.034	3.40×10^{-5}	0.778	0.310
284.484	0.270	0.712	0.071	0.127	1.27×10^{-4}	0.255	-0.851
334.686	0.260	0.491	0.049	0.072	7.19×10^{-5}	0.063	-0.759
393.749	0.250	0.000	0.000	0.035	3.50×10^{-5}	0.010	-0.275
463.234	0.240	0.276	0.028	0.028	2.75×10^{-5}	0.004	-0.542
641.154	0.240	0.315	0.032	0.028	2.76×10^{-5}	0.086	-0.492
887.411	0.230	0.000	0.000	0.003	3.20×10^{-6}	0.175	-0.058

Table C.2: Constrained nanoaggregation region estimation of E2 asphaltene, monomeric boundary selection using constrained optimisation, $w_2 = 10$, $w_3 = 1000$. The length, outlier and slope penalties are abbreviated P_1 , P_2 and P_3 respectively. Grey shading indicates concentrations with the highest R^2 and R_p^2 .

Appendix C. Supplementary Material for Ultrasonic Characterisation Studies

Conc. (mg L ⁻¹)	P_1	w_2P_2	P_2	w_3P_3	P_3	R^2	R_p^2
29.236	0.230	0.000	0.000	1.70×10^{-3}	1.70×10^{-6}	0.557	0.325
40.465	0.240	0.000	0.000	1.00×10^{-3}	1.00×10^{-6}	0.585	0.348
56.008	0.240	0.281	0.028	2.60×10^{-3}	2.60×10^{-6}	0.592	0.066
77.519	0.250	0.000	0.000	1.90×10^{-3}	1.90×10^{-6}	0.641	0.389
91.199	0.260	0.000	0.000	1.50×10^{-3}	1.50×10^{-6}	0.668	0.408
107.293	0.270	0.000	0.000	1.70×10^{-3}	1.70×10^{-6}	0.682	0.413
126.227	0.280	0.000	0.000	1.20×10^{-3}	1.20×10^{-6}	0.696	0.417
148.502	0.290	0.293	0.029	3.80×10^{-3}	3.80×10^{-6}	0.678	0.092
174.708	0.300	0.320	0.032	4.60×10^{-3}	4.60×10^{-6}	0.674	0.047
205.539	0.320	0.000	0.000	4.20×10^{-3}	4.20×10^{-6}	0.678	0.358
241.811	0.330	0.455	0.045	8.10×10^{-3}	8.10×10^{-6}	0.672	-0.125
284.484	0.350	0.000	0.000	1.00×10^{-3}	1.00×10^{-6}	0.902	0.547
334.686	0.380	0.000	0.000	5.00×10^{-4}	5.00×10^{-7}	0.905	0.526
393.749	0.410	0.000	0.000	2.20×10^{-3}	2.20×10^{-6}	0.895	0.485
463.234	0.450	0.000	0.000	1.10×10^{-3}	1.10×10^{-6}	0.878	0.430
641.154	0.500	0.164	0.016	8.50×10^{-3}	8.50×10^{-6}	-5.000	-5.000
887.411	0.580	0.125	0.013	9.30×10^{-3}	9.30×10^{-6}	-5.000	-5.000

Table C.3: Constrained nanoaggregation region estimation of E2 asphaltene, aggregated boundary selection using constrained optimisation, $w_2 = 10, w_3 = 1000$. The length, outlier and slope penalties are abbreviated P_1 , P_2 and P_3 respectively. Grey shading indicates concentrations with the highest R^2 and R_p^2 .

Conc. (mg L ⁻¹)	P_1	w_2P_2	P_2	w_3P_3	P_3	R^2	R_p^2
17.955	0.580	0.060	0.006	2.214	2.21×10^{-3}	-5.000	-5.000
21.123	0.500	0.000	0.000	0.267	2.67×10^{-4}	-5.000	-5.000
24.851	0.450	0.087	0.009	2.160	2.16×10^{-3}	0.690	-2.005
29.236	0.410	0.000	0.000	0.789	7.89×10^{-4}	0.780	-0.418
34.396	0.380	0.093	0.009	1.748	1.75×10^{-3}	0.617	-1.603
40.465	0.350	0.088	0.009	1.417	1.42×10^{-3}	0.469	-1.389
47.606	0.330	0.083	0.008	1.118	1.12×10^{-3}	0.337	-1.198
56.008	0.320	0.097	0.010	1.077	1.08×10^{-3}	0.166	-1.325
65.891	0.300	0.000	0.000	0.278	2.78×10^{-4}	0.161	-0.419
77.519	0.290	0.000	0.000	0.598	5.98×10^{-4}	0.365	-0.522
91.199	0.280	0.000	0.000	0.062	6.17×10^{-5}	0.445	0.106
107.293	0.270	0.000	0.000	0.178	1.78×10^{-4}	0.484	0.039
126.227	0.260	0.717	0.072	2.891	2.89×10^{-3}	0.510	-3.356
148.502	0.250	0.442	0.044	1.460	1.46×10^{-3}	0.339	-1.813
174.708	0.240	0.358	0.036	0.971	9.71×10^{-4}	0.226	-1.346
205.539	0.240	0.214	0.021	0.478	4.78×10^{-4}	0.190	-0.737
241.811	0.230	0.213	0.021	0.392	3.92×10^{-4}	0.152	-0.687
284.484	0.220	0.221	0.022	0.337	3.37×10^{-4}	0.108	-0.674
334.687	0.220	0.176	0.018	0.223	2.23×10^{-4}	0.081	-0.536
393.749	0.210	0.269	0.027	0.283	2.83×10^{-4}	0.029	-0.737
463.234	0.210	0.000	0.000	0.131	1.31×10^{-4}	0.012	-0.327
544.981	0.200	0.000	0.000	0.083	8.27×10^{-5}	0.004	-0.283
641.154	0.200	0.000	0.000	0.085	8.53×10^{-5}	0.000	-0.285

Table C.4: Constrained nanoaggregation region estimation of E3 asphaltene, monomeric boundary selection using constrained optimisation, $w_2 = 1$, $w_3 = 1000$. The length, outlier and slope penalties are abbreviated P_1 , P_2 and P_3 respectively. Grey shading indicates concentrations with the highest R^2 and R_p^2 .

Conc. (mg L ⁻¹)	P_1	w_2P_2	P_2	w_3P_3	P_3	R^2	R_p^2
17.955	0.200	0.169	0.017	0.018	1.80×10^{-5}	0.041	-0.343
21.123	0.200	0.151	0.015	0.017	1.69×10^{-5}	0.055	-0.317
24.851	0.210	0.000	0.000	0.006	5.50×10^{-6}	0.068	-0.146
29.236	0.210	0.000	0.000	0.005	4.60×10^{-6}	0.071	-0.147
34.396	0.220	0.000	0.000	0.017	1.67×10^{-5}	0.073	-0.162
40.465	0.220	0.000	0.000	0.020	1.98×10^{-5}	0.086	-0.158
47.606	0.230	0.000	0.000	0.024	2.39×10^{-5}	0.102	-0.151
56.008	0.240	0.202	0.020	0.033	3.30×10^{-5}	0.124	-0.346
65.891	0.240	0.177	0.018	0.031	3.11×10^{-5}	0.159	-0.291
77.519	0.250	0.000	0.000	0.013	1.31×10^{-5}	0.192	-0.072
91.199	0.260	0.000	0.000	0.024	2.36×10^{-5}	0.197	-0.085
107.293	0.270	0.000	0.000	0.029	2.92×10^{-5}	0.214	-0.082
126.227	0.280	0.762	0.076	0.188	1.88×10^{-4}	0.236	-0.991
148.502	0.290	0.000	0.000	0.009	8.90×10^{-6}	0.634	0.337
174.708	0.300	0.000	0.000	0.011	1.05×10^{-5}	0.647	0.335
205.539	0.320	0.060	0.006	0.020	2.02×10^{-5}	0.662	0.266
241.811	0.330	0.060	0.006	0.023	2.28×10^{-5}	0.623	0.208
284.484	0.350	0.000	0.000	0.018	1.82×10^{-5}	0.571	0.199
334.687	0.380	0.080	0.008	0.041	4.08×10^{-5}	0.491	-0.007
393.749	0.410	0.054	0.005	0.033	3.31×10^{-5}	0.400	-0.096
463.234	0.450	0.000	0.000	0.003	2.50×10^{-6}	0.621	0.171
544.981	0.500	0.000	0.000	0.024	2.38×10^{-5}	-5.000	-5.000
641.154	0.580	0.114	0.011	0.182	1.82×10^{-4}	-5.000	-5.000

Table C.5: Constrained nanoaggregation region estimation of E3 asphaltene, aggregated boundary selection using constrained optimisation, $w_2 = 1$, $w_3 = 1000$. The length, outlier and slope penalties are abbreviated P_1 , P_2 and P_3 respectively. Grey shading indicates concentrations with the highest R^2 and R_p^2 .

Conc. (mg L ⁻¹)	P_1	w_2P_2	P_2	w_3P_3	P_3	R^2	R_p^2
18.638	0.580	0.104	0.010	0.37	3.66×10^{-4}	-5.000	-5.000
21.927	0.500	0.101	0.010	0.28	2.79×10^{-4}	-5.000	-5.000
25.797	0.450	0.000	0.000	0.04	3.52×10^{-5}	0.773	0.291
30.349	0.410	0.000	0.000	0.01	1.15×10^{-5}	0.824	0.404
35.705	0.380	0.000	0.000	0.04	4.12×10^{-5}	0.857	0.438
42.006	0.350	0.463	0.046	0.72	7.15×10^{-4}	0.686	-0.846
49.418	0.330	0.321	0.032	0.41	4.14×10^{-4}	0.553	-0.515
58.139	0.320	0.000	0.000	0.08	8.02×10^{-5}	0.615	0.218
68.399	0.300	0.470	0.047	0.41	4.11×10^{-4}	0.364	-0.818
80.470	0.290	0.000	0.000	0.10	1.04×10^{-4}	0.524	0.131
94.670	0.280	0.434	0.043	0.25	2.53×10^{-4}	0.366	-0.598
111.377	0.270	0.613	0.061	0.29	2.92×10^{-4}	0.576	-0.596
131.031	0.260	0.674	0.067	0.26	2.62×10^{-4}	0.403	-0.791
154.155	0.250	0.463	0.046	0.15	1.48×10^{-4}	0.326	-0.535
181.358	0.240	0.679	0.068	0.18	1.78×10^{-4}	0.160	-0.939
213.363	0.240	0.506	0.051	0.11	1.09×10^{-4}	0.072	-0.778
251.015	0.230	0.540	0.054	0.10	9.58×10^{-5}	0.009	-0.856
295.312	0.220	0.000	0.000	0.04	4.43×10^{-5}	0.000	-0.268
347.425	0.220	0.000	0.000	0.02	1.74×10^{-5}	0.004	-0.231
480.866	0.210	0.000	0.000	0.02	2.30×10^{-5}	0.032	-0.204
665.558	0.210	0.000	0.000	0.02	1.93×10^{-5}	0.112	-0.116

Table C.6: Constrained nanoaggregation region estimation of E4 asphaltene, monomeric boundary selection using constrained optimisation, $w_2 = 10, w_3 = 1000$. The length, outlier and slope penalties are abbreviated P_1 , P_2 and P_3 respectively. Grey shading indicates concentrations with the highest R^2 and R_p^2 .

Appendix C. Supplementary Material for Ultrasonic Characterisation Studies

Conc. (mg L ⁻¹)	P_1	w_2P_2	P_2	w_3P_3	P_3	R^2	R_p^2
18.638	0.210	0.421	0.042	3.60×10^{-3}	3.60×10^{-6}	0.520	-0.113
21.927	0.210	0.272	0.027	2.40×10^{-3}	2.40×10^{-6}	0.564	0.076
25.797	0.220	0.294	0.029	2.80×10^{-3}	2.80×10^{-6}	0.585	0.070
30.349	0.220	0.283	0.028	2.80×10^{-3}	2.80×10^{-6}	0.609	0.099
35.705	0.230	0.270	0.027	2.80×10^{-3}	2.80×10^{-6}	0.631	0.129
42.006	0.240	0.000	0.000	3.30×10^{-3}	3.30×10^{-6}	0.651	0.413
49.418	0.240	0.000	0.000	2.30×10^{-3}	2.30×10^{-6}	0.644	0.399
58.139	0.250	0.000	0.000	4.00×10^{-4}	4.00×10^{-7}	0.655	0.405
68.399	0.260	0.299	0.030	4.10×10^{-3}	4.10×10^{-6}	0.644	0.0826
80.470	0.270	0.000	0.000	3.70×10^{-3}	3.70×10^{-6}	0.672	0.401
94.670	0.280	0.000	0.000	2.60×10^{-3}	2.60×10^{-6}	0.657	0.377
111.377	0.290	0.956	0.096	1.66×10^{-2}	1.66×10^{-5}	0.662	-0.599
131.031	0.300	0.000	0.000	1.80×10^{-3}	1.80×10^{-6}	0.932	0.628
154.155	0.320	0.248	0.025	5.30×10^{-3}	5.30×10^{-6}	0.931	0.361
181.358	0.330	0.000	0.000	1.00×10^{-4}	1.00×10^{-7}	0.974	0.640
213.363	0.350	0.000	0.000	9.00×10^{-4}	9.00×10^{-7}	0.971	0.616
251.015	0.380	0.138	0.014	4.40×10^{-3}	4.40×10^{-6}	0.968	0.448
295.312	0.410	0.055	0.005	2.20×10^{-3}	2.20×10^{-6}	0.990	0.525
347.425	0.450	0.067	0.007	3.50×10^{-3}	3.50×10^{-6}	0.992	0.474
480.866	0.500	0.041	0.004	2.80×10^{-3}	2.80×10^{-6}	-5.000	-5.0000
665.558	0.580	0.047	0.005	4.60×10^{-3}	4.60×10^{-6}	-5.000	-5.0000

Table C.7: Constrained nanoaggregation region estimation of E4 asphaltene, aggregated boundary selection using constrained optimisation, $w_2 = 10, w_3 = 1000$. The length, outlier and slope penalties are abbreviated P_1 , P_2 and P_3 respectively. Grey shading indicates concentrations with the highest R^2 and R_p^2 .



Figure C.18: Barplot of the CNR_1 and CNR_2 estimation of E3 asphaltene as a function of varying penalty weights.



Figure C.19: Barplot of the CNR_1 and CNR_2 estimation of E4 asphaltene as a function of varying penalty weights.

Appendix D. Supplementary Material for the Empirical Bayesian Inference of the Apshaltene Critical Nanoaggregation Region

D.1 Synthetic data

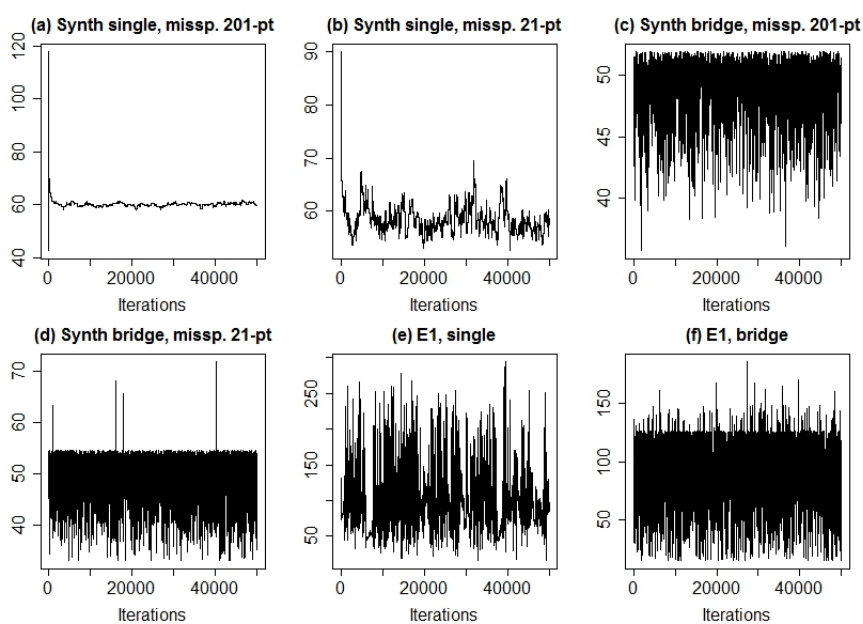


Figure D.1: MCMC traces of the initial 5×10^4 simulations of γ (a,b,e) or γ_1 (c,d,f). In plots (a-d) synth. and missp. abbreviates synthetic and misspecified.

Appendix D. Supplementary Material for the Empirical Bayesian Inference of the Apshaltene Critical Nanoaggregation Region

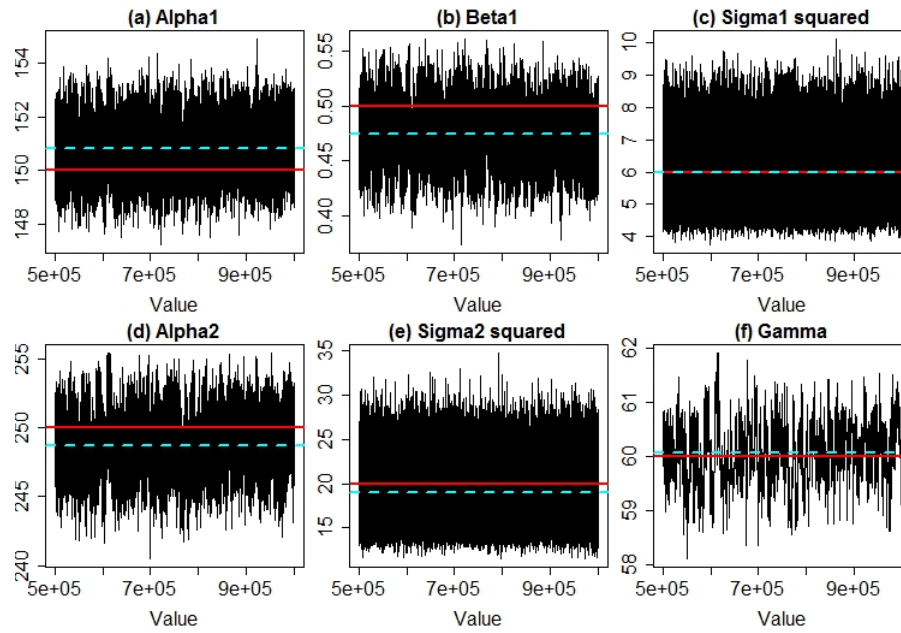


Figure D.2: MCMC trace plots of the one-changepoint model using 201-point synthetic data, prior means are set at the true parameter values. Solid red and dashed cyan lines indicate prior and posterior means respectively.

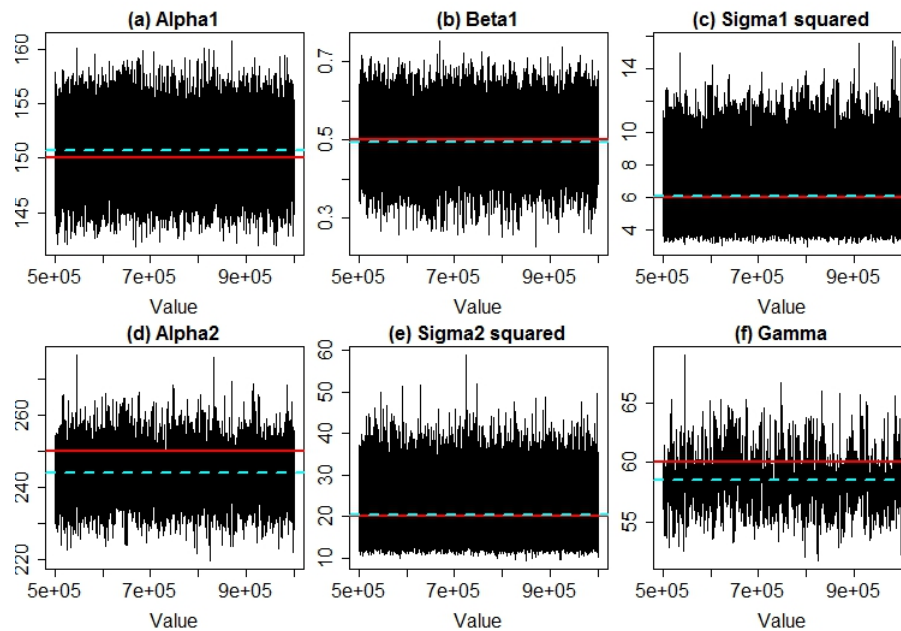


Figure D.3: MCMC trace plots of the one-changepoint model using 21-point synthetic data, prior means are set at the true parameter values. Solid red and dashed cyan lines indicate prior and posterior means respectively.

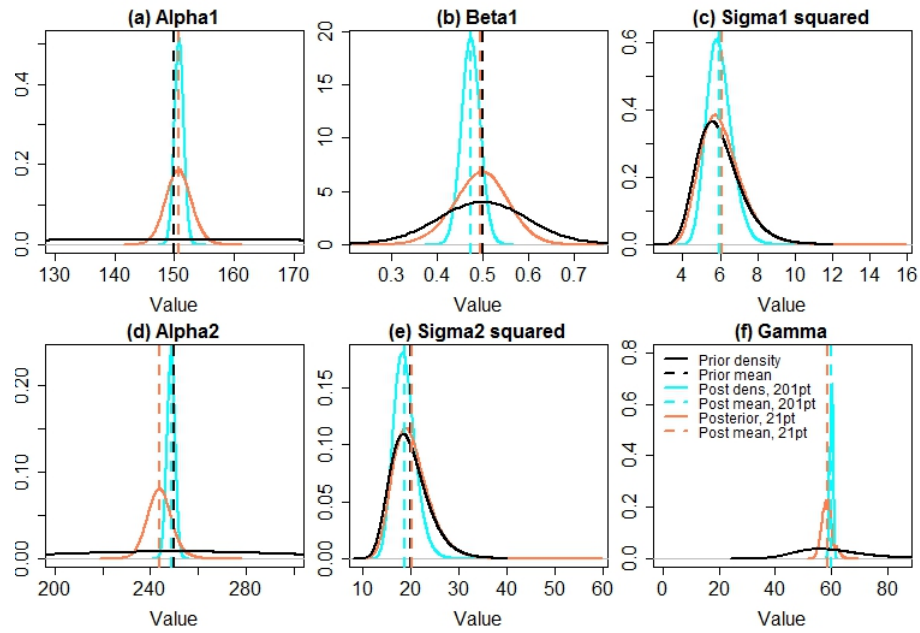


Figure D.4: Posterior density plots of the one-change point model using synthetic data, prior means are set at the true parameter values. In the legend, data obtained using the 201-point and 21-point data sets are abbreviated '201pt' and '21pt'.

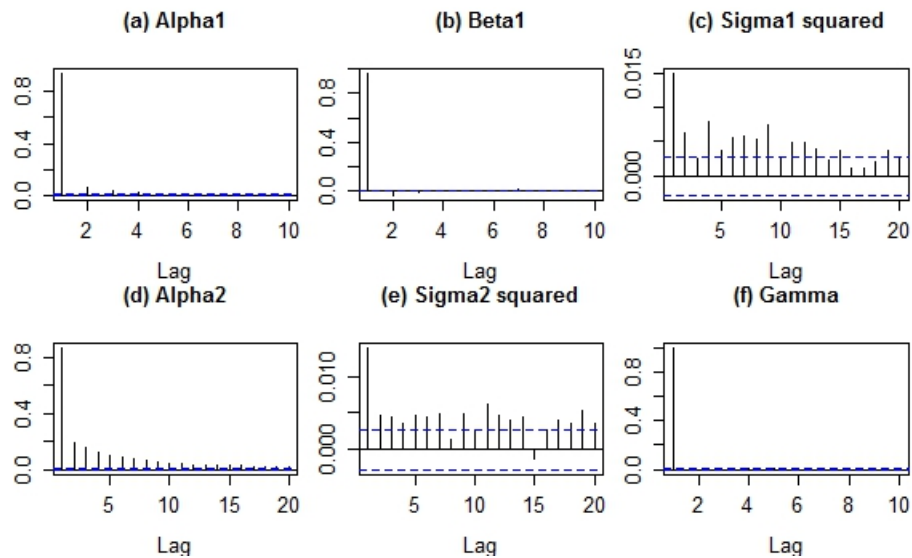


Figure D.5: Plots of the partial autocorrelation function for the 201-point synthetic data set posterior conditional marginal draws assuming a single-change point underlying model, prior means are set at true parameter values.

Appendix D. Supplementary Material for the Empirical Bayesian Inference of the Apshaltene Critical Nanoaggregation Region

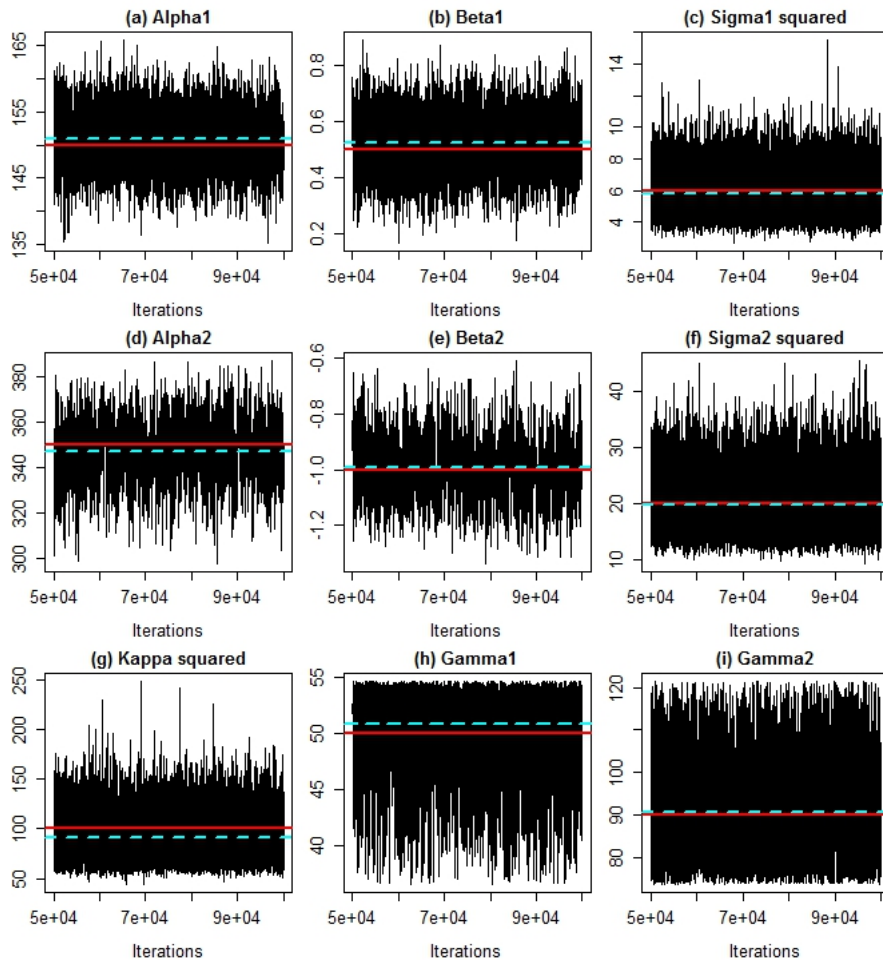


Figure D.6: MCMC trace plots of the Brownian bridge model using 21-point synthetic data, prior means are set at the true parameter values. Solid red and dashed cyan lines indicate prior and posterior means respectively.

Appendix D. Supplementary Material for the Empirical Bayesian Inference of the Apshaltene Critical Nanoaggregation Region

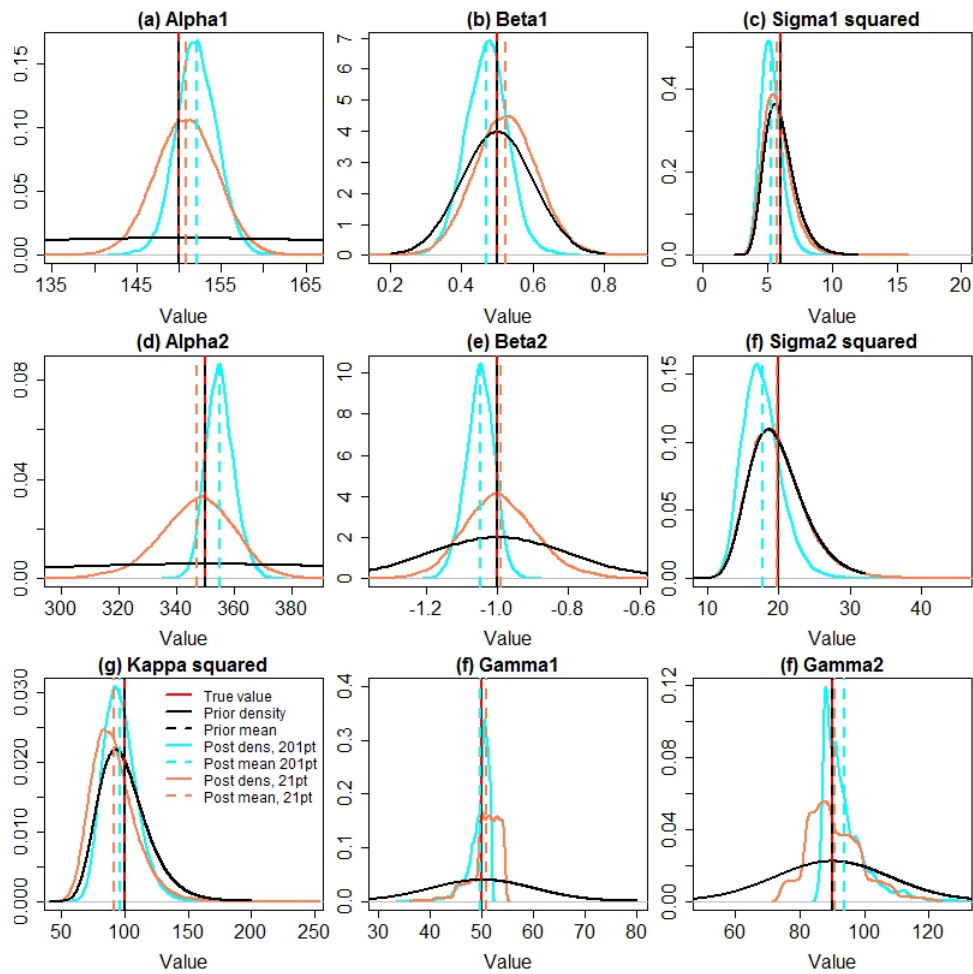


Figure D.7: Posterior density plots of the Brownian bridge using synthetic data, prior means are set at true parameter value, orange and cyan vertical lines indicate density means.

Appendix D. Supplementary Material for the Empirical Bayesian Inference of the Apshaltene Critical Nanoaggregation Region

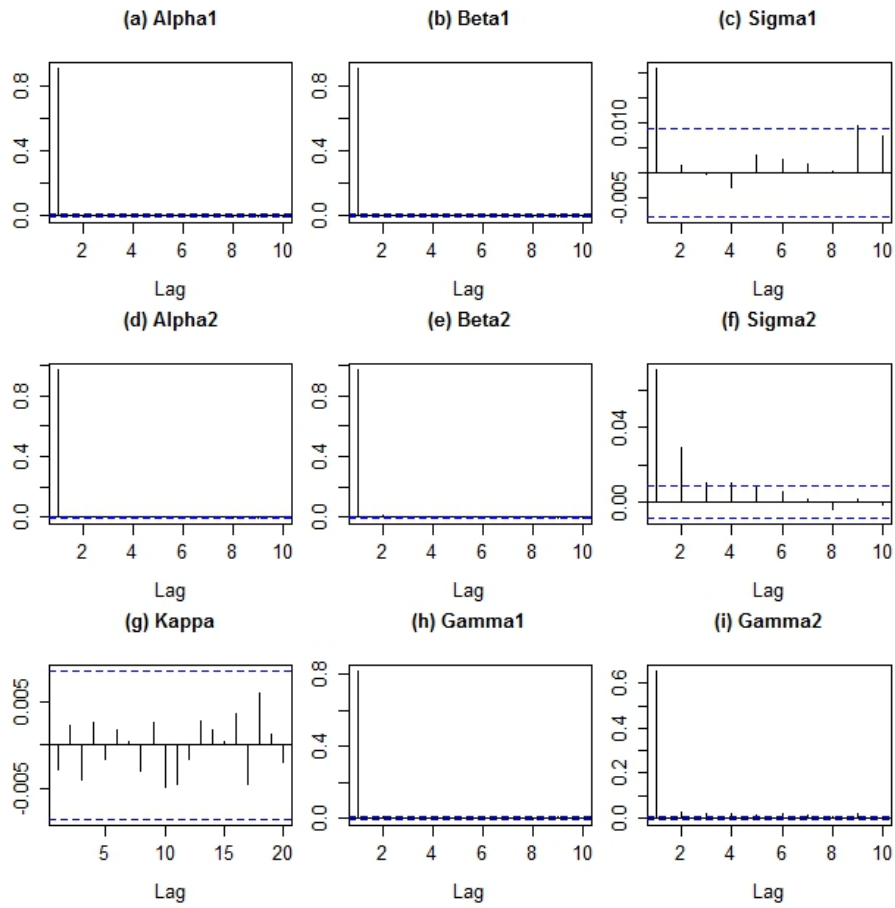


Figure D.8: Plots of the partial autocorrelation function for the 201-point synthetic data set posterior conditional marginal draws assuming a Brownian bridge underlying model, prior means are set at true parameter values.

D.2 Sample data

D.2.1 One-changepoint model

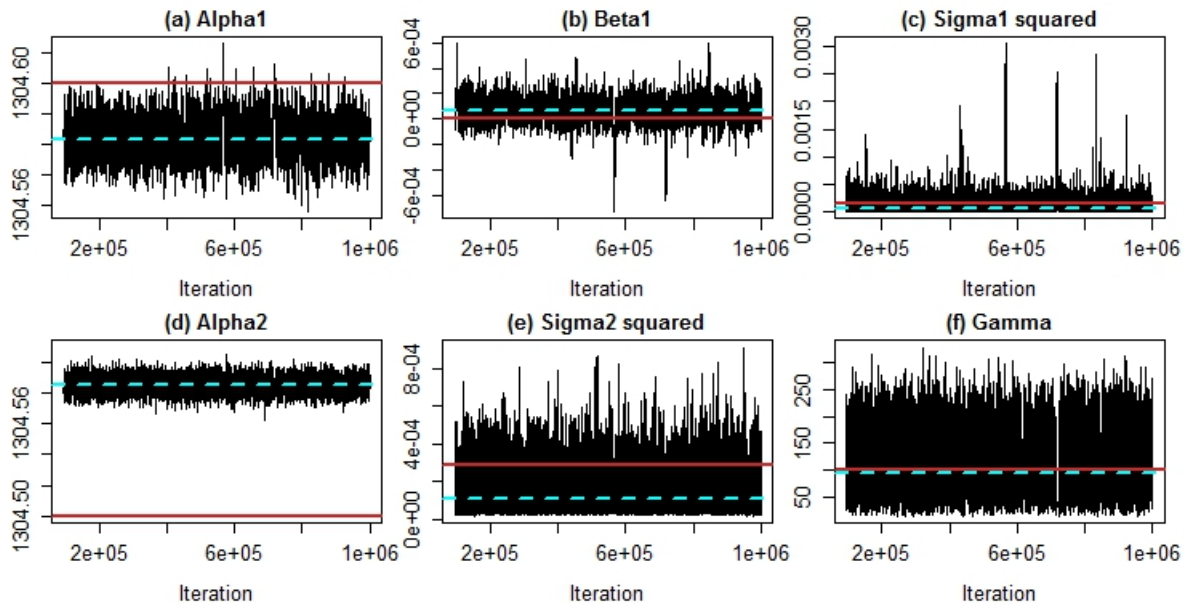


Figure D.9: Chain mixing plots of the MCMC sampling from the conditional posterior distributions of the single changepoint model of E1 asphaltene.

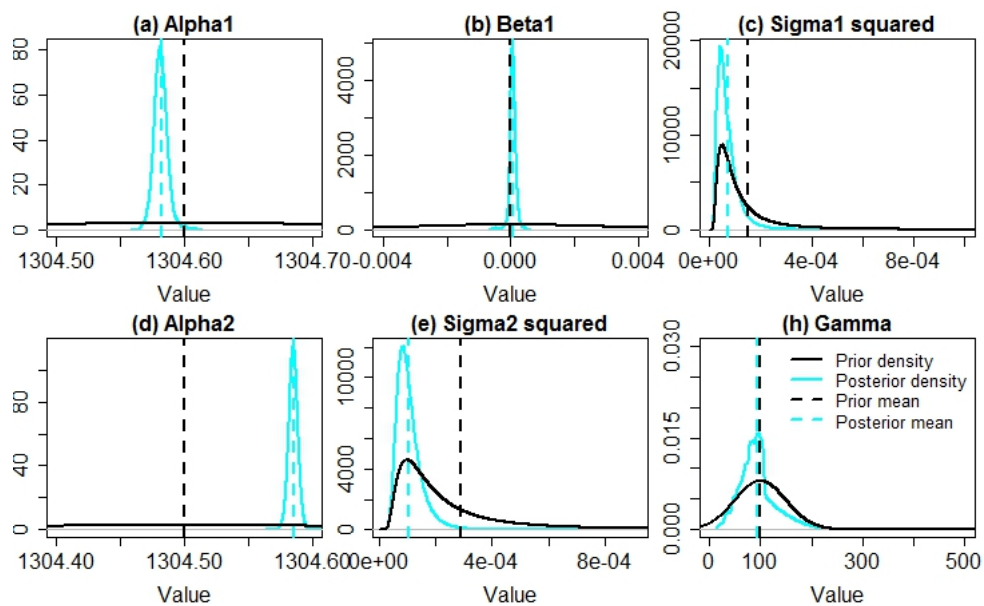


Figure D.10: Conditional posterior density plots of the single changepoint model of E1 asphaltene. Solid red and dashed cyan lines indicate prior and posterior means respectively.

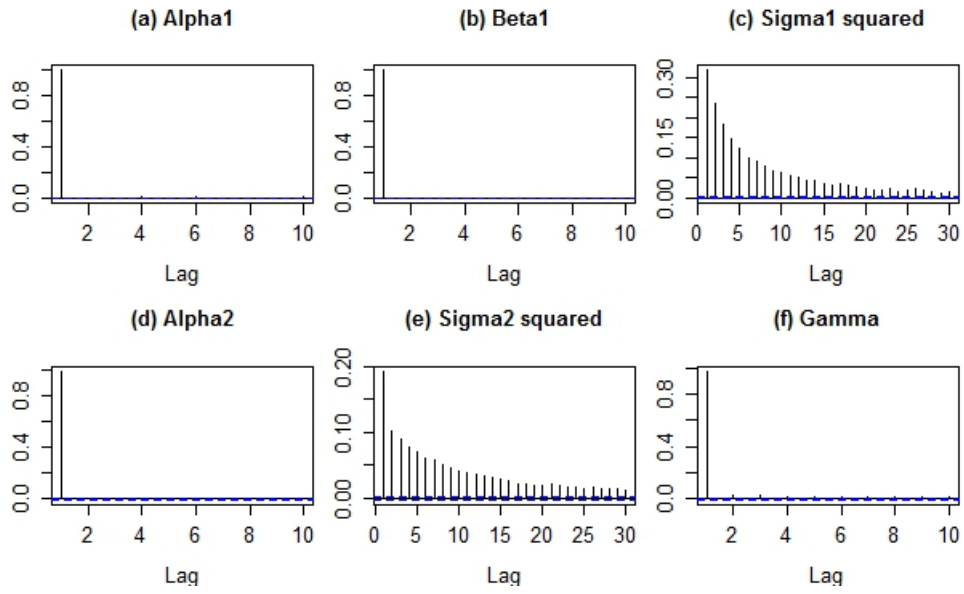


Figure D.11: Partial autocorrelation plots of the MCMC sampling from the conditional posterior distributions of the single changepoint model of E1 asphaltene.

D.2.2 Brownian bridge model

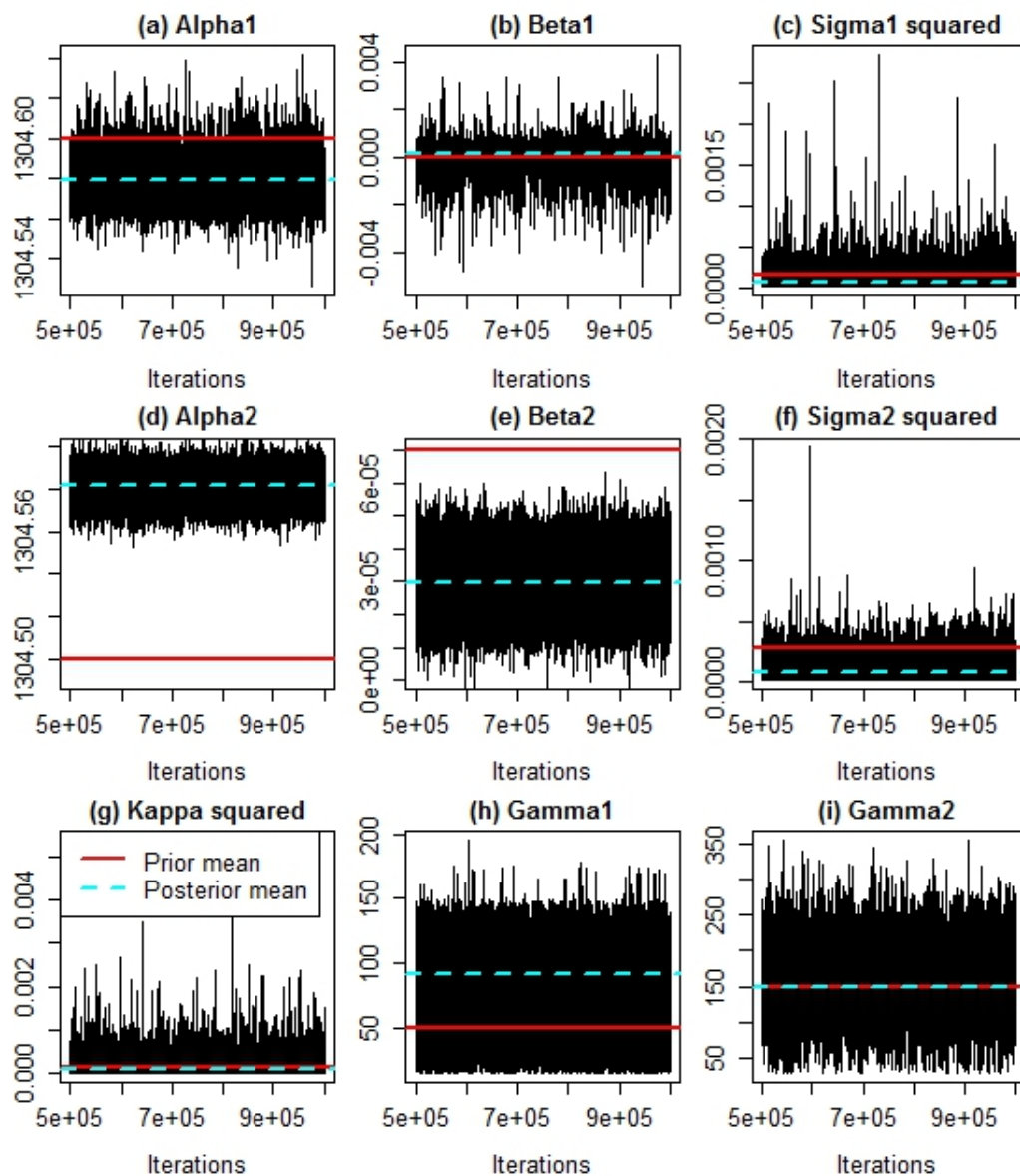


Figure D.12: Chain mixing plots of the MCMC sampling from the conditional posterior distributions of the Brownian bridge model of E1 asphaltene. Solid red and dashed cyan lines indicate prior and posterior means respectively.

%endfigure

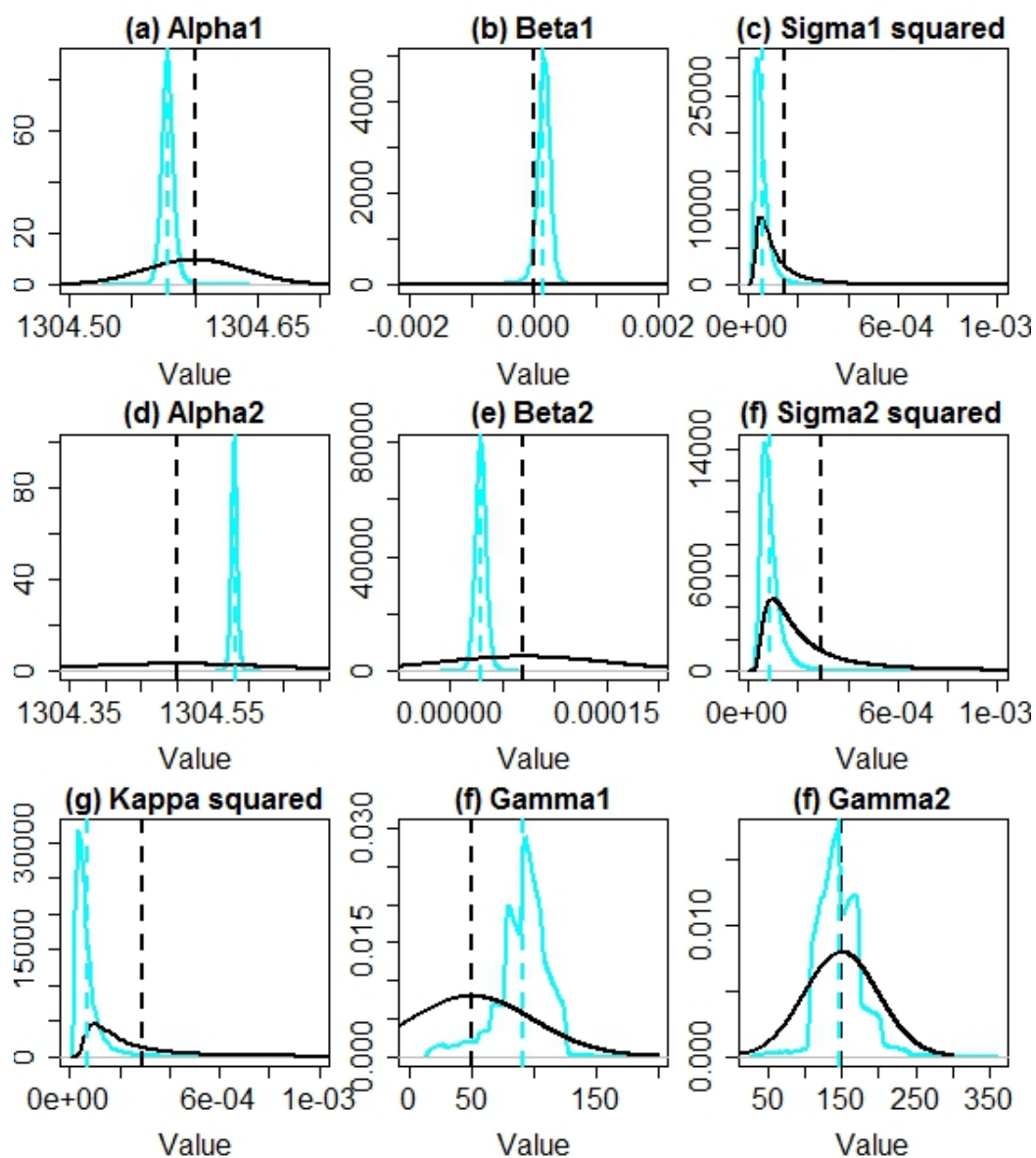


Figure D.13: Conditional posterior density plots of the Brownian bridge model of E1 asphaltene.

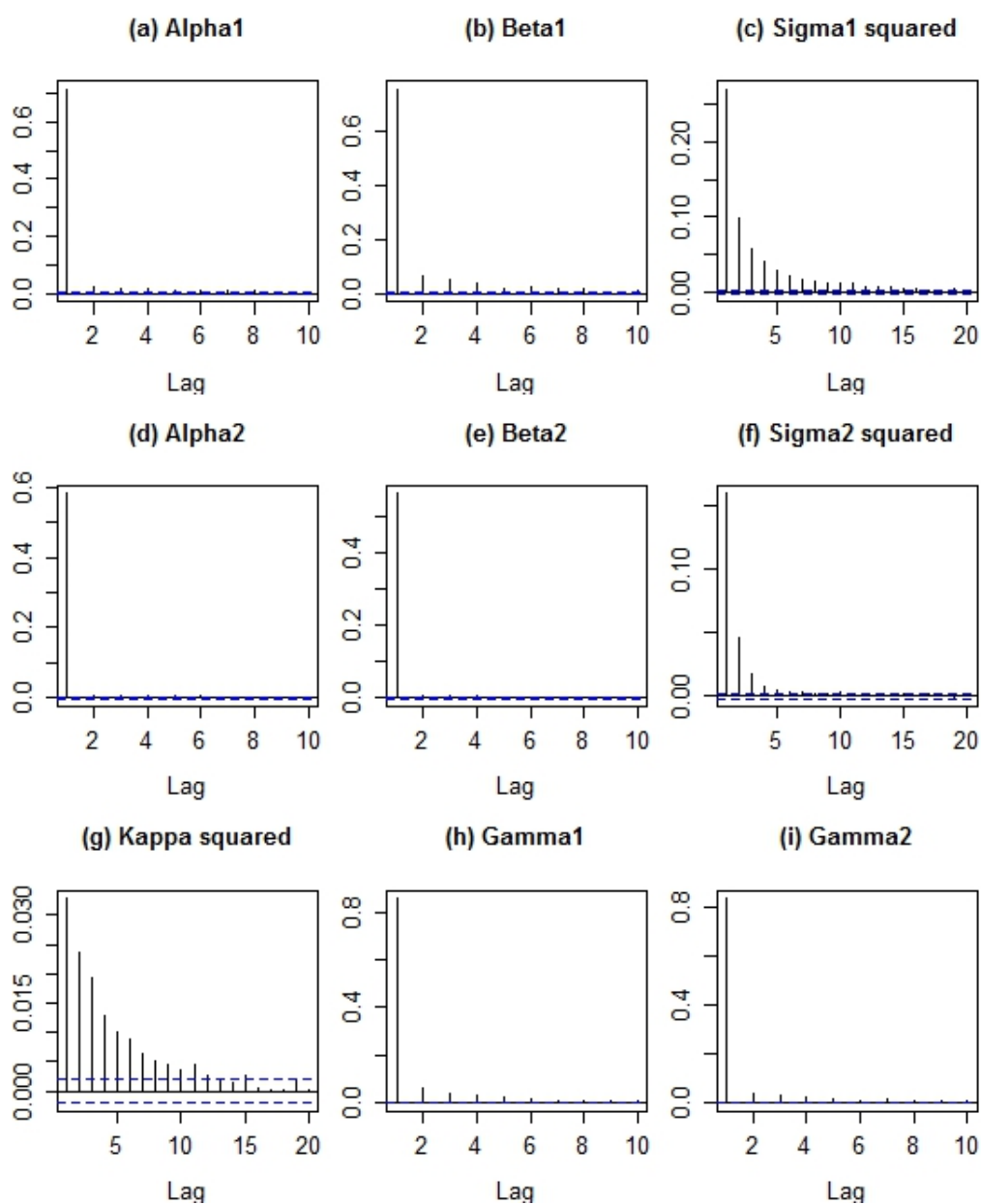


Figure D.14: Partial autocorrelation plots of the MCMC sampling from the conditional posterior distributions of the Brownian bridge model of E1 asphaltene.